Solar radiative transfer parameterizations for three-dimensional effects in cloudy atmospheres

Matthias Peter Jerg

München 2006

Solar radiative transfer parameterizations for three-dimensional effects in cloudy atmospheres

Matthias Peter Jerg

Dissertation
an der Fakultät für Physik
der Ludwig–Maximilians–Universität
München

vorgelegt von
Matthias Peter Jerg
aus Ludwigshafen am Rhein

München, den 14.09.2006

Erstgutachter: Prof. Dr. Susanne Crewell
Zweitgutachter: Prof. Dr. Thomas Trautmann
Tag der mündlichen Prüfung: 11.12.2006

Für meine Eltern.

To my parents.

Contents

List of Figures

List of Tables

Zusammenfassung

Diese Arbeit befaßt sich mit zwei Hauptproblemen des Strahlungstransportes (ST) in der Erdatmosphäre. Das erste Problem ist eng verbunden mit dem Bedarf des ST an Computerresourcen innerhalb eines dreidimensionalen (3D) Atmosphärenmodells. Obgleich nur hocheffiziente eindimensionale (1D) Modelle Säule für Säule unabhängig voneinander verwandt werden, ist es nicht möglich die Strahlungstransportgrößen ebenso häufig wie die meteorologischen Variablen zu berechnen. Daher werden die Strahlungsgrößen für einen längeren Zeitraum konstant gehalten, während die meteorologischen Variablen ständig neu berechnet werden. Trotz des Fehlens detaillierter Untersuchungen über die Folgen dieses Mißverhältnisses, wird in dieser Arbeit der Versuch gemacht ein ST Modell zu entwickeln, mit dem die schnelle Berechnung von grundlegenden Strahlungsgrößen möglich ist und diese häufiger als bisher berechnet werden könnten. Das entwickelte Modell basiert auf der Anwendung der Strahlungsstörungstheorie auf realistische Wolken Säule für Säule. Es wurde durch mehrere Test demonstriert, daß dieses Verfahren, welches als Ersatz für die Independent Pixel Approximation (IPA) dienen soll, siehe unten, anwendbar ist, und innerhalb der gemachten Annahmen vielversprechende Resultate erzielt werden. Abhängig vom konkreten Fall bleiben Fehler in der Transmission und Reflektion einzelner Pixel auf $10\% - 15\%$ beschränkt. In einem Fall konnte die erzielte Rechenzeitersparnis untersucht werden. Obgleich keine numerische Optimierung verwandt wurde, wurde eine Beschleunigung der Rechnung gegenüber dem herkömmlichen IPA Verfahren um den Faktor vier erreicht.

Das zweite Problem betrifft die realistische Beschreibung der 3D Wechselwirkungen von Wolken und solarer Strahlung. Wie zuvor angedeutet werden gewöhnlich 1D ST Modelle im IPA Modus innerhalb eine Atmospärenmodells aufgerufen. Durch dieses Verfahren werden grundlegende 3D Effekte vernachlässigt. Diese umfassen nicht nur kleinräumige Beiträge durch diffusen ST, sondern auch großräumige Muster wie geometrische Effekte der schrägen Sonneneinstrahlung. Beispiele sind unscharfe Strahlungsstrukturen und die verschobene Position von Schatten. Während der letzten Jahre wurden verstärkt Anstrengungen unternommen diese Effekte zu parametrisieren. Keine Methode hat sich jedoch bisher als vollständig zufriedenstellend und implementierbar erwiesen. Um diese Entwicklung einen Schritt weiter zu treiben wurden zwei Ansätze aufgegriffen und weiterentwickelt. Der Erste ist die Tilted Independent Pixel Approximation (TIPA). Im Gegensatz zur IPA, die die solare Geometrie ignoriert, bildet dieses Verfahren die schräge Beleuchtung durch eine Verfolgung des direkten Strahles korrekt ab. Dadurch finden sich die optischen Eigenschaften in schrägen Säulen in einer realistischeren Reihenfolge wieder, und die Schwächung und Position der Strahlungsgrößen werden exakter als bei der IPA wiedergegeben. Um die Methode zu verbessern wurde eine Transformation entwickelt, die es erlaubt eine 3D Auflösung der Strahlungsgrößen zu erhalten. Da die TIPA jedoch keinen horizontalen Photonenaustausch gestattet, wurde noch der Ansatz der Nonlocal Independent Pixel Approximation (NIPA) hinzugezogen. Dieses Verfahren benutzt 1D Resultate und führt ein Faltungsprodukt aus, um Strahlungsgrößen über Säulen hinweg zu verteilen. Um eine vollständig unabhängige Anwendung zu erhalten, wurde eine vereinfachte Bestimmung der Faltungsparameter entwickelt. Zu guter Letzt wurden TIPA und NIPA zur NTIPA kombiniert. Diese Ansätze haben sich bezüglich einer Reihe von Kriterien als der IPA überlegen erwiesen. Die Verbesserung gegenüber dieser bewegt sich zwischen einigen Prozent und bis zu 50% bezüglich der maximalen Fehler von Transmission und Reflektion. Ergebnisse wie die Verteilung der Fehler oder die Vertikalprofile sind ebenfalls günstiger als bei der IPA.

Abstract

This thesis addresses two major problems in the field of radiative transfer (RT) in the earth's atmosphere. The first problem is linked with the need for significant computational resources of RT in a three-dimensional (3D) atmospheric model. Although only highly efficient one-dimensional (1D) RT models are employed for each pixel of the model domain separately and independently, it is still not possible to utilize these models on a frequent basis, compared to the rate at which meteorological variables are computed. That means that the calculated radiative properties (RP) are held constant for a longer period of time, while the prognostic meteorological variables are updated at a rapid rate. Even though there is no detailed study about the consequences of this disproportion, an attempt was made to develop an RT model which permits the fast computation of basic radiative transfer properties which could be used in the future to update this information more frequently. The developed model is based on the application of the radiative transfer perturbation theory to realistic cloud fields column by column. It turned out that the application, intended to replace the Independent Pixel Approximation (IPA), see below, is possible and promising within the assumptions and constraints of the utilized methods. It could be demonstrated that, depending on the actual case, errors in the pixel transmission and reflection stay bounded to values of up to $10\% - 15\%$. In one case the achieved acceleration could be investigated. It was about a factor of four compared to the direct application of the usual forward variant of the model, although no numerical optimization was carried out.

The second problem concerns the realistic treatment of the 3D interactions of clouds and solar radiation. As implied in the above paragraph, 1D RT models are usually employed column by column which suppresses the exchange of radiation between those columns. Thus, fundamental 3D effects are neglected by this so-called Independent Pixel Approximation (IPA). These comprise not only small scale contributions due to diffuse radiative transport, but also large scale patterns like geometric effects of the inclined solar illumination. Examples are blurred radiative structures due to radiative smoothing and the shifted location of shadows and bright areas. To parameterize those effects strong efforts have been undertaken during the last couple of years. However, no method has proven to be completely satisfactory and ready for implementation. To carry this research one step further two approaches have been adopted and extended. The first is the concept of the Tilted Independent Pixel Approximation (TIPA). In contrast to the IPA, which ignores the solar geometry, this method correctly accounts for the slant illumination due to the correct tracking of the direct beam. As a result, the optical parameters in the slant columns are arranged in a more realistic order and the attenuation and the positions of the RP are less erroneous. To further improve this method a transformation has been developed which yields 3D resolution of the RP in the original grid. Since the TIPA still does not include any diffuse radiative exchange as another approach the Nonlocal Independent Pixel Approximation (NIPA) has been explored. This technique uses 1D results and carries out a convolution product to distribute RP across column boundaries. In order to arrive at a fully independent treatment of this method a simplified derivation of the convolution parameters was developed. Finally, TIPA and NIPA are combined to form NTIPA. These approaches have proven to be superior to IPA with respect to several aspects. The improvement ranges from several percent to 50% if maximum errors of the transmitted and reflected light are considered. Criteria like the distribution of the errors or the vertical profiles of the RP are also more preferable than their counterparts derived by IPA.

Chapter 1

Introduction

> All models are wrong, but some are useful.
>
> ――――――――――――――――――――
>
> George E. P. Box

In this introductory chapter the motivation of the thesis and the potential interrelation of the conducted work with other areas of atmospheric modeling will be described. Furthermore, a brief overview of the current state of the art of science and of the methods and models applied for this work will be given together with an outline of the thesis.

1.1   Motivation of the Conducted Work

The presented study was part of the project 4D-clouds (2005) and is dedicated to the development of solar radiative transfer parameterizations for cloudy atmospheres. Clouds are highly variable in space and time. Their scales cover a broad range from several hundreds of meters of isolated clouds to many kilometers of coherent large scale cloud clusters and weather systems. Clouds also contribute in manyfold ways to the complexity of atmospheric physics and chemistry. Examples are the interaction of evaporation, cloud formation and decay, and precipitation. Solar radiation plays an important role in driving and coupling these dynamic and thermodynamic processes with other parts of the geophysical system like the surface of the earth and the oceans, see Figure 1.1. The detailed and realistic treatment of cloud-radiation interactions is for these reasons an inevitable necessity. Although the magnitude of the general mean and global effects of these interactions on the radiative budget of the earth seems to be reasonably well understood and estimated, see Figure 1.2, there are still numerous uncertainties in the details of these processes. Even if the resulting radiative forcing is small with respect to the average global and annual budget the implications for climate on all scales can be significant. This fact is also documented by the relatively large uncertainties associated with the radiative forcing exerted by clouds and aerosols, see Figure 1.3. The cloud effects are summarized by the term "Aerosol indirect effect" which refers to the role aerosols play in cloud droplet formation.

From Figure 1.3 it can be learned that the scientific understanding of those effects is rather low, while the assumed impact on the radiative forcing is among the highest of all processes relevant to climate. However, this contribution refers rather to the microphysical processes which are involved in the formation and conversion of aerosols and cloud droplets. Yet, clouds not only solely interact via their pure microphysical parameters with radiation but also due to the spatial distribution of those parameters and the resulting cloud texture and shape. Those features are also believed to fundamentally affect the radiative transfer budget by three-dimensional (3D) interactions of clouds and radiation. The inappropriate treatment of those interactions can lead to related effects like errors in the computed planetary albedo. This could further result in an erroneous estimate for the global mean temperature. These feedbacks are not even fully accounted for and therefore not included in the scope of uncertainties.

However, current atmospheric models, this term is supposed to comprise all kinds of classes of models describing the interactions of the components of atmospheric physics like Large Eddy Simulation (LES) models, weather prediction models and climate models, mostly lack a detailed representation of clouds and the radiative processes associated, no matter at which spatial and temporal scales they are applied. For a comparison of these models with respect to their spatial scales see Table 2.1. As a result, atmospheric models generally suffer from two major setbacks concerning the interaction of clouds and radiation. Both result from the inhomogeneity of the optical properties of clouds, their distribution and shape, and their steady evolution in time. Additionally, computational constraints exacerbate the problem.
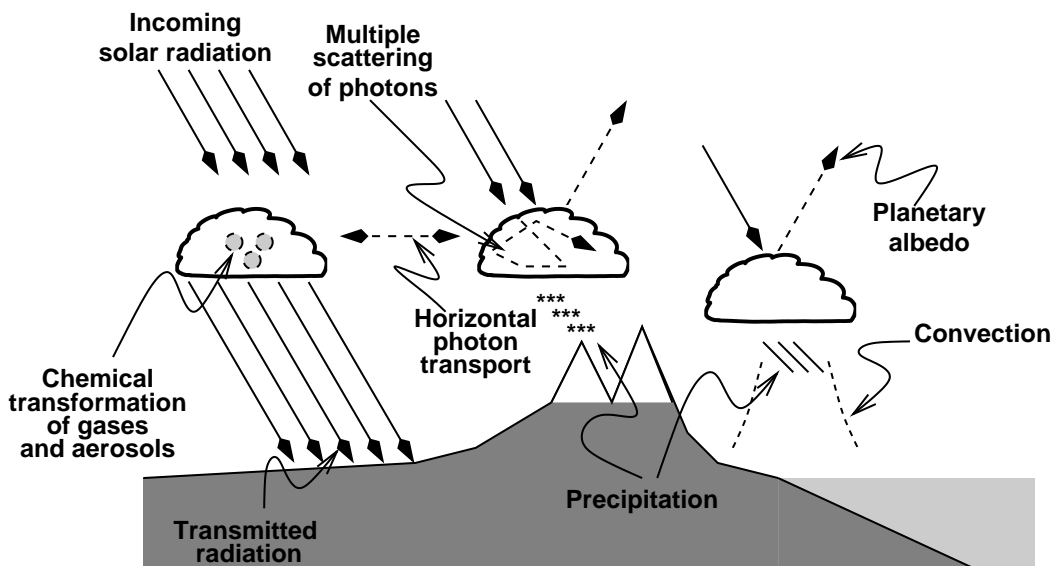
Figure 1.1: Some of the interactions of clouds and radiation and their connection to other processes.
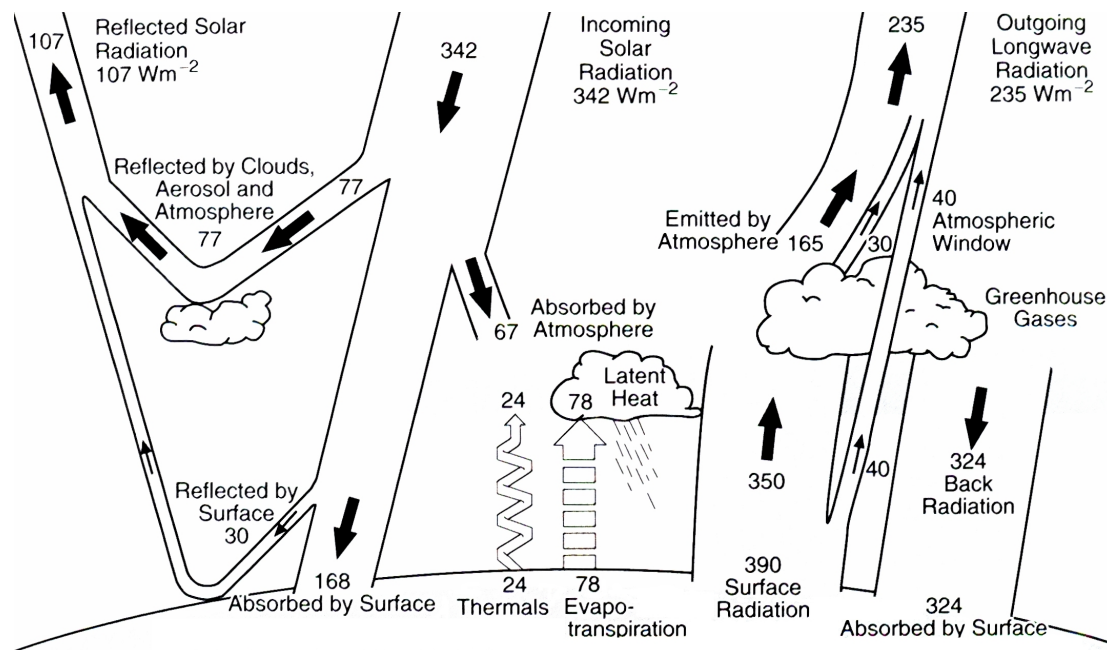
Figure 1.2: Annual global mean energy budget of the earth. Units are in Wm^{-2}. Adapted from Kiehl and Trenberth (1997).

The first drawback is the lack of realistic treatment of 3D interaction of clouds and radiation. Atmospheric models usually employ one-dimensional (1D) radiative transfer models pixel-by-pixel. This procedure is termed Independent Pixel Approximation (IPA). It only requires the 1D radiative transfer code to be applied in each model column independently of its neighbors, see Cahalan et al. (1994b). Because of the tremendous computational burden, an immediate application of a 3D radiative transfer model is out of the question. As a result of the IPA, the optical properties are incorporated in the computation three-dimensionally correct, yet no full 3D propagation of photons is accounted for as no horizontal radiative exchange is possible in this configuration.

The second drawback is related to the computational burden even the IPA poses. The radiative transfer part of an atmospheric model comprises only one module among many others, and therefore has to share computational resources. Moreover, the dynamic and thermodynamic equations of atmospheric models have to be integrated incrementally with the help of numerical techniques. The applied time step results from the size of the grid and the maximum speed of propagation of the meteorological processes which are described by the model's physics and is a consequence of the demand for numerical stability of the solution. It is usually in the range of several dozens of seconds for weather prediction models, but can also be considerably smaller. In contrast to that, the radiative transfer code is called far less frequently. Typically, radiative properties like fluxes and heating rates are updated in weather prediction models only every hour. In the weather prediction model which is referred to in this study for all other points of time between two updates the radiative properties are held constant.
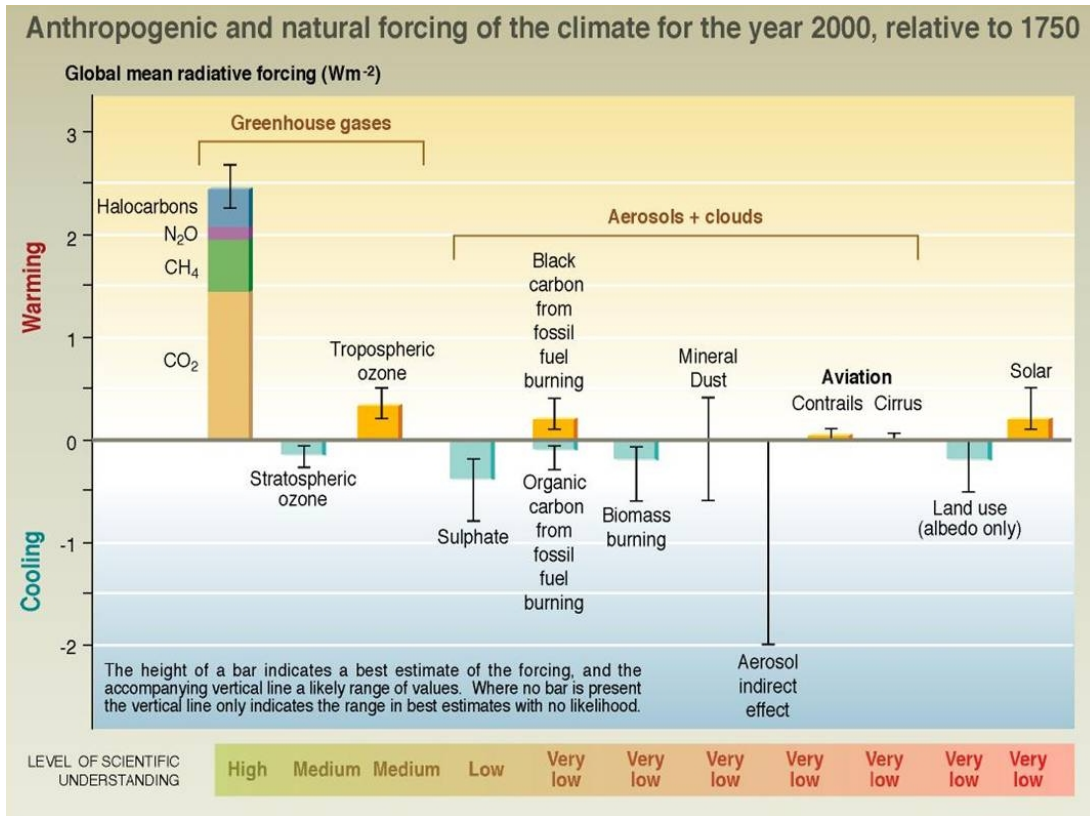
Figure 1.3: Global mean radiative forcing of different anthropogenic and natural processes and their error estimates together with the associated scientific understanding. Units are in Wm^{-2}. Taken from Houghton et al. (2001).

Both problems are believed to impact model results and, as a consequence of the coupling of the atmospheric processes and scales, also the forecast reliability. Moreover, the implications of these shortcomings not only affect atmospheric models of limited domains, but also global climate models. Thus, those uncertainties could have significant consequences for the predicted planetary radiative budget and climate, most crucially via the influence on the planetary albedo, see Houghton et al. (2001). The necessity of the development of parameterizations for these groups of problems is not limited to forward radiative transfer, but it has also value for radiative transfer inversion techniques for remote sensing of clouds, as the underlying 3D effects and assumptions are the same, see Marshak and Davis (2005).

The presented work pursues for these reasons two separate but combinable contributions to tackle the problems mentioned above. The first is the development a parameterization approach in order to accelerate 1D radiative transfer calculations. Furthermore, the potential applicability of the method to independent pixel calculations for high resolution cloud scenes is investigated. The constructed approach is based on the radiative transfer perturbation theory. This innovative technique is utilized to derive radiative transfer results by interpreting the state of the optical properties of the atmosphere as a combination of

a base case and deviations from this base case, which are then termed perturbations. The impact of those on radiative properties can be accounted for by linearizing the radiative transfer problem which in general permits rapid computation.

The second aim of the thesis is to develop radiative transfer parameterizations for 3D cloud-radiation interactions and to enhance existing techniques, respectively. As a first step, a modified version of the Tilted Independent Pixel Approximation (TIPA), see Várnai and Davies (1999), which accounts for 1D calculations in slant columns, is developed. The primary effect tackled by this concept is the geometrically correct transfer of direct and slightly scattered light leading to the deepest shadows of clouds. As a second parameterization, the Nonlocal Independent Pixel Approximation (NIPA), see Marshak et al. (1995), has been adopted and has been equipped with an idealized physical background to describe horizontal photon transport. This concept aims at modeling diffuse radiative transport which blurs radiative patterns by radiative smoothing due to massive multiple scattering. Both approaches are then combined and all of the three resulting parameterizations are applied to several cloud scenes differing due to their source and horizontal resolution. All 3D parameterizations are compared both with the IPA and exact 3D results from a Monte-Carlo model, see below, which serve as references.

1.2 State-of-the-art of Science

As mentioned above, the IPA is the state-of-the-art solar radiative transfer method to compute fluxes and heating rates in atmospheric models. For a couple of years it has been noted that this technique causes significant errors on a local level, see for example O'Hirok and Gautier (1998). A comprehensive overview of the inabilities of the IPA with respect to realistic 3D effects will be given in section 4.1. Ever since, there have been efforts to improve not only the understanding of 3D cloud-radiation interactions but also to develop parameterizations. Those are always governed by the trade-off between accuracy and computational resources, primarily with respect to computational speed. Some parameterizations are based on deterministic radiative transport and can be regarded as extensions of the 1D technique. As this includes the ones developed in this study, a detailed description is postponed to later sections. As yet, parameterizations which truly employ a 3D radiative transfer model are rare, see for example Chen et al. (2005). Other parameterizations make use of stochastic approaches, see Lane-Veron and Sommerville (2004), or are based on features concerning the 3D variablity of the optical properties, see Cairns et al. (2000). A comprehensive overview has been compiled by Davis (2000).

Concerning the above mentioned slow update rate of radiative transfer calculations, there seems to be no existing flexible approach facing this problem besides the radiative transfer perturbation theory which has also been used in this study. For existing applications of this technique to accelerate radiative transfer see Gabriel et al. (1998). These authors applied the perturbation theory to broadband calculations while this study focuses on monochromatic IPA calculations.

It has also to be noted that the actual impact of both the neglect of 3D effects and of the

slow update rate of the radiative field on the forecast of atmospheric models seems to be almost un-investigated. Regarding 3D effects, there have been studies by Fu et al. (2000) with a climate model which reveal an impact on the planetary albedo of several percent. Schumann et al. (2002) have investigated the consequences for vertical motion and heat flux with the help of a simple conceptual approach together with an idealized LES model, while a simplified realization of radiative transport and the resulting cloud shadows was adopted. With these assumptions the authors find only small differences between modeling the shadows directly below clouds, as computed by the IPA, and modeling them shifted sidewards according to the solar illumination. However, both the atmospheric model and the radiative transfer representation are rather simplified and no conclusive estimates for realistic situations have been derived yet. There are no systematic investigations about the impact of the update interval of the radiative transfer field on atmospheric model results known to the author. Given the sometimes rapid formation, decay, and movement of clouds, depending on the meteorological situation, it can only be assumed that the impact is significant at least at a local temporal and spatial level.

This work as well does not investigate these questions directly but rather seeks to advance the current knowledge in providing improved parameterizations. These parameterizations are still simple enough for potential implementation in atmospheric models, yet yield radiative transfer results with 3D resolution. Furthermore, the parameterizations have been applied to several cloud scenes among them some which are originating from a weather prediction model. The 3D effects associated with those clouds are investigated as well as the capability of the parameterizations in accounting for them.

1.3   Outline of the Thesis and Applied Methods and Models

As this thesis focuses on the development and modification of parameterization approaches, extensive use of radiative transfer theory has been made of. This is mainly reflected by chapter 2 which provides the theoretical background of radiative transfer modeling, as it was utilized in the presented work. It introduces radiative and optical properties, as well as the basic radiative transfer equations especially for the 1D problem, and with explicit reference to the discrete ordinate radiative transfer model DISORT, see Stamnes et al. (1988). This model has been used for all 1D calculations. All exact 3D results have not been derived by the author but were provided by Sebastián Gimeno García and derived by the Leipzig Monte Carlo Model (LMCM), if not stated otherwise. For details about the LMCM and its application see Gimeno García (2006) and Gimeno García and Trautmann (2003). Chapter 3 provides an introduction in adjoint radiative transfer together with its utilization for the radiative transfer perturbation technique. This technique is elaborated on a general 1D perspective, and several examples are given for the different stages and features of the development. This chapter provides the background for the derived radiative transfer acceleration. Chapter 4 discusses the 3D parameterizations starting with a

general description of the problem, the different 3D effects, and an overview of the various parameterization approaches. Subsequently, an introduction in the variant of the TIPA which was developed here is given. As a novelty of this technique, a slant coordinate is derived geometrically in a simple fashion and in the course of the simulation radiative properties are derived at every position of the grid. This section is followed by several examples in order to shed some light on the basic features of the technique. The following section deals with the NIPA which is the second parameterization approach adapted here. As a second novelty, the physical core of this approach has been based on a simplified simulation of the radiative diffusion process itself. The outline of this method is briefly described together with its assumptions and prerequisites. The chapter finally ends with a combination of both aforementioned parameterizations, and several idealized examples again show the capabilities and shortcomings of the techniques. Chapter 5 contains in its first part the application of the developed radiative transfer acceleration technique to some high resolution realistic cloud fields while the second part deals with the results of the 3D parameterization approaches for several classes of cloud scenes. These comprise high, intermediate, and coarse resolution scenes. Chapter 6 finally reviews the developments and results, relates them to the purpose of this study, and suggests several steps for further improvements and prerequisites for the actual implementation in atmospheric models.

Chapter 2

Radiative Transfer Fundamentals

> Things should be made as simple as
> possible, but no simpler.
>
> ――――――――――――――――――
>
> Albert Einstein

This chapter mainly serves to introduce the basic definitions of radiative and optical properties of solar radiative transfer in the earth's atmosphere which are used in the context of this work. Furthermore, the exact equations governing this transfer in one and three dimensions will be introduced. Yet, only the solution of the former will be further discussed as no exact 3D radiative transfer was dealt with directly by the author.

2.1 Definition of Radiative Properties

In order to model radiative transfer (RT) and measure radiative properties some basic quantities are defined in the next sections. A similar but more comprehensive introduction can be found in Liou (2002) and in Chandrasekhar (1960).

The probably most basic radiative property is the photon density f_ν:

$$f_\nu(\boldsymbol{r}, \boldsymbol{\Omega}, t) \tag{2.1}$$

It describes the number of photons per volume, propagating in a certain direction $\boldsymbol{\Omega}$ into the section $d\Omega$ of the solid angle, see Figure 2.1, in the frequency interval $[\nu, \nu + \Delta\nu]$, at the position $\boldsymbol{r} = (x, y, z)$, and time t. The general coordinate system is shown in Figure 2.2. Frequency ν and wavelength λ are connected by:

$$c = \lambda\nu \tag{2.2}$$

where c is the speed of light.
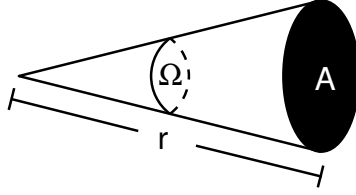
Figure 2.1: Definition of the solid angle Ω created by the surface A at distance r.

The solid angle is hereby defined as:

$$\Omega = \frac{A}{r^2} \tag{2.3}$$

It can be considered as the opening of a cone which cuts out the area A of the surface of a sphere at distance r. The solid angle is measured in steradian, sr. For the general description of the direction of propagation of light usually the spherical coordinate system is used as the local coordinate system at the point of interest, see Figure 2.3. The unit vector of propagation takes then the form:

$$\boldsymbol{\Omega} = \begin{pmatrix} \sin\theta\cos\varphi \\ \sin\theta\sin\varphi \\ \cos\theta \end{pmatrix} \tag{2.4}$$

The system's origin can be considered positioned in point C in Figure 2.2 with its vertical axis parallel to the vertical axis of the general coordinate system. The position of C is usually prescribed in Cartesian coordinates. With the help of the azimuthal angle φ and the zenith angle θ for $d\Omega$ follows:

$$d\Omega = \frac{dA}{r^2} = \sin\theta d\theta d\varphi \tag{2.5}$$

The integration over the whole unit sphere is expressed by the following notation:

$$\int_{4\pi} d\Omega = \int_0^{2\pi}\int_0^{\pi} \sin\theta d\theta d\varphi = 4\pi \tag{2.6}$$

A more handy radiative property is derived by multiplying the photon density with the photon energy $h\nu$ and the speed of light c. The resulting quantity:

$$I(\boldsymbol{r},\boldsymbol{\Omega},t) = ch\nu f_\nu(\boldsymbol{r},\boldsymbol{\Omega},t) \tag{2.7}$$

is called intensity or more often radiance. It describes the power per square meter of the photons, propagating in direction $\boldsymbol{\Omega}$ into the section $d\Omega$, in the frequency interval $[\nu,\nu+\Delta\nu]$, at position $\boldsymbol{r}$, and time t.
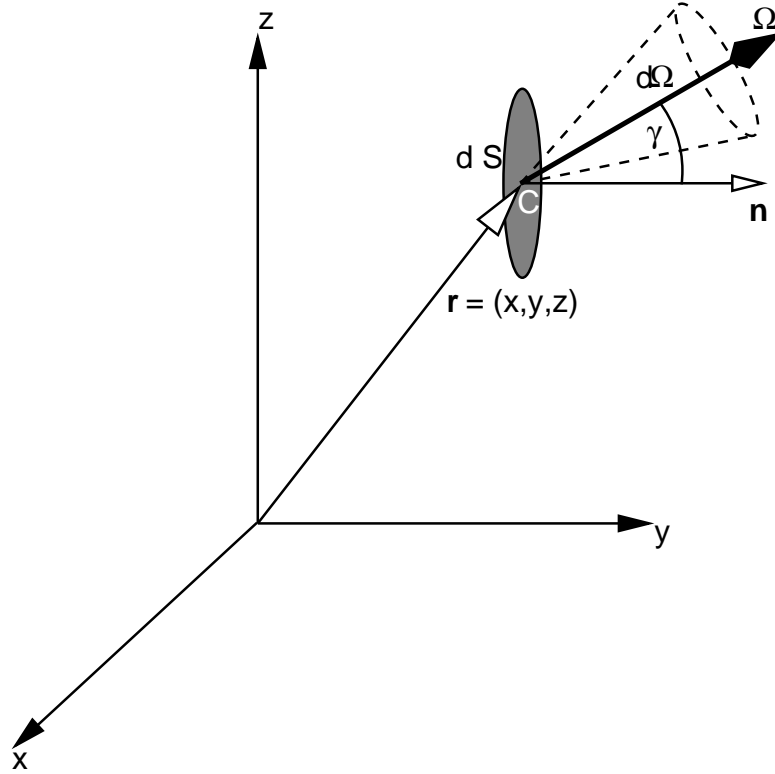
Figure 2.2: Definition of the general Cartesian coordinate system. dS is an arbitrary surface element at position $\boldsymbol{r}$ with the normal $\boldsymbol{n}$ forming the angle γ with the radiation propagating in direction $\boldsymbol{\Omega}$ centered in the solid angle $d\Omega$.

Radiative properties, derived by integrating the intensity over the solid angle, are of special interest for the connection of radiative power with thermodynamics and photo-chemistry. Most important are the net flux-density $\boldsymbol{E}_N$ and the actinic flux F_{act}. $\boldsymbol{E}_N$ is defined as the radiative power crossing the unit sphere in all directions. It has the form of a vector:

$$\boldsymbol{E}_{N,\nu}(\boldsymbol{r},t) = \int\limits_{4\pi} \boldsymbol{\Omega} I_\nu(\boldsymbol{r},\boldsymbol{\Omega},t)d\Omega \qquad (2.8)$$

From here on the subscript ν, indicating frequency dependence, will be dropped, as all radiative and optical quantities are believed to depend on the frequency of the light, if not stated otherwise.
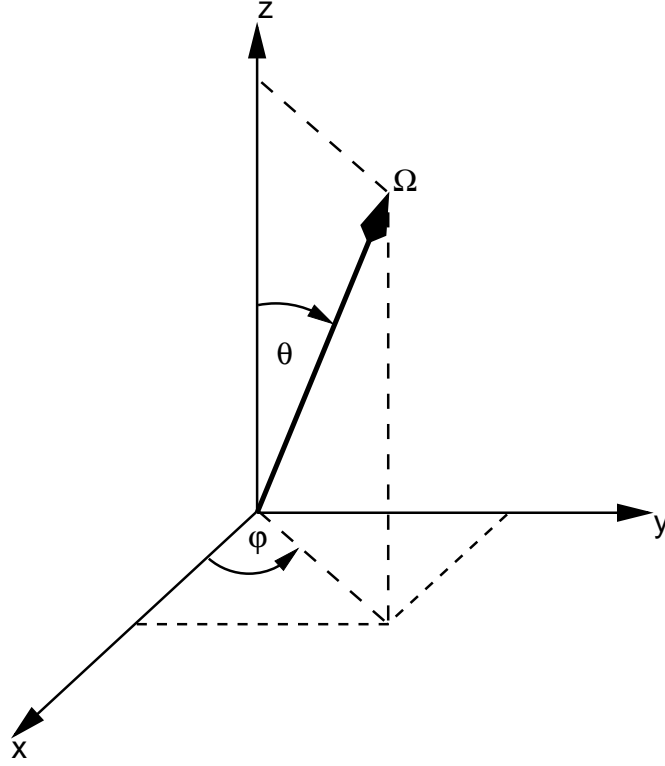
Figure 2.3: Definition of the local coordinate system. Radiation propagates in direction
$\mathbf{\Omega}$ which is defined by the zenith angle θ and azimuthal angle φ in spherical
coordinates.

After introducing $\mu = \cos\theta$, the three spatial components of $\boldsymbol{E}_N$ in spherical coordinates
can be written with the help of relation 2.4 in the form:

$$E_{N,x}(\boldsymbol{r},t) \;=\; \int_0^{2\pi}\int_0^{\pi} I(\boldsymbol{r},\theta,\varphi,t)\cos\varphi\sin^2\theta d\theta d\varphi \tag{2.9}$$

$$=\; \int_0^{2\pi}\int_{-1}^{1} I(\boldsymbol{r},\mu,\varphi,t)\cos\varphi\sqrt{1-\mu^2}d\mu d\varphi \tag{2.10}$$

$$E_{N,y}(\boldsymbol{r},t) \;=\; \int_0^{2\pi}\int_{-1}^{1} I(\boldsymbol{r},\mu,\varphi,t)\sin\varphi\sqrt{1-\mu^2}d\mu d\varphi \tag{2.11}$$

$$E_{N,z}(\boldsymbol{r},t) \;=\; \int_0^{2\pi}\int_{-1}^{1} I(\boldsymbol{r},\mu,\varphi,t)\mu d\mu d\varphi \tag{2.12}$$

Components of equations 2.10 to 2.12 with respect to hemispheres are derived by choosing

appropriate integration limits for μ. From equation 2.12 upwelling $E_\uparrow$ and downwelling $E_\downarrow$ flux-densities can be derived accordingly. These are sometimes called irradiances or slightly incorrect just fluxes. They are important for defining transmission T and reflection R:

$$T(x,y) = \frac{E_\downarrow(x,y,z=0)}{E_\downarrow(x,y,z=TOA)} \quad ; R(x,y) \quad = \frac{E_\uparrow(x,y,z=TOA) - E_\uparrow(x,y,z=0)}{E_\downarrow(x,y,z=TOA)} \quad (2.13)$$

TOA stands for Top Of Atmosphere and represents the upper boundary of the considered domain. Similar to the net flux-density is the definition of the actinic flux:

$$F_{act}(\boldsymbol{r},t) = \int\limits_{0}^{2\pi} \int\limits_{-1}^{1} I(\boldsymbol{r},\mu,\varphi,t)d\mu d\varphi \quad (2.14)$$

The connection of the net-flux with heating-rates is given by the first law of thermodynamics, see Zdunkowski and Bott (2004):

$$c_p \frac{dT(\boldsymbol{r},t)}{dt} = -\alpha(\boldsymbol{r},t)\boldsymbol{\nabla}\cdot(\boldsymbol{J}^q(\boldsymbol{r},t) + \boldsymbol{E}_N(\boldsymbol{r},t)) + \alpha\boldsymbol{\mathcal{J}}(\boldsymbol{r},t)\cdot\cdot\boldsymbol{\nabla}\boldsymbol{v}(\boldsymbol{r},t) \quad (2.15)$$

All terms except $-\alpha\boldsymbol{\nabla}\cdot\boldsymbol{E}_N$ refer to non-radiative heat sources and can therefore be neglected in this context. One derives:

$$\left(\frac{\partial T(\boldsymbol{r},t)}{\partial t}\right)_{rad} = -\frac{1}{\rho(\boldsymbol{r},t)c_p}\boldsymbol{\nabla}\cdot\boldsymbol{E}_N(\boldsymbol{r},t) \quad (2.16)$$

The different components of the net-flux can be interpreted as fluxes across the coordinate layers. For example E_z is the flux density balance with respect to the light crossing the surface with $z = const.$ in vertical direction. In contrast to that, the actinic flux describes the omnidirectional power across the unit sphere towards the sphere's center, which can be a molecule for example. Therefore, it is of importance when one is interested in the radiative budget with respect to a point. This is the case when calculating photodissociation coefficients in atmospheric chemistry.

2.2   Definition of Optical Properties

The effects of radiation interacting with matter can be divided in three major phenomena: 1.) absorption, 2.) scattering, 3.) emission.

Absorption

The absorption of a photon, meaning the reception of the photon's energy by a molecule or a particle, is described by the absorption coefficient σ_a and the mass absorption coefficient χ_a. Both are connected by the absorber density ρ_a via:

$$\sigma_a(\boldsymbol{r},t) = \rho_a(\boldsymbol{r},t)\chi_a(\boldsymbol{r},t) \quad (2.17)$$

A measure for the probability of absorption within the path increment ds is the differential absorption optical depth $d\tau_a$:

$$d\tau_a(\boldsymbol{r}, t) = \sigma_a(\boldsymbol{r}, t)ds \tag{2.18}$$

Scattering

The process of scattering changes the direction of propagation and, in case of inelastic scattering, the energy and thus the frequency of the photon. Analogously to the absorption, the differential scattering optical depth is defined as:

$$d\tau_s(\boldsymbol{r}, t) = \sigma_s(\boldsymbol{r}, t)ds \tag{2.19}$$

with σ_s being the scattering coefficient. Apart from that, the differential scattering optical depth can be defined as:

$$d\tau_s(\boldsymbol{r}, t) = \sigma_{s,d}(\boldsymbol{r}, \nu' \rightarrow \nu, \boldsymbol{\Omega}' \rightarrow \boldsymbol{\Omega}, t)dsd\nu d\Omega \tag{2.20}$$

where $\sigma_{s,d}$ is the differential scattering coefficient. It describes the change of the direction of propagation from $\boldsymbol{\Omega}'$ to $\boldsymbol{\Omega}$ and the shift in frequency from ν' to ν. Both scattering coefficients are connected:

$$\sigma_s(\boldsymbol{r}, t) = \int\limits_0^\infty \int\limits_{4\pi} \sigma_{s,d}(\boldsymbol{r}, \nu' \rightarrow \nu, \boldsymbol{\Omega}' \rightarrow \boldsymbol{\Omega}, t)d\Omega d\nu \tag{2.21}$$

The differential scattering coefficient can be split up itself:

$$\sigma_{s,d}(\boldsymbol{r}, \nu' \rightarrow \nu, \boldsymbol{\Omega}' \rightarrow \boldsymbol{\Omega}, t) = \frac{1}{4\pi}\sigma_s(\boldsymbol{r}, t)\, p(\boldsymbol{r}, \nu' \rightarrow \nu, \boldsymbol{\Omega}' \rightarrow \boldsymbol{\Omega}, t) \tag{2.22}$$

The phase function p describes the dependence between the sets of variables $(\nu', \boldsymbol{\Omega}')$ and $(\nu, \boldsymbol{\Omega})$. It can be regarded as the probability density distribution for the scattering from the primed to the unprimed state. To this end it is normalized:

$$\frac{1}{4\pi} \int\limits_0^\infty \int\limits_{4\pi} p(\boldsymbol{r}, \nu' \rightarrow \nu, \boldsymbol{\Omega}' \rightarrow \boldsymbol{\Omega}, t)d\Omega d\nu = 1 \tag{2.23}$$

In the atmosphere usually the reciprocity of the way the light travels is assumed. That means that the phase function does not depend on the values of $\boldsymbol{\Omega}'$ and $\boldsymbol{\Omega}$ in an absolute manner but rather on the angle between those two which is called scattering angle Θ. It is:

$$\boldsymbol{\Omega}' \rightarrow \boldsymbol{\Omega} \leftrightarrow \boldsymbol{\Omega}' \cdot \boldsymbol{\Omega} = \cos\Theta = \mu\mu' + \sqrt{1-\mu'^2}\sqrt{1-\mu^2}\cos(\varphi-\varphi') \tag{2.24}$$

Extinction

The addition of absorption and scattering coefficient leads to the extinction coefficient:

$$\sigma_t(\boldsymbol{r}, t) = \sigma_a(\boldsymbol{r}, t) + \sigma_s(\boldsymbol{r}, t) \tag{2.25}$$

It describes the combined attenuation of light propagating in a certain direction $\boldsymbol{\Omega}$ and frequency ν by both processes. Therefore, the extinction optical depth becomes:

$$d\tau_t(\boldsymbol{r}, t) = \sigma_t(\boldsymbol{r}, t)ds = d\tau_a(\boldsymbol{r}, t) + d\tau_s(\boldsymbol{r}, t) \tag{2.26}$$

This property is usually referred to as differential optical depth. The relation between scattering and extinction is called single scattering albedo ω_o:

$$\omega_o(\boldsymbol{r}, t) = \frac{\sigma_s(\boldsymbol{r}, t)}{\sigma_t(\boldsymbol{r}, t)} = 1 - \frac{\sigma_a(\boldsymbol{r}, t)}{\sigma_t(\boldsymbol{r}, t)} \tag{2.27}$$

It gives the fraction of scattering processes in relation to all interactions. A medium with $\omega_o = 1$ is referred to as conservative medium.

Emission

Emission is the release of photons from a source within the medium. The source can be either of thermal or artificial nature. The source function J is given as:

$$J(\boldsymbol{r}, \boldsymbol{\Omega}, t) = h\nu j \tag{2.28}$$

where j is the emission coefficient, describing the number of emitted photons per volume, time, solid angle interval, and frequency interval. The source function gives the released power per volume, solid angle interval, and frequency interval.

Integrated optical depth

The optical depth not only serves as optical property but also as coordinate, see Figure 2.4. The above introduced extinction differential optical depth can be written as:

$$d\tau(\boldsymbol{r}, t) = \sigma_t(\boldsymbol{r}, t)ds$$

The component of $d\tau(\boldsymbol{r}, t)$ along the z-axis is referred to as normal optical depth $d\tau_\perp(\boldsymbol{r}, t)$:

$$d\tau_\perp(\boldsymbol{r}, t) = \sigma_t(\boldsymbol{r}, t)ds_\perp$$

If we assume solar illumination and the atmosphere is considered to be plane-parallel, the optical properties are then independent of the lateral coordinates, one can connect the optical depth with the angle θ_o^*:

$$d\tau(z, t) = \frac{1}{\mu_o^*}d\tau_\perp(z, t)$$

If the normal component $ds_\perp$ is chosen to be oriented in the opposite direction than z, which is natural as $\theta_o \epsilon [\frac{\pi}{2}, \pi]$, $ds_\perp = -dz$, it follows that:

$$d\tau(z,t) = -\frac{\sigma_t(z,t)}{\mu_o^*}dz$$

As $\cos\theta_o^* = -\cos\theta_o$, one derives for the integrated optical depth from TOA to position p:

$$\tau(z,t) \;=\; \int_0^p \sigma_t(s,t)ds = \frac{1}{\mu_o^*}\int_0^{p_z} \sigma_t(s,t)ds_\perp = \frac{1}{\mu_o}\int_{TOA}^z \sigma_t(z',t)dz' \tag{2.29}$$

$$= \; \frac{1}{|\mu_o|}\int_z^{TOA} \sigma_t(z',t)dz' \tag{2.30}$$

It was assumed that the origin of the coordinate s ($s = 0$) is located at TOA. For the last equality in equation 2.29 to hold it was used that $|\mu_o| = \mu_o^*$. The optical depth which is finally deduced is the slant optical depth along the solar beam in an horizontally homogeneous atmosphere. However, optical depth is supposed to refer to the normal optical depth from hereafter:

$$\tau(z,t) = \int_{TOA}^z \sigma_t(z',t)dz' \tag{2.31}$$

The total optical depth is then derived by integrating from TOA to the lower boundary $z = 0$.

Asymmetry factor

The last property, the asymmetry factor g is the first moment of the phase function. It is defined as:

$$g(\boldsymbol{r},t) \;=\; \frac{1}{4\pi}\int_0^{2\pi}\int_{-1}^1 \cos\Theta p(\boldsymbol{r}, \nu' \to \nu, \cos\Theta, t)d(\cos\Theta)d\phi \tag{2.32}$$

$$= \; \frac{1}{2}\int_{-1}^1 \cos\Theta p(\boldsymbol{r}, \nu' \to \nu, \cos\Theta, t)d(\cos\Theta) \tag{2.33}$$

where Θ is the scattering angle as in equation 2.24, and the phase function was assumed to be independent of the azimuthal direction ϕ.

The asymmetry factor is a measure of the shape of the phase function. If $g > 0$ most of the light is scattered into the forward hemisphere, if $g < 0$ backscattering dominates. In the atmosphere the former is usually the case. Isotropic and pure molecular (Rayleigh) scattering are characterized by $g = 0$, see below.
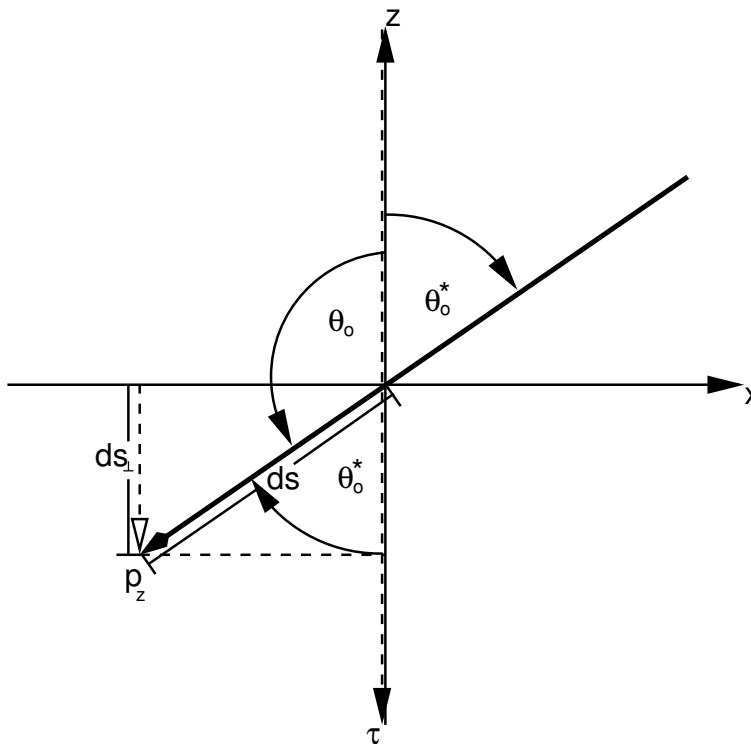
Figure 2.4: The τ-coordinate. θ_o is the solar zenith angle and θ_o^* its supplementary angle. p_z is the geometric position with distance ds along the direction of propagation and $ds_\perp$ perpendicular to the horizontal axis. The coordinate system can be considered positioned at a reference point, usually TOA.

2.3 Optical Properties of the Atmosphere

In the previous section the basic optical properties, which can be directly employed for radiative transfer calculations, have been introduced. In this section a brief description of the derivation of those properties and their relation to the constituents of the atmosphere will be given. This section is based on material presented by Früh (2000) and Salby (1995).

In the earth's atmosphere radiation interacts with molecules of various gases, with suspended aerosol particles, and with cloud droplets. Furthermore, precipitation particles and ice crystals also contribute to those interactions, but those will not be dealt with here and were not considered for the following studies.

Gaseous absorption

Various gases in the atmosphere interact with radiation by absorption. The resulting absorption lines create very distinct patterns in the wavelength spectrum of the radiation which reaches the ground, see Figure 2.5. It is obvious from this figure that O_3, CO_2, and H_2O are the most dominant species in the solar wavelength region.

The absorption coefficient of a species is defined as:

$$\sigma_a = \hat{\sigma}_a(T, z) N_c(z) \tag{2.34}$$

where $\hat{\sigma}_a$ is the absorption cross section of an individual gas molecule as a function of temperature T and vertical position z. N_c is the vertically variable molecular concentration of the species.

Equation 2.34 has to be considered for each atmospheric gas separately. All presented calculations for this study have been monochromatic meaning that only one wavelength has been taken into account. If the radiative transfer budget in a wavelength interval has to be determined, broadband calculations have to be carried out in order to correctly describe wavelength dependent characteristics and interactions of all gases which absorb in this interval. A widespread method to achieve this aim is the k-distribution method, see for example Liou (2002).
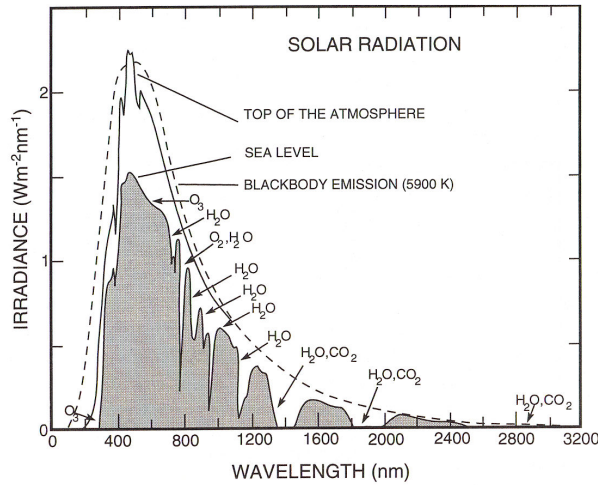
Figure 2.5: Shortwave irradiance as a function of wavelength. Solid line: Solar radiation at the top of the atmosphere. Dashed line: Emission spectrum of a blackbody at 6000K. Shaded area: Radiation at sea level. Several absorbing species are indicated. Adapted from Salby (1995).

Rayleigh scattering

Apart from absorption, air molecules and solar radiation also interact due to scattering. This so-called Rayleigh scattering, see Rayleigh (1871), appears when the particle, here the molecule, is considerably smaller than the wavelength of the radiation. A molecule can then be considered as an electric dipole which oscillates when excited by radiation. The scattering coefficient can be expressed as:

$$\sigma_{ray} = \hat{\sigma}_{ray} N_{air}(z) \tag{2.35}$$

with $\hat{\sigma}_{ray}$ the Rayleigh scattering cross section and N_{air} the vertically variable concentration of air molecules. $\hat{\sigma}_{ray}$ can be formally derived from the dipole formalism. The resulting wavelength dependence of the scattering cross section is given by the proportionality:

$$\hat{\sigma}_{ray} \propto \lambda^{-4} \tag{2.36}$$

Due to this relation light with shorter wavelength, for example blue, is scattered much more effectively than light with longer wavelength, say red. As a result, at the surface of the earth blue light is incident as diffuse radiation from all directions. That is why the sky appears blue. When the sun is near the horizon during sunrise or sunset, in the oblique path photons have to travel a longer distance compared to situations where the sun is close to the zenith. As a result of equation 2.36, light with short wavelength is then scattered out of the direct beam which leaves the radiation with wavelengths of red and yellow to illuminate the sky.
The wavelength independent Rayleigh phase function also follows directly from the dipole theory:

$$p(\cos \Theta) = \frac{3}{4}(1 + \cos^2 \Theta) \tag{2.37}$$

with Θ the scattering angle. From equation 2.37 it is evident that forward and backward scattering are equally prominent, and perpendicular to the incident direction a local minimum of the scattered radiation exists which is also expressed by $g = 0$ for Rayleigh scattering, see above.

Mie scattering

Aerosols and cloud droplets have dimensions similar to or larger than the wavelengths of solar radiation. Additionally, cloud droplets can be regarded as spheres of liquid water. From aerosols it is known that these often have a water coating which results in a more spherical shape of these otherwise irregular objects. Furthermore, for radiative transfer calculations aiming at directionally integrated radiative properties like fluxes, according to Mishchenko et al. (1995) aerosols can also be safely regarded as spheres. As a result of these prerequisites, optical properties of individual aerosol particles and cloud droplets can be derived by Mie theory, see Mie (1908). A comprehensive treatment of this theory is far beyond the scope of this section, and only the most important features are addressed next. The scattering and extinction coefficients of cloud droplets and aerosols are connected with the dimensionless scattering and extinction efficiencies Q_s and Q_t via:

$$\hat{\sigma}_s = Q_s \pi a^2 \tag{2.38}$$
$$\hat{\sigma}_t = Q_t \pi a^2 \tag{2.39}$$

Q_s and Q_t are derived by Mie theory and describe the fraction of the area of the incident beam which is removed by the spherical particle with radius a through scattering or

extinction. For particles much smaller than the wavelength of the incident light Rayleigh scattering is derived as a special case from Mie theory. For large particles like cloud droplets Mie theory yields $Q_s \approx 2$. The wavelength dependence becomes very weak in this limit. As a consequence, solar radiation is scattered almost equally strong for all wavelengths which is the reason why clouds are white.

In contrast to air molecules, which are assumed to have all the same size, clouds and aerosol populations consist of particles of a large variety of sizes. To derive their so-called bulk optical properties, which are related to a volume rather than to an individual particle, differential number distributions $dn(a)/da$ have to be introduced. These give the number of particles per radius interval per unit volume of air. The total number concentration of particles $N_{part}(a)$ in the radius interval $[a_o, a]$ is then:

$$N_{part}(a) = \int_{a_o}^{a} \frac{dn(a')}{da'} da' \qquad (2.40)$$

In Figure 2.6 several examples for number distributions of different clouds are given.
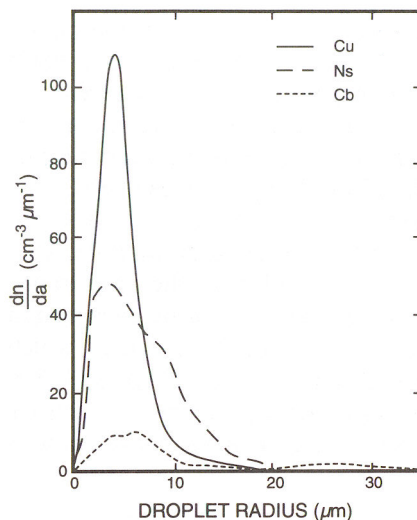
Figure 2.6: Cloud droplet number distributions for several water clouds. Cu: cumulus, fair weather cloud; Ns: nimbostratus, rain cloud; Cb: cumulonimbus, thunderstorm cloud. Adapted from Salby (1995).

The bulk optical properties are defined as:

$$\sigma_s = \int_0^\infty \frac{dn(a)}{da} \hat{\sigma}_s(a) da \tag{2.41}$$

$$\sigma_t = \int_0^\infty \frac{dn(a)}{da} \hat{\sigma}_t(a) da \tag{2.42}$$

$$g = \frac{1}{\sigma_t} \int_0^\infty \frac{dn(a)}{da} g_{part}(a) \hat{\sigma}_s(a) da \tag{2.43}$$

where g_{part} is the asymmetry factor of a single particle or droplet which also has to be calculated by Mie theory.

An approximation for cloud phase functions entirely based on g is given by the Henyey-Greenstein phase function:

$$p(\cos\Theta) = \frac{1-g^2}{(1+g^2-2g\cos\Theta)^{\frac{3}{2}}} \tag{2.44}$$

Exact Mie phase functions can be derived by calculating higher moments of the phase function than g_{part}.

Connection of microphysical parameters and optical properties of clouds

For many practical applications, it is not possible to carry out Mie calculations and numerous integrations of size distributions due to computational limitations. Yet, to derive the relevant optical parameters of clouds, a number of approximations exist. With regard to the optical depth, one such approximation can be quickly derived as follows. The cloud liquid water content ρ_l, which is the liquid water mass per volume of air, can be expressed as:

$$\rho_l = \frac{4}{3}\pi\rho_w \int_0^\infty a^3 dn(a) \tag{2.45}$$

where ρ_w is the density of water. The vertical integral of the liquid water content is called liquid water path Σ_l. If ρ_l is constant over the increment Δz it is:

$$\Sigma_l = \Delta z \rho_l \tag{2.46}$$

Let us further assume that the extinction coefficient is constant over the increment Δz. For the incremental cloud optical depth $\Delta\tau_{cl}$ one derives then:

$$\Delta\tau_{cl} = \Delta z \sigma_t \tag{2.47}$$

With the help of $Q_t \approx 2$ in the limit of large particles and equations 2.39, 2.42, 2.45, and 2.46, one gains for the incremental cloud optical depth:

$$\Delta\tau_{cl} = \frac{3\Sigma_l}{2\rho_w a_e} \tag{2.48}$$

a_e is called effective radius of the cloud droplet number distribution:

$$a_e = \frac{\displaystyle\int_0^\infty a^3 dn(a)}{\displaystyle\int_0^\infty a^2 dn(a)} \tag{2.49}$$

From equations 2.48 and 2.49 it is evident that the cloud optical depth is dominated by the liquid water content, while details of the size distribution of the cloud have only minor impact via the effective radius. More sophisticated approaches include parameterizations of the asymmetry factor and the single scattering albedo. For this study the approximations suggested by Slingo (1989) were used, see section 2.4. Furthermore, in order to avoid the determination of the effective radius by explicitly integrating the size distribution, parameterizations for a_e have been derived as well. Those also involve the liquid water content, see Peng and Lohmann (2003) and Ritter and Geleyn (1992). For the latter see also section 2.4. For aerosols explicit Mie calculations have to be carried out. However, for irregularly shaped particles Mie theory is not sufficient and has to be replaced by more advanced techniques like the T-matrix method, see Mishchenko et al. (1996). Due to the considerable computational burden of both of these methods, standard size distributions and tabulated optical properties for different aerosol types have to be used in applications where computational time is a crucial component.

2.4   Deriving Cloud Optical Properties

In order to investigate different parameterization approaches for 3D radiative transfer, the need for accurate and realistic cloud properties arises. These microscopic parameters can be employed to deduce cloud optical properties as described in the previous section. However, the degree of accuracy can also be defined with respect to the clouds a numerical weather prediction (NWP) model is able to create. These are certainly not always as close to real clouds as clouds from specialized models are. Nevertheless, clouds from weather prediction models are the ones for which 3D RT parameterizations have to be developed and investigated as well. Thus, the next section gives a brief overview of the various methods which can be used to gain realistic clouds by both measurements and models. More emphasis is on the modeling part as all clouds which were available to the author were based on models rather than on pure measurements. However, it is understood that those models in turn rely on realistic initial data from measurements. This section is partly

based on material from Zinner (2004). In the next section, the technique which was used for the offline generation of cloud properties from a weather prediction model for this thesis is described. The deduced clouds are possibly not completely identical with the clouds the model had produced during its original run, but are closely related to those. The reason for this caveat will become clear in the course of the section.

Measuring and modeling clouds

Measuring clouds is a challenging task as clouds are highly variable in space and time. The information necessary to be able to accurately describe clouds not only comprises 3D fields of thermodynamic quantities like the liquid water content and effective radius, but also macroscopic information like the cloud texture via cloud top and base height information. Satellites can be used to observe large areas of the earth, and 2D distributions of cloud properties can be retrieved by employing radiative transfer inversion techniques. Those properties can then be either used for direct radiative transfer simulations or for further investigations of the cloud structure. The resolution of those measurements strongly depends on the instrument and satellite system and ranges from several kilometers to several decameters. In the latter case, this approach has been successfully applied to LANDSAT cloud scenes whose investigation led to fundamental insights concerning the scale invariance of cloud fields and radiative smoothing, see Davis et al. (1997). Furthermore, aircraft measurements can be undertaken to infer cloud parameters either by remote sensing or by in-situ measurements of the microphysical properties. Those measurements are usually limited to the one-dimensional flight path or directly neighboring areas and can therefore only cover small parts of the atmosphere but the temporal and spatial resolution is very high. Finally, ground based measurements can be carried out by numerous techniques, ranging from RADAR and LIDAR, which give vertical profiles and 2D cross sections of the atmosphere, to microwave soundings to deduce the liquid water path. The most complete impression is yielded by combining a multitude of data sources, see Löhnert et al. (2004). These not only include the ones mentioned above but also radiosonde soundings and other meteorological measurements. As these instruments are operated from a fixed position at the ground, the inferred information is generally representative only for a limited area. In summary, it can be said that all methods have their specific limitations and shortcomings concerning accuracy and/or resolution. As a consequence, cloud models are not only used for a direct derivation of microphysical variables but also as an important tool to further extract and extend information from measured data. The former approach is closely related to models which either explicitly or approximately solve the underlying thermodynamic equations. The second approach is more attributed to statistical cloud models. The basic idea of this class of models is to start with a measured, modeled, or idealized initial distribution of a cloud quantity, for example the cloud liquid water, and to derive a new or even more realistic distribution of this quantity, while a set of statistical parameters remains fixed. This method assures the close relation between the derived cloud and realistic cloud features inherent in the original data. It is motivated by the fact that a number of cloud parameters show a very distinct scaling behavior. For example, when investigating

the wavenumber spectrum of the liquid water content, Davis et al. (2003) found that the energy spectrum $E(k)$ of the data series approximately follows the proportionality:

$$E(k) \propto k^{\beta} \tag{2.50}$$

where k is the wavenumber. If $E(k)$ is plotted on logarithmic scales, the resulting line has a slope of $\beta \approx -\frac{5}{3}$. In Figure 2.7 an example for a data series of the liquid water content and the respective energy spectrum, which approximately follows this behavior, is shown. This power law has already been theoretically predicted by Kolmogorov (1941) and confirmed by Corrsin (1951) for the gradual transformation of turbulent kinetic energy from larger scales to smaller scales until the dissipation regime is reached, and all energy has been converted to heat. The constant slope over large ranges of k means that the observed property is scale invariant, and as a consequence the resulting structures are self-similar.
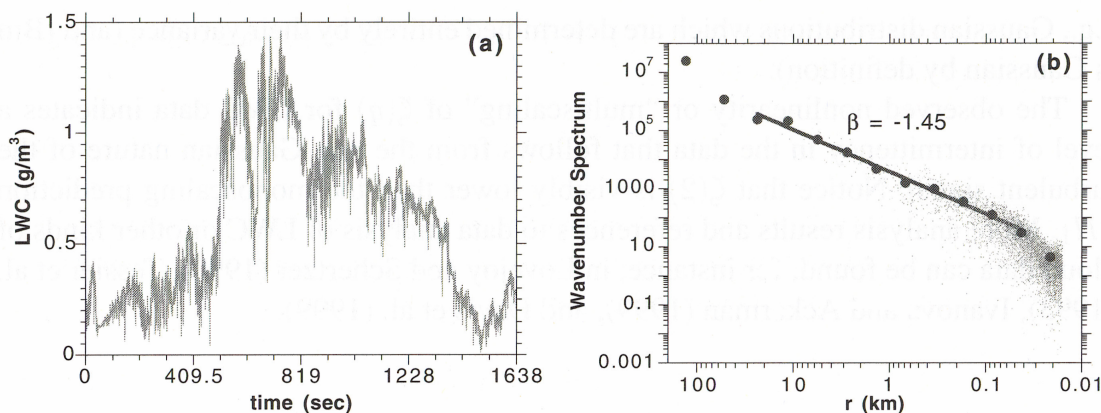
Figure 2.7: Time series of liquid water content (a) and related energy spectrum (b). Solid circles represent averaged data with slope $\beta = -1.45$. Adopted from Marshak and Davis (2005).

The analogical behavior of the turbulent kinetic energy and the distribution of the liquid water content suggests that both are determined by similar or even identical physical processes. Other quantities, like the optical depth, have also been found to follow this power law which seems to hint at a fundamental structure of clouds. Statistical cloud models make use of this feature. In the following, three different approaches are briefly described to shed some light on the common basics of these models but also to underline their distinct capabilities.

Let $F(k)$ be the Fourier transform of the data series $f(n)$ consisting of N values:

$$F(k) = \sum_{n=0}^{N-1} f(n)e^{-2\pi ikn/N} \tag{2.51}$$

$$f(n) = \frac{1}{N} \sum_{k=0}^{N-1} F(k)e^{-2\pi ikn/N} \tag{2.52}$$

Since $F(k)$ is a complex number it can be written as:

$$F(k) = A(k)e^{i\phi(k)} \tag{2.53}$$

$A(k)$ is called amplitude, and $\phi(k)$ is referred to as phase. The energy spectrum of $f(n)$ is formally defined as:

$$E(k) = |F(k)|^2 = F(k)F^*(k) = A^2(k) \tag{2.54}$$

$F^*(k)$ is the complex conjugate of $F(k)$. $E(k)$ is obviously independent of the phase. That means, a data series which is characterized by $\beta = -\frac{5}{3}$ as exponent in its energy spectrum can be transformed in a new series, which also follows the $\beta = -\frac{5}{3}$ rule, by adding an arbitrary phase to the amplitude spectrum $A(k)$ of the original series and subsequent transformation of the new $F(k)$ according to equation 2.52. This is the fundamental outline of most cloud generators. One of the more sophisticated approaches is the bounded cascade model, see Cahalan et al. (1994b). This model starts with a uniform liquid water field and distributes the liquid water by partitioning the domain's volume in more and more sections with each step (cascade), while a decreasing amount of water is transferred between the new sections. The process, which reminds of the generation of the Cantor set, is controlled by two variables. The first, the so called scaling parameter, is fixed and forces the scaling behavior of the resulting fractal liquid water distribution to be in agreement with the $\beta = -\frac{5}{3}$ rule. The remaining parameter, which is called variance parameter, is determined by the standard deviation of the liquid water path of realistic measured clouds. This is an additional feature the pure Fourier approach misses. As a result, the derived clouds also have a realistic liquid water distribution. Another approach, which was used to generate several of the clouds which have been subsequently made available to the author, is called Iterative Amplitude Adapted Fourier Transform (IAAFT), see Venema et al. (2006). It is capable of directly dealing with measured or modeled fields of cloud properties. The scaling behavior and the amplitude distributions need not to be fixed and are adjusted to the original data. This results in highly consistent cloud fields, in the sense that domain averaged radiative properties are closely resembled when compared to the respective results of the original clouds. The algorithm is best suited for broken stratiform clouds but has also been used to generate cumulus clouds.

As mentioned above, it is also possible to directly physically model clouds by either solving the fundamental differential equations or by parameterizing the underlying thermodynamic processes. In connection with radiative transfer calculations, clouds originating from

dynamic models, like large eddy simulation (LES) models, numerical weather prediction (NWP) models, and general circulation models (GCM), which are climate models operated on a global scale, are of special interest. Those models can be used to study how radiative transfer spatially and temporally interacts with other meteorological variables. These questions are of eminent importance in relation to climate predictions. However, the scales those models are operated on differ greatly, see Table 2.1. High resolution models like LES models can be generally expected to simulate more realistic cloud structures than operational weather prediction models or even global climate models, as with increasing scale and computational burden the model resolution and physical complexity has to decrease. As a result, none of those models is able to explicitly provide sophisticated parameters like the cloud droplet size distribution. Common to all classes of those models is the neglect of 3D radiative transfer effects. Hence, in general the 3D radiative transfer approximations presented in chapter 4 could be applied to all of them. In order to at least carry out some basic investigations of those approximations with respected to weather prediction models, cloud optical properties have been deduced from data generated by the Lokal-Modell (local model, LM) of the German Weather Service (DWD). Details are provided in the next section.

Table 2.1: Scale and resolution of different atmospheric models. GCM: Global Circulation Model; NWP: Numerical Weather Prediction; LES: Large Eddy Simulation.

Model	Resolution	Scale
LES	Decameters	Several kilometers
NWP	Several kilometers	Thousands of kilometers
GCM	Hundred kilometers	Global

The Lokal-Modell of the German Weather Service

This section briefly describes the relevant model features and the process of obtaining optical properties for radiative transfer calculations from the model's output. For a full documentation of the LM see Doms et al. (2003) and Doms and Schättler (1999).

The LM is based on the well known differential equations for atmospheric motion and thermodynamics, thus, comprising the unfiltered prognostic equations for the wind field, the so-called Navier-Stokes equations, the temperature, specific humidity, specific cloud water content, and specific cloud ice content. This makes the LM a non-hydrostatic limited area model, which means that boundary conditions have to be provided by another model surrounding the LM model domain. The model equations are solved on a spherical grid. In its operational version the model is operated with a horizontal resolution of $7km$ and the standard domain is composed of 325×325 grid points. This information is as of September 2003. The setup used for the case studies here has a horizontal resolution of $2.8km$, which will become operational in 2007, and includes a variable number of pixels from case to case.

In Figure 2.8 the overall domain of the available LM data is shown. For computational reasons actual calculations will use only subsets of this domain. The typical time step for the integration of the prognostic equations is $25s$. The vertical coordinate of the LM for these studies is the hybrid η-coordinate. This coordinate is so-called terrain following, meaning that the lowest coordinate layer coincides with the surface of the earth, while the resulting curvature of the coordinate layers decreases with increasing height, reaching a plane shape after a certain level. As the coordinate is based on a temporally constant reference pressure value, the positions of the coordinate levels are fixed with respect to time.
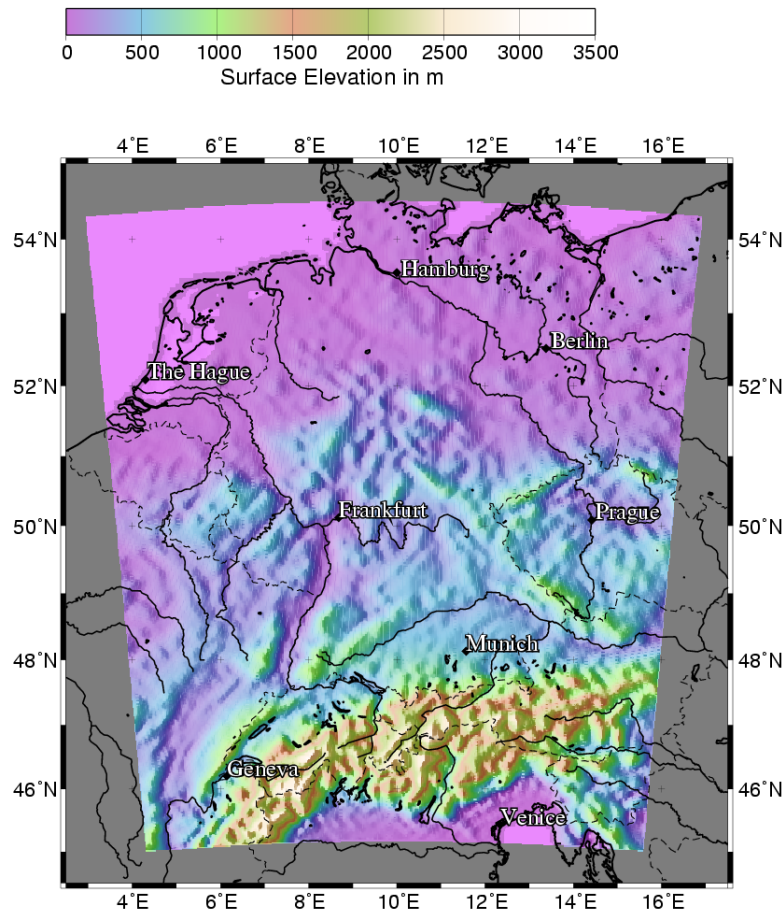
Figure 2.8: Surface elevation in meter of the approximate overall domain of the available LM data. Solid lines represent the coastline and major rivers, dashed lines stand for political borders.

For the purpose on focus only the clouds produced by the model and the radiative transfer scheme itself are of interest. All other model physics will not be considered. For all cases, which will be discussed later, the convection scheme of the LM was turned off, thus, leaving the cloud formation explicitly to model physics. The only two types of clouds which then

can form are grid scale clouds and subgrid scale clouds. The former are produced if in the grid cell under consideration cloud liquid water is explicitly predicted. Thus, these clouds are formed when supersaturation occurs. If so, the cloud is believed to occupy the whole grid cell. The latter form of clouds are parameterized with the help of the cloud cover and the liquid water content of the cell. The cloud cover is parameterized with the help of the relative humidity, the height of the layer, and the vertical mass propagation.

The optical properties were not generated during an actual LM run but rather offline by operating the radiative transfer module as a stand-alone model. The LM stores its output in binary files complying with the GRIB format, see NCEP (2005). Each of these files is produced for hourly output and comprises all relevant prognostic, diagnostic and auxiliary variables. The data was provided by Dr. Nicole van Lipzig, see BBC2 Webpage (2003) and QUEST Webpage (2005), and by Dr. Felix Ament, see DAQUA Webpage (2004). Yet, a complication arises because of the vertical coordinate system of the LM. The radiative transfer models used in this study all rely on the Cartesian coordinate system. In contrast to that, the η-system produces three-dimensionally variable z-increments. This difference makes it necessary to develop an algorithm which transforms the variables extracted from the GRIB files to a regular Cartesian lattice.

To do so, the column whose lower boundary has the lowest elevation above sea-level is chosen. The structure of the vertical z-increments of this column will be the vertical structure of all columns after the algorithm is finished. Thereafter, all vertical levels of all columns are stored in increasing order in one large vector. This vector constitutes an intermediate vertical coordinate. As a next step, in each pixel this intermediate coordinate is processed and filled with the properties of the respective column. The part of the column which is below surface elevation is treated as vacuum. This way, the whole domain receives a plane lower boundary. The upper boundary has been flat even in the original system. In order to reduce the number of layers from $N_x \times N_y \times N_z$ to the original number N_z, which is 35 for all simulations, a weighted average is carried out in the vertical, weighing all optical properties which are located between two vertical levels of the respective original column with its proportionate thickness. The main steps of the algorithm are shown in Figure 2.9. It has to be admitted that this algorithm is rather clumsy as it produces a tremendous number of vertical levels in the intermediate vertical coordinate and requires significant computational resources. There might be more sophisticated ways to carry out the required transformation. As a result, it is by no means applicable on a frequent basis. Yet, for just a few case studies it is suitable. To demonstrate the accuracy of the transformation, the differences of the partial cloud cover are investigated along a transect. It touches some of the highest peaks of the alps as well as lowlands. In Figure 2.10(a) the elevation along this transect is shown, and in Figure 2.10(b) the relative difference of the transformed partial cloud cover to the original field is depicted. Even for regions of maximum elevation the errors are negligible. The maximum error in the entire domain does not exceed 0.2%. Similar magnitudes exist for the remaining input variables.

After this step, the thermodynamic quantities together with the uniform z-coordinate are fed into the stand-alone radiative transfer module of the LM in order to produce optical properties offline. The model splits up the solar spectrum into three intervals,
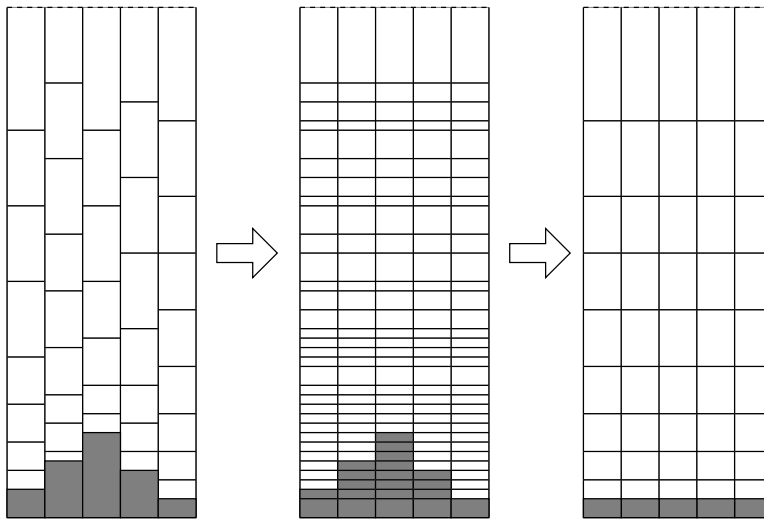
Figure 2.9: Transformation from η to Cartesian coordinates in three steps. The shown vertical structure is idealized and not deduced from the model.

$0.25\mu m - 0.7\mu m$, $0.7\mu m - 1.53\mu m$ and $1.53\mu m - 4.64\mu m$, respectively. In all intervals the atmosphere is described by grey constituents, which means only weakly wavelength dependent, like aerosols, liquid and ice components of clouds, and Rayleigh scattering for air molecules. Absorption coefficients for gases are determined by an exponential sum fitting technique. For all calculations in the presented work the second spectral interval has been chosen. Gaseous absorption was not considered in this basic investigation in order to keep the configuration of the stand-alone model as simple as possible. This approach also avoids difficulties with the correct calculation of absorption coefficients in the LM by the exponential sum fitting technique and their subsequent application in the other RT models. This certainly affects the results, yet, all qualitative findings can be expected to hold. Gaseous absorption clearly modulates and shortens the photon paths, but the dominant cloud effects can be expected to remain largely unaffected which in total overemphasizes 3D effects quantitatively. Some absorption is present as aerosols are fully considered. Explicit cloud ice, which is formed when supersaturation occurs, had to be neglected as well. This simplification had to be introduced as it was not possible to reproduce the corresponding interface with the radiative transfer model in agreement with its original counterpart of the LM. However, implicit cloud ice, that means subgrid ice water content in the cells where no supersaturation is reached, is included. A remark concerning this inconsistent treatment will be made when the results of those scenes are discussed. A detailed description of the RT module can be found in Ritter and Geleyn (1992). It employs a standard 2-stream model with random/maximum overlap capabilities for treatment of partial cloudiness. As mentioned in section 2.3, the cloud optical properties are calculated based on the approximations proposed by Slingo (1989).

In detail:

$$\Delta\tau = \left(c_1 + \frac{c_2}{a_e}\right)\rho_l\Delta z \tag{2.55}$$

$$\omega_o = c_3 + c_4 a_e \tag{2.56}$$

$$g = c_5 + c_6 a_e \tag{2.57}$$

As the model is not able to determine the effective radius a_e from cloud droplet size distributions, it is parameterized as a function of the liquid water content ρ_l:

$$a_e = c_7 + c_8\rho_l \tag{2.58}$$

The c_i, $i\epsilon\{1,2,3,4,5,6\}$, are a set of constants for each of the LM's wavelength intervals. They are determined from a fit of the parameterizations to optical properties of different cloud types. The consideration of partial cloudiness leads to two sets of optical properties. The first set, which represents the clear sky contribution, consists of Rayleigh scattering, aerosol scattering and absorption. The cloudy contribution uses the same properties, plus cloud scattering and absorption. If gaseous absorption is not neglected, it has to be introduced in both sets as water vapor is included. In the LM's radiative transfer module both types of parameters are then further processed by the 2-stream model. Unfortunately, both DISORT and the LMCM are not capable of treating partial cloudiness. This makes it necessary to generate a unified set of optical properties by the following weighted average:

$$P_{tot} = (1 - C_{pclc})P_f + C_{pclc}P_c \tag{2.59}$$

where P_{tot} is the resulting mixed value, P_f and P_c are the cloud-free and cloudy representatives of the optical property and $C_{pclc}\ \epsilon\ [0,1]$ is the partial cloud cover. The resulting 3D fields of all optical properties are then stored for subsequent input for the radiative transfer models.

Although considerable effort has been undertaken in order to assure that the LM data is transformed into clouds which match the originally generated ones as closely as possible, it cannot precluded that the former differ to some extent from the latter. Therefore it is justified to state that the clouds derived from the LM output are strongly related to those of the LM but are not absolutely identical with these. However, the intention is not to precisely repeat the radiative transfer calculation as carried out during the original LM run and to re-establish the exact synoptic situation with all its details. This would not only include the consideration of all optical properties of the atmosphere but also the two-dimensional surface albedo and the two-dimensionally variable SZA the model uses according to the geographic position of each of the pixels. In any event, the last two prerequisites wouldn't have been possible to meet as the used RT models and 3D approximations are not capable of these features. Thus, the aim here is to conduct case studies in order to investigate the fundamental characteristics, capabilities, and the future potential of the different approximation approaches. As a result, it is accepted that the

(a) Surface elevation of the example transect along parts of the Alps and lowlands.

(b) Relative difference of transformed partial cloud cover and original partial cloud cover in % as a function of height and horizontal position along the transect.
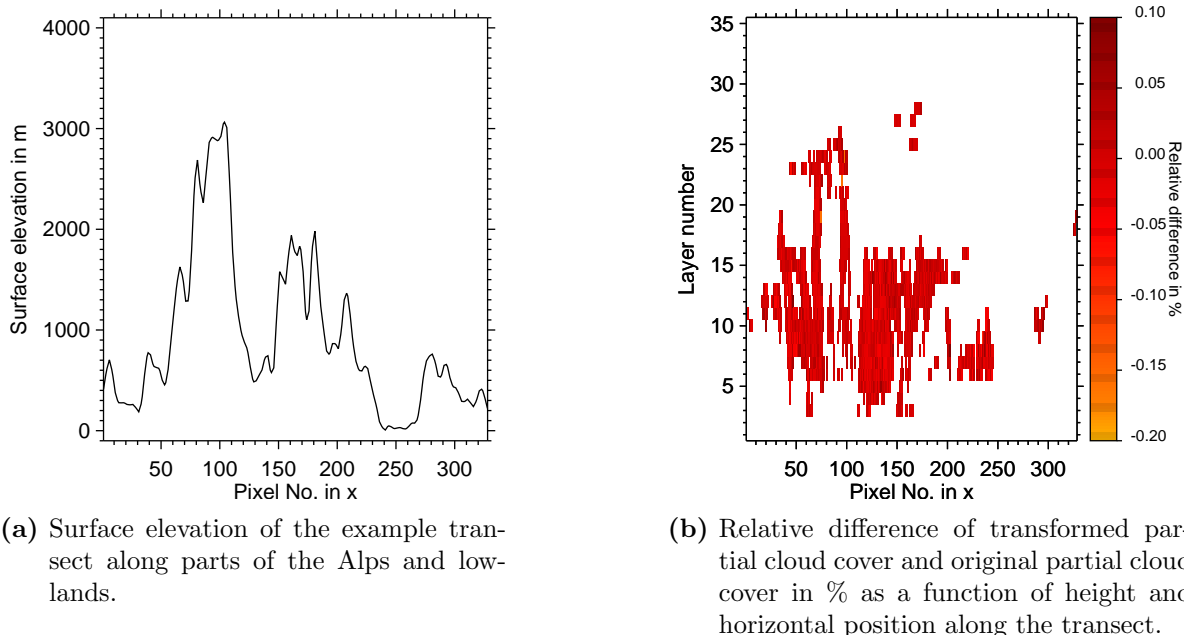
Figure 2.10: Comparison of original and transformed partial cloud cover along a transect with pronounced surface elevation.

gained clouds have some idealized features, as well as the setup of the RT calculation, but are assumed to be sufficient for this purpose.

2.5 Radiative Transfer Equation for 1D and 3D Problems

The radiative transfer equation (RTE) describes the propagation of light in space and time, and the interactions of light with the matter and the boundaries forming the medium. Numerous approaches exist for its derivation, ranging from mainly straightforward phenomenological approaches, see for example Liou (2002), Lenoble (1993), and Chandrasekhar (1960), to mathematically formal ones, see Mishchenko (2006).

In order not to unnecessarily increase the amount of theoretical material presented here, only fundamental assumptions regarding the derivation of the RTE will be addressed, followed by the most basic forms which also can be found in most textbooks.

The RTE can be regarded as a balance equation for photons traveling in the direction $\boldsymbol{\Omega}$ and having the frequency ν. The state space therefore comprises six dimensions, namely the position $\boldsymbol{r} = (x, y, z)$, the directions θ, φ, and the frequency ν. It can be regarded as a multidimensional cube. The balance which is set up consists of five contributions:

1. Photon exchange with the cube's surrounding environment.

2. Absorption of photons inside the cube.

3. Scattering of photons with $(\mathbf{\Omega}, \nu)$ into $(\mathbf{\Omega'}, \nu')$, called outscattering as it is a photon sink for the considered direction and frequency.

4. Scattering of photons with $(\mathbf{\Omega'}, \nu')$ into $(\mathbf{\Omega}, \nu)$, called inscattering as it is a photon source for the considered direction and frequency.

5. Emission inside the cube.

For most atmospheric applications the following assumptions are justified:

1. The refractive index is spatially and temporally constant, meaning $\frac{\partial \mathbf{\Omega}}{\partial \mathbf{r}} = 0$ and $\frac{\partial \mathbf{\Omega}}{\partial t} = 0$, resulting in linear propagation of photons between the above interactions.

2. Absorption and emission are isotropic.

3. Only elastic scattering is taken into account, $\nu = \nu'$, that is no frequency shift due to scattering.

4. The radiative field can be considered to be stationary $\frac{\partial I}{\partial t} = 0$.

5. The scattering particles are required to be homogeneous, meaning $\mathbf{\Omega'} \rightarrow \mathbf{\Omega'} = \mathbf{\Omega'} \cdot \mathbf{\Omega'} = \cos \Theta$ which was already used in equation 2.24.

The radiative transfer equation for the total radiative field in three dimensions can then be deduced as the balance where sources and sinks are combined in Q:

$$\frac{dI(\mathbf{r}, \mathbf{\Omega})}{ds} \equiv \mathbf{\Omega} \cdot \nabla I(\mathbf{r}, \mathbf{\Omega}) = -\sigma_t(\mathbf{r}) \left[I(\mathbf{r}, \mathbf{\Omega}) - Q(\mathbf{r}, \mathbf{\Omega}) \right] \tag{2.60}$$

and explicitly:

$$\frac{dI(\mathbf{r}, \mathbf{\Omega})}{ds} \equiv \mathbf{\Omega} \cdot \nabla I(\mathbf{r}, \mathbf{\Omega}) = J(\mathbf{r}) - \sigma_t(\mathbf{r}) I(\mathbf{r}, \mathbf{\Omega}) + \frac{\sigma_s(\mathbf{r})}{4\pi} \int_{4\pi} p(\mathbf{r}, \mathbf{\Omega'} \cdot \mathbf{\Omega}) I(\mathbf{r}, \mathbf{\Omega'}) d\Omega' \tag{2.61}$$

Sometimes it is useful to obtain separate equations for the direct sunlight and the diffuse light, where photons are scattered at least once. Therefore, the intensity of the direct beam is separated from the diffuse intensity I_d:

$$I(\mathbf{r}, \mathbf{\Omega}) = I_d(\mathbf{r}, \mathbf{\Omega}) + S(\mathbf{r}, \mathbf{\Omega}) \delta(\mathbf{\Omega} - \mathbf{\Omega}_o) \tag{2.62}$$

with $\mathbf{\Omega}_o$ containing the solar zenith angle (SZA) $\theta_o \epsilon [\frac{\pi}{2}, \pi]$ and solar azimuth $\varphi_o \epsilon [0, 2\pi]$.

The separation leads to:

$$\frac{dI_d(\boldsymbol{r}, \boldsymbol{\Omega})}{ds} + \frac{dS(\boldsymbol{r}, \boldsymbol{\Omega}_o)}{ds} = J(\boldsymbol{r}) - \sigma_t(\boldsymbol{r})I_d(\boldsymbol{r}, \boldsymbol{\Omega}) - \sigma_t(\boldsymbol{r})S(\boldsymbol{r}, \boldsymbol{\Omega})\delta(\boldsymbol{\Omega} - \boldsymbol{\Omega}_o)$$

$$+ \frac{\sigma_s(\boldsymbol{r})}{4\pi} \int\limits_{4\pi} p(\boldsymbol{r}, \boldsymbol{\Omega}' \cdot \boldsymbol{\Omega})I_d(\boldsymbol{r}, \boldsymbol{\Omega}')d\Omega' \qquad (2.63)$$

$$+ \frac{\sigma_s(\boldsymbol{r})}{4\pi} p(\boldsymbol{r}, \boldsymbol{\Omega}_o \cdot \boldsymbol{\Omega})S(\boldsymbol{r}, \boldsymbol{\Omega}_o)$$

Collecting all terms in equation 2.63 relating to the direct beam retrieves after straightforward solution the well-known Lambert-Beer law:

$$S(\boldsymbol{r}, \boldsymbol{\Omega}_o) = F_o\, e^{-\int\limits_0^{s(\boldsymbol{r})} \sigma_t(s')ds'} \qquad (2.64)$$

where F_o is the incoming solar flux at the top of the atmosphere. For all calculations, which have been carried out for this study, $F_o = 1.0\,Wm^{-2}$ was used. The remaining terms in equation 2.63 form the RTE for diffuse radiation:

$$\frac{dI_d(\boldsymbol{r}, \boldsymbol{\Omega})}{ds} = J(\boldsymbol{r}) - \sigma_t(\boldsymbol{r})I_d(\boldsymbol{r}, \boldsymbol{\Omega})$$

$$+ \frac{\sigma_s(\boldsymbol{r})}{4\pi} \int\limits_{4\pi} p(\boldsymbol{r}, \boldsymbol{\Omega}' \cdot \boldsymbol{\Omega})I_d(\boldsymbol{r}, \boldsymbol{\Omega}')d\Omega' + \frac{\sigma_s(\boldsymbol{r})}{4\pi} p(\boldsymbol{r}, \boldsymbol{\Omega}_o \cdot \boldsymbol{\Omega})S(\boldsymbol{r}, \boldsymbol{\Omega}_o) \qquad (2.65)$$

While equation 2.64 is usually not too difficult to evaluate, equation 2.65 is subject to further treatment to be solved. Starting from equation 2.60, the formal solution of the RTE can be gained by integration. The resulting so-called integral form of the RTE then yields:

$$I(s, \boldsymbol{\Omega}) = I(s = 0, \boldsymbol{\Omega})e^{-\int_0^s \sigma_t(s')ds'} + \int\limits_0^s \sigma_t(s')Q(s', \boldsymbol{\Omega})e^{-\int_{s'}^s \sigma_t(s'')ds''}ds' \qquad (2.66)$$

Equation 2.61 offers the possibility to relate the flux divergence and therefore heating rates to the actinic flux. Because of $\boldsymbol{\Omega} \cdot \nabla I = \nabla \cdot (\boldsymbol{\Omega}I)$ subsequent integration over the unit sphere leads to:

$$\nabla \cdot \boldsymbol{E}_N = 4\pi J(\boldsymbol{r}) - \sigma_a(\boldsymbol{r})F_{act}(\boldsymbol{r}) \qquad (2.67)$$

with the consequence that a purely scattering atmosphere without internal sources conserves the net-flux spatially.

If horizontal homogeneity is assumed (plane-parallel atmosphere), the RTE for the total light becomes:

$$\mu\frac{dI(z,\mu,\varphi)}{dz} = J(z) - \sigma_t(z)I(z,\mu,\varphi) + \frac{\sigma_s(z)}{4\pi}\int\limits_{0}^{2\pi}\int\limits_{-1}^{1} p(z,\mu',\varphi',\mu,\varphi)I(z,\mu',\varphi')d\mu'd\varphi' \quad (2.68)$$

If by virtue of $d\tau = -\sigma_t dz$ the optical depth is chosen as vertical coordinate and the source is omitted, equation 2.68 transforms into:

$$\mu\frac{dI(\tau,\mu,\varphi)}{d\tau} = I(\tau,\mu,\varphi) - \frac{\omega_o(\tau)}{4\pi}\int\limits_{0}^{2\pi}\int\limits_{-1}^{1} p(\tau,\mu',\varphi',\mu,\varphi)I(\tau,\mu',\varphi')d\mu'd\varphi' \quad (2.69)$$

and for the diffuse light only:

$$\mu\frac{dI_d(\tau,\mu,\varphi)}{d\tau} = I_d(\tau,\mu,\varphi) - \frac{\omega_o(\tau)}{4\pi}\int\limits_{0}^{2\pi}\int\limits_{-1}^{1} p(\tau,\mu',\varphi',\mu,\varphi)I_d(\tau,\mu',\varphi')d\mu'd\varphi'$$
$$- \frac{\omega_o}{4\pi}F_o\, e^{-\frac{\tau}{|\mu_o|}}p(\tau,\mu_o,\varphi_o,\mu,\varphi)\delta(\mu-\mu_o)\delta(\varphi-\varphi_o) \quad (2.70)$$

The second term on the right hand side is called multiple scattering term as it represents the scattering of already diffuse light. The third term is called single scattering term as it describes the transformation of direct solar radiation in single scattered diffuse light. In order to solve the RTE boundary conditions have to be imposed. One speaks of vacuum boundary conditions if there is no incident diffuse radiation:

$$I_d(\mu < 0, \varphi, z = TOA, x, y) = 0$$
$$I_d(\mu > 0, \varphi, z = 0, x, y) = 0 \quad (2.71)$$

In case of a reflecting surface at the lower boundary, the boundary conditions are:

$$I_d(\mu < 0, \varphi, z = TOA, x, y) \;=\; 0 \quad (2.72)$$
$$I_d(\mu > 0, \varphi, z = 0, x, y) \;=\; I_g(\mu, \varphi, x, y) \quad (2.73)$$

while the determination of I_g is subject to the kind of reflection. A general discussion of surface reflection is beyond the scope of this section.

Another variant of the upper boundary condition can be introduced if the RTE for the total light is used, see equation 2.61. If the upper boundary condition is chosen to be regarded as a source, the RTE reads:

$$\frac{dI(\boldsymbol{r},\boldsymbol{\Omega})}{ds} + \sigma_t(\boldsymbol{r})I(\boldsymbol{r},\boldsymbol{\Omega}) - \frac{\sigma_s(\boldsymbol{r})}{4\pi}\int\limits_{4\pi} p(\boldsymbol{r},\boldsymbol{\Omega}'\!\cdot\!\boldsymbol{\Omega})I(\boldsymbol{r},\boldsymbol{\Omega}')d\Omega' = |\mu_o|F_o\delta(\boldsymbol{\Omega}-\boldsymbol{\Omega}_o)\delta(z-z_o) \quad (2.74)$$

If scattering is omitted, the Lambert-Beer law is regained in a more formal form:

$$I(s, \mu < 0, \varphi) = F_o \delta(\mu - \mu_o) \delta(\varphi - \varphi_o) \eta(s) e^{-\int\limits_0^s \sigma_t(s')ds'} \tag{2.75}$$

2.6   Discrete Ordinate Method for 1D Problems

In order to solve the RTE and to gain a form which is suitable for the approximations, in the following chapters the RTE in its representation of equation 2.68 is taken into account. It is restated here without the source J as solar radiative transfer is treated only:

$$\mu \frac{dI(z, \mu, \varphi)}{dz} = -\sigma_t(z) I(z, \mu, \varphi) + \frac{\sigma_s(z)}{4\pi} \int\limits_0^{2\pi} \int\limits_{-1}^{1} p(z, \mu', \varphi', \mu, \varphi) I(z, \mu', \varphi') d\mu' d\varphi' \tag{2.76}$$

The phase function is expanded in a series of Legendre polynomials. The following form is chosen for convenience:

$$p(z, \mathbf{\Omega}' \cdot \mathbf{\Omega}) = \sum_{l=0}^{\infty} (2l + 1) \chi_l(z) P_l(\mathbf{\Omega}' \cdot \mathbf{\Omega}) \tag{2.77}$$

where χ_l are the expansion coefficients and P_l is the Legendre polynomial of order l. In order to be able to represent the phase function with the scattering angle expanded as in equation 2.24, the addition theorem for Legendre polynomials is applied. For a summary of the most important characteristics of P_l and the addition theorem see Liou (2002). After some manipulations the scattering term in equation 2.76 becomes:

$$\frac{\sigma_s(z)}{4\pi} \int\limits_{4\pi} I(z, \mathbf{\Omega}') p(z, \mathbf{\Omega}' \cdot \mathbf{\Omega}) d\Omega' = \frac{1}{4\pi} \int\limits_0^{2\pi} \int\limits_{-1}^{1} I(z, \mu', \varphi') \times$$
$$\sum_{l=0}^{\infty} (2l + 1) \eta_l(z) \sum_{m=0}^{l} (2 - \delta_{m0}) \frac{(l-m)!}{(l+m)!} P_l^m(\mu) P_l^m(\mu') \cos m(\varphi' - \varphi) d\mu' d\varphi' \tag{2.78}$$

The same procedure can be translated to the single and multiple scattering terms of equation 2.70. The intensity I represents then the diffuse contribution. Furthermore, in this equation the intensity I will be expanded in a Fourier series with the coefficients I_m:

$$I(\tau, \mu, \varphi) = \sum_{m=0}^{\infty} I_m(\tau, \mu) \cos m(\varphi - \varphi_o) \tag{2.79}$$

After a number of manipulations, see for example Chandrasekhar (1960), an equation for I_m is derived which has the same structural form as the original RTE for the diffuse light:

$$
\mu \frac{dI_m(\tau, \mu)}{d\tau} = I_m(\tau, \mu)
$$

$$
- \frac{\omega_o}{2} \int\limits_{-1}^{1} \sum_{l=m}^{\infty} (2l+1) \frac{(l-m)!}{(l+m)!} P_l^m(\mu) P_l^m(\mu') I_m(\tau, \mu') d\mu' \qquad (2.80)
$$

$$
- \frac{\omega_o}{4\pi} F_o e^{-\frac{\tau}{|\mu_o|}} (2 - \delta_{m0}) \sum_{l=m}^{\infty} (2l+1) \frac{(l-m)!}{(l+m)!} P_l^m(\mu) P_l^m(\mu_o)
$$

with $m = 0, 1, 2 \dots$. In reality, the expansion in m has to be truncated, leaving a finite number of expansion terms and therefore equations. The whole preceeding procedure was performed to separate μ from φ. After solving the system of equations in 2.80, the intensity can then be put together by equation 2.79. One way of solving 2.80 is to further split up μ by descretizing it in a vector:

$$
\mu = \begin{pmatrix} \mu_{-N} \\ \vdots \\ \mu_{-1} \\ \mu_1 \\ \vdots \\ \mu_N \end{pmatrix} \qquad (2.81)
$$

μ_i, $i\epsilon[\pm 1, 2, 3 \dots \pm N]$, is referred to as discrete ordinate. $2N$ is called "number of computational streams". Therefore, equation 2.80 turns into an equation for each of the μ_i:

$$
\mu_i \frac{dI_m(\tau, \mu_i)}{d\tau} = I_m(\tau, \mu_i)
$$

$$
- \frac{\omega_o}{2} \sum_{\substack{j=-N \\ j \neq 0}}^{N} \sum_{l=m}^{\infty} (2l+1) \frac{(l-m)!}{(l+m)!} P_l^m(\mu_i) P_l^m(\mu_j) I_m(\tau, \mu_j) \qquad (2.82)
$$

$$
- \frac{\omega_o}{4\pi} F_o e^{-\frac{\tau}{|\mu_o|}} (2 - \delta_{m0}) \sum_{l=m}^{\infty} (2l+1) \frac{(l-m)!}{(l+m)!} P_l^m(\mu_i) P_l^m(\mu_o)
$$

with $i\epsilon[\pm 1, 2, 3 \dots \pm N]$. The specific choice of the weights w_i and discrete angles μ_i which appear because of the discretization of the integral, for example by Gauss-Quadrature, is a feature of the numerical implementation, and is not considered any further here. Equation 2.82 and its solution procedures form the backbone of the radiative transfer model DISORT (DIscrete Ordinate Radiative Transfer). It has been used in this work for all exact 1D

calculations of fluxes. For a detailed discussion of the model, regarding also the treatment of the vertical coordinate, see Stamnes et al. (1988) and Thomas and Stamnes (1999). As for many studies, including this one, only fluxes are of significance, it is important to note that:

$$E(z) = \int\limits_{-1}^{1} \int\limits_{0}^{2\pi} \mu I(z, \mu, \varphi) d\mu d\varphi = 2\pi \int\limits_{-1}^{1} \mu I_{m=0}(\tau, \mu) d\mu \tag{2.83}$$

and for the azimuthally averaged intensity $\bar{I}$:

$$\bar{I}(z, \mu) = \frac{1}{2\pi} \int\limits_{0}^{2\pi} I(z, \mu, \varphi) d\varphi = I_{m=0}(\tau, \mu) \tag{2.84}$$

which decreases the computational burden to calculate these quantities significantly as only the first expansion term needs to be considered.

Chapter 3

Adjoint Radiative Transfer and the Perturbation Theory

> As far as the laws of mathematics refer to reality, they are not certain; and as far as they are certain, they do not refer to reality.
>
> ——————————————
>
> Albert Einstein

In this section, the formal outline of adjoint radiative transfer and its subsequent application to the linearization of the radiative transfer problem, resulting in the linear radiative transfer perturbation theory (RTPT), will be introduced. A comprehensive presentation of the theoretical background can be found in textbooks like Bell and Glasstone (1970). For atmospheric radiative transfer and remote sensing problems the technique has been tailor-made by Ustinov (1990), Ustinov (1991), Box et al. (1988), and Marchuk (1964).

3.1 Adjoint Radiative Transfer Equation

For reasons explained later in the course of this section, it is appropriate to observe the total intensity in z-coordinates. As only one-dimensional problems are treated here, equation 2.74 now reads:

$$\mu\frac{dI(z,\mu,\varphi)}{dz} + \sigma_t(z)I(z,\mu,\varphi) - \frac{\sigma_s(z)}{2\pi}\int\limits_{0}^{4\pi}\int\limits_{-1}^{1}p(z,\mu',\varphi',\mu,\varphi)I(z,\mu',\varphi')d\mu'd\varphi' = \\ |\mu_o|F_o\delta(\mu-\mu_o)\delta(\varphi-\varphi_o)\delta(z-z_o) \tag{3.1}$$

For the formalism applied it is restated in operator notation:

$$LI = Q \tag{3.2}$$

with:

$$L = \mu\frac{d}{dz} + \sigma_t(z) - \frac{\sigma_s(z)}{4\pi}\int\limits_{0}^{2\pi}\int\limits_{-1}^{1}d\mu'd\varphi'p(z,\mu',\varphi',\mu,\varphi)\circ \tag{3.3}$$

$$Q = |\mu_o|F_o\delta(\mu - \mu_o)\delta(\varphi - \varphi_o)\delta(z - z_o) \tag{3.4}$$

The "○" in equation 3.3 denotes that the intensity has to be included in the integral. As explained in section 2.5, the term Q acts as source and upper boundary condition for the direct light. For the diffuse light vacuum boundary conditions are applied. The adjoint intensity I^+ is then introduced as the property which is connected with the intensity I by the relationship:

$$\int\limits_{0}^{\infty}dz\int\limits_{0}^{2\pi}d\varphi\int\limits_{-1}^{1}d\mu I^+(z,\mu,\varphi)[LI(z,\mu,\varphi)] = \int\limits_{0}^{\infty}dz\int\limits_{0}^{2\pi}d\varphi\int\limits_{-1}^{1}d\mu[LI^+(z,\mu,\varphi)]I(z,\mu,\varphi) \tag{3.5}$$

For brevity the following notation is introduced:

$$\langle a,b\rangle = \int\limits_{0}^{\infty}\int\limits_{0}^{2\pi}\int\limits_{-1}^{1}a\,b\,d\mu d\varphi dz \tag{3.6}$$

Equation 3.5 then reads:

$$\langle I^+, LI\rangle = \langle L^+I^+, I\rangle \tag{3.7}$$

I^+ is required to fulfill the adjoint radiative transfer equation:

$$L^+I^+ = Q^+ \tag{3.8}$$

where Q^+ represents the adjoint source which is to be defined below. The adjoint radiative transfer operator is postulated as:

$$L^+ = -\mu\frac{d}{dz} + \sigma_t(z) - \frac{\sigma_s(z)}{4\pi}\int\limits_{0}^{2\pi}\int\limits_{-1}^{1}d\mu'd\varphi'p(z,\mu',\varphi',\mu,\varphi)\circ \tag{3.9}$$

From equation 3.5 it follows that the boundary conditions for the adjoint radiative transfer equation read:

$$I_d(\mu > 0, \varphi, z = TOA, x, y) = 0$$
$$I_d(\mu < 0, \varphi, z = 0, x, y) = 0 \tag{3.10}$$

if vacuum boundary conditions for the forward problem are imposed. One immediately notes that the adjoint boundary conditions show a somewhat complementary behavior if compared with the forward counterpart, see equation 2.71, resulting in the constraint that no adjoint radiation leaves the medium.

Fortunately, no newly designed radiative transfer code is necessary to solve equation 3.8 as existing techniques can be readily utilized by substituting:

$$I^+(z, -\mathbf{\Omega}) = \Psi(z, \mathbf{\Omega}) \tag{3.11}$$

which transforms equation 3.8 into a pseudo problem by considering the reciprocity of the propagation of light:

$$L\Psi(z, \mathbf{\Omega}) = Q^+(-\mathbf{\Omega}) \tag{3.12}$$

That means one has to exert the usual solution technique to equation 3.12 with Q^+ having its angular dependence swapped and the forward boundary conditions applied. Moreover, the homogeneous solution of the forward problem also applies to 3.12. After the pseudo intensity Ψ is derived I^+ is gained by rule 3.11.

3.2 Linear Perturbation Theory

For the following steps it is convenient to introduce the quantity of the radiative effect E formally as:

$$E = \langle I, R \rangle \tag{3.13}$$

where R is called response function. If the upwelling flux at level z_r was the demanded property the response function would be:

$$R = \mu\eta(\mu)\delta(z - z_r) \tag{3.14}$$

At this stage, many texts dealing with this technique just postulate that, in order to derive the linear perturbation theory, one has to chose the response function R as adjoint source Q^+. However, this can be formally motivated by a variational principle as shown by Pomraning (1965). Another consequence of that choice is that the effect E can be written by virtue of relation 3.5 as:

$$E = \langle R, I \rangle = \langle I^+, Q \rangle \tag{3.15}$$

By equation 3.15 an excellent way to verify the adjoint intensity result is at hand. But it is also a way to calculate E for a different set of problems, namely the one where E is derived only at one spatial position but where the dependence on the solar angle is rapidly included by the integration represented by $\langle \cdot, \cdot \rangle$. This can be achieved as I^+ is independent of the solar illumination.

With this prerequisite it is possible to gain some insight in the behavior of the adjoint intensity. With a response function as for the upwelling flux in equation 3.14 the adjoint source would be radiating upwards, see Figure 3.1 a). By virtue of the pseudo problem the source would be inverted and the pseudo intensity would look like sketched in Figure 3.1 b). After inverting the angular dependence of Ψ I^+ is derived as in 3.1 c). The "adjoint photons" therefore travel backwards with respect to time and space. This is reflected in the unusual boundary conditions stated above.
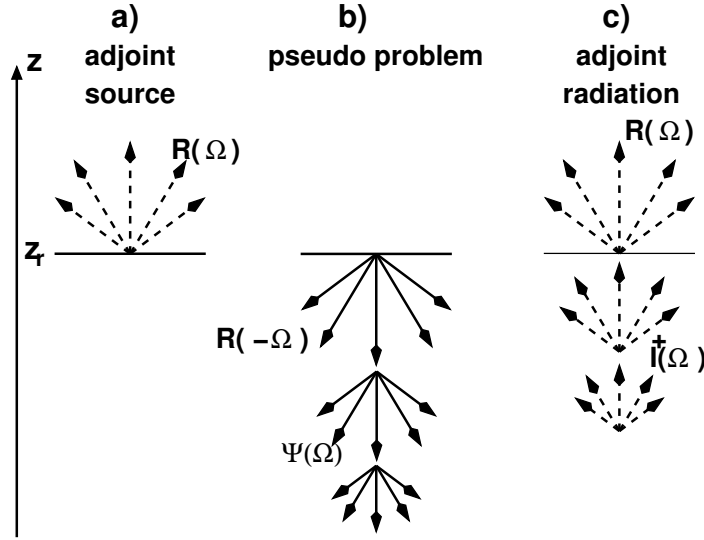
Figure 3.1: The pseudo problem for adjoint radiative transfer. a) An adjoint source R is positioned at level z_r. b) The pseudo problem yields the intermediate solution Ψ. c) Inversion of the directions Ω leads to the adjoint solution I^+.

To proceed with the perturbation theory, one splits up the atmospheric properties into base case "b" and perturbation contributions "Δ":

$$\sigma_s(z) = \sigma_{s,b}(z) + \Delta\sigma_s(z)$$
$$\sigma_a(z) = \sigma_{a,b}(z) + \Delta\sigma_a(z) \tag{3.16}$$
$$\chi_l(z) = \chi_{l,b}(z) + \Delta\chi_l(z)$$

with χ_l the Legendre expansion coefficient of order l of the phase function p. The transport operators then are:

$$L(z, \boldsymbol{\Omega}) = L_b(z, \boldsymbol{\Omega}) + \Delta L(z, \boldsymbol{\Omega}) \tag{3.17}$$
$$L^+(z, \boldsymbol{\Omega}) = L_b^+(z, \boldsymbol{\Omega}) + \Delta L^+(z, \boldsymbol{\Omega}) \tag{3.18}$$

Additionally to the radiative transfer equations 3.2 and 3.8, the following ones are required to be valid:

$$L_b I_b = Q_b \qquad (3.19)$$
$$L_b^+ I_b^+ = R \qquad (3.20)$$

Following the derivation of Ustinov (1991), see Appendix A, for the perturbation of the effect one arrives at:

$$\Delta E = \langle I_b^+, \Delta Q \rangle - \langle I_b^+, \Delta L I_b \rangle \qquad (3.21)$$

with:

$$\Delta Q = Q - Q_b$$
$$\Delta L = L - L_b \qquad (3.22)$$

The first term on the right hand side of equation 3.21 refers to the perturbation of the source and is only in thermal radiative transfer of significance. The second term on the right hand side represents the perturbation of the medium. The resulting perturbation series for the effect E in solar radiative transfer is then:

$$E \approx E_b + \Delta E = \langle R, I_b \rangle - \langle I_b^+, \Delta L I_b \rangle \qquad (3.23)$$

The important fact about relation 3.23 is that only base case radiative transfer results are included. This circumstance leaves the procedure of accounting for small perturbations to a simple integration. In general ΔL will be:

$$\Delta L = \Delta \sigma_t(z) - \frac{1}{4\pi} \int_0^{2\pi} \int_{-1}^{1} d\mu' d\varphi' \Delta \left[\sigma_s(z) p(z, \mu', \varphi', \mu, \varphi) \right] \circ \qquad (3.24)$$

In this form, it is obvious why the z-coordinate system was chosen. If the τ-coordinate had been chosen, ΔL would also consist of the streaming term $\frac{d}{d\tau}$ as a perturbation of the optical properties would have resulted in a perturbation of the the optical depth. Thus, the perturbation of the optical depth would have changed the increments of the coordinate system with each perturbation. This undesirable effect is of course avoided in geometric coordinates.

The scattering term in equation 3.24 can be expanded analogously as in equation 2.78. As only azimuthally independent effects are taken into account $m = 0$ is chosen in the expansion, resulting in:

$$\Delta L = \Delta \sigma_t(z) - \frac{1}{4\pi} \int_0^{2\pi} \int_{-1}^{1} d\mu' d\varphi' \sum_{l=0}^{\infty} (2l + 1) \Delta \eta_l(z) P_l(\mu) P_l(\mu') \circ \qquad (3.25)$$

Inserting equation 3.25 in equation 3.23 one derives after some straightforward steps:

$$
\begin{aligned}
\Delta E(z_r) &= -\langle I_b^+, \Delta L I_b \rangle \\
&= -2\pi \int_0^\infty dz \left(\Delta\sigma_t(z)\Xi(z) - \frac{1}{2} \sum_{l=0}^\infty (2l+1)\Delta\eta_l(z)\xi_l^+(z)\xi_l(z) \right)
\end{aligned}
\tag{3.26}
$$

where:

$$
\bar{I}_b(z,\mu) = \frac{1}{2\pi} \int_0^{2\pi} d\mu I_b(z,\mu,\varphi) \qquad \bar{I}_b^+(z,\mu) = \frac{1}{2\pi} \int_0^{2\pi} d\mu I_b^+(z,\mu,\varphi) = I_b^+(z,\mu)
\tag{3.27}
$$

$$
\Xi(z) = \int_{-1}^1 d\mu \bar{I}_b^+(z,\mu)\bar{I}_b(z,\mu)
\tag{3.28}
$$

$$
\xi_l(z) = \int_{-1}^1 d\mu \bar{I}_b(z,\mu)P_l(\mu) \qquad\qquad \xi_l^+(z) = \int_{-1}^1 d\mu \bar{I}_b^+(z,\mu)P_l(\mu)
\tag{3.29}
$$

$$
\Delta\eta_l(z) = \eta_l(z) - \eta_{l,b}(z) = \Delta\sigma_s(z)\chi_{l,b}(z) + \sigma_{s,b}\Delta\chi_l(z)
\tag{3.30}
$$

Equation 3.26 can also be expanded according to its physical meaning:

$$
\Delta E(z_r) = \Delta E_{s,e}(z_r) + \Delta E_{s,is}(z_r) + \Delta E_{a,e}(z_r) + \Delta E_{s,p}(z_r)
\tag{3.31}
$$

with:

$$
\Delta E_{s,e}(z_r) = -2\pi \int_0^{TOA} \Delta\sigma_s(z)\Xi(z)dz
\tag{3.32}
$$

$$
\Delta E_{s,is}(z_r) = \pi \int_0^{TOA} \sum_{l=0}^\infty (2l+1)\Delta\sigma_s\chi_{l,b}(z)\xi_l^+(z)\xi_l(z)dz
\tag{3.33}
$$

$$
\Delta E_{a,e}(z_r) = -2\pi \int_0^{TOA} \Delta\sigma_a(z)\Xi(z)dz
\tag{3.34}
$$

$$
\Delta E_{s,p}(z_r) = \pi \int_0^{TOA} \sum_{l=0}^\infty (2l+1)\Delta\chi_l\sigma_{s,b}(z)\xi_l^+(z)\xi_l(z)dz
\tag{3.35}
$$

Here infinity as the upper boundary of the integration in z has been replaced with the Top Of Atmosphere (TOA) of the model domain.

Equation 3.32 accounts for the extinction (outscattering) contribution by changes in the scattering coefficient, while equations 3.35 and 3.33 model the inscattering contribution by changes in the phase function and the scattering coefficient, respectively. Finally, equation 3.34 reflects the extinction by absorption. By comparison with the well known Taylor expansion one notes that the perturbation integrals simply adopt the role of derivatives multiplied with the incremental changes Δ of the respective property.

In the presented work, the adjoint calculation and the calculation of the perturbation integrals have been implemented in the radiative transfer model DISORT, see Stamnes et al. (1988). This work has been carried out by modifying the existing solution procedures. For example, to solve the adjoint radiative transfer equation the implemented source function has to be replaced with the inverted adjoint source for all considered effects at all layer interfaces and to hand over the result of both the re-inverted adjoint solution and the forward solution to solve the perturbation integral by Gauss-Quadrature, again for all investigated effects at all layer interfaces. Technically, to do so in the DISORT code simply the right hand side of equation 3.2 had to be replaced by the right hand side of equation 3.12 as explained above, while observing the correct boundary conditions, externally and internally, to guarantee the solution is steady. Effects can then be calculated at all computational layer interfaces and boundaries, comprising up- and downwelling flux-densities, the net flux-density, and the actinic flux. Perturbations of all optical parameters can be imposed as a function of the vertical coordinate while the selected base case can be chosen at will and can also be a function of the vertical.

3.3 Examples

At this point examples of idealized situations will be given to illuminate the features of the perturbation theory.

Example 1: Perturbation of the extinction coefficient

In this example the atmosphere has a total geometric height of $2000m$, and the atmospheric base case is represented by a non-absorbing column with optical properties constant with height. The extinction coefficient is $\sigma_t = 0.01m^{-1}$ and $\omega_o = 1.0$. The cosine of the solar zenith angle is $\mu_o = 0.7$, and the surface albedo is zero. A Henyey-Greenstein phase function with $g = 0.75$ is used, which is also constant with height, and remains unaffected by the perturbation. For simplicity only four computational streams have been used. This setup could be regarded as an idealized planetary boundary layer where the opacity changes with time due to increasing activity of a particle source or by advection. As imposed perturbation the extinction coefficient is increased by 10% per step below $500m$, by 7.5% per step between $500m$ and $1500m$, and by 5% per step above $1500m$. All relative values refer to the original base case value. A total of ten perturbation steps is employed.

This leads to the staircase like shape depicted in Figure 3.2.
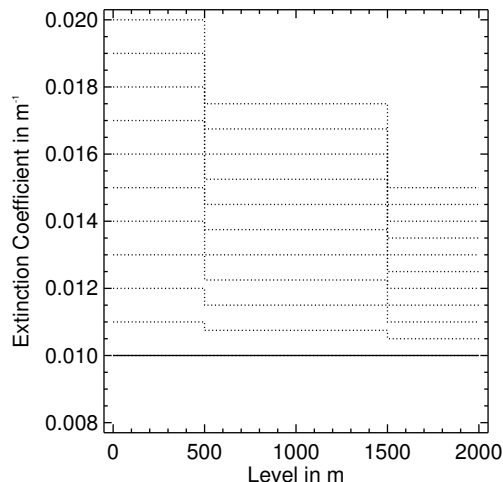
Figure 3.2: Vertical structure of the perturbation of the extinction coefficient for Example 1. Note that the height is given by the x-axis. Solid line: vertically constant base case with $\sigma_t = 0.01m^{-1}$. Dotted lines: perturbation steps of the base case, $z < 500m$: 10% per step, $500m \leq z \leq 1500m$: 7.5% per step, $z > 1500m$: 5% per step. A total of ten steps is applied.

The result of the ten perturbation steps in comparison with the exact forward (FW) solution computed by DISORT in the conventional manner is shown in Figure 3.3. There, the net flux-density at $500m$, right at the lowest discontinuity of the extinction coefficient, is shown as a function of the perturbation step. One clearly notes the linearity of the perturbation integral which results in a tangent to the exact solution.

As in a Taylor series, this result is in good agreement in close vicinity of the base case, but leads to severe errors for perturbation steps larger than two. At step two, the relative error just slightly exceeds one percent, whereas for the last step it is beyond thirty percent. If absorption had been added the drop of the net flux-density predicted by the perturbation theory would have been more significant, also further decreasing the range of applicability of the perturbation integral. Thus, the perturbation theory is in this simple form not able to accurately describe saturation effects which occur in mediums with large scattering optical depths.

Example 2: Perturbation of the phase function

In this example, the atmosphere is vertically entirely homogeneous with $\sigma_t = 0.01m^{-1}$ and $\omega_o = 1.0$. Again, $\mu_o = 0.7$ and the surface albedo is set to zero. Here, a Henyey-Greenstein phase function with $g = 0.75$ is transformed in 10 steps into a phase function of the same type with $g = 0.85$. This case might represent a particle cloud whose composition is gradually transformed by chemical processes. Figure 3.4 again shows the net flux-density as a function of the perturbation step. One recognizes that the phase function perturbation
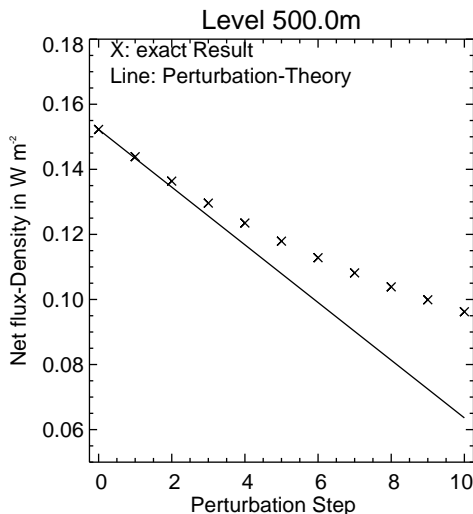
Figure 3.3: Example 1: Linear perturbation (solid line) and exact result (crosses) for the net flux-density at $500m$ as a function of the perturbation step of the extinction coefficient as shown in Figure 3.2. Remaining parameters: $\omega_o = 1.0$, $g = 0.75$, $\mu_o = 0.7$.

results in increasing net flux-density which is in agreement with the notion that a larger asymmetry factor pronounces more the forward, here downward, scattering.

One can also gather from Figure 3.4 that the perturbation of the phase function is a crucial component as errors grow quickly. For example, the relative error is still below one percent after perturbation step three ($g = 0.78$) and reaches 30% for the last perturbation step. However, by means of this example, it can be demonstrated that the perturbation theory can not only serve as a tool to quickly calculate radiative transfer results by evaluating a simple integral, but that it is also useful for gaining a better understanding of sensitivities.

3.4 Treatment of Lambertian Surface Reflection

So far every formula of the radiative transfer perturbation theory has been deduced with respect to vacuum boundary conditions. For many purposes, including modeling radiative transfer within an atmospheric model, it is inevitable to account for at least Lambertian surface reflection which means isotropic backscattering at the ground. One approach which could be pursued is to include the surface reflection by deducing boundary conditions for the forward as well as for the adjoint mode and then directly include those in the solution procedures of the radiative transfer model. This is the standard procedure. However, that would result in direct incorporation of the surface albedo in the output which would be inseparable from the contribution of the atmospheric properties. This way, a base case with respect to certain atmospheric conditions would be coupled with a specific albedo used in this case. For another surface albedo the complete recalculation of base case and perturbation integral would be required, even if the change in the albedo is marginal and
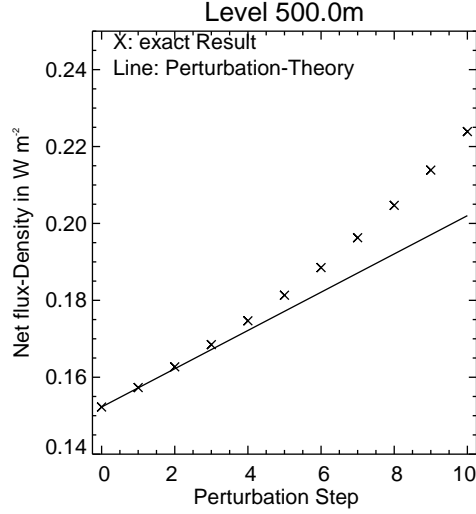
Figure 3.4: Example 2: Linear perturbation (solid line) and exact result (crosses) for the net flux-density at $500m$ as a function of the phase function perturbation of a Henyey-Greenstein phase function. The asymmetry factor is transformed in ten steps from $g = 0.75$ to $g = 0.85$ with the constant values $\sigma_t = 0.01m^{-1}$, $\omega_o = 1.0$, $\mu_o = 0.7$.

the atmospheric conditions are fully maintained. So as to keep as much flexibility as possible, a superposition approach is applied. This approach has already been proposed in connection with the perturbation theory by Box et al. (1988). A rigorous mathematical derivation was recently readdressed by Muldashev et al. (1999). Similarly, the Lambertian reflection follows from a general context which has been worked out by Landgraf et al. (2002).

As shown by Liou (2002), the intensity is described by the following superposition:

$$I(z, \boldsymbol{\Omega}) = I_v(z, \boldsymbol{\Omega}) + F_v(z = 0) \frac{A}{1 - A\bar{s}} I_s(z, \boldsymbol{\Omega}) \tag{3.36}$$

where Lambertian reflection of a surface with albedo A was assumed for the lower boundary. Here, I_v is the intensity gained by the calculation with vacuum boundary conditions applied. The other quantities are:

$$F_v(z = 0) = \frac{1}{\pi} \int\limits_0^{2\pi} d\varphi \int\limits_{-1}^0 d\mu |\mu| I_v(z = 0, \boldsymbol{\Omega}) \tag{3.37}$$

$$\bar{s} = \frac{1}{\pi} \int\limits_0^{2\pi} d\varphi \int\limits_{-1}^0 d\mu |\mu| I_s(z = 0, \boldsymbol{\Omega}) \tag{3.38}$$

I_s is the solution of a special radiative transfer problem defined by the radiative transfer

equation:

$$LI_s = Q_s \tag{3.39}$$

and the source Q_s:

$$Q_s = \mu\eta(\mu)\delta(z) \tag{3.40}$$

thus describing an artificial isotropic source at the lower boundary which is radiating upwards. Similarly, for the adjoint radiance a related superposition exists:

$$I^+(z, \vec{\Omega}) = I_v^+(z, \vec{\Omega}) + F_v^+(z = 0)\frac{A}{1 - A\bar{s}}I_s(z, -\vec{\Omega}) \tag{3.41}$$

There are two remarks worth mentioning at this point. First, formula 3.41 contains the same radiative transfer results for I_s, thus reducing the computational burden to evaluate equations 3.41 and 3.36. Second, if one closely examines equation 3.39, one notes that Q_s is exactly the adjoint source if one needs to compute the adjoint radiance field for upwelling flux at the lower boundary with respect to vacuum boundary conditions. This way no additional radiative transfer calculation has to be performed, careful selection of the required subset of the adjoint solution is the only task left. Inserting equations 3.36 and 3.41 in 3.23 leads after a tedious but straightforward calculation to:

$$E = E_b + \Delta E = E_{b,v} + E_{b,a} + \Delta E_v + \Delta E_a \tag{3.42}$$

where:

$$E_{b,v} = \int\limits_0^{TOA}\int\limits_0^{2\pi}\int\limits_{-1}^1 RI(z, \mu, \varphi)d\mu d\varphi dz$$

$$E_{b,a} = 2\pi\mathcal{A}F_{v,b}(0)\int\limits_0^{TOA}\int\limits_{-1}^1 d\mu dz RI_{s,b}(z, \mu)$$

$$\Delta E_v = -2\pi\int\limits_0^{TOA} dz\left(\Delta\sigma_t(z)\Xi(z) - \frac{1}{2}\sum_{l=0}^\infty(2l+1)\Delta\eta_l(z)\xi_{l,v}^+(z)\xi_{l,v}(z)\right) \tag{3.43}$$

$$\Delta E_a = -2\pi\mathcal{A}\int\limits_0^{TOA} dz\Big\{\Delta\sigma_t(z)\left(\mathcal{F}_1(z) + \mathcal{F}_2(z) + \mathcal{A}\mathcal{F}_3(z)\right)$$

$$-\frac{1}{2}\sum_{l=0}^\infty(2l+1)\Delta\eta_l(z)\left(\mathcal{F}_{\xi_1}(z) + \mathcal{F}_{\xi_2}(z) + \mathcal{A}\mathcal{F}_{\xi_3}(z)\right)\Big\}$$

and:

$$\mathcal{A} = \frac{A}{1 - A\bar{s}_{b,v}} \qquad (3.44)$$

For the definition of the remaining quantities see Appendix B. The subscript "v" refers to vacuum boundary conditions, and "b" stands for a derivation with respect to the base case. The remarkable feature of equations 3.43 is that now indeed all quantities are related either to the forward and adjoint vacuum solution or to the special problem defined by equation 3.39. The solution of this radiative transfer equation is of course also derived with respect to vacuum boundary conditions. As a result, the only impact on the formula the albedo has is in the factor $\mathcal{A}$. The surface reflection is then easily incorporated without the need of any recalculation of radiative transfer results.

3.5 Examples

Example 3: Pure albedo change

At first the albedo is considered independently, meaning no perturbation is included in this calculation. In Figure 3.5, the results are shown for an atmospheric column with a scattering coefficient of $\sigma_s = 0.01 m^{-1}$, an absorption coefficient $\sigma_a = 5.0 \cdot 10^{-7} m^{-1}$, and a Henyey-Greenstein phase function with $g = 0.75$, all independent of the vertical. The albedo has been changed over the complete considerable range from zero to one. A realistic background of this example could be the alteration of the surface properties from purely absorbing to totally reflecting by snowfall on a black area. It is again $\mu_o = 0.7$. One clearly notes that the solution is exact and not an approximation as one might think.

Example 4: Perturbation and albedo

Here ,the same atmospheric parameters are used as in the first perturbation example, and the perturbation is also identical. The albedo is selected as in the previous example, thus forming a worst case scenario where perturbation and surface albedo increase simultaneously. The result for the net flux-density at $500m$ is depicted in Figure 3.6. The accuracy is surprisingly good, maximum errors are about seven percent. Yet, the superposition cannot reproduce the (almost) obvious result for an albedo of one. As can be gathered from equations 3.43, multiple multiplications of the albedo factor $\mathcal{A}$ and the perturbations of the atmospheric parameters exist. As a result, errors are in general expected to amplify.

3.6 Multiple Base Cases and Interpolation

As was shown in the preceeding sections, the radiative transfer perturbation theory cannot adequately handle massive perturbations exceeding the linear range. Basically, there are two conceivable ways to circumvent this shortcoming. First, the extension of the
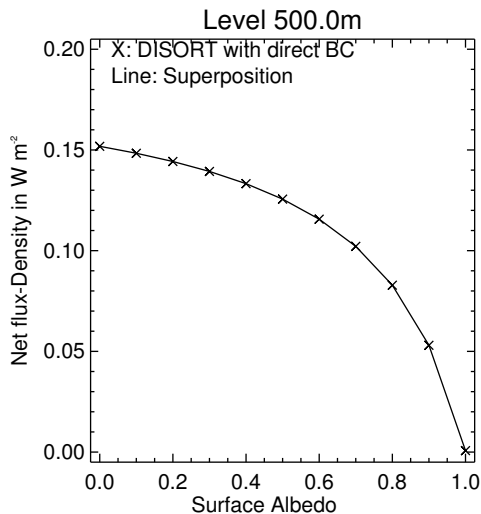
Figure 3.5: Example 3: Comparison of the direct albedo treatment in DISORT (crosses) by an explicit reflecting lower boundary and the superposition approach (line) for the net flux-density at $500m$. Remaining parameters: $\sigma_s = 0.01m^{-1}$, $\sigma_a = 5.0 \cdot 10^{-7}m^{-1}$, $g = 0.75$, $\mu_o = 0.7$.

perturbation series to second and higher order terms is accomplishable, see Box (2002). Unfortunately, this involves the Green's function which is neither easy nor computationally inexpensive to derive. This application of the perturbation theory is for these reasons a subject of ongoing basic research. The second possible approach involves multiple base cases and the interpolation of values located in the range between them. As mentioned before, the linear perturbation theory delivers the first order derivatives analytically without the need for a lengthy and unstable derivation by finite differences. This circumstance enables the utilization of the Hermite interpolation. This technique makes use of the derivatives additionally to the functional values. Therefore, for a chosen pair of values the intermediate points can be derived by a third order interpolation. An overview of the Hermite interpolation can be found in Maess (1988) and Kahaner et al. (1989).

There are two necessary remarks concerning the limitations associated with the application of this technique. First, the phase function cannot easily be incorporated in the interpolation as this would require a multivariate technique for each of the phase function expansion coefficients. Second, the interpolation is only carried out with respect to the total optical depth or more precisely with respect to the perturbation of the total optical depth. This has several reasons. First, an interpolation with respect to scattering and absorption optical depth separately would also require a multivariate interpolation. This neither seems to be meaningful under the computational point of view nor for reasons of accuracy. Yet, it is possible to use the total (extinction) optical depth as interpolation parameter. However, not the optical depth increment at each layer can be used but the optical depth perturbation of the whole column. This can be motivated by the integral nature of radiative transfer meaning that the intensity at a certain point is not only determined by the optical
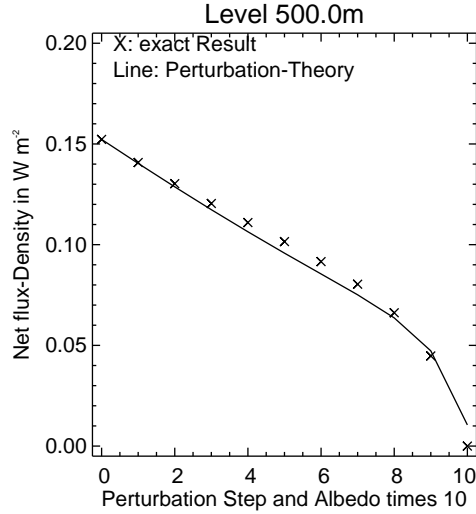
Figure 3.6: Example 4: Results for the net flux-density for DISORT (crosses) and perturbation (line) computations of the net flux-density at $500m$. Perturbation as shown in Figure 3.2, albedo change and remaining parameters as in Figure 3.5.

quantities in its direct vicinity but from the whole distribution in the column. The basic form of the Hermite interpolation for the effect E therefore is:

$$E(\tau_t) = E_0(\tau_0)(1 - 3s^2 + 2s^3) + E_1(\tau_1)(3s^2 - 2s^3) + \Delta E_0(\tau_0)(s - 2s^2 + s^3) + \Delta E_1(\tau_1)(s^3 - s^2)$$

(3.45)

with the interpolation parameter s:

$$s = \frac{\tau_t - \tau_0}{\tau_1 - \tau_0}$$

(3.46)

E_0 and E_1 stand for the base case forward solutions while ΔE_0 and ΔE_1 represent the perturbation integrals. τ_0 and τ_1 are the total extinction optical depths for the two base cases. All perturbations which lead to τ with $\tau_0 < \tau < \tau_1$ are then treated by 3.45. Perturbation results for the phase function are added linearly. This way an arbitrary number of base cases can be involved. The interpolation is then applied in each interval separately leading to a third order interpolation for each section.

3.7 Example

Example 5: Employing three base cases to the first example.

The original perturbation of the scattering coefficient is readdressed here, see Figure 3.2. Three base cases are employed, one at perturbation step zero, the second at step five, and

the last at step ten. The results of each individual linear perturbation estimate, as well as the combined interpolation in the two sections, are shown in Figure 3.7 for the net flux-density at $500m$.
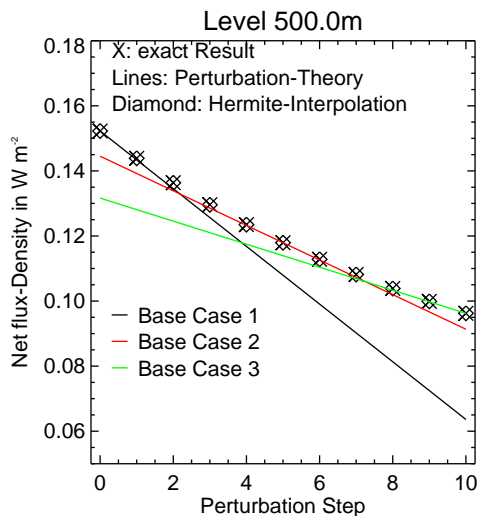
Figure 3.7: Example 5: Results for the net flux-density at $500m$ for DISORT (crosses), perturbations of the three base cases (black line: RTPT with base case 1, red line: RTPT with base case 2, green line: RTPT with base case 3) and the interpolation (diamonds) for the variation of the scattering coefficient as in Example 1, see Figure 3.2. Remaining parameters: $g = 0.75$, $\mu_o = 0.7$.

It can be recognized that base case two clearly offers the best individual result which is not surprising as it is located in the center of the total interval. However, even the third base case delivers superior results compared to base case one. This is supported by the evaluation of the relative errors, see Figure 3.8.

As expected, all results are indeed exceeded in precision by the interpolation which is able to reduce the errors to negligible values. For this reason the interpolation can be expected to extend the range of applicability greatly. Nevertheless, this improvement does not come without a cost as it increases the computational burden for the additional base cases as well as for the interpolation itself. Similar results are obtained if the surface albedo is included. In case of a simultaneous perturbation of the phase function expansion coefficients the accuracy decreases as expected. However, in case of a superposition of phase function and scattering perturbation, effectively combining examples one and two, the relative error stays well limited and only reaches two percent when approaching the last perturbation step, not shown here. All base cases were calculated with the same Henyey-Greenstein phase function. This behavior can be explained with the opposite characteristics of both radiative transfer features. Thus, errors are accidentally mutually canceling out, see Figures 3.3 and 3.4. This is not expected to happen in general.
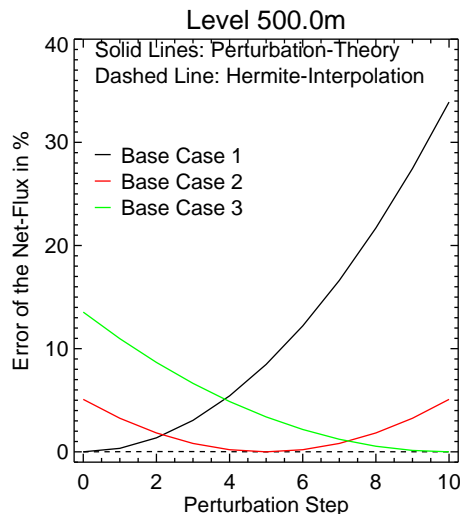
Figure 3.8: Relative errors in per cent of the perturbation and interpolation results shown in Figure 3.7 with respect to the DISORT calculation. Lines correspond to perturbation estimates (black: RTPT with base case 1, red: RTPT with base case 2, green: RTPT with base case 3), the dashed line refers to the interpolation.

3.8   Remarks

To summarize the scope of the work so far it can be said that an adjoint radiative transfer perturbation model for azimuthally independent effects was implemented in and built around the core routines of DISORT. Related work has been carried out by Hu (1994). Perturbation integrals for up- and downwelling flux-densities, the net flux-density and the actinic flux can be derived at all computational layer interfaces for a freely selectable number of computational streams. The base cases as well as the perturbations of all three optical parameters can be functions of height. An arbitrary number of base cases with respect to the total optical depth can be chosen, and results are gained individually as well as by third order Hermite interpolation between pairs of base cases. Lambertian surface reflection can be accounted for by superposition.

The given idealized examples have been chosen to explain the basic features of the applied methods to the reader with maximum ease. Configurations more related to RT in cloudy atmospheres have not been shown due to their less obvious characteristics. All examples generally show good accuracy of the perturbation results when restricted to the direct neighborhood of base cases. The Hermite interpolation also gives good estimates of the true forward results beyond that limit. Concerning the accuracy of the derivatives gained by the perturbation integrals a very simple test was set up. The derivative deduced from a vertically constant perturbation of ten percent of a base case with $\sigma_s = 0.005m^{-1}$, equally constant with height, was compared with the slope yielded by two finite difference calculations differing by the thousandth part of a percent. The relative error was of a magnitude of a hundredth of a percent at the most. Variations of the increment of the

finite difference calculations showed the occurrence of numerical instabilities especially for values at the model boundaries. In contrast to that, the derivative gained by the perturbation is unconditionally stable.

There are several other fields of application which could not be considered here. First, there is no obvious reason why the perturbation theory could not be applied to long-wave radiative transfer. However, as the source function then involves the absorption coefficient the perturbation of the source has to be included in the perturbation series, see equation 3.21. Second, an equally challenging task is the perturbation of the optical properties with respect to their wavelength dependence. For the UV-region such an approach has been carried out by Loughlin (1995). Finally, for a computationally efficient realization an analytic 2- or 4-stream model would be the best choice. Gabriel et al. (1998) have successfully linearized broadband radiative transfer by applying the RTPT to a 2-stream model.

Chapter 4

3D radiative transfer parameterizations

> God does not care about our
> mathematical difficulties.
> He integrates empirically.
>
> ———————————————
> Albert Einstein

4.1   Introduction

For several reasons the problem of three-dimensional (3D) radiative transfer has been attracting attention for a number of years. One motivation to address this subject is the need for atmospheric models to simulate 3D cloud-radiation interactions with reasonable accuracy. Those interactions have been identified as highly relevant for the climate system, see chapter 1. However, atmospheric models, no matter whether operated for high resolution mesoscale modeling or on a global scale, usually employ the Independent Pixel Approximation (IPA) or the Plane-Parallel assumption (PPA), an even coarser representation of radiative transfer in realistic atmospheres. Both approaches have shown to encounter certain problems when applied to inhomogeneous cloud fields. In the following sections, these difficulties will be related to exact 3D RT effects. Moreover, the 3D RT approximations constructed in this study will be introduced.

There are at least three basic methods to treat radiative transfer in cloudy atmospheres. First, it is possible to employ the Monte-Carlo (3DMC) and Spherical Harmonics Discrete Ordinate Method (SHDOM) techniques to fully account for the 3D variability of the optical properties of the atmosphere and to model the resulting spatial propagation of radiation. Figure 4.1 sketches some idealized photon paths in an inhomogeneous atmosphere. A widely used textbook about the 3DMC technique has been written by Marchuk et al. (1980), for SHDOM see Evans (1998). 3DMC is based on the generation of a photon

statistics and SHDOM explicitly solves the 3D RTE, see equation 2.60. Both are computationally expensive if reasonable degrees of accuracy are required which prevents them from being considered as an operational radiative transfer module for atmospheric models.
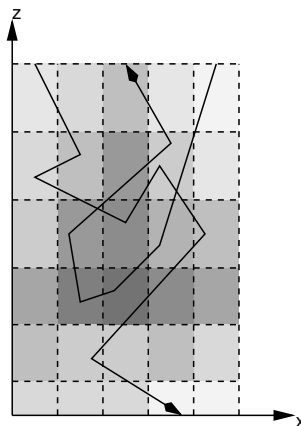
Figure 4.1: Realistic behavior of photons in an heterogeneous medium. Different shades of grey represent different values of the optical depth and other optical properties.

Second, in order to at least consider the 3D fluctuation of the optical properties each atmospheric column can be treated independently of its neighbors. The resulting Independent Pixel Approximation (IPA) applies then a one-dimensional (1D) radiative transfer model to each of the columns separately, see Figure 4.2, effectively neglecting horizontal photon exchange. Some authors inseparably connect the term Independent Pixel Approximation with the determination of the domain averaged transmission and reflection following the 1D RT calculation in all columns. However, in agreement with Marshak and Davis (2005), this seems in the authors point of view an unnecessary restriction of this term. As a consequence, the IPA is here only regarded as the 3D result following from the successive application of the 1D RT model to all columns. The basic three-dimensional effects resulting from the horizontal exchange and the shortcomings of the IPA with respect to their accurate modeling can be taken from Figures 4.3 to 4.8.

In Figure 4.3 the trapping effect is shown. Multiple scattering leads to subsequent propagation of photons deeper and deeper into a cloud by crossing horizontal cell boundaries. In the IPA this effect is neglected, and photons on trajectories leaving the column at the lateral boundaries are re-injected at the opposite side by periodic boundary conditions. That is sketched by the open dashed arrow. The opposite effect is called leaking, see Figure 4.4, which means that photons can leave clouds by penetrating their sides from inside out whereas in case of the IPA clouds can be entered or left only through their tops and bottoms. The third effect is the possibility of interactions between clouds in different layers and pixels by mutual scattering of photons. In the IPA only vertical interaction between cloudy cells in the same column is possible, see Figure 4.5. Similar is the shadowing effect where in three dimensions the photons can travel through gaps between clouds, thus effectively contributing to a shadow on the surface according to the geometry of the solar illumination, see Figure 4.6. In contrast to this, the IPA can only produce shadows directly
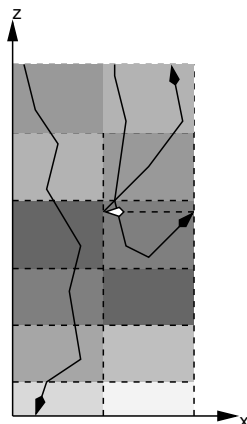
Figure 4.2: Example for independent pixel radiative transport. The open dashed arrow represents periodic boundary conditions. Shades of grey stand for different optical properties.
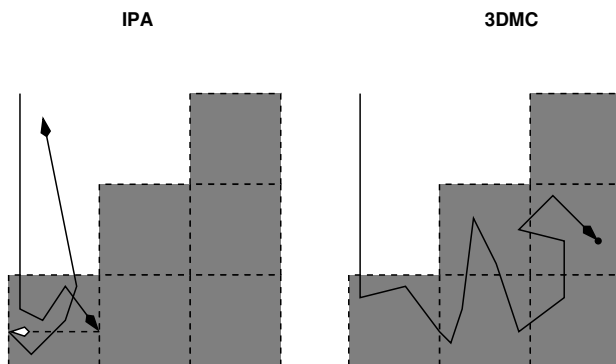
Figure 4.3: Trapping of photons inside clouds represented as grey cubes. Idealized photon paths for IPA (left) and 3DMC (right). The open dashed arrow represents periodic boundary conditions. Adapted from O'Hirok and Gautier (1998).

below the cloud, ignoring the direction of the incoming solar illumination. A combination of the aforementioned effects of photon exchange across columns are interactions involving cloud sides as shown in Figure 4.7 and 4.8.

The coarsest approximation of radiative transfer in cloudy atmospheres is the so-called Plane-Parallel Assumption (PPA), see Figure 4.9. Here the optical properties depend only on the vertical coordinate and all lateral variations in the domain have been lost due to averaging or due to another technique to build a horizontally homogeneous cloud. As a result of the large errors, this assumption is not considered appropriate which will be addressed below. However, it has been successfully employed by reproducing domain averaged results of inhomogeneous clouds by rescaling the optical properties of homogeneous clouds.

The errors of the IPA and PPA with respect to 3DMC can be classified in two categories. The first one is the error between the IPA and the PPA. It is termed plane-
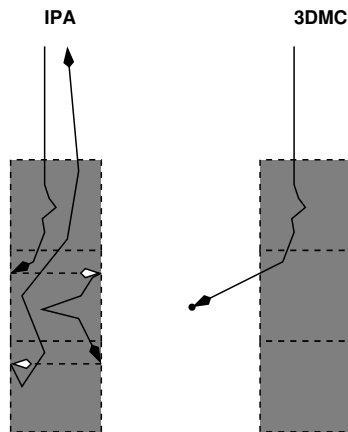
Figure 4.4: Leaking of photons through cloud sides. Remarks as for Figure 4.3.
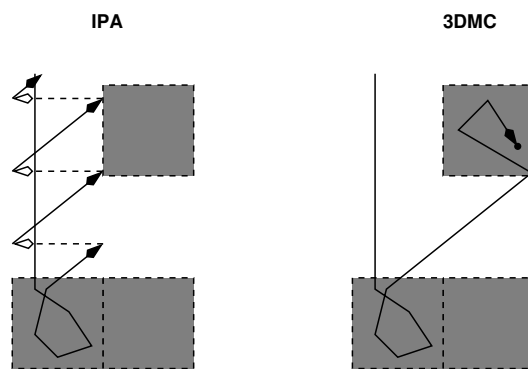
Figure 4.5: Interaction of cloud layers by scattering of photons. Remarks as for Figure 4.3.

parallel bias or heterogeneity effect, see Cahalan et al. (1994b) and Várnai and Davies (1999). The second one is the error due to the neglect of horizontal photon transport. It is called horizontal transport effect or independent pixel bias, see Cahalan et al. (1994a) and Várnai and Davies (1999). It was demonstrated by Cahalan et al. (1994b) that the global planetary albedo has a tremendous impact on the global temperature. These authors show that an underestimation of the global albedo by 10% results in a global warming of about 5° C. This is approximately the same magnitude in global warming experienced since the last ice age. Thus, inaccurate radiative transfer modeling can have a serious impact on the interpretation of climate predictions. Investigations of the plane-parallel albedo bias show, see Cahalan et al. (1994a), that it is likely to introduce errors of the above magnitude. Its origin can be explained by the convex dependence of the reflection on the optical depth. Figure 4.10 shows the result of a generalized reflection function, see Cahalan et al. (1994b) for details, depending on the optical depth.
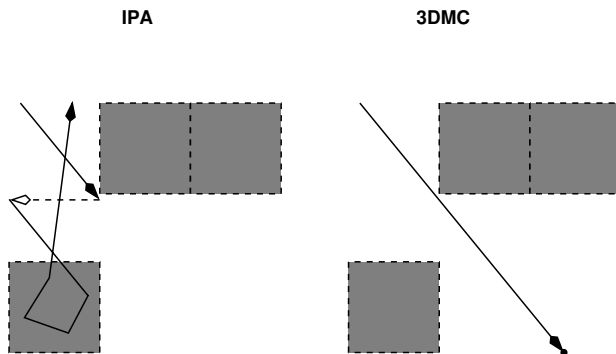
Figure 4.6: Shadowing by propagation of photons through cloud gaps. Remarks as for Figure 4.3.
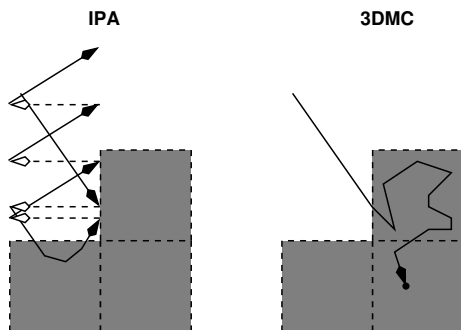
Figure 4.7: Penetration of photons through cloud sides. Remarks as for Figure 4.3.

It can be easily concluded that due to its nonlinear behavior always:

$$R(\langle \tau \rangle) \geq \langle R(\tau) \rangle \tag{4.1}$$

is valid. This is a unique feature of this class of functions which was already investigated by Jensen (1906). The direct consequence of this behavior is the plane-parallel albedo bias. In relation 4.1 the right hand side can be identified as the mean reflection of all pixels which can be deduced from the IPA, and the left hand side corresponds to the plane-parallel assumption as only one calculation based on the mean optical depth of all pixels has to be carried out. The rescaling mentioned above can be graphically motivated by choosing the reduced optical depth $\tau(\langle R \rangle)$ for the plane-parallel medium. A very similar dependence exists for the transmitted light. Compared to the plane-parallel albedo bias, the differences between 3DMC and IPA are rather small when domain averages of the transmission and albedo are referred to, see for example Marshak et al. (1995). This is at least true if weak internal inhomogeneity in overcast situations is considered. For broken cloud fields this impression might vary from case to case. Yet, difficulties arise when smaller scales on a local level are in focus. Marshak et al. (1995) and Davis et al. (1997) showed by investigating wavenumber spectra of the optical depth field and of the radiance computed by the IPA
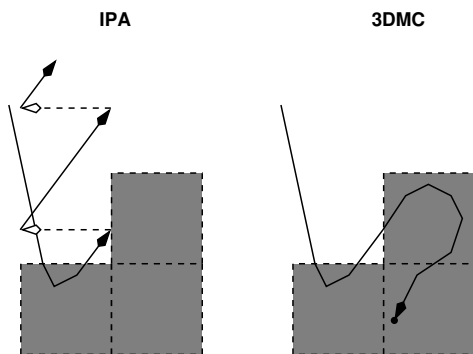
Figure 4.8: Interaction of cloud top and cloud side. Remarks as for Figure 4.3.
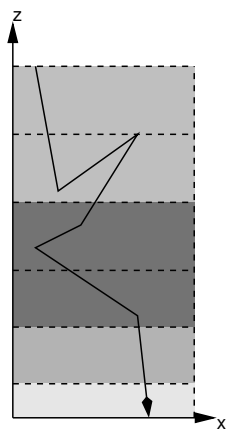
Figure 4.9: Plane-parallel radiative transfer. No lateral variations of optical properties, vertical structure implied by different shades of grey.

and 3DMC that at scales of about $200m$ to $300m$ a scale break occurs, see Figure 4.11. For scales above this break the slope of the power spectrum of the 3DMC results follows closely the spectrum of the IPA computations which are scale invariant and which in turn show the same scaling behavior as the optical depth, see also section 2.4. The average slope above the scale break in the spectrum is approximately $-\frac{5}{3}$ if logarithmic axes are applied. This was also determined from studies of 3D atmospheric turbulence by Corrsin (1951). Below the scale break the slope steepens which is a sign of smoother structures and an indication for a change of the physical process controlling the behavior at this scale. Marshak et al. (1995) and Davis et al. (1997) found that this can be explained with the diffusion process dominating this scale and driving the photon exchange between pixels.

As a result of the discussed 3D effects, in reality the local photon balance can violate the law of energy conservation. According to that law, the sum of transmission, reflection, and absorption has to amount to unity. An exemption from that rule for example exists if the transmission alone exceeds unity, see equation 2.13. That implies that at a certain position a larger number of photons is arriving at the ground than the number of photons that has
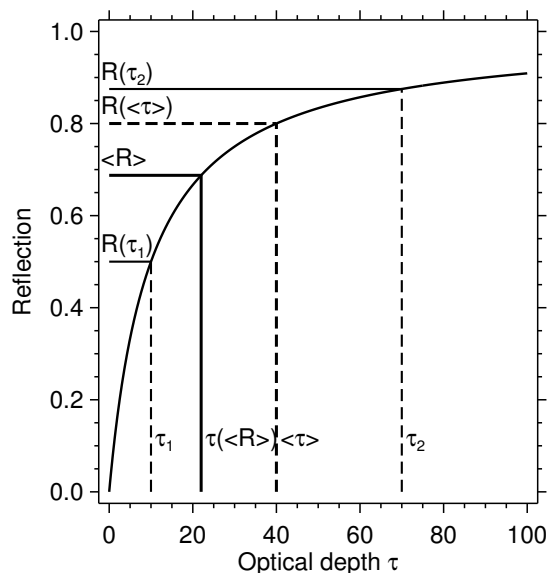
Figure 4.10: Reflection as a function of total optical depth τ. τ_1 and τ_2 are individual values of columns with average $\langle\tau\rangle$. $R(\langle\tau\rangle)$ is derived by the PPA while $\langle R\rangle$ is the average computed by the IPA from the individual pixels with $R(\tau_1)$ and $R(\tau_2)$. $\tau(\langle R\rangle)$ is the rescaled optical depth derived by inversion.

been injected at this position at the top of the atmosphere. The additional photons are supplied by horizontal transport so that locally a photon gain is suffered at the expense of a photon loss elsewhere. As a matter of fact, the domain's total budget levels all of these local imbalances as the total energy has to be conserved, meaning that the domain averaged sum of absorption, reflection and transmission has to equal unity under all conditions.

Marshak et al. (1999) also investigate the dependence of horizontal fluxes and the accuracy of the IPA on the scale applied. These authors demonstrate that the errors associated with the IPA decrease with increasing averaging scale. While this result is expectable, it is also reported that even at a scale of several kilometers a notable difference between 3DMC and IPA persists. That is especially true for reflectance and is less pronounced for absorptance and transmittance but even holds for absorbing wavelengths. From these findings it can be concluded that 3D effects make also a significant contribution to radiative transfer in case of a horizontal resolution of several hundreds of meters to several kilometers.

On the other hand, numerical weather prediction models have successively refined their horizontal resolution from dozens of kilometers to several kilometers and are expected, at least for high resolution modeling, to approach one kilometer or less in the immediate future. As these models usually employ the Delta-2-stream technique in independent pixel mode, the need for a parameterization of 3D effects arises. The spectrum of approaches conceived can be split up into two distinct parts, see Davis (2000). The first one comprises approaches which can be termed probabilistic. Examples are stochastic radiative transfer, see Lane-Veron and Sommerville (2004), and renormalization approaches, see Petty (2002) and Cairns et al. (2000), which are partly based on the rescaling described above. Many of
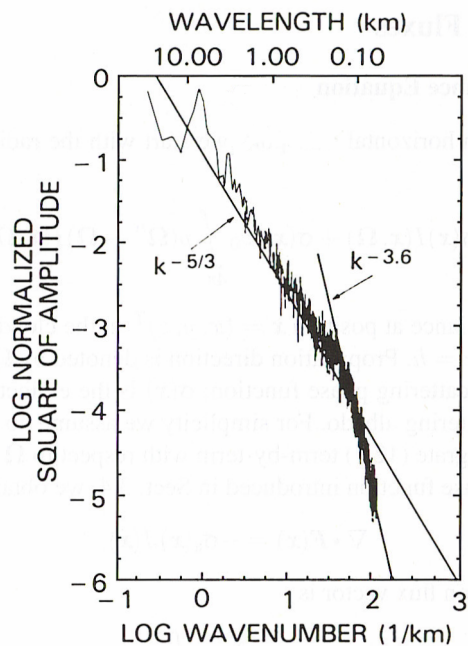
Figure 4.11: Wavenumber spectrum of a LANDSAT cloud reflectivity field. The lower horizontal axis corresponds to the wavenumber, the upper axis to the scale. The straight lines are fits to the data and represent the different slopes and spectral exponents, respectively. Adapted from Marshak and Davis (2005).

these models yield domain averaged results, some of them give no vertical resolution of the radiative properties and need specially adapted input data. The second set of approaches can be called deterministic as these derive an approximate form or application of the radiative transfer equation suitable to describe 3D effects. Examples are the 3D realization of the diffusion approximation (DiA), Chen et al. (2005), the Tilted Independent Pixel Approximation (TIPA), Várnai and Davies (1999), and the Nonlocal Independent Pixel Approximation (NIPA), see Marshak et al. (1995) and Marshak et al. (1998). With respect to the applicability of the specific method to parameterize 3D effects in atmospheric models, the following criteria are believed to be meaningful. First, the chosen method has to be reasonably computationally efficient. Second, the method has to give 3D resolution in order to enable the model to gain at least some vertical structure of heating rates and fluxes etc. Third, the input data provided by the other modules of the model environment have to be suitable for the radiation module without too comprehensive transformations.

4.2   Tilted Independent Pixel Approximation

The main focus of this study is the development of parameterizations for atmospheric models with horizontal resolutions of several dozens of meters to several kilometers. The primary 3D effect on this range of scales is believed to be the oblique path of propagation of

radiation according to the geometry of the solar illumination. For this reason, the concept of the Tilted Independent Pixel Approximation (TIPA) was chosen as primary parameterization. The original outline of the method was presented by Várnai and Davies (1999). The geometric realization developed in this study enables the method to be operated in connection with an ordinary 1D radiative transfer model. For this purpose, the path the direct solar beam would follow through the atmosphere is tracked starting at the upper model boundary in the centers of the pixels, see Figure 4.12. All encounters with grid cells are registered and the length of the respective line of intersection with the grid cell is stored together with the cell's coordinate. By means of that procedure the vertical coordinate is transformed and redefined according to the solar azimuth and zenith, see Figure 4.13. The optical properties are then also transformed according to the intersection length. Even if the horizontal resolution is not too fine for the intended application, it has to be noted that generally the penetration of horizontal grid cells generates numerous additional levels in the new slant coordinate. In order to circumvent a subsequent increase in the computational burden for the radiative transfer model, a weighted mean is applied. It averages all new vertical levels introduced by horizontal transitions between two intersections of vertical coordinate levels in the original grid. This way, no additional resources for the radiative transfer calculation are necessary in comparison with traditional IPA calculations, as the number of vertical levels is kept constant, see Figure 4.13. After the radiative transfer calculations, which proceed as in the usual IPA, have been carried out, the results in the slant columns are transformed to the appropriate positions in the original lattice. Thus, a three-dimensional radiative transfer result is derived at the end of the process. Finally, it has to be noted that for overhead sun by definition no difference between IPA and TIPA exists.
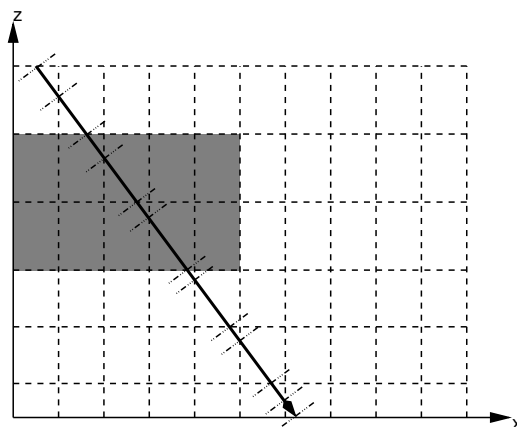
Figure 4.12: Concept of the geometric TIPA. A x-z cross section of a cloud is shown as grey cube. The path of the direct light emanating from the center of the pixels at the top of atmosphere is depicted as solid line. Intersections with horizontal and vertical cell boundaries are symbolized by dashed-dotted lines.
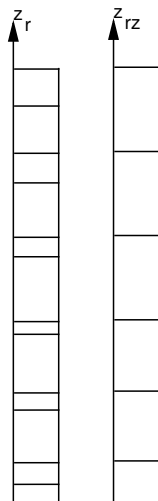
Figure 4.13: Vertical coordinates as defined by TIPA for the slant column as shown in Figure 4.12 with all intersections (z_r, left) and averaged to maintain the original number of levels (z_{rz}, right).

4.3   Examples

Purely absorbing case

In order to give an example for the procedure described above, a highly artificial test case which shows the main feature of the TIPA is set up, and results are compared with exact 3DMC computations. A cloud which is purely absorbing is placed inside a vacuum as shown in Figure 4.12. The domain is $60 \times 20 \times 27$ cells large. The cloud occupies one third of the horizontal space of the domain, thus extending over 20×20 pixels and reaches vertically from $1000m$ to $1300m$. The total vertical extension is $2000m$ and the horizontal resolution is $50m$. The vertical resolution in the range of the cloud is $30m$. The sun illuminates the scene from left to right along the x-axis with $\mu_o = 0.5$. The surface is purely absorbing. The resulting total optical depth of the cloud is 1.5. The result for the downwelling flux at pixel (20,10) is depicted in Figure 4.14(a). One recognizes that the TIPA matches the 3DMC profile quite accurately. This result is not unexpected as no scattering is included, and as a consequence, no inter-column exchange of light can develop. The pronounced curvature in the profiles stems from the simulated shadow below the cloud. In contrast to this, the IPA profile matches half the bow and cannot correctly reproduce the increase of radiation below the cloud due to the sideways solar illumination. This results in erroneous downwelling flux at the ground. The impression changes if the leftmost column is chosen, pixel (1,10), see Figure 4.14(b). Here, the slant beams enter the cloud via the side and not from the top as before. The inverse transformation of the results leads then to a very ragged profile of TIPA within the cloud because of errors due to the discretization of the medium. More precisely, the inverse transformation piles results directly above one another which originate from different slant columns. Because these columns intersect

different parts of the medium, the results are fundamentally different, while the neglect of inter-column exchange prevents the results to become smoothed. This is an effect that impacts all calculations including realistic atmospheres. Yet, below and above this area the profiles still match. The error due to the discretization of course decreases with increasing distance from the cloud side. As this position is still below the cloud, the IPA result is the same as in position (20,10).
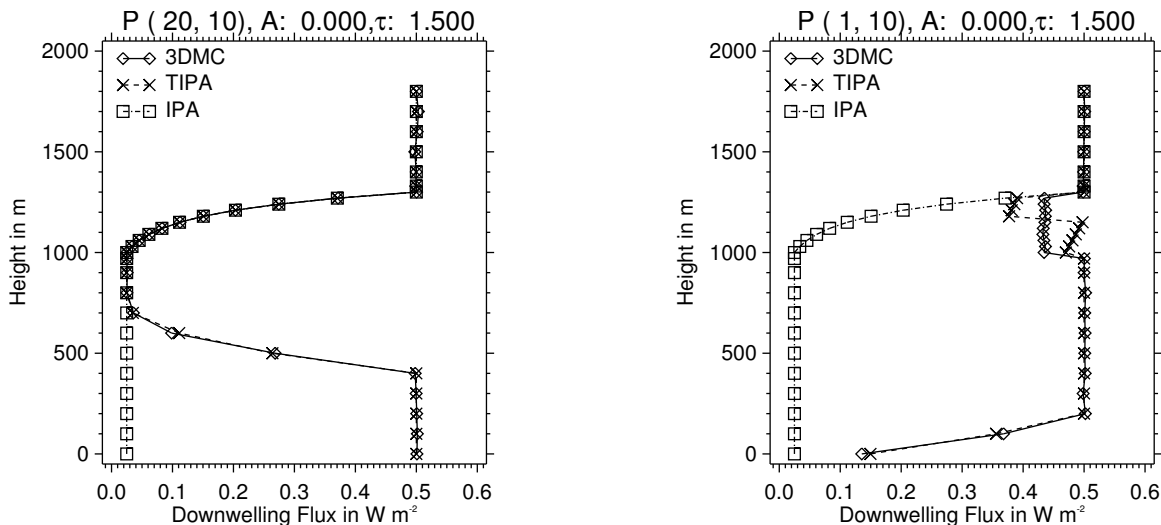
(a) Vertical profiles of IPA, TIPA and 3DMC at the right side, pixel (20,10), of the artificial cloud.

(b) Vertical profiles of IPA, TIPA and 3DMC at the left side, pixel (1,10), of the artificial cloud.

Figure 4.14: Examples of vertical profiles of the downwelling flux-density in pixel (20,10) and pixel (1,10) for the artificial cloud sketched in Figure 4.12 in the purely absorbing case. $\mu_o = 0.5$ and $\varphi_o = 0°$.

Mixed case

To conclude this section a more realistic example is considered. Here, the horizontal resolution is increased to $500m$, while the cloud is characterized by $\omega_o = 0.989$ and $g = 0.8452$ of a Henyey–Greenstein phase function. It is located between $2000m$ and $3500m$. The surrounding atmosphere has $\omega_o = 0.9$ and isotropic scattering. The cloudy pixels have a total optical depth of $\tau = 12.225$ and the clear sky area has $\tau = 0.225$. All other parameters remain unchanged, and the cloud is again positioned as shown in Figure 4.12. In Figures 4.15(a) and 4.15(b) the histograms of the absolute errors of transmission and reflection (albedo) of all pixels are shown. The differences are always formed by subtracting the 3DMC result from the result derived by the respective approximation:

$$\Delta P = P(Approx.) - P(3DMC) \tag{4.2}$$

Table 4.1: Domain averaged results of IPA, TIPA and 3DMC for the mixed example.

Model	$\bar{T}$	$\bar{R}$
3DMC	0.592	0.294
IPA	0.606	0.286
TIPA	0.590	0.301

P stands for the investigated property, for example the transmission T, while *Approx.* represents the radiative transfer approximation. This definition of ΔP applies to all results presented in this thesis, if not stated otherwise. One clearly notes from the above mentioned figures that TIPA improves the computation of the transmission as no extremely large outliers occur compared to IPA. However, TIPA is less accurate than IPA with respect to reflection. Domain averaged results, see Table 4.1, show that TIPA is slightly more precise in this case, yet all differences are small and cannot be used to draw sound conclusions. However, cumulative distributions of the absolute values of the errors, Figures 4.15(c) and 4.15(d), can be derived by integrating the histograms. These figures give a graphical impression which fraction of pixels is assigned with a specific maximum error. The main aspects of this type of graphs are:

- All cumulative distributions approach the cumulative probability of 1.0.

- A graphical criteria for all parameterizations is the slope of the respective curves for transmission and reflection if the same scale at the x-axis is applied. The steeper this slope the smaller the range of errors.

- The most preferable case is a delta function approach of 1.0 within just a few percent.

As one recognizes by comparison, the transmission computed by the IPA is rather inaccurate even if the mean does not suggest that at first sight. The transmission calculated by TIPA is more realistic, thus confirming the original prospect of better accounting for shadowing. Judging from the slope of the curve associated with reflection, it performs slightly worse than the reflection computed by the IPA.
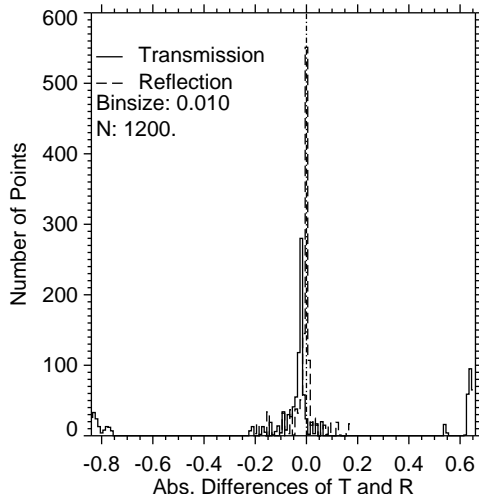
(a) Histogram of the absolute errors ΔT and ΔR of the IPA realization compared to 3DMC.
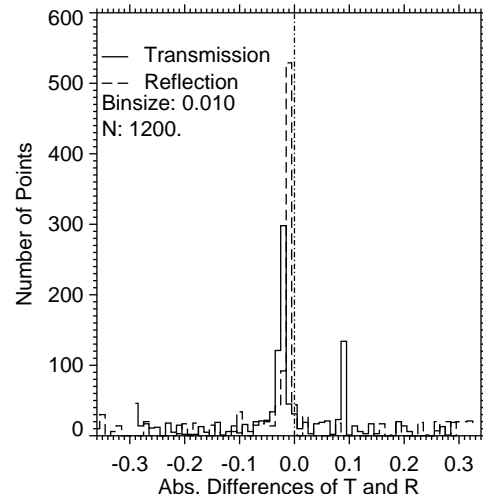
(b) Histogram of the absolute errors ΔT and ΔR of the TIPA calculation compared to 3DMC.
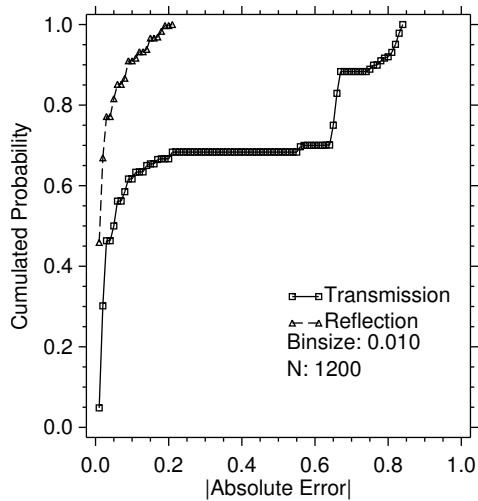
(c) Cumulative probability of the absolute errors ΔT and ΔR of the IPA calculation compared to 3DMC.
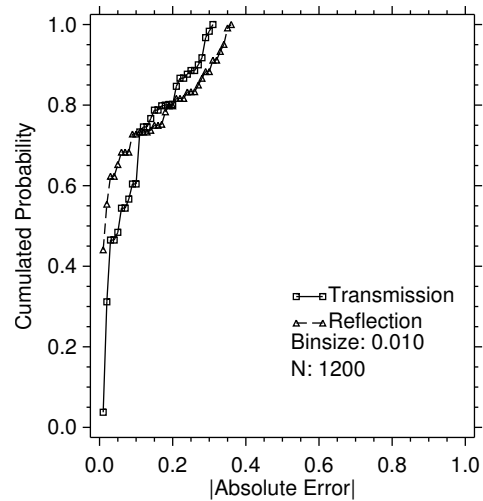
(d) Cumulative probability of the absolute errors ΔT and ΔR of the TIPA calculation compared to 3DMC.

Figure 4.15: Histograms and cumulative distributions for ΔT and ΔR for the mixed case cloud.

4.4   Nonlocal Independent Pixel Approximation

The Nonlocal Independent Pixel Approximation (NIPA) was first conceived by Marshak et al. (1995). The underlying concept is to account for horizontal transport of photons across columns by using the IPA results and forming a convolution product for each pixel. It formally reads:

$$R_{NIPA}(x,y,z) = G * R_{1D} = \int\limits_{x_a}^{x_b} \int\limits_{y_a}^{y_b} G(\sigma,x,y,x_k,y_k,z) R_{1D}(x_k,y_k,z) dy_k dx_k \qquad (4.3)$$

where x, y, z are the coordinates of the domain, and x_k, y_k are the local coordinates which constitute the convolution kernel which reaches from $[x_a, x_b]$ and $[y_a, y_b]$, see Figure 4.16. R_{1D} represents the original IPA result, and R_{NIPA} is finally derived by integrating the former together with the convolution kernel G. σ symbolizes one or more parameters which control the shape of the kernel. If the problem was exactly determined, one would derive the Green's function as a kernel. However, for practical purposes the derivation of the exact Green's function is not feasible in this context. Yet, in order to carry out the convolution though, the kernel is approximated by an appropriate distribution. Marshak et al. (1995) originally seize an approach of v. d. Hulst (1980) and propose to use gamma distributions to model the problem's Green's function. The distribution is assumed to have the following form:

$$G = C \, \frac{\alpha^\alpha}{\Gamma(\alpha)} \frac{1}{\langle\rho\rangle} \left[\frac{\sqrt{x_k^2 + y_k^2}}{\langle\rho\rangle} \right]^{\alpha-1} exp\left\{ -\alpha \frac{\sqrt{x_k^2 + y_k^2}}{\langle\rho\rangle} \right\} \qquad (4.4)$$

with:

$$\alpha = \left[\frac{\langle\rho^2\rangle}{\langle\rho\rangle^2} - 1 \right]^{-1} \qquad (4.5)$$

Other authors, see Zuidema and Evans (1998), have used Gaussian distributions as kernels which are numerically easier to handle. This type of distribution was adopted for this study as well. The kernel is assumed to have the form:

$$G = C \, exp\left\{ -\frac{x_k^2 + y_k^2}{\sigma^2} \right\} \qquad (4.6)$$

and:

$$\sigma^2 = \langle\rho^2\rangle - \langle\rho\rangle^2 \qquad (4.7)$$

The properties $\langle\rho\rangle$ and $\langle\rho^2\rangle$ are the first and second moment of the distances between photon entry and photon exit. As the medium is in general inhomogeneous, the parameters of the kernel will depend on x and y. A more comprehensive description is given in the next
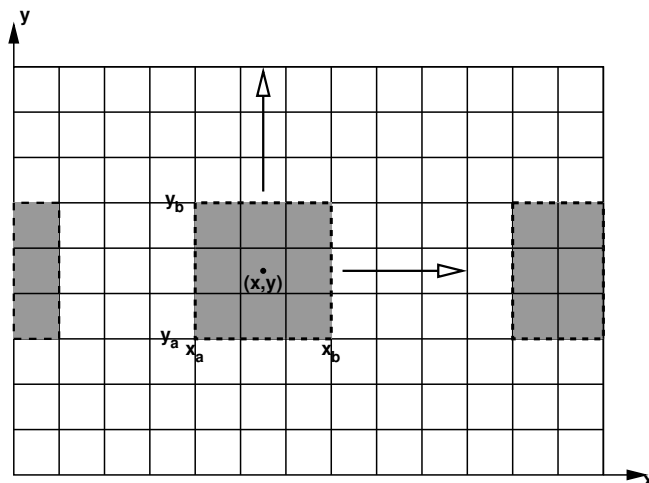
Figure 4.16: Convolution of a 2D field. Each pixel (x, y) is visited by the kernel (grey square) which covers the local area $[x_a, x_b] \times [y_a, y_b]$. "Edge-wrap" ensures periodic boundary conditions and energy conservation.

section together with the details of the derivation of those parameters which was conceived in the presented study.

The resulting field R_{NIPA} is smoother than the original R_{1D} field as the local redistribution of photons across columns levels differences to some extend. However, domain averages remain the same due to energy conservation. This is mathematically realized by demanding that the following normalization holds:

$$\int\limits_{x_a}^{x_b} \int\limits_{y_a}^{y_b} G(x, y, x_k, y_k) dy_k dx_k = 1 \tag{4.8}$$

Practically, via equation 4.8 the normalization constant C is determined. In Figure 4.17 cross-sections of kernels for different values of σ are shown. The resulting contribution of the pixels to the convolution kernel is plotted as a function of the position along the x-axis. Given the low weights even in the centers of the kernels, one can understand why this approximation is termed nonlocal.

4.5   Diffusion Approximation

The convolution parameters for the NIPA approach are usually determined numerically by exact 3D RT modeling. This can be either achieved by direct numerical modeling of the diffusion process or by comparison of NIPA results for carefully chosen values of these parameters with the 3D RT result for the scene. The former approach has been carried out by Marshak et al. (1995), the latter by Zuidema and Evans (1998) and Kniffka (2006). In order to use the NIPA as a fully autonomous parameterization approach, it is
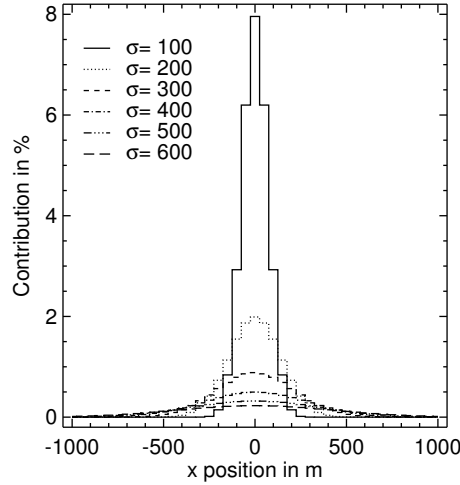
Figure 4.17: Example of 2D Gaussian convolution kernels for different values of σ given in meters. All curves are central cross-sections and give the contribution to the convolution product in % as a function of horizontal position.

desirable to eliminate the need for a mandatory exact 3D calculation and yet to obtain a reasonable estimate for the convolution kernels. In order to tackle this issue, the Diffusion Approximation (DiA) was employed. This technique has been applied by Davis et al. (1997) and Marshak et al. (1995) in order to form the basis for the approach of these authors to estimate the number of transmitted and reflected photons by a cloud which successively led to the concept of the NIPA approach. In the work carried out here, it was investigated whether DiA can be directly utilized for the determination of NIPA's convolution parameters. To this end a brief introduction in the DiA technique will be presented in the following.

The Diffusion Approximation originates from neutron transport theory. Comprehensive introductions in this technique can be found in textbooks like Case and Zweifel (1967), Bell and Glasstone (1970), and Ishimaru (1997). In the context of the diffusion equation two radiative properties of the diffuse light are of special importance. The first one is the net flux-density defined as in equation 2.8 for the total light and restated here for the diffuse part:

$$\boldsymbol{E}_d(\boldsymbol{r}) = \int\limits_{4\pi} \boldsymbol{\Omega} I_d(\boldsymbol{r}, \boldsymbol{\Omega}) d\Omega \tag{4.9}$$

and the so-called density:

$$U_d(\boldsymbol{r}) = \frac{\int\limits_{4\pi} I_d(\boldsymbol{r}, \boldsymbol{\Omega}) d\Omega}{\int\limits_{4\pi} d\Omega} = \frac{1}{4\pi} \int\limits_{4\pi} I_d(\boldsymbol{r}, \boldsymbol{\Omega}) d\Omega \tag{4.10}$$

In diffusion theory both are assumed to be connected by the diffusion approximation of the diffuse intensity, see Ishimaru (1997):

$$I_d(\boldsymbol{r}, \boldsymbol{\Omega}) = U_d(\boldsymbol{r}) + \frac{3}{\displaystyle\int_{4\pi} d\Omega} \boldsymbol{E}_d(\boldsymbol{r}) \cdot \boldsymbol{\Omega} = U_d(\boldsymbol{r}) + \frac{3}{4\pi} \boldsymbol{E}_d(\boldsymbol{r}) \cdot \boldsymbol{\Omega} \qquad (4.11)$$

The explicit integrals of the solid angle over the unit sphere in equations 4.10 and 4.11 are necessary to normalize the respective quantities and assure the correct units of the resulting properties.
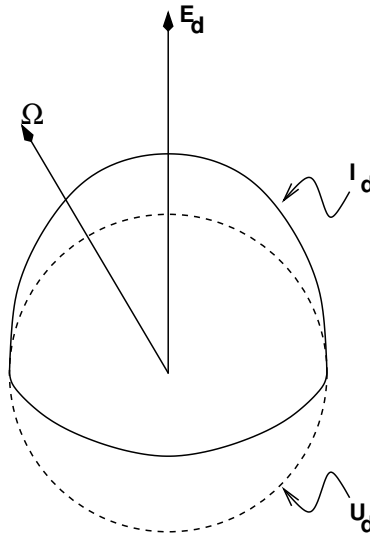
Figure 4.18: Diffusion approximation of the intensity. The isotropic contribution U_d (dashed line) forms together with $\boldsymbol{E}_d \cdot \boldsymbol{\Omega}$ (arrows) the resulting anisotropic I_d (solid line) according to equation 4.11. Adapted from Ishimaru (1997).

Equation 4.11 can be interpreted as a superposition of a large isotropic part, which is U_d, and a smaller anisotropic part, $\boldsymbol{E}_d \cdot \boldsymbol{\Omega}$, which has only a simple angular dependence, see also Figure 4.18. From equation 4.11 one can already conclude the overall features of DiA. As the resulting diffuse intensity has only weak angular dependence and is hardly entangled, the DiA can be expected to be a good approximation if the single scattering albedo is close to unity, the asymmetry parameter is close to zero, and if the point of interest is located sufficiently distant from sources and sinks of radiation. Starting from equations 2.65 and 4.11, the 3D diffusion equation can be derived as:

$$\nabla^2 U_d(\boldsymbol{r}) - 3\sigma_a(\boldsymbol{r})\sigma_{tr}(\boldsymbol{r})U_d(\boldsymbol{r}) =$$
$$\frac{3}{(4\pi)^2}\sigma_s(\boldsymbol{r})\nabla \cdot \int_{4\pi} \boldsymbol{\Omega}S(\boldsymbol{r})p(\boldsymbol{r}, \boldsymbol{\Omega}_o \cdot \boldsymbol{\Omega})d\Omega - \frac{3}{4\pi}\sigma_{tr}(\boldsymbol{r})\sigma_s(\boldsymbol{r})S(\boldsymbol{r}) \qquad (4.12)$$
$$- 3\sigma_{tr}(\boldsymbol{r})J(\boldsymbol{r}, \boldsymbol{\Omega})$$

with the transport coefficient:

$$\sigma_{tr}(\boldsymbol{r}) = \sigma_t(\boldsymbol{r}) - g(\boldsymbol{r})\sigma_s(\boldsymbol{r}) \tag{4.13}$$

The strength of the DiA is the fact that for equation 4.12 powerful solution methods exist. For example, it is possible to solve the diffusion equation analytically in 1D and 3D if some additional assumptions are made.

Concerning boundary conditions, it is obvious from equation 4.11 that exact boundary conditions for the diffuse intensity like the ones given in equation 2.71 cannot be fulfilled by the diffusion approximation. As a result, the boundary condition is usually required to match the solution of the Milne problem, which is the determination of the radiation in an infinite source-free half space with zero incident flux and a source at infinity. This leads to the conditions:

$$U_d(z = -\chi, x, y) = 0$$
$$U_d(z = z_T + \chi, x, y) = 0 \tag{4.14}$$

where χ is the extrapolated endpoint length beyond the boundary of the Milne problem.

Isotropic localized source

In the following, the analytical solution of equation 4.12 for an homogeneous medium with a localized isotropic source is discussed. If these assumptions are implemented, the resulting equation reads:

$$\nabla^2 U_d(\boldsymbol{r}) - 3\sigma_a\sigma_{tr}U_d(\boldsymbol{r}) = -3\sigma_{tr}J(\boldsymbol{r}) \tag{4.15}$$

where the source is:

$$J(\boldsymbol{r}) = J_o\delta(z - z_s)\delta(x)\delta(y) \tag{4.16}$$

meaning that the source is always located horizontally centered in the homogeneous domain. The vertical location of the source is given by z_s. J_o is the source strength which describes the released power per solid angle interval.

The solution for this diffusion equation was carried out by Polonsky and Davis (2003). With the help of these authors it was deduced in geometric coordinates for this work:

$$U_d(\rho, z) = \frac{3}{4\pi}J_o\sigma_{tr}\sum_{n=-\infty}^{\infty}\left\{\frac{1}{S_a}e^{-3\sqrt{\sigma_a\sigma_{tr}}S_a} - \frac{1}{S_b}e^{-3\sqrt{\sigma_a\sigma_{tr}}S_b}\right\} \tag{4.17}$$

with the following definitions:

$$S_a = \sqrt{\rho^2 + a_n^2} \qquad\qquad S_b = \sqrt{\rho^2 + b_n^2} \tag{4.18}$$
$$a_n = |2(z_T - 2\chi)n + |z - z_s|| \qquad b_n = |2(z_T n + \chi(2n + 1)) + z + z_s| \tag{4.19}$$

and:

$$\chi = \frac{2}{\sigma_t(1 - \omega_o g)} \tag{4.20}$$

χ is the extrapolation length, z_s is the vertical location of the source, z_T is the geometrical thickness of the medium and ρ is the horizontal distance from the source, $\rho = \sqrt{x^2 + y^2}$.

Results

To show the accuracy of the DiA with respect to numerical solutions, a test case was set up. The model domain has a geometrical thickness of $300m$, the optical depth is 16, and the asymmetry factor is zero and 0.85, respectively. The single-scattering albedo is 0.99999 which had to be chosen in order to avoid singularities of the solution. The source is located at the top of the medium, and the source strength was set to π. Figure 4.19 shows the density derived from equation 4.17 compared with exact 3DMC simulations as a function of the radius ρ at the lower boundary of the medium. It has been divided by the transmission of the domain which was derived from an approximate formula based on diffusion theory. The 3DMC data was kindly provided by I. Polonsky and A. Davis from Los Alamos National Laboratory.

(a) Comparison for $g = 0.0$.   **(b)** Comparison for $g = 0.85$.
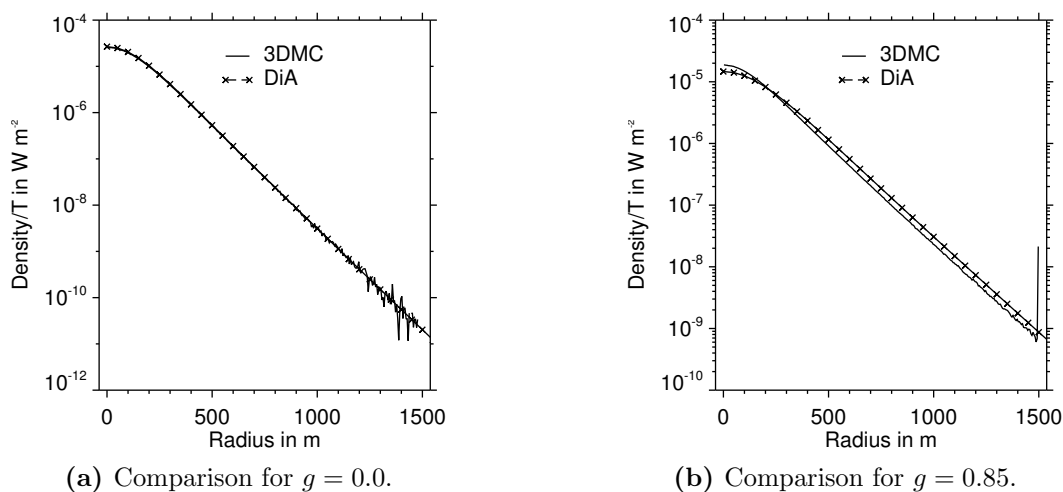
Figure 4.19: Comparison of U_d/T derived from DiA (crosses) and 3DMC (line) as a function of ρ for the two different asymmetry factors $g = 0.0$ and $g = 0.85$ at the bottom of the homogeneous medium with $\tau = 16$ and $\omega_o = 0.99999$ and a geometrical thickness of $300m$.

For the isotropic case the agreement is quite reasonable as one would expect from the features of DiA, although DiA is expected to deteriorate at model boundaries. For $g = 0.85$ one notes a difference between DiA and 3DMC. However, the slope of the radial dependence is still modeled quite accurately, and DiA is expected to yield a good estimation for the moments of the density distribution even in that case.

For the DiA simulation it is necessary to truncate the infinite series of equation 4.17 to a meaningful number of terms. For the presented examples the limit was set so that $-120 \leq i \leq 120$. The truncation is mainly influenced by the amount of absorption. The larger the single scattering albedo is, the more terms have to be used. Otherwise the DiA result saturates for larger distances from the symmetry axis, meaning that the slope approaches zero. In the next section, a quantitative statement about the range of applicability of the DiA will be made. The overall impression of DiA is not expected to change for results at the upper boundary, yet it is necessary to exclude the source from any successive computations to avoid numerical problems.

Connection to NIPA

It was pointed out that the meaningful estimation of the convolution parameters for NIPA independent of a lengthy computation is desirable. In order to carry out that task the DiA was employed to calculate the zeroth, first and second moment of the density with respect to its radial dependence. This approach is motivated by the notions conveyed by Marshak et al. (1995). These authors use DiA as a basis for first principle estimations of the number of reflected and transmitted photons and arrive in the course of the paper at an approximate formula for each of these values. This concept was further developed to form the basis for off-beam LIDAR remote sensing inversion techniques, see Davis et al. (1999). Those use Fourier space representations for the convolution parameters. The aim of the presented study here is to directly derive the convolution parameters for NIPA from a diffusion calculation in physical space. This approach is closely related with the implemented remote sensing concept of the above mentioned LIDAR technique for practical applications, see also Polonsky et al. (2005). This is an example for the fruitful exploitation of a theoretical concept for both active and passive applications.

It can be gathered from equations 4.5 and 4.7 that the crucial parts of information for the convolution kernel are the expectation values $\langle \rho \rangle$ and $\langle \rho^2 \rangle$. $\langle \rho \rangle$, which is called "spot-size", can be regarded as the mean distance between the entry point of the light in the domain, which is fixed, to the exit points of the photons. From this explanation it is clear that always two sets of expectation values exist, one for the transmitted and one for the reflected light. That is where DiA comes into play. It is obvious from definition 4.10 that the density is proportional to the number of photons. Hence, the moments are estimated by DiA by numerically integrating the derived radial distribution of U_d at the bottom and the top of the model domain. The computed moments are defined as:

$$\langle U_d \rangle \;=\; \int_A U_d(\rho, z) dA \tag{4.21}$$

$$\langle \rho \rangle \;=\; \frac{\int_A U_d(\rho, z)\rho \, dA}{\langle U_d \rangle} \tag{4.22}$$

$$\langle \rho^2 \rangle \;=\; \frac{\int_A U_d(\rho, z)\rho^2 \, dA}{\langle U_d \rangle} \tag{4.23}$$

Figure 4.20 gives an impression of the 2D result of U_d/T and also shows the deduced moments $\langle \rho \rangle$ and $\langle \rho^2 \rangle$.
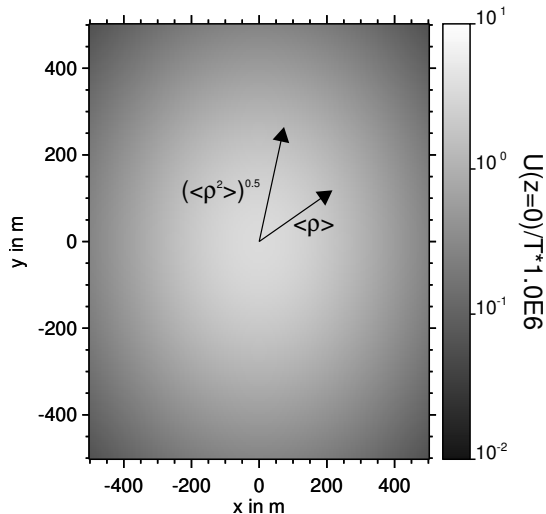
Figure 4.20: 2D field of U_d/T at the lower boundary of a $500m \times 500m$ domain for the previous example, see Figure 4.19, with $g = 0.85$. The arrows symbolize the first moment and the square-root of the second moment of ρ.

Analogously, results for the reflected light can be derived at the upper boundary. The procedure is then made available for NIPA by averaging horizontally and vertically over the area chosen to be affected by the convolution kernel. The derived homogeneous domain is then used by DiA to deliver the moments which are in turn fed into a convolution procedure which was developed from routines kindly provided by A. Kniffka, Institute for Meteorology, University of Leipzig. See also Kniffka (2006). The whole domain is worked on as depicted in Figure 4.16.

One major theoretical setback of this approach is certainly the requirement of the applied technique for a homogeneous domain. However, the underlying process which is to be modeled is the diffusion driven horizontal propagation of photons. This process is known to smooth radiative fields. For the pursued approach, it is then assumed that small scale variations of the optical properties are less important, once the diffusion regime is reached meaning that then multiple scattering levels the impact small inhomogeneities of the optical properties have on the radiative field.

Davis and Marshak (2001) give an overview of the features of DiA and relate the optical properties to the applicability of the method. The main results which are of importance here are briefly discussed. First, for diffusion of photons to happen in a conservative medium the smallest dimension H of the model domain is required to be connected with the optical properties so that:

$$(1 - g)\sigma_t H \gtrsim 1 \tag{4.24}$$

holds. Second, it is understood that the more scattering and the less absorption occurs,

the more the diffusion approximation is justified. It is believed that a sufficiently large number of scattering events occurs if:

$$\omega_o \gtrsim \frac{2}{3 - g} \qquad (4.25)$$

is valid. It can then be assumed that the diffusion approximation for the intensity, equation 4.11, is fulfilled. Third, concerning the value of the asymmetry factor, it is obvious that phase functions with large forward scattering peaks contradict the diffusion approximation. However, in summary it can be said that for typical magnitudes of H, which would generally be the vertical extension of the cloud, it can be assumed that the first requirement is fulfilled even for asymmetry factors of over 0.85. On the other hand, from the second condition it can be estimated that even for those values of g realistic clouds exceed the required value of ω_o. From these conclusions it seems to be reasonable to employ DiA for the purpose in focus, even though the required homogeneity remains a strong assumption.

4.6   Example

Alike the other sections presenting a technique, this theoretical discussion of the NIPA with diffusion kernel is succeeded by an example in order to illustrate the preceeding statements. In this case a "$\sin x \times \cos y$" shaped variation of the cloud extinction coefficient in a model domain of $66 \times 66 \times 68$ grid cells is used. This variation is confined to a vertical layer of $400m$ thickness while the clouds single scattering albedo is set to the constant value of $\omega_o = 1.0$, and the asymmetry factor is chosen to be $g = 0.85$ in order to generate a Henyey-Greenstein phase function and is equally held constant. The cloud base is $600m$ above ground. This idealized periodic, but completely closed cloud, is superimposed on a vertically inhomogeneous atmosphere which includes optical properties for Rayleigh scattering and ozone absorption characteristic for a wavelength of $330nm$. The resulting optical depth field is depicted in Figure 4.21. It varies between $\tau_{min} = 2.91$ and $\tau_{max} = 18.8$ with a mean of $\langle \tau \rangle = 10.84$. For the calculation the illumination was set to $\mu_o = 0.5, \varphi_o = 0°$ and surface reflection was not considered. The horizontal resolution is $\Delta x = \Delta y = 40m$ while the vertical resolution in the range of the cloud is $\Delta z = 40m$ and variable elsewhere. In Figure 4.22(a) the histogram of the absolute errors of transmission and reflection of the IPA calculation with respect to 3DMC is shown. Once more, one notes the ragged behavior of ΔT whose magnitude and shape owes its existence to the inability of IPA to correctly represent shadows. The symmetry of the results is also remarkable. In Figure 4.22(b) the cumulative distributions of ΔT and ΔR are depicted. Both curves virtually coincide underlining the equal accuracy of both properties. As Rayleigh scattering is quite strong in this example and the cloud field is not broken, either errors of transmission and reflection are moderate leading to maximum errors of $\Delta T_{max} = 16\%$, $\Delta T_{min} = -11\%$ and $\Delta R_{max} = 11\%$, $\Delta R_{min} = -16\%$.
In Figures 4.23(a) and 4.23(b) ΔT and ΔR are shown as a function of total optical depth. Interestingly, both have convex shape just as generally the values of T and R itself have,
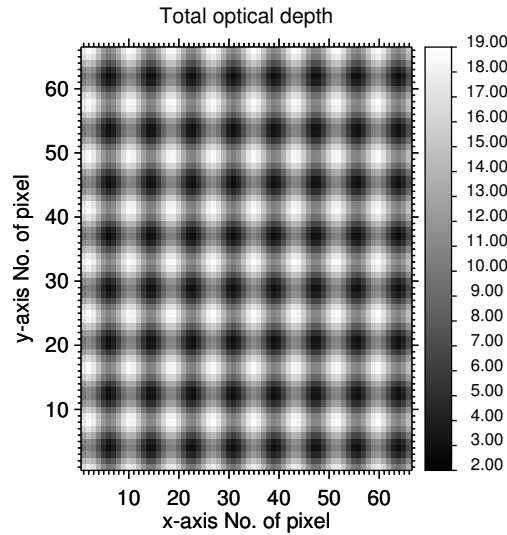
Figure 4.21: 2D field of the total optical depth of the $\sin x \times \cos y$ example consisting of 66×66 pixels with $\Delta x = \Delta y = 40m$.

see Figure 4.10. The same graphs but with the relative error depicted, not shown here, give no distinct pattern. The scaling behavior is investigated with the help of Figures 4.24(a) and 4.24(b). Here, the coarse grained moving average is used to determine the dependence of the maximum residual error on the size of the area used for averaging. More precisely, a moving average is successively applied to the IPA field by increasing the averaging area with each step by two pixels in each direction. The absolute values of the maximum and minimum errors of the resulting smoothed fields are shown as a function of the edge lengths of the averaging area. This kind of investigation or deduced information will also be synonymously addressed as scaling behavior in the course of the thesis. The resulting functions generally have the following characteristics:

- In the trivial case of a 1pixel $\times$ 1pixel area, the maximum and minimum errors of the original field are retrieved which can be confirmed by comparing with Figure 4.22(a).

- For an increasing number of pixels the functions generally decline,

- moreover, the functions converge to each other, and

- for sufficiently large pixel numbers, the functions approach the domain averaged values of ΔT and ΔR.

In the case here, the decline is strong for the first couple of pixels but still leaves a residual error of about three percent in case of the transmission and nearly two percent for the reflection if an area with 7pixels $\equiv 280m$ edge length is chosen. Variables depending on T and R should be in reasonable agreement with 3DMC results if averaged over areas with an edge length of seven or more pixels for this cloud. However, even in that case errors of

(a) Histogram of ΔT and ΔR for the comparison of IPA and 3DMC.

(b) Cumulative probability of ΔT and ΔR for the comparison of IPA and 3DMC.
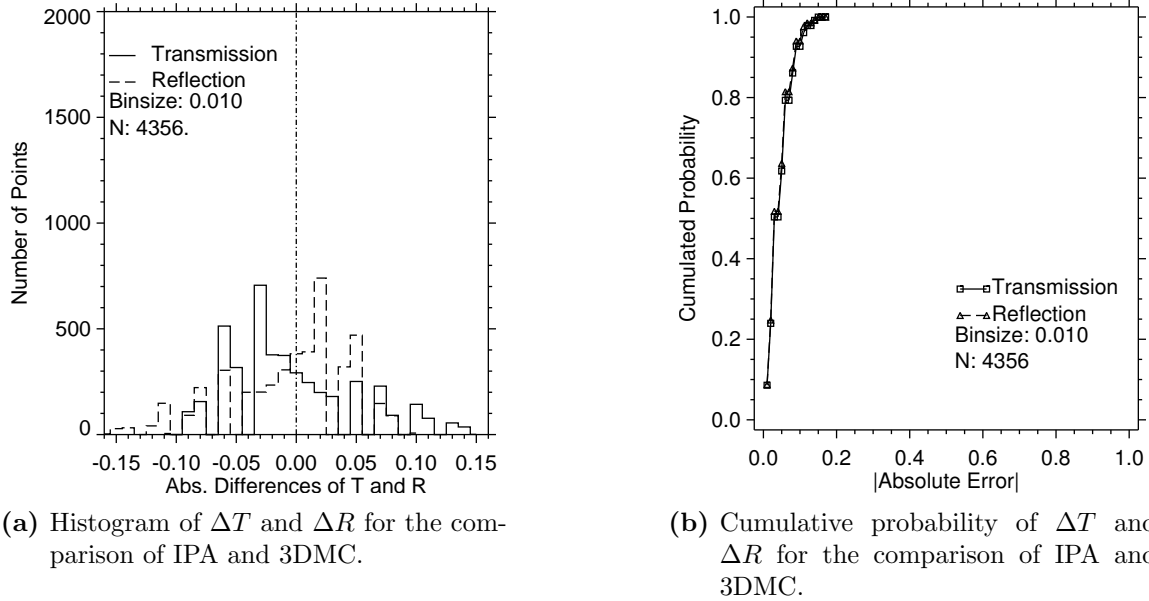
Figure 4.22: Histograms and cumulative distributions of the absolute errors ΔR and ΔT derived from IPA and 3DMC for the $\sin x \times \cos y$ example. The geometry of the illumination was $\mu_o = 0.5, \varphi_o = 0°$. Remaining parameters as in Figure 4.21.

several percent persist, and increasing the edge length by one or two pixels not necessarily improves the results. This behavior seems to be one facet of the characteristics of the IPA results. Because of the roughness of the IPA fields, including more pixels into the average might even lead to an even rougher averaged result, especially in the case of a periodic or quasiperiodic cloud.

The aforementioned interrelations mainly apply to the maximum values of the errors. As for the minimum value two remarks are necessary:

- It can also be gathered from Figure 4.22(a) that quite a number of IPA results show no or no significant deviation from 3DMC.

- For this reason the minimum error can in this context generally only increase for increasing edge lengths till it finally reaches the domain averaged value.

Concerning the 2D fields of ΔT and ΔR, not shown here, those spatial distributions closely resemble the distribution of the total optical depth. Bearing the results already discussed in mind, this consequence of the scale invariance of IPA is not surprising.

As for the NIPA, all results change significantly. The convolution has been carried out with an edge length of the kernel of 25 pixels $\equiv 1000m$. One immediately notes from the histogram, Figure 4.25(a), that NIPA improves the results considerably. Not only that the magnitude of the errors of ΔT and ΔR is reduced to about $\pm 4 - 6\%$, but also
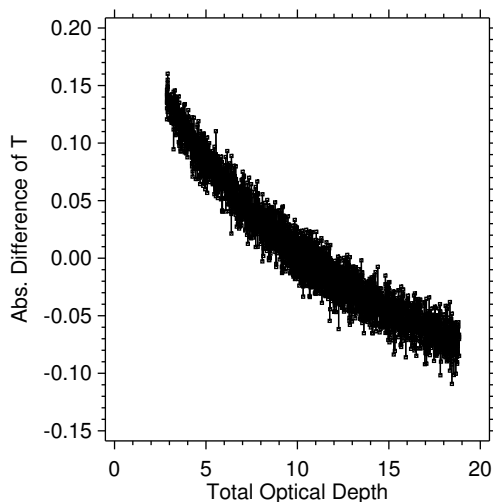
(a) ΔT as a function of the total optical depth.
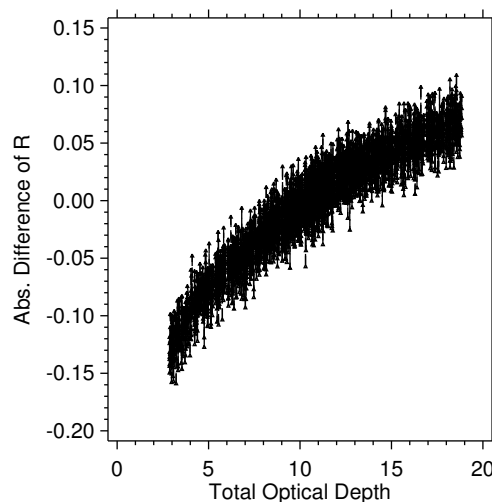
(b) ΔR as a function of the total optical depth.

Figure 4.23: Absolute errors ΔT and ΔR derived from IPA and 3DMC as functions of optical depth for the $\sin x \times \cos y$ example. Parameters as given for Figure 4.22 and 4.21.

the histograms are not ragged anymore hinting at the smoothing of the radiative field. Comparing the cumulative distributions, Figure 4.25(b) shows almost an ideal behavior compared to Figure 4.22(b) as both curves almost instantaneously approach the terminal value. The dependence of the errors on the optical depth, shown in Figures 4.26(a) and 4.26(b), does not seem to follow any distinct function as more or less the full bandwidth of errors is adopted for every given optical depth interval. As a result of this blurred functional dependence, the coarse grained moving averages, Figures 4.27(a) and 4.27(b), now show monotonically decreasing behavior. Unlike the IPA results, both pairs of curves have smooth shape and almost steadily converge to each other. At an edge length of 7 pixels $\equiv 280m$ the residual maximum error in the field has dropped to about one percent for both reflection and transmission. From these results it is clear that the adopted realization of NIPA is capable of improving IPA calculations for this simple cloud. However, as mentioned above, NIPA is not able to change any domain averages. While $\bar{T}(3DMC) = 0.288$ and $\bar{R}(3DMC) = 0.583$, it is $\bar{T}(IPA) = \bar{T}(NIPA) = 0.291$ and $\bar{R}(IPA) = \bar{R}(NIPA) = 0.580$. The last two sets of equalities are consequences of the energy conservation of NIPA. Yet, in this case the 3D effect on domain averages is very small.
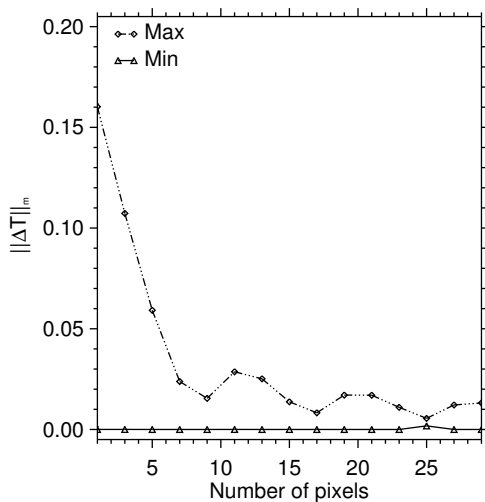
(a) Scaling behavior of $|\Delta T|_{max,min}$ as a function of the edge length of the averaged area.
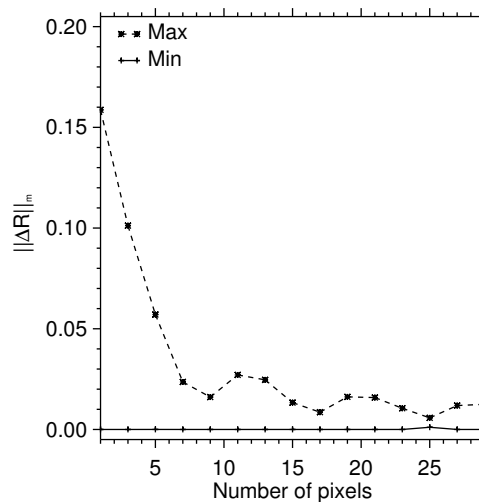
(b) Scaling behavior of $|\Delta R|_{max,min}$ as a function of the edge length of the averaged area.

Figure 4.24: Absolute errors ΔT and ΔR derived from IPA and 3DMC as functions of averaging area (coarse grained moving average) for the $\sin x \times \cos y$ example. Parameters as for Figure 4.22 and 4.21.
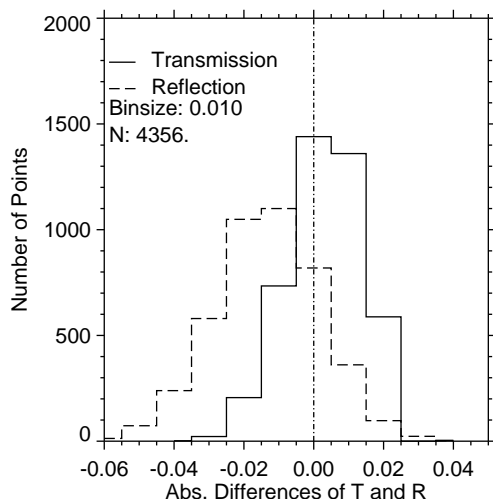
(a) Histogram of ΔT and ΔR derived from NIPA and 3DMC.
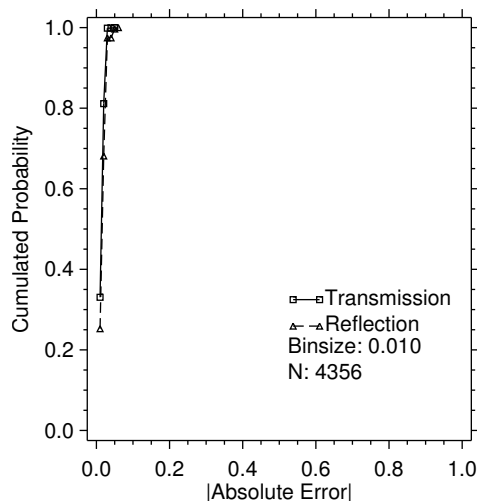
(b) Cumulative probability of ΔT and ΔR derived from NIPA and 3DMC.

Figure 4.25: Distributions of absolute errors ΔR and ΔT derived from NIPA and 3DMC for the $\sin x \times \cos y$ example. Parameters as for Figure 4.22 and 4.21.
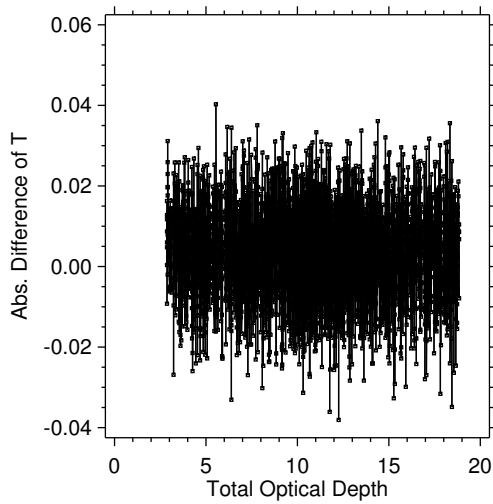
(a) ΔT as a function of the total optical depth.
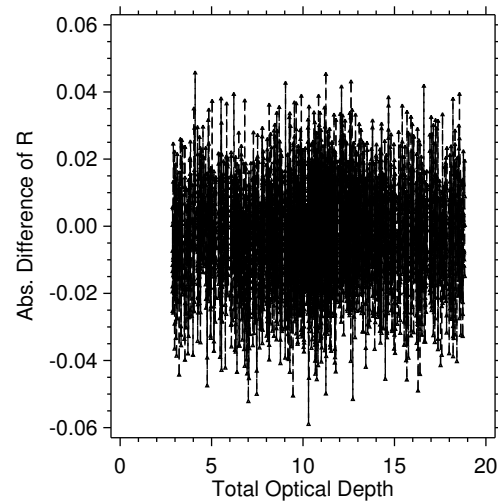
(b) ΔR as a function of the total optical depth.

Figure 4.26: Absolute errors ΔT and ΔR deduced from NIPA and 3DMC as functions of optical depth for the $\sin x \times \cos y$ example. Parameters as for Figure 4.22 and 4.21.
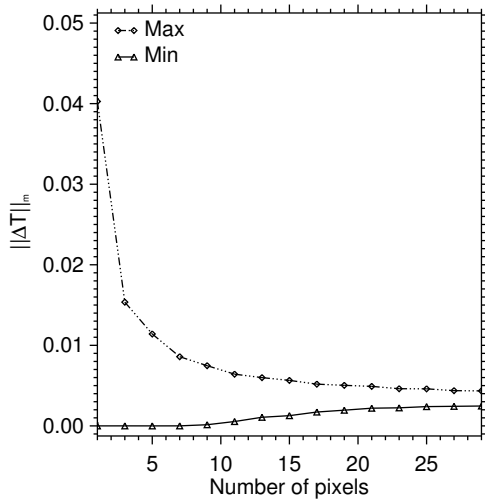
(a) Scaling behavior of $|\Delta T|_{max,min}$ as a function of the edge length of the averaged area.
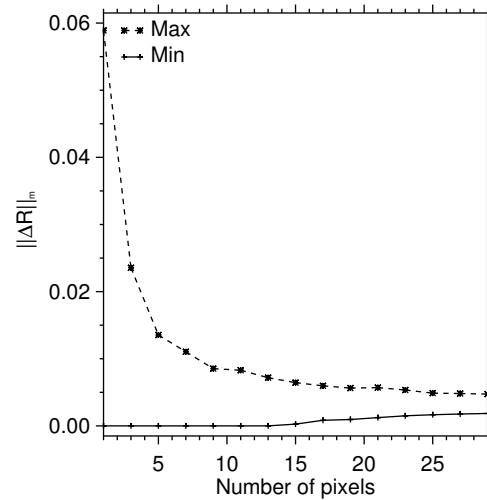
(b) Scaling behavior of $|\Delta R|_{max,min}$ as a function function of the edge length of the averaged area.

Figure 4.27: Absolute errors ΔT and ΔR deduced from NIPA and 3DMC as functions of averaging area for the $\sin x \times \cos y$ example. Parameters as for Figure 4.22 and 4.21.

4.7 Nonlocal Tilted Independent Pixel Approximation

The obvious combination of TIPA and NIPA finally leads to the Nonlocal Tilted Independent Pixel Approximation (NTIPA). The intention of this concept is of course to superimpose the respective advantages of both methods complementing each other.

(a) Concept of the TIPA for geometric effects.

(b) Concept of the NIPA for horizontal diffusion effects.
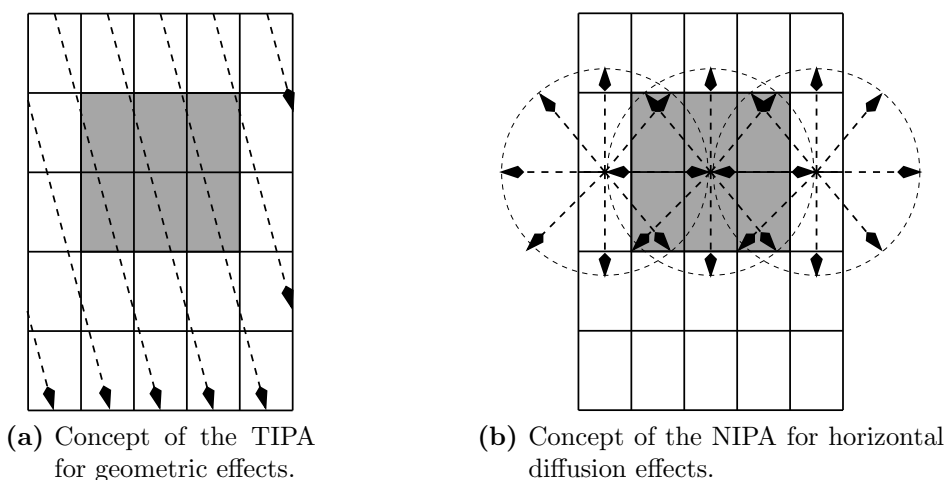
Figure 4.28: Combination of TIPA and NIPA to form NTIPA.

It was pointed out that TIPA lacks photon exchange across columns just like IPA does. Furthermore, it was discussed that 3D results of TIPA suffer from discretization errors due to the applied inverse transformation. On the other hand, it was described that NIPA smoothes the radiative field but cannot accurately account for geometric effects like shadowing. NIPA is also not able to influence domain averages. These shortcomings are tackled by the combination of TIPA and NIPA which then could be called NTIPA. The basic idea of this concept is reflected by Figure 4.28. Technically, the convolution is carried out with the computed radiative properties still in the slant columns. After the convolution is complete, the resulting radiative properties are mapped to the original Cartesian grid. Obviously, the converse procedure is also possible meaning that the convolution is carried out after the inverse transformation. However, some tests have suggested to follow the former procedure as results have been slightly more favorable. Apart from that, in the authors point of view, it also seems to be the more natural succession. A conceptually similar, but in detail different approach which also lacks the DiA driven derivation of the convolution kernels, was implemented by Zuidema and Evans (1998).

4.8   Examples

To investigate the overall characteristics of this last method developed, two examples will be discussed. The first is identical with the previous one. The second consists of cloudy and clear sky areas in a chequered pattern style. It is used to investigate the capabilities of the method in case of a broken cloud field.

Extinction variation $\sin x \times \cos y$

This example is the same as the one for NIPA. All properties and parameters remain unchanged.

Figure 4.29 shows the histogram of ΔT and ΔR of the NTIPA calculation in relation to 3DMC. NTIPA clearly improves the results similar to the results of NIPA as shown before. For NTIPA the magnitude of the maximum errors is only 5% which is slightly better than NIPA. The structure of the histograms is now more centered and symmetric compared to NIPA. Moreover, as NIPA is now coupled with TIPA, the domain averages change as well. Table 4.2 presents these values for all calculations.
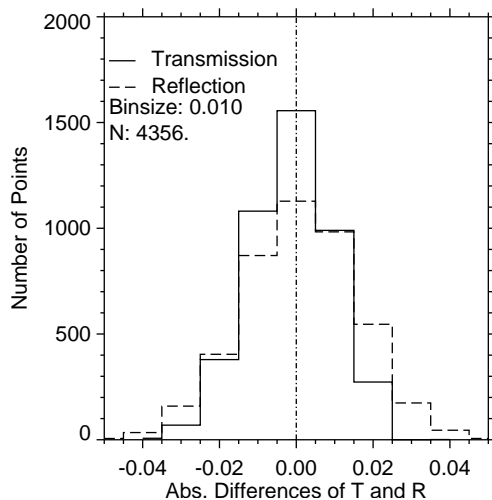
Figure 4.29: Histograms of transmission and reflection errors for NTIPA with respect to 3DMC for the trigonometric example. Parameters as for Figure 4.22 and 4.21.

As for the scaling behavior, Figures 4.30(a) and 4.30(b), NTIPA slightly outperforms NIPA and clearly beats TIPA which shows the same bumpy characteristics of $|\Delta T|_{max,min}$ and $|\Delta R|_{max,min}$ as a function of averaging edge length as IPA does. For brevity only NTIPA results are shown.

The curves for NTIPA are smooth and decline monotonously. However, the mutual convergence does hardly start in the investigated range of edge lengths. When seven pixels are reached the residual error has reached and passed, respectively, the one percent mark.

Table 4.2: Domain averaged results of the trigonometric example for all models.

Model	$\bar{T}$	$\bar{R}$
3DMC	0.288	0.583
IPA and NIPA	0.291	0.580
TIPA and NTIPA	0.287	0.584
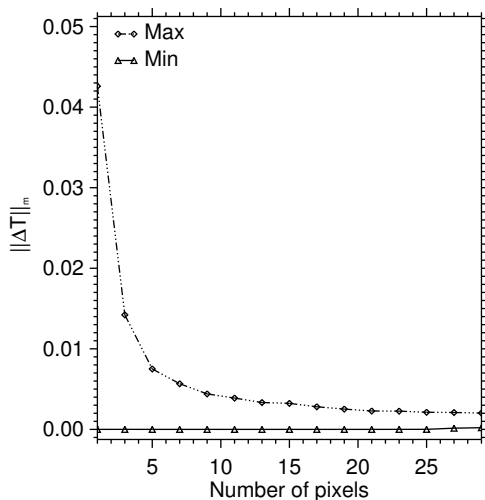
(a) Scaling behavior of $|\Delta T|_{max,min}$ as a function of the averaging edge length.
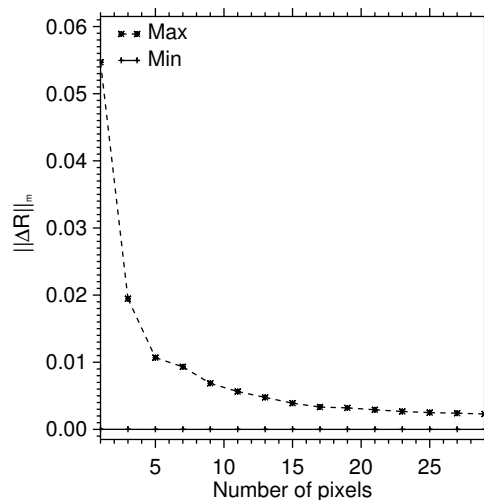
(b) Scaling behavior of $|\Delta R|_{max,min}$ as a function of the averaging edge length.

Figure 4.30: Coarse grained moving averages of ΔT and ΔR of NTIPA with respect to 3DMC for the trigonometric example. Parameters as for Figure 4.22 and 4.21.

Concerning the dependence of ΔR and ΔT on the optical depth, the impression of the NIPA results are confirmed, thus leaving blurred 2D fields with hardly any notable structure.

Chequered pattern

This example is comprised of isolated cubic clouds which are characterized by a single scattering albedo of unity, $\omega_o = 1.0$, an asymmetry factor of $g = 0.85$, and an extinction coefficient of $\sigma_t = 0.05m^{-1}$. All optical properties are held constant within the clouds. The clouds have a geometrical thickness of $400m$, and the uniform cloud base is $600m$ above ground. The horizontal distance between them is $320m$ in each direction. The horizontal resolution is $\Delta x = \Delta y = 40m$ with a total number of $64 \times 64 \times 68$ cells. The vertical resolution in the range of the clouds is also $\Delta z = 40m$. Thus, they are forming a chequered pattern, while the parameters of the superimposed Rayleigh scattering and ozone absorption are again typical for a wavelength of $330nm$. The resulting optical depth

field is depicted in Figure 4.31. The two resulting values of the combined total optical depth are 20.85 and 0.85.

For this example two solar zenith angles are considered. The first one, $\mu_o = 0.5$, ensures that at y-direction between the clouds at the ground a pattern of regularly increasing and decreasing intensity occurs. The second angle is chosen to be $\mu_o = 0.95$. With this angle the direct light can partly reach the ground in y-direction between the clouds without encountering cloudy areas such that shaded areas and bright spots alternate. In both cases the surface albedo is zero.
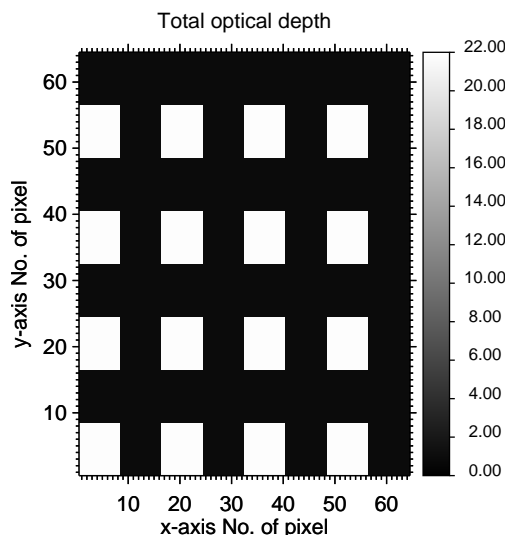
Figure 4.31: 2D field of the total optical depth of the chequered pattern composed of 64×64 pixels with $\Delta x = \Delta y = 40m$.

Experiment 1: $\mu_o = 0.5$, $\varphi_o = 0°$

As implied above, for this solar zenith angle all direct beams which encounter the scene in y-direction at regions of x-values which are occupied by clouds have to penetrate these. Nevertheless, 3D effects exist as the histogram of ΔT and ΔR for the IPA to 3DMC differences, see Figure 4.32(a), shows. Both transmission and reflection are affected to a significant extent.

This is contrasted by the respective results for NTIPA, Figure 4.32(b). For this case results clearly deteriorate due to the inhomogeneity of the scene, but NTIPA is still capable of reducing errors significantly. This is reflected by errors for transmission of -7% to -3% and for reflection of -5% to 8%. This finding is supported by the cumulative distributions. Deduced from these are the results of Table 4.3 which shows the approximate fraction of pixels which have an absolute error value for ΔT and ΔR of 5% or less for all four approximations. The value of 5% was chosen because it allows a better distinction between the different approximations due to the steep slope of the respective cumulative distributions.

(a) Histogram for transmission and reflection errors for IPA.

(b) Histogram for transmission and reflection errors for NTIPA.
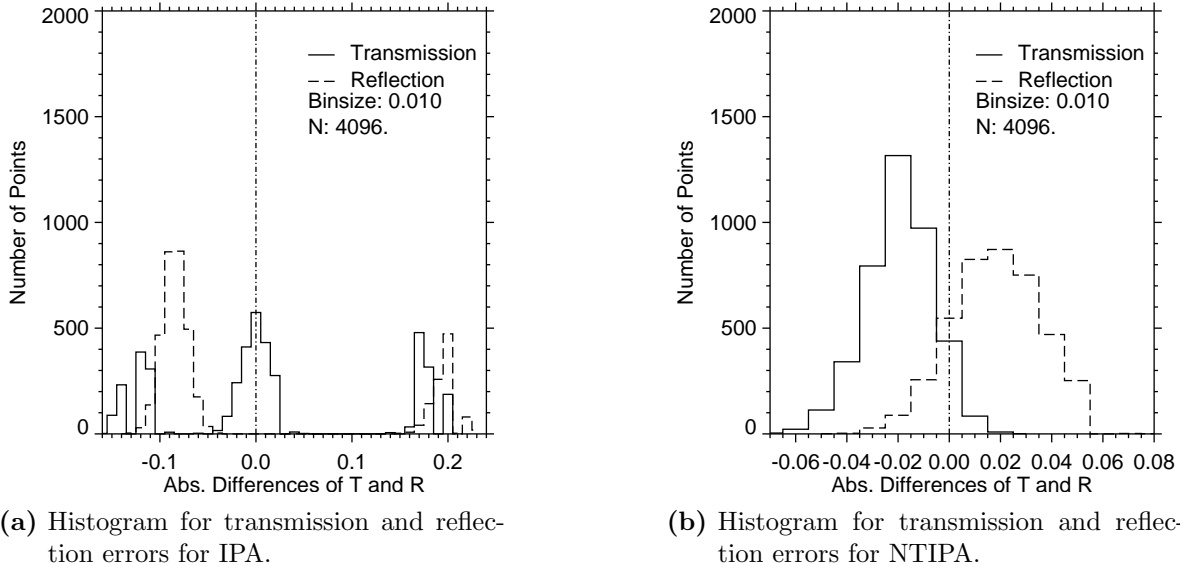
Figure 4.32: Histograms of transmission and reflection errors for IPA and NTIPA with respect to 3DMC for Experiment 1 of the chequered pattern example. For the remaining parameters see Figure 4.31.

Table 4.3: Comparison of the pixel fractions for a 5% error threshold for T and R for the four approximations for Experiment 1 of the chequered pattern.

Model	Fraction of pixels with $\Delta T \leq 5\%$	Fraction of pixels with $\Delta R \leq 5\%$
IPA	50%	$\lesssim 1\%$
TIPA	84%	$\lesssim 1\%$
NIPA	64%	96%
NTIPA	96%	93%

Although only rounded values are given for the fraction, it is clear that NTIPA outperforms all other approximations in this example. TIPA can gain some ground compared to IPA for the transmitted light while NIPA does well for the reflected light and is even for the transmitted light more accurate than IPA. For reflection it is also actually slightly better than NTIPA. These two findings are certainly related to the geometry of the applied illumination.

The scaling behavior is worth investigating for this example as well. Table 4.4 gives the maximum residual errors of transmission and reflection for an edge length of seven pixels $\equiv 280m$ for all four approximations. This length is chosen because the scale break in realistic clouds mentioned in the introductory sections which was found by Davis et al. (1997) is supposed to occur at $200m - 300m$. Therefore, it can be assumed that in these idealized clouds at this scale also no or only slight horizontal diffusion occurs. In general the conclu-

sions from the cumulative distributions are confirmed. However, from the perspective of the averaged results TIPA seems to deliver smoother fields for transmission than IPA which is due to the geometric blurring of the optical depth field by the slant path. NIPA cannot accurately describe the true path of the direct beam while it is the best approximation for the averaged reflection. NTIPA proves again to be the best approximation if ΔT and ΔR are considered in combination.

Table 4.4: Comparison of the coarse grained moving averages of $|\Delta T|_{max}$ and $|\Delta R|_{max}$ for an edge length of seven pixels for all four approximations for Experiment 1 of the chequered pattern.

Model	$|\Delta T|_{max}(s = 7pix.)$	$|\Delta R|_{max}(s = 7pix.)$
IPA	19%	20%
TIPA	5%	13%
NIPA	16%	3%
NTIPA	3%	3%

To conclude the statistical discussion of this case the domain averages of T and R are shown in Table 4.5. Judging from this criteria, TIPA and NTIPA drop slightly behind IPA and NIPA. The slight degradation of the results of TIPA and NTIPA does not come unexpected as the small differences between IPA and TIPA were already observed in section 4.3. The reason for this behavior remains ambiguous but contributes only to a tenth of a percent to the error.

Table 4.5: Domain averaged results of all models for Experiment 1 of the chequered pattern.

Model	$\bar{T}$	$\bar{R}$
3DMC	0.414	0.467
IPA and NIPA	0.430	0.452
TIPA and NTIPA	0.395	0.485

Experiment 2: $\mu_o = 0.95$, $\varphi_o = 0°$

The cosine of the solar zenith angle of $\mu_o = 0.95$ of this case ensures that some light unaffected by clouds reaches the area which lies in y-direction between the clouds. For illustration the resulting slant optical depth field used by TIPA and NTIPA is shown in Figure 4.33. Although the SZA has been decreased compared to the previous case, stronger 3D effects are expected since now a mixture of interactions between shaded and unshaded areas can occur.
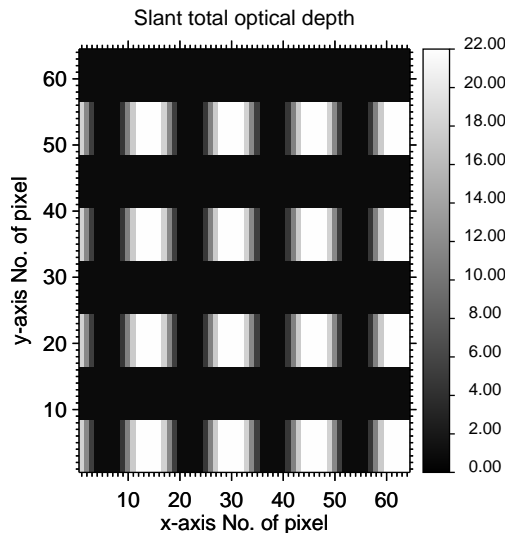
Figure 4.33: 2D field of the slant optical depth of the chequered pattern for $\mu_o = 0.95$. Parameters of the domain as given in Figure 4.31.

Table 4.6 shows the fraction of pixels associated with an error of 5% or less for ΔT and ΔR. The overall succession of the quality of the approximations nearly stays the same as for $\mu_o = 0.5$. TIPA shows again better results concerning transmission than IPA.

Table 4.6: Comparison of the pixel fractions for a 5% error threshold for T and R for the four approximations for Experiment 2 of the chequered pattern.

Model	Fraction of pixels with $\Delta T \leq 5\%$	Fraction of pixels with $\Delta R \leq 5\%$
IPA	19%	$\lesssim 1\%$
TIPA	40%	6%
NIPA	27%	98%
NTIPA	94%	95%

However, for reflection it can gain some ground. NIPA though significantly falls back behind TIPA for the downwelling light and is just able to slightly outperform IPA. For the reflected light IPA and TIPA are yet no match for NIPA. The reason clearly is the relative dominance of the direct light causing distinct alternations of shadows and bright areas at the ground. The pure convolution is inadequate to account for these patterns. Yet, the reflection, mainly emerging from the cloud tops, is more realistically modeled by NIPA. NTIPA tops all other three approximations if both T and R are considered in combination. This result is also supported by the scaling behavior. In Table 4.7 the maximum residual error after forming the coarse grained moving average over 7 pixels is shown again. The accuracy of NIPA is now at the level of IPA for transmission while TIPA nearly matches NTIPA. For reflection NTIPA and NIPA are nearly equally accurate.

Table 4.7: Comparison of the coarse grained moving averages of $|\Delta T|_{max}$ and $|\Delta R|_{max}$ for an edge length of seven pixels for all four approximations for Experiment 2 of the chequered pattern.

Model	$|\Delta T|_{max}(s = 7pix.)$	$|\Delta R|_{max}(s = 7pix.)$
IPA	36%	27%
TIPA	6%	26%
NIPA	37%	3%
NTIPA	3%	4%

Table 4.8: Domain averaged results of all models for Experiment 2 of the chequered pattern.

Model	$\bar{T}$	$\bar{R}$
3DMC	0.581	0.346
IPA and NIPA	0.573	0.354
TIPA and NTIPA	0.564	0.362

Concerning domain averages, see Table 4.8, TIPA and NTIPA yield about 2% percent error for both transmission and reflection while IPA and NIPA are below one percent. Thus, the solar zenith angle has no significant impact on this feature and the general result that IPA already delivers a good estimate is affirmed.

Lastly a remark about 3D resolution will be made. It was emphasized in the respective sections that all methods which have been developed here are capable of determining 3D results in the domain's original Cartesian lattice. To illustrate this capability, several vertical profiles of the net flux, which is important for the atmosphere's thermodynamics, see equations 2.16 and 2.15, will be given. It has been already mentioned that the implemented realization of TIPA is able to produce these 3D results by an inverse transformation from the slant coordinate system to the original Cartesian system. It was pointed out that profiles of 3DMC are reasonably met, but at the positions where cloud sides are encountered very ragged profiles due to discretization errors appear. It was suggested that this discretization error could be appeased if inter-column exchange was included. With the combination of TIPA and NIPA to NTIPA this is now the case. To investigate this capability, profiles near the cloud sides in pixel $(18, 4)$ are compared for TIPA and NTIPA, see Figures 4.34. From this figure it can be easily concluded that NTIPA is superior to TIPA in all sections of the vertical. In the upper part of the cloud and above till TOA the TIPA profile is heavily fluctuating which is a result of the discretization error of the upwelling flux. Even the vertical average does not improve the offset from the exact profile. Contrary to this, the NTIPA profile is smooth due to the convolution and closely resembles the

(a) Vertical profiles of the net flux-density in position (18,4) for TIPA.

(b) Vertical profiles of the net flux-density in position (18,4) for NTIPA.
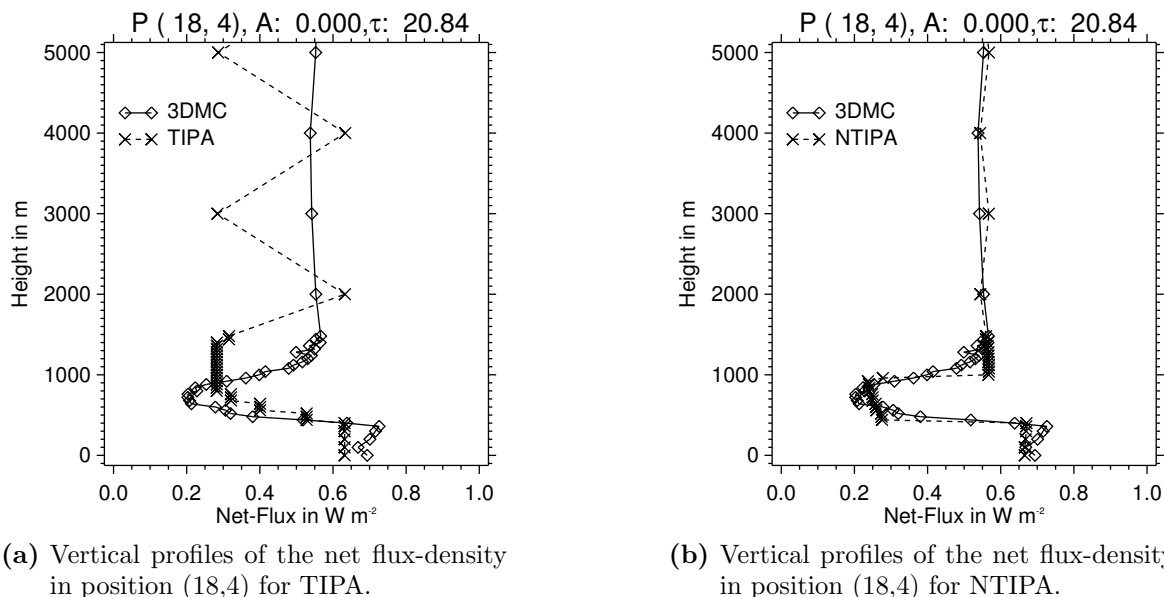
Figure 4.34: Vertical profiles of the net flux-density in position (18,4) with $\tau = 20.84$ for TIPA and NTIPA compared with 3DMC for the chequered pattern and $\mu_o = 0.95$.

3DMC profile. Above the cloud only a trace of the strong fluctuations persists. From the examples given here, it can be concluded that generally both upwelling and downwelling fluxes are subject to the fluctuations with the upwelling stronger affected. This is a result of the dominating geometric effects of the downwelling radiation. NIPA produces a good profile above the cloud while below the cloud the profiles do not match at all. Needless to say that IPA only accidentally gets reasonably close to the 3DMC results at a short section inside the cloud. In all other vertical sections of this pixel it is nowhere near the actual profile. For brevity no graphs are shown for IPA and NIPA. Exactly at the boundary of the clouds, which would be one pixel to the left, similar results can be deduced for TIPA while NTIPA does not match the exact profile as closely as shown for position $(18, 4)$ but still outperforms TIPA by far.

4.9   Remarks

In summary, for the 3D parameterizations it can be claimed that a cascade of three approximations for 3D cloud–radiation interactions has been developed. The first two, the Tilted Independent Pixel Approximation and the Nonlocal Independent Pixel Approximation, are combined to form the third, the Nonlocal Tilted Independent Pixel Approximation.

Remarkable features of the implemented realization of TIPA are the geometric tracking of the direct beam in order to compose the slant coordinate and the inverse transformation of the radiative transfer results succeeding the 1D computation in order to retrieve the

correct positions of the results in the original grid. A special feature of the implemented variant of NIPA is the derivation of the convolution parameters by direct utilization of a diffusion theory result from an analytical solution in physical space for each of the applied convolution kernels.

Common to all three approaches is the usage of three-dimensionally variable optical properties, and all three yield in turn three-dimensional results of the upwelling, downwelling, and net flux-densities. An extension to include the actinic flux is straightforward.

As input data no newly deduced parameters specific for these approximations have to be supplied, the standard set of optical properties comprising scattering and absorption coefficient plus the phase function expansion coefficients or at least the asymmetry factor as for any usual 1D radiative transfer model suffices.

Regarding the size of the convolution kernel a definite rule was neither found nor applied. As demonstrated by Davis et al. (1997), the scale break in the radiative behavior occurs around $200m$. As a result, the convolution kernel always extends significantly beyond that range. Generally, an edge length of at least $1000m$ is maintained, given the horizontal resolution is not too large kernels are extended if the computational cost stays limited.

As for the intermediate findings of the idealized applications presented in the previous sections all approximations give reasonable output in the respective field of applicability and results look promising so that realistic cloud scenes can be tackled as a next step.

A precise estimate concerning the computational cost is neither reasonable nor fair to give, as none of the presented 3D approximations can currently match the IPA with regard to computational optimization. All of them are at an experimental stage where rather the overall applicability is in focus than the quest for computational efficiency. However, a general description is possible. As far as TIPA is concerned, it has been explained before that the actual RT calculation consumes the same time as IPA. Although, additional computational time is necessary to build the slant coordinate and to perform the inverse transformation. For the presented examples, including the realistic examples in section 5.2, the computational time for the former is of the magnitude of several dozens of seconds to just a few minutes depending of course on the number of grid points. For the inverse transformation less time is required, typically several seconds, as only grid indices have to be recomputed from information which has already been derived by the transformation of the optical properties. These coarse estimates apply to a workstation with an Intel Xeon 2.8GHz processor. The computational cost of the convolution necessary for NIPA and NTIPA is about of the magnitude of the IPA, respectively TIPA calculation both are based on. Thus, the computational time is about doubled depending largely on the size of the convolution kernel. However, the opening statement about comparability of computational time applies especially to this method. Considerable simplifications could be made once investigations of the fundamental characteristics of this method have been finished.

Chapter 5

Application of the Methods and Results

> If the only tool you have is a hammer, you tend to see every problem as a nail.
>
> ———————————
>
> Anonymous

In this chapter, the parameterization approaches of chapter 3 and chapter 4 will be applied to clouds based on the methods introduced in section 2.4. In the first part, the accuracy and applicability of the radiative transfer perturbation theory (RTPT) to radiative transfer calculations in IPA mode is investigated. Results are compared with the usual forward calculations, and the subject of a possible calculation acceleration is briefly touched on. In the second part, the TIPA and NIPA approaches are applied both individually and in combination to parameterize 3D effects. All results there are compared with 3DMC results which have not been derived by the author but were provided by Sebastián Gimeno García and computed with the Leipzig Monte Carlo Model (LMCM), if not stated otherwise. For details about the 3DMC model and its application see again Gimeno García (2006) and Gimeno García and Trautmann (2003).

5.1   1D Radiative Transfer Perturbation Theory

A possible application of the RTPT arises when considering IPA calculations. This can be realized by selecting a certain number of pixels as base cases with respect to the total optical depth. Radiative transfer results of the pixels with optical depths located between the ones of the base cases are calculated by applying the RTPT and subsequent interpolation as presented in chapter 3. The motivation for studying this type of application is the disproportion of the dynamic time step of atmospheric models, that is the update interval for prognostic meteorological variables, and the update interval for radiative transfer results. In the case of the LM, the former is about several dozens of seconds, whereas the latter

is one hour. RT results are held constant throughout that period of time until the next update. Although no comprehensive study about the impact of the ratio between both on the forecast reliability and quality seem to exist, it can be assumed that especially in conjunction with cloud formation and decay there is room for improvement by accelerating radiative transfer calculations leading to more frequent updates of heating rates.

The RTPT could be used to find a remedy for this problem by carrying out adjoint calculations for the base cases additionally to the usual forward calculation. By applying the RTPT and the interpolation for pixels in the model domain with suitable optical depth at additional points of time, a correction to the otherwise constant radiative transfer results could be derived. The overall applicability to IPA calculations in cloudy atmospheres is investigated in the following examples. Their characteristics with respect to the cloud type and total optical depth is summarized in Table 5.1.

Table 5.1: Overview of the three examples for the radiative transfer perturbation theory. "Sc": stratocumulus, "St": stratus, "Cu": cumulus.

	Example	Horizontal resolution	$\langle \tau \rangle$	τ_{max}	τ_{min}
1	INSPECTRO Sc	$200m$	3.13	34	0.14
2	FIRE St	$50m$	25.05	27.64	14.98
3	ARM Cu	$100m$	3.78	106.8	0.85

5.1.1   Example 1: INSPECTRO stratocumulus

The cloud data of this example was kindly provided by A. Kniffka from the University of Leipzig, see Kniffka (2006). It was derived from data generated by the statistical cloud model CLABAUTAIR (CLoud liquid wAter content and effective radius retrieval By an AUTomated use of AIRcraft measurements), see Scheirer and Schmidt (2005), which used data from measurements derived during the campaign INSPECTRO. This campaign focuses, among other topics, on the investigation of the effect broken cloud fields have on the 3D variability of the actinic flux and the resulting consequences for chemical transport and its modeling. For details see the INSPECTRO Webpage (2002). In a later section of this thesis, a subset of the domain will be utilized for the study of the 3D parameterizations as well. The 2D field of the total optical depth is shown in Figure 5.1(a). The domain is composed of 112×193 pixels and 75 vertical layers. The horizontal resolution is $200m$. The cloud is rather inhomogeneous, clear sky areas alternate with cloudy parts of optical depth of up to 34. Vertically, the cloud is roughly located between $1425m$ and $1725m$, thus forming a geometrically rather thin layer. To activate all terms of the perturbation series, a surface albedo of 0.08 was assumed. The solar angles were set to $\mu_o = 0.398$ and $\varphi_o = 38.69°$ and the incident solar flux F_o was set to unity. The number of computational streams, see equations 2.81 and 2.82, was set to $N = 4$.

(a) 2D field of the total optical depth of the stratocumulus.

(b) Histogram of the distribution of the total optical depths.
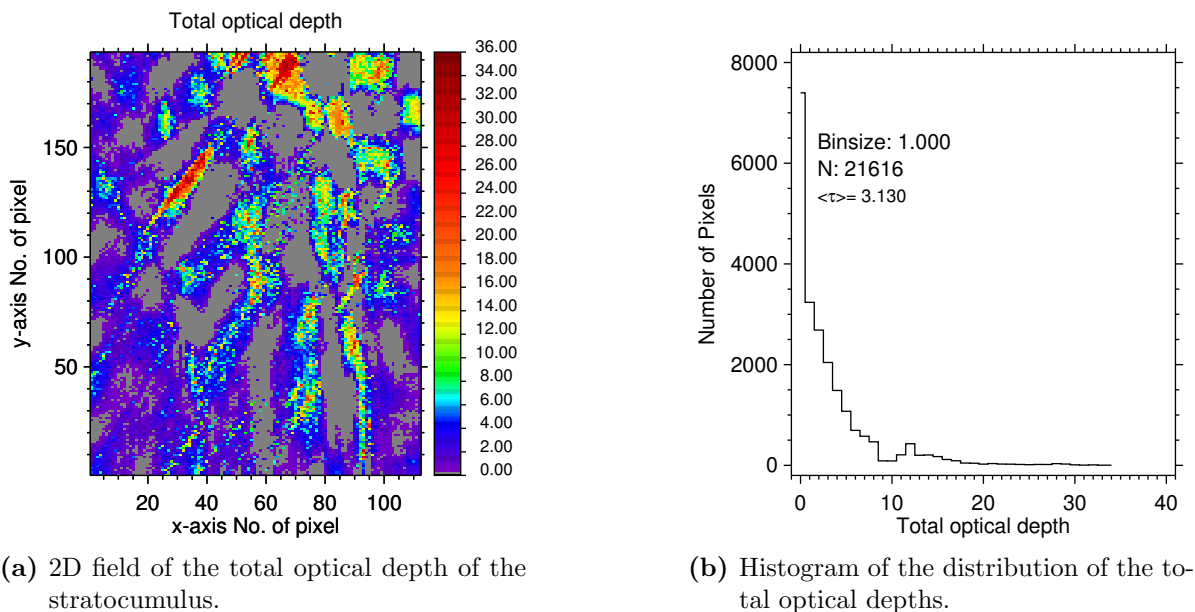
Figure 5.1: Total optical depth information of the stratocumulus of RTPT Example 1. The scene consists of 112×193 pixels with $\Delta x = \Delta y = 200m$.

As shown in chapter 3, one can only expect the RTPT to yield meaningful results if multiple base cases and interpolation between those is used. The eight pixels selected as base cases are presented in Table 5.2. The base cases are chosen in a semi-automatic manner, the first three and the last one are determined by the distribution of optical depths in cloudy and clear sky pixels. All other base cases are chosen at will. As for the angular scattering contribution to the perturbation, two different base case phase functions were used. The first is computed by forming the average of the expansion coefficients layer by layer of all pixels which are considered as clear sky. The second is derived by proceeding in the same way with all cloudy pixels. In the resulting seven intervals radiative transfer results are then computed by RTPT and Hermite-Interpolation. The clear sky phase function is assigned to the first two base cases and its cloudy counterpart to all remaining base cases. One recognizes that the base cases are clustered at low and moderate optical depths to account for the rapid decay of the radiative field in this range.

In Figure 5.2(a), the histograms of the absolute differences of pixel-by-pixel transmission and reflection, often also termed albedo, computed according to equations 2.13, are shown. Inserted in Figure 5.2(a) are the values for the mean transmission and reflection of forward (FW) calculation and perturbation (RTPT). Most individual pixel values are located in the sharp peaks around zero, but a smaller number of errors at the far sides of the spectra exist as well. However, the cumulative distributions, Figure 5.2(b), show that only a relatively small number of pixels is affected by large errors. From this figure, the symmetry of transmission and reflection, which results in two inseparable curves, is also evident. The domain averaged absolute errors are $|\Delta T| = 0.031$ and $|\Delta R| = 0.029$. The maximum and minimum errors of individual pixels are $\Delta T_{max} = 0.093$, $\Delta T_{min} \approx 0.0$ and $\Delta R_{max} \approx 0.0$,

Table 5.2: Base Case setup and phase functions for the stratocumulus cloud: cl: cloud phase function, cs: clear-sky phase function.

No.	Pixel (x,y)	Optical Depth (approx.)	Phase Function
1	(16,1)	$\mathrm{Min}(\tau_t)= 0.14$	cs
2	(5,172)	0.282	cs
3	(16,40)	0.283	cl
4	(112,155)	1.01	cl
5	(112, 132)	1.99	cl
6	(112,160)	7.99	cl
7	(101,132)	16.02	cl
8	(66,189)	$\mathrm{Max}(\tau_t)=34$	cl

$\Delta R_{min} = -0.09$. Although no investigation about the feedback on atmospheric dynamics was carried out, an absolute error of about 5% can be roughly regarded as tolerable, as this is also a typical value for the error of forward 2-stream models used for RT in dynamic models with respect to benchmark methods like the doubling algorithm, see Liou (1980) and Meador and Weaver (1980).

The relationship of the errors as a function of the total optical depth can investigated with the help of Figure 5.3. In Figures 5.3(a) and 5.3(b) errors for both R and T behave like a fading wave. Interestingly, around base cases No. 6 and No. 8 errors are at a maximum, while for base case No. 7 errors are significantly reduced. Similar patterns exist for the base cases at smaller optical depths.

In Figures 5.4(a) and 5.4(b) the same is plotted but for the case that the phase function is isotropic throughout the whole medium, thus effectively canceling the phase function perturbation. Errors are now considerably smaller, but also the approach of the wave-like structures towards the base case optical depths is much more evident. The large peak around an optical depth of four suggests to use one more base case. From these two figures, it is apparent that the largest uncertainty results from the phase function perturbation, while the error due to the pure extinction perturbation does not exceed two percent and would become negligible if another base case at $\tau = 4$ was employed. One inevitable problem is the fact that a column which has an optical depth close to a base case optical depth has not necessarily the same vertical distribution of optical properties as the base case column has. This can lead to an interpolation of the values in the column which does not reflect the actual change of the optical properties. In the special case of a vertical redistribution of the optical properties in a pixel which has the same total optical depth as one of the base cases and where the redistribution preserves the total optical depth, no interpolation is carried out at all. The perturbation of the phase function adds to that problem. In general, it can be said that the more uniform upper and lower cloud boundaries are and the smoother varying the optical properties are from pixel to pixel and with height,

(a) Histograms of the absolute errors of transmission and albedo.

(b) Cumulative distributions of the absolute errors of T and R.
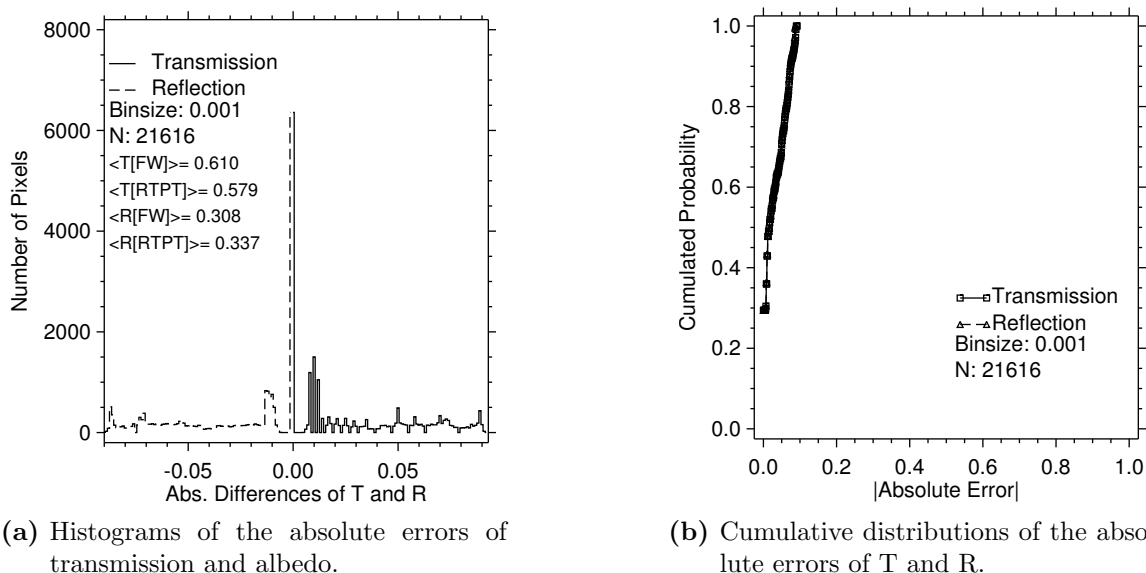
Figure 5.2: Distributions of the absolute errors of T and R for the RTPT with respect to the forward IPA calculation for Example 1 ($\mu_o = 0.398$ and $\varphi_o = 38.69°$). For information about the domain see Figure 5.1.

the more accurate the RTPT will be. This result will be readdressed and made more clear in the next two examples. It also seems to be reasonable to develop a more sophisticated algorithm to determine the optimal base cases with respect to optical depth and phase function in the future. The distribution of the optical depth, Figure 5.1(b), might be one foundation of this automatic algorithm.

As for the vertical structure of the results, one example column is chosen. In Figure 5.5 vertical profiles of net flux and mean intensity in pixel $(30, 130)$ with $\tau = 28.7$ are depicted. This position is affected by comparatively large absolute transmission and reflection errors, see Figure 5.3. The mean intensity is proportional to the actinic flux, see equation 2.14. It is modeled quite accurately by the RTPT, thus rather qualifying equation 2.67 to determine heating rates by means of equation 2.16, than using the vertical derivative of the net flux-density directly, as that would involve very small numbers as finite differences which might result in numerical problems.

Another feature that is remarkable is the symmetry of the errors in the histograms, Figure 5.2(a). This is not only a statistical effect, but also notable in individual pixels. In these, the upwelling flux is overestimated by the RTPT above the cloud and fairly accurate below. As for the downwelling flux, the result of the RTPT above the cloud matches the exact calculations with reasonable accuracy and underestimates it below cloud base. This can be explained by the fact that the cloud modulates the fluxes by perturbing the base case results. Naturally, the downwelling radiation is largely unaffected by the cloud above cloud top. While penetrating the cloud, the RTPT error comes into play causing the uncertainties below the cloud. In the same way the upwelling flux gets modulated twice.
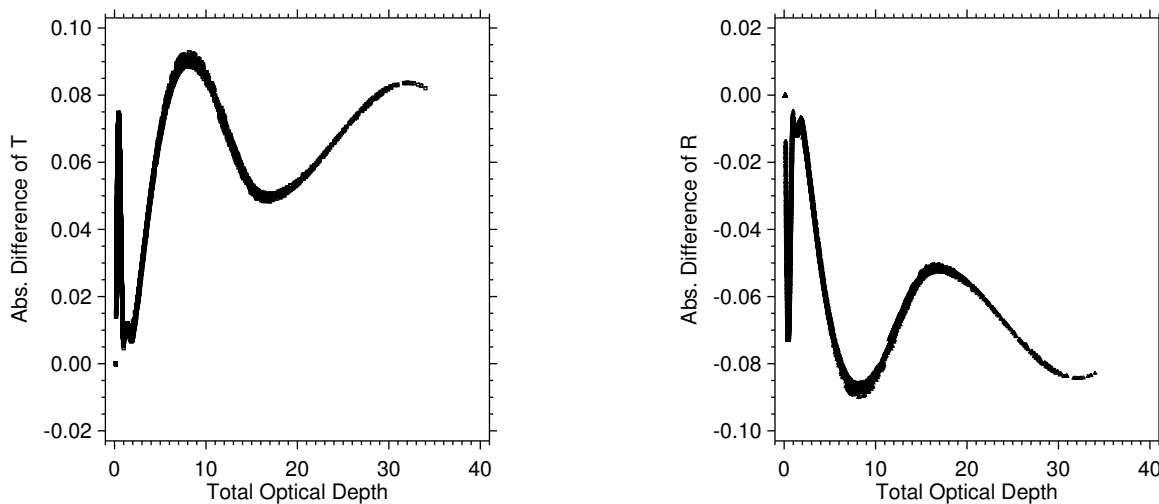
(a) Absolute error of the transmission as a function of the total optical depth.

(b) Absolute error of the albedo as a function of the total optical depth.

Figure 5.3: ΔT and ΔR of the RTPT with respect to the forward IPA as a function of total optical depth of RTPT for Example 1. For the applied parameters see Figure 5.2.

Once by the contribution of the fraction of the downwelling flux below cloud base, which is transformed into upwelling radiation by scattering, and once by the resulting upwelling flux when encountering the cloud on its way to the upper boundary of the medium.

To finish this section, a brief statement about computational speed is made, as acceleration of RT modeling is the long term aim of the RTPT. To yield full vertical resolution, meaning that a result is computed at every vertical level of each pixel, an adjoint solution is necessary at all levels of all base cases. This requires considerable computational time. Another computationally demanding part is the calculation of the phase function perturbation, as this perturbation integral has to be evaluated at every grid cell. However, if only three output levels are chosen, for example top and bottom of the column and cloud base, the RTPT calculations are about four times faster than the forward calculations in this example. The time for choosing base cases is not included in this figure. This way, the heating rates of the cloud and the surface could be determined together with column albedo and transmission. In this connection, it has to be emphasized that the developed code is by no means optimized and with the appropriate realization of the technique in an analytical 2-stream model a more advantageous acceleration might be possible. This was pointed out by Gabriel et al. (2000). These authors did not consider interpolation between multiple base cases but broadband radiative transfer which is another topic also of importance in NWP.
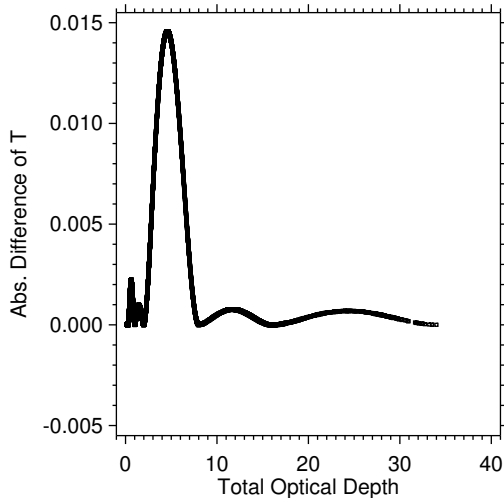
(a) Absolute error of the transmission as a function of the total optical depth.
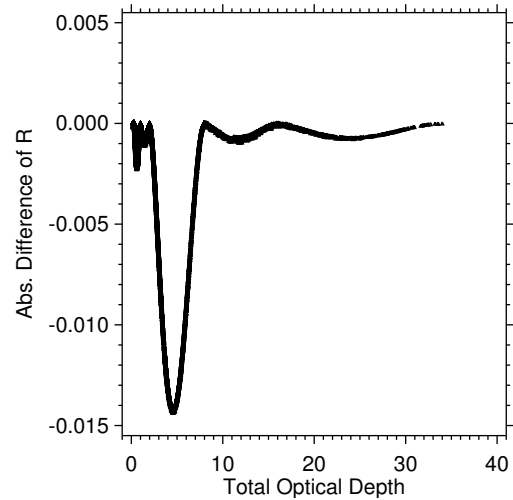
(b) Absolute error of the albedo as a function of the total optical depth.

Figure 5.4: As Figure 5.3 but for the modified cloud (homogenous isotropic phase function).
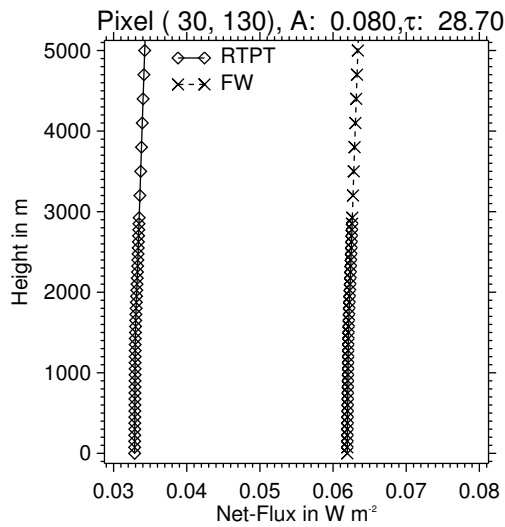
(a) Vertical profile of the net flux density.
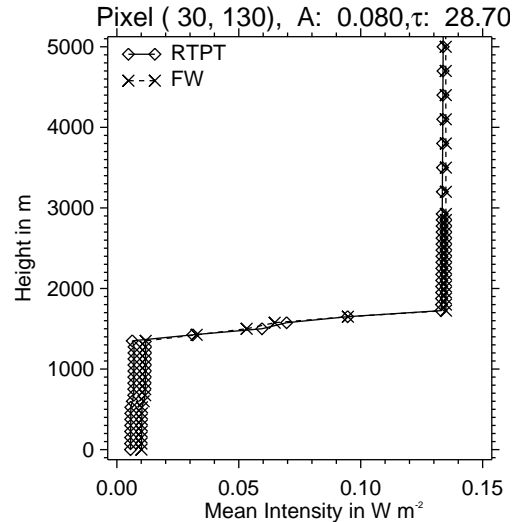
(b) Vertical profile of the mean intensity.

Figure 5.5: Vertical profiles of the net flux-density and the mean intensity in pixel (30,130) with $\tau = 28.7$ derived from the RTPT and the forward IPA for Example 1.

5.1.2   Example 2: FIRE stratus

In order to give an example of a cloud attributed to the less critical part of the spectrum of cases, a stratus cloud is chosen. It was derived from FIRE (First ISCCP Regional Experiment) I data, see FIRE I Webpage (2002), and has been originally modeled by Duynkerke et al. (2004) with an LES model and postprocessed by Venema et al. (2006) with the IAAFT algorithm to determine liquid water content and liquid water path. The scene is made up of $52 \times 52 \times 79$ grid points where each pixel has a horizontal resolution of $50m$. Solar illumination, surface albedo, and all other parameters remain as in the previous example. The cloud stands out by its moderate horizontal and vertical inhomogeneity which can be taken from Figure 5.6. The distinct cloud top and bottom has virtually no vertical variation with horizontal position. The histogram of the optical depth, Figure 5.7(a), restates the difference to the previous case, thus it suggests to reduce the number of base cases and makes their selection less crucial.

(a) Total optical depth field of the stratus cloud.

(b) Vertical cross-section of the horizontal optical depth integrated in x direction.
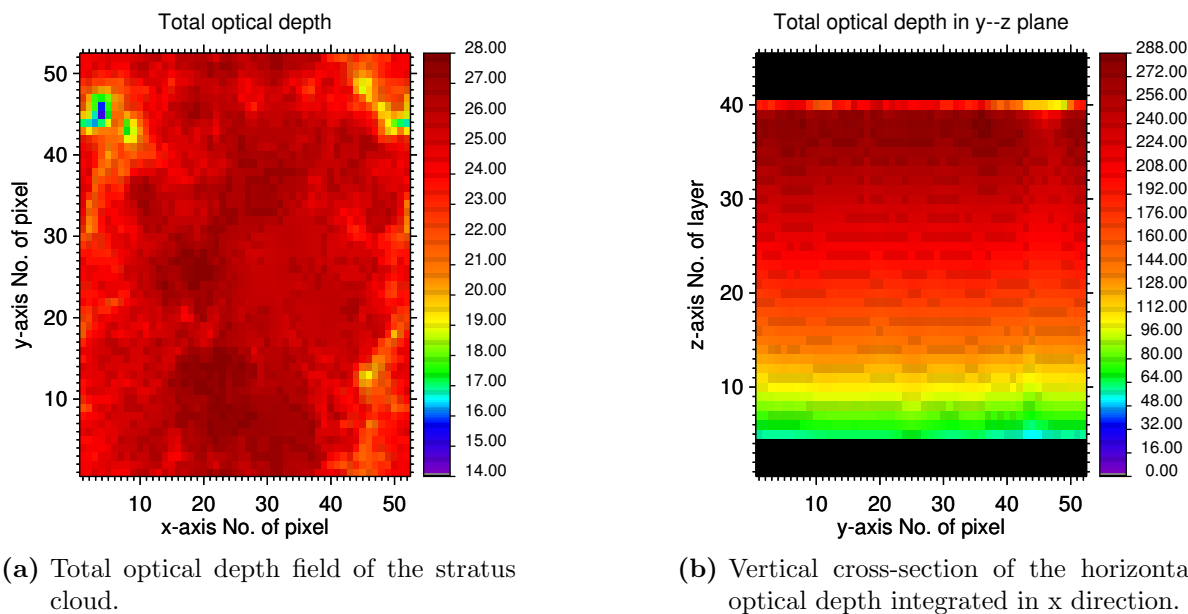
Figure 5.6: Optical depth information of the 52×52 pixel stratus cloud with $\Delta x = \Delta y = 50m$.

As a result, the minimum number of four base cases is chosen, see Table 5.3, and no clear sky base case phase functions have been generated. In Figure 5.7(b) the histograms of the absolute differences are depicted as before. The RTPT is fairly accurate, only three pixels have small outliers not exceeding 3% error. As expected, the symmetry of the errors in the histograms persists as well. At zero percent error there are only few pixels contrasting with the picture of the stratocumulus where the maximum of pixels was associated with that error region. This is a result of the total cloud cover of this scene. The domain averaged errors are $\Delta T = 3.95 \cdot 10^{-3}$ and $\Delta R = -4.88 \cdot 10^{-3}$. As the scene consists only of a small number of pixels, no comparison between forward calculation and RTPT with

Table 5.3: Base case setup and phase functions for the stratus cloud of Example 2.

No.	Pixel (x,y)	Optical Depth (approx.)	Phase Function
1	(44,3)	$\mathrm{Min}(\tau_t)$= 14.98	cl
2	(44,49)	16.29	cl
3	(46,5)	16.7	cl
4	(9,22)	27.64	cl
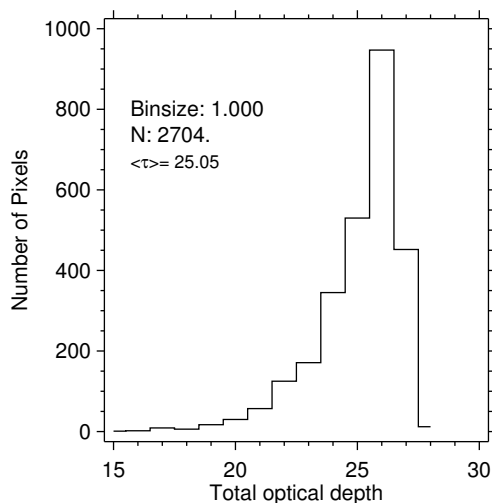
(a) Histogram of the total optical depth of the stratus cloud of Example 2.
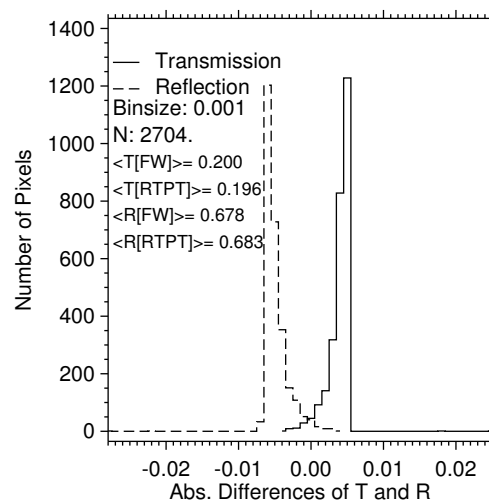
(b) Histograms of the absolute errors of T and R for the RTPT with respect to the forward IPA calculation.

Figure 5.7: Histograms of the total optical depth and ΔT and ΔR of RTPT with respect to the forward IPA calculation for Example 2 with $\mu_o = 0.398$ and $\varphi_o = 38.69°$.

respect to computational speed has been carried out. The RTPT cannot make use of its computational advantage if the scene is not composed of a reasonably large number of pixels, which enables the interpolation to (over)compensate the longer calculation of the base cases.

5.1.3   Example 3: ARM cumulus

In order to point out the limitations of the RTPT and to show the breakdown of the applicability, the following example of a cumulus cloud was chosen. The cloud was derived from measurements of the Atmospheric Radiation Measurement (ARM) Program, see ARM Webpage (2004). Based on these measurements, the data was postprocessed by an LES model, and the stochastic IAAFT algorithm was used to derive 3D liquid water content distributions. For details see Venema et al. (2006), who also provided the data. The model domain comprises $66 \times 66 \times 70$ grid points with a horizontal resolution of $100m$. The setup concerning the illumination, computational angles etc. is unchanged.

From the 2D field of the total optical depth, Figure 5.8(a), one recognizes that the scene consists of a number of cloudy areas with large optical depths of up to over 100. However, most of the scene is clear atmosphere. Contrary to the examples before, the cloud here is not confined to a flat layer but has considerable vertical structure which is depicted in Figure 5.8(b). In order to account for the large span of optical depths, ten base cases as shown in Table 5.4 have been employed.
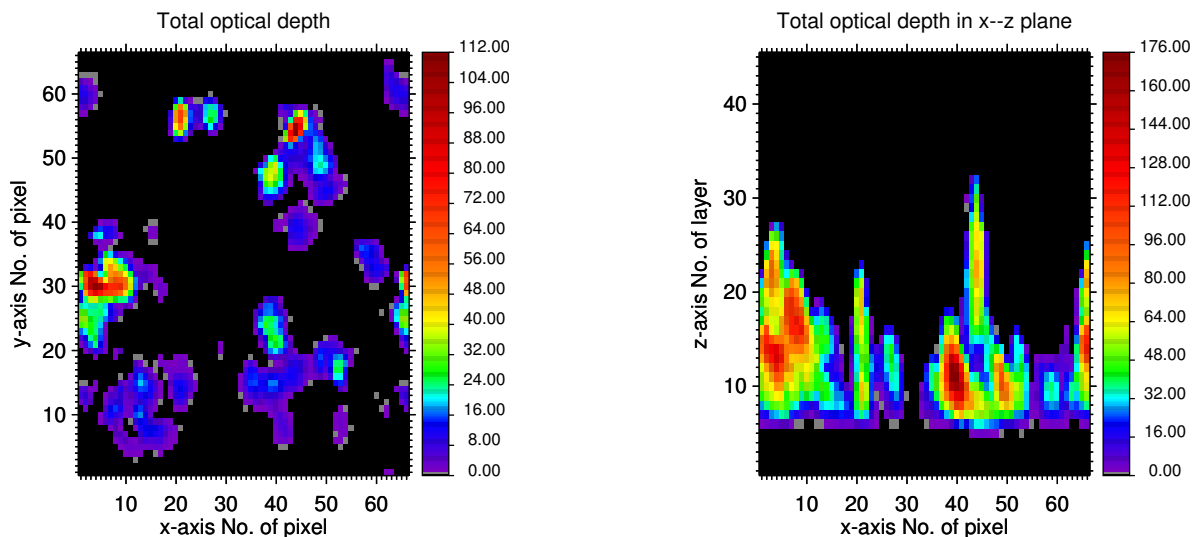
(a) Total optical depth field of the cumulus cloud.

(b) Vertical cross-section of the horizontal optical depth integrated in y direction.

Figure 5.8: Optical depth information of the cumulus cloud with 66×66 pixels and $\Delta x = \Delta y = 100m$.

Yet, in this example significant errors occur. The domain averaged errors amount to $\Delta T = 3.95 \cdot 10^{-2}$ and $\Delta R = -3.84 \cdot 10^{-2}$. Investigation of their respective histograms, see Figure 5.9(a), reveals that both have a strong peak around zero error but also suffer from large outliers. The symmetry of the errors is also remarkable. The error of the transmission is always positive while the one of the reflection consists only of negative values. One group of values is located at about $|17\%|$ and a smaller number at $|19\%|$. Investigation of the dependence of the errors on the optical depth, Figure 5.9(b), shows that maximum errors

occur not at the largest optical depths but rather at cloudy areas of comparatively low optical depth of about 1 to 15.

Table 5.4: Base Case setup and phase functions for the cumulus cloud: cl: cloud phase function, cs: clear-sky phase function

No.	Pixel (x,y)	Optical Depth (approx.)	Phase Function
1	(1,1)	$Min(\tau_t)$= 0.13	cs
2	(40,59)	0.19	cs
3	(40,29)	0.2	cl
4	(66,63)	0.73	cl
5	(66,58)	4.9	cl
6	(66,61)	7.56	cl
7	(65, 23)	15.7	cl
8	(66,24)	31.1	cl
9	(66,31)	60.94	cl
10	(44,54)	$Max(\tau_t)$=106.4	cl

As already addressed in the example of the stratocumulus cloud, these errors seem to stem from the choice of the phase function. The cloudy phase function is derived by forming the average of the expansion coefficients in each layer in all pixels which are considered to have a total optical depth above a threshold. Unfortunately, this leads to an unrealistic vertical phase function in the pixels where the cloud top is geometrically lower than the average. As shown in section 3.3, large perturbations of the phase function can lead to tremendous errors and should be avoided. By performing additional calculations, which employed another two base cases with respect to optical depth, not shown here, it could be demonstrated that the results only slightly improve, thus backing the above explanation for the errors. With this example, it is clear that a more sophisticated and flexible treatment of the phase function perturbation is necessary if highly variable cloud tops and bottoms are to be treated.

5.1.4   Remarks

Concluding this topic, it can be summarized that the RTPT is applicable to IPA calculations in cloudy atmospheres if some constraints are observed. As long as the horizontal and more important the vertical inhomogeneity of the clouds remains moderate, results with justifiable error of typically around an absolute value of 5% for transmission and reflection of individual pixels are obtained. This demand is especially necessary for the phase function. In view of a computational acceleration of the IPA calculations by the RTPT, it is important to select only a few output levels where results are desired. This is a result
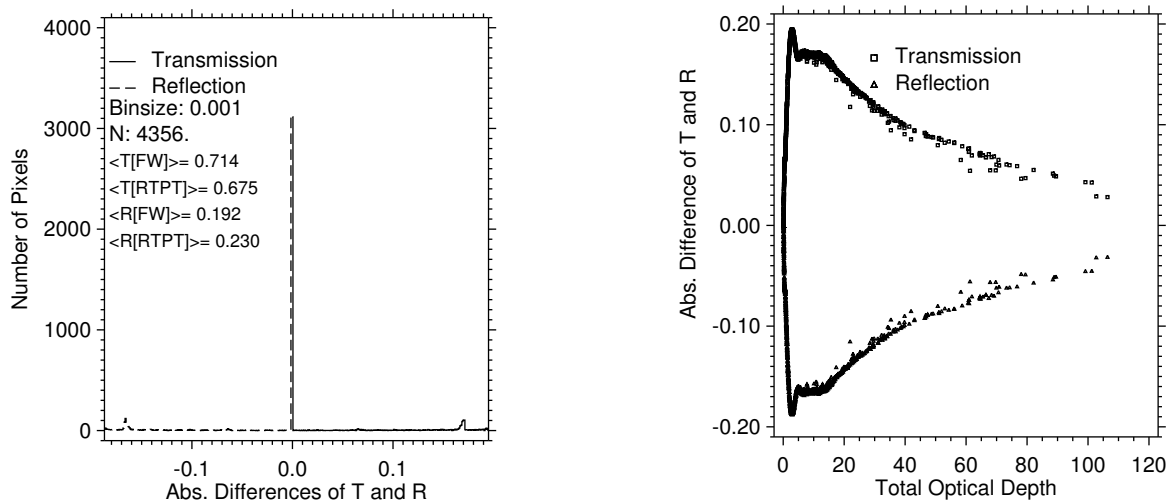
(a) Histograms of the absolute errors of T and R for the cumulus cloud.

(b) Absolute errors as a function of total optical depth.

Figure 5.9: Errors of T and R for Example 3 with $\mu_o = 0.398$ and $\varphi_o = 38.69°$.

of the computational cost which is attributed to the calculation of the adjoint solution for each output level in each base case. Similarly, the phase function perturbation and the albedo contribution to the perturbation integral have to be computed in each output level in each pixel. Moreover, the computational domain should preferably comprise a larger number of pixels than in the last two examples so as to make good advantage of the fast interpolation between base cases. A general rule of thumb cannot be easily stated as it would involve the number of pixels, output levels, base cases, and computational streams. Issues which remain undone are the fully automatic selection of base cases based on the distribution of the total optical depth. Equally important is the flexible and more realistic determination of base case phase functions in order to at least partially level the shortcoming in the aforementioned example. Lastly the implementation of the RTPT in a NWP model remains a challenging task and should be preceded by studies investigating the meaningful update interval of radiative transfer calculations. This recommendation could be used as "target criteria" for the RTPT implemented in an analytic 2- or 4-stream model.

5.2   3D Approximations

In this section the investigation of the different 3D cloud–radiation parameterizations will be extended from idealized cases, which have been discussed in sections 4.6 and 4.8, to realistic clouds. In all experiments, the applied approximations are compared with the LMCM 3DMC, see Gimeno García (2006) and Gimeno García and Trautmann (2003). It is understood that all denoted errors and differences are calculated by comparing the approximations with this 3DMC in the way presented by rule 4.2, if not stated otherwise. As only a very limited number of cloud scenes was available to the author, the following analysis had to be confined to just a few case studies. However, a more systematic discussion involving numerous scenes and set-ups concerning solar illumination and surface albedo as well as optical properties would have been highly desirable in order to arrive at a more general and statistically more reliable result. Yet, to associate at least some systematic structure with the derived results and conclusions, the cases investigated here will be grouped, according to the respective horizontal resolution, into three categories.

The first group is considered to comprise resolutions from several meters to about $100m$. Thus, the cases two and three of phase one of the I3RC project, see Várnai (2006a), were chosen to represent this range. However, not all experiments which are suggested by the I3RC group have been carried out. Furthermore, the original cloud setups do not involve any atmospheric effect which mainly means that the clouds are embedded in vacuum. Although this is completely reasonable if exact models are compared, it is not suitable in the authors point of view for approximate methods. These mainly rely on emulating one or more physical processes in a planetary atmosphere. For example, NIPA tries to mimic horizontal photon diffusion. If the cloud scenes miss a fundamental element of the natural behavior, in this example this is scattering and absorption by an atmosphere surrounding the cloud, the approximations generally cannot be expected to yield results or even encounter numerical problems. For this reason, the I3RC clouds have been embedded in a very simple idealized atmosphere which will be specified below. This first class of clouds is completed by a cloud scene deduced from the ARM program. All the three of these clouds scenes stand for high resolution cloud scenes where horizontal photon diffusion is expected to play an important role.

For the second class of resolutions it seems to be meaningful to cover the range of the scale break at around $200m$, where the major influence of horizontal diffusion is expected to fade, and the regions extending beyond up to $1000m$. However, this class comprises just one cloud, namely a section of the INSPECTRO cloud which was already introduced in one of the preceeding sections. This cloud can be regarded as a medium resolution cloud which poses a significant challenge for the 3D parameterizations because of its small vertical extension and its highly inhomogeneous structure. It will be investigated in three different setups.

For the third and last class of cloud scenes the future horizontal resolution of operational weather prediction models was taken into account. These are believed to arrive at $3000m$ and less in the immediate future. As a result, this range comprises two cases which have been deduced from the Lokal-Modell (LM) and stand for coarse resolution clouds. Table 5.5

gives an overview of all investigated cloud fields. For all examples at least two experiments have been carried out. The first experiment always employs vertical solar illumination ($\mu_o = 1.0$) while the second experiment deals with slant illumination ($\mu_o = 0.5$). In some cases additional experiments have been carried out.

Table 5.5: Overview of the cloud fields available to investigate the 3D approximations. "Sc": stratocumulus, "Cu": cumulus. "Hor. res.": Horizontal resolution.

Category		Example	Hor. res.	$\langle\tau\rangle$	τ_{max}	τ_{min}
High resolution	1	ARM Cu	$100m$	3.78	106.8	0.85
	2	I3RC Phase 1 Case 2	$50m$	19.71	51.73	6.69
	3	I3RC Phase 1 Case 3	$30m$	10.28	43.33	0.22
Medium resolution	4	INSPECTRO Sc	$200m$	4.3	34.0	0.141
Coarse resolution	5	LM DAQUA	$2800m$	14.85	179.8	0.086
	6	LM QUEST	$2800m$	18.3	317.6	0.99

5.2.1 High Resolution Clouds

Example 1: ARM cumulus

In this example, the same cumulus cloud scene is discussed as in the last example of the RTPT, see page 104. The whole atmosphere reaches up to $60000m$. Just as in some of the idealized examples, it is composed of the cloud optical properties and an atmosphere with Rayleigh scattering and O_3 absorption characteristic for $330nm$. The 2D distribution of the total optical depth is depicted in Figure 5.8(a). The cloud's distribution is rather speckled which is reflected by the values $\tau_{min} = 0.85$, $\tau_{max} = 106.8$, and $\langle\tau\rangle = 3.78$.

Experiment 1: $\mu_o = 1.0$, $\varphi_o = 0°$, $A = 0.0$

In this case, the cloud is vertically illuminated by the sun, and the surface is non-reflecting. It can serve as an example for pure horizontal diffusion as geometric effects are not supposed to occur. As a result, only IPA and NIPA are investigated. The latter is employed twice differing in the size of the convolution kernels. In accordance with the remarks made with regard to the size of the kernel at the end of the idealized example on page 92, a kernel comprising 11×11 pixels $\equiv 1100m \times 1100m$ was chosen. The second kernel processed has 25×25 pixels. The former is termed NIPA(11), and the latter is termed NIPA(25) in the following.

In Figure 5.10 the histograms of ΔT and ΔR of the three calculations compared to 3DMC are plotted. The IPA calculation produces an extended but sharp peak for the reflected light at small error values but has large outliers at the same time. In contrast to that, for both NIPAs the distributions are less peaked but generally smoother and more consolidated

towards the centers. For transmission NIPA(25) produces a distinct peak compared to NIPA(11). These findings are supported by the results of Table 5.6 which shows the fraction of pixels for a 5% and 8% error threshold. Although the peak in the histogram for ΔR for IPA is slightly below 5% error, both NIPA calculations turn out to be more accurate as a consequence of the more composed distributions. Between both NIPA calculations differences are rather small and tend to be more significant for transmission.
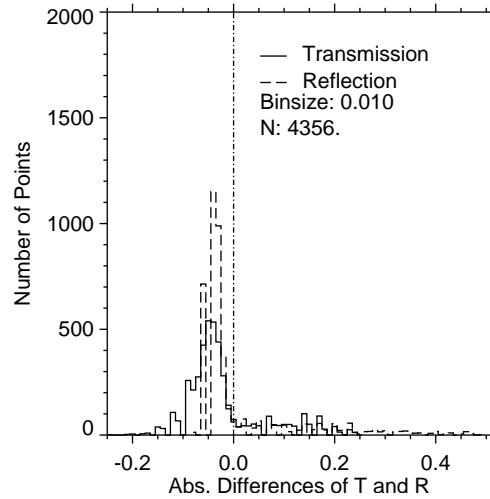
(a) Histogram of the errors for IPA.
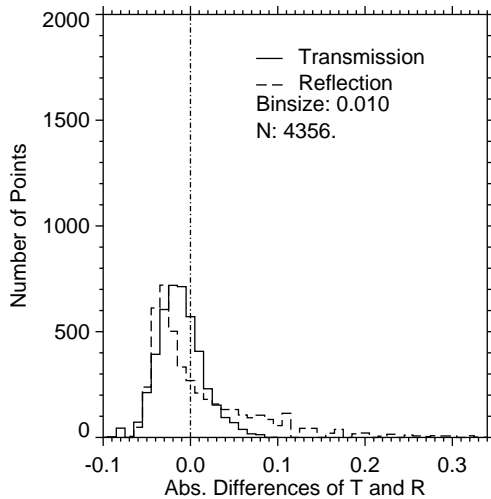
(b) Histogram of the errors for NIPA(11).
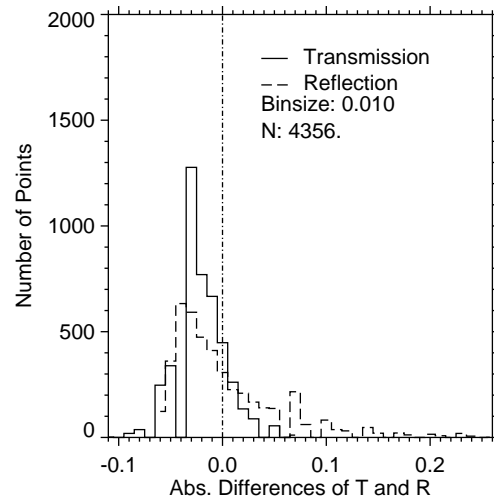
(c) Histogram of the errors for NIPA(25).

Figure 5.10: Histograms of ΔR and ΔT for IPA, NIPA(11) and NIPA(25) for Experiment 1 of the ARM cumulus. The figures in parentheses give the edge length of the convolution kernel in pixels.

Table 5.7 shows the scaling behavior of the three computations by comparing maximum residual errors of $|\Delta T|$ and $|\Delta R|$ at averaging kernels of one, seven, and 15 pixels edge lengths. The first being located within the diffusion regime, the second clearly above it, and

Table 5.6: Comparison of the pixel fractions for a 5% and 8% error threshold of T and R for the three simulations of Experiment 1 of the ARM cumulus.

Model	$\Delta T \leq 5\%$	$\Delta R \leq 5\%$	$\Delta T \leq 8\%$	$\Delta R \leq 8\%$
IPA	49%	65%	73%	84%
NIPA(11)	89%	72%	99%	85%
NIPA(25)	91%	78%	99%	89%

Table 5.7: Comparison of the coarse grained moving averages of $|\Delta T|_{max}$ and $|\Delta R|_{max}$ for edge lengths of one, seven, and 15 pixels for the three simulations of Experiment 1 of the ARM cumulus.

Model	$|\Delta T|(1)$	$|\Delta R|(1)$	$|\Delta T|(7)$	$|\Delta R|(7)$	$|\Delta T|(15)$	$|\Delta R|(15)$
IPA	26%	51%	9%	38%	4%	21%
NIPA(11)	10%	34%	5%	28%	3%	17%
NIPA(15)	11%	26%	4%	22%	2%	15%

the third beyond the scope of the 11×11 convolution kernel. As for transmission, differences between NIPA(11) and NIPA(25) are rather small due to the geometric dominance of the downwelling radiation. However, with regard to IPA one notes that NIPA cuts the error in half at one and seven pixels, whereas the difference at 15 pixels is almost negligible. Yet, that is not true for the reflected light. Here, the differences between both NIPAs are larger and remain two percent even for the largest averaging kernel. The differences of both NIPAs with respect to IPA decline from large values to just a few percent. This is a result of the inherent averaging nature of the reflected light.

In summary, it can be claimed that within and slightly beyond the diffusion regime NIPA delivers by far superior results. However, at scales in excess of $1000m$ the differences in this example for the reflected light were still notable, yet for the transmitted light negligible. One has to keep in mind that the quoted errors are the maximum residuals. Between both NIPAs there is almost no difference for transmission, yet for reflection there is. When comparing both NIPAs with IPA the conclusions hardly change qualitatively. As a result, convolution kernels with larger edge lengths will be discussed only as an exception in the following examples. Finally, the domain averages are $\bar{T}(3DMC) = 0.636$ and $\bar{T}(IPA) = 0.625$ and $\bar{R}(3DMC) = 0.297$ and $\bar{R}(IPA) = 0.307$ which leaves one percent error. Due to the conservation of energy NIPA cannot improve any domain averages regardless of the size of the convolution kernel.

Experiment 2: $\mu_o = 0.5$, $\varphi_o = 0°$, $A = 0.0$

Here, the solar illumination has been inclined to 60°, thus effects are expected to consist of a mixture of geometric and diffuse components. As a result, the full set of approximations has been applied. As for NTIPA, two convolution calculations have been carried out, one with 11×11 pixels and the second with 25×25 pixels just as in the previous case. NIPA was employed only with a kernel with the former number of pixels.

In Table 5.8 the 5% and 8% thresholds for the five simulations are shown. Without discussing each single figure, one notes that IPA's shortcomings for both threshold values are equally unsatisfying with respect to transmission. Although the scene consists of many clear sky pixels, the cloud cover being only about 30%, this bad performance of IPA is caused by the structure of the cloud top height which leads to pronounced shadows, see below.

Table 5.8: Comparison of the pixel fractions for a 5% and 8% error threshold of T and R for the five simulations of Experiment 2 of the ARM cumulus.

Model	$\Delta T \leq 5\%$	$\Delta R \leq 5\%$	$\Delta T \leq 8\%$	$\Delta R \leq 8\%$
IPA	53%	63%	59%	83%
TIPA	76%	61%	88%	81%
NIPA	54%	72%	58%	88%
NTIPA(11)	90%	71%	97%	86%
NTIPA(25)	91%	77%	98%	90%

In contrast, both NTIPA realizations yield results superior to all other approximations. When comparing both NTIPAs with TIPA one can estimate that the convolution actually accounts for an improvement of $10 - 15\%$ of all pixels. When comparing NTIPA with NIPA the difference, this time caused by the correct geometric tracking, is even $35\% - 40\%$. The differences with respect to reflection are smaller, NIPA is even superior to NTIPA(11) and IPA outperforms TIPA. These values clearly underline the importance to include a parameterization for horizontal diffusion but also emphasize the inabilities of NIPA to solely account for shadows.

In order to give an impression of the 2D distribution of the 3D effects, for this case the 2D fields of ΔT for IPA and NTIPA(25) are shown in Figure 5.11. As for IPA, one clearly recognizes that due to the incorrect succession of optical properties large errors occur not only in the "radiative lee" of the clouds but also in the "radiative luff". For NTIPA there is only little structure in the field, the fringes of the cloud shadows remain mostly traces. Only one larger contiguous area of significant errors exists as a result of the coherent cloudy area around pixel (20,30).

Table 5.9 shows the results for the coarse grained moving average for one, seven, and 15 pixels edge length. Due to the shadows being shifted sidewards the $\Delta T(1)$ error for IPA is now significantly larger than in Experiment 1. Yet, for the reflected light errors

(a) 2D field of ΔT for IPA.

(b) 2D field of ΔT for NTIPA(25).
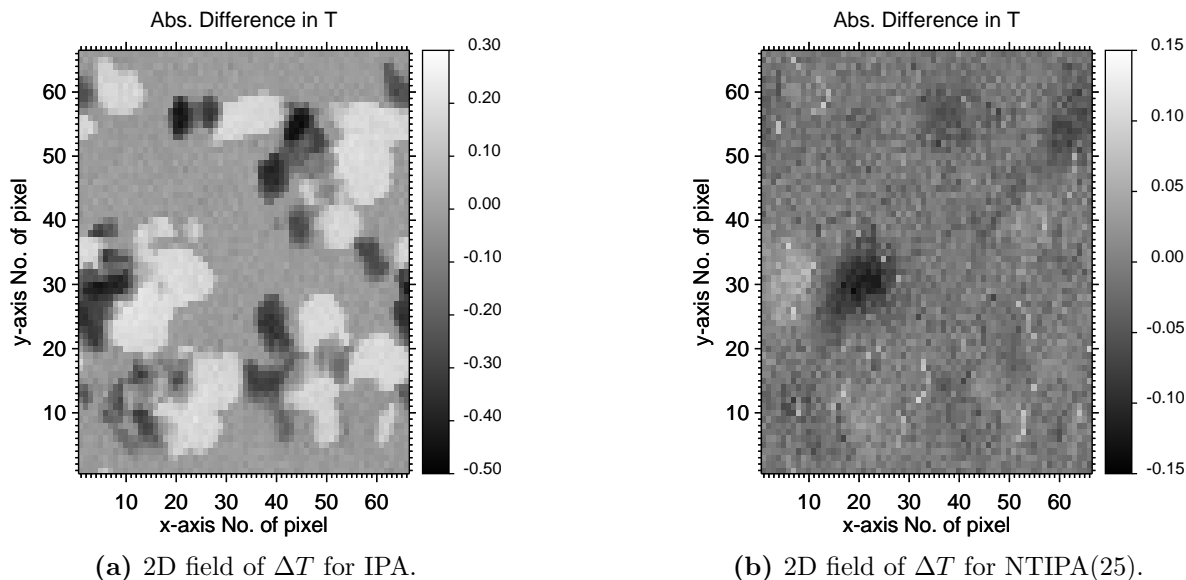
Figure 5.11: 2D field of ΔT for IPA and NTIPA(25) of Experiment 2 of the ARM cumulus. The scene consists of 66×66 pixels with $\Delta x = \Delta y = 100 m$. The illumination was set to $\mu_o = 0.5$ and $\varphi_0 = 0°$.

are diminished. TIPA seems to be only of use for the transmitted light where for all smoothing kernels better results are obtained while the reflected light stay as erroneous as for IPA. For NIPA it is almost visa versa, yet the reflected light is only improved if no smoothing is applied, and the transmitted light is slightly improved by blurring the shadows directly below the cloud. However, both NTIPAs combine the advantages and outperform the respective individual parameterizations, that is TIPA for transmission and NIPA for reflection. The larger convolution kernel is especially useful for the reflected light.

Table 5.9: Comparison of the coarse grained moving averages of $|\Delta T|_{max}$ and $|\Delta R|_{max}$ with edge lengths of one, seven, and 15 pixels for all simulations of Experiment 2 of the ARM cumulus.

Model	$|\Delta T|(1)$	$|\Delta R|(1)$	$|\Delta T|(7)$	$|\Delta R|(7)$	$|\Delta T|(15)$	$|\Delta R|(15)$
IPA	47%	39%	33%	30%	15%	17%
TIPA	29%	37%	19%	30%	7%	16%
NIPA	34%	28%	28%	23%	14%	14%
NTIPA(11)	16%	25%	11%	20%	6%	13%
NTIPA(25)	14%	20%	10%	16%	5%	11%

Concerning domain averages, see Table 5.10, IPA and NIPA are superior with errors below one percent. For TIPA and NTIPA errors are just slightly above one percent.
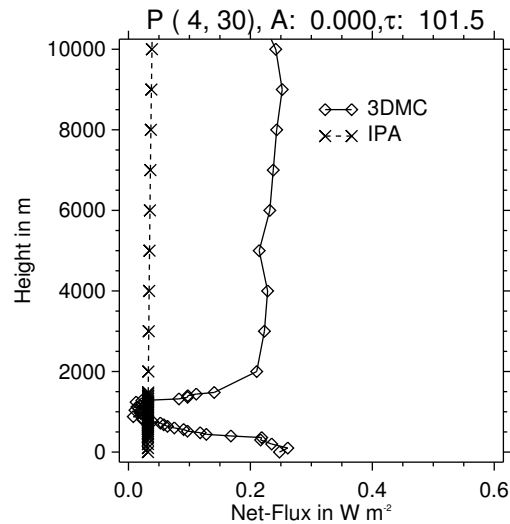
(a) Vertical profile of the IPA calculation.
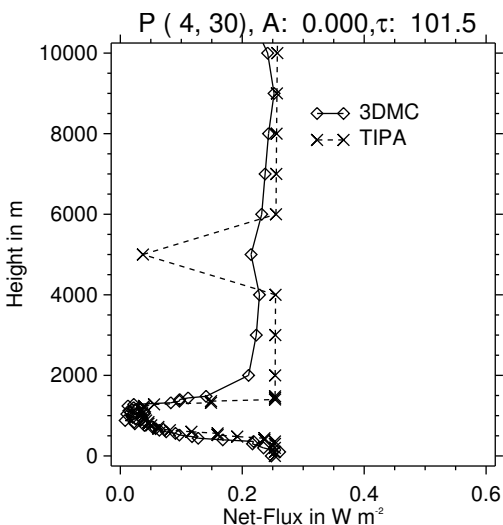
(b) Vertical profile of the TIPA calculation.
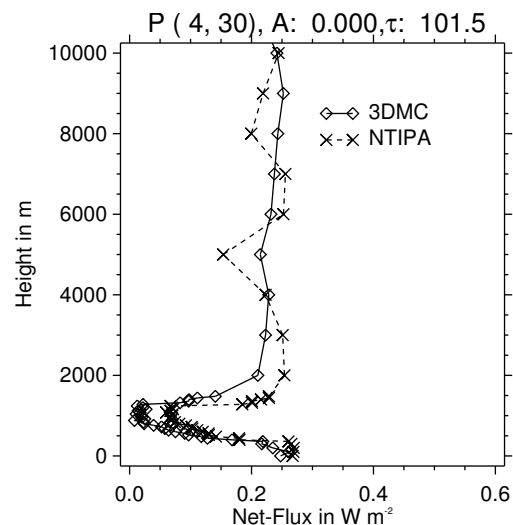
(c) Vertical profile of the NTIPA(11) calculation.

Figure 5.12: Vertical profiles of the net flux-density in pixel (4,30), $\tau = 101.5$, see also Figure 5.11, derived by IPA, TIPA and NTIPA(11) for Experiment 2 of the ARM cumulus.

As a last feature of this investigation, an example for the vertical profile is discussed, see Figure 5.12. The investigated pixel $(4, 30)$ is one of the pixels with very high optical depth. At the same time, it is located in the middle of a cloud which is vertically extensive, thus cloud tops and sides are both encountered in close neighborhood, see Figure 5.8(b). Hence, this position is ideally suited to investigate the discretization problem of TIPA and NTIPA and to compare both with the vertical profile delivered by IPA. Mean profiles are available as well, but those are useless for this task as all individual fluctuations are lost due to averaging. From this figure it is evident that IPA is clearly a technique which can only

yield meaningful domain averaged results, if any. Although, it is widely used in atmospheric models to compute vertical distributions of radiative properties. TIPA, however, describes the flux inside and below the cloud quite accurately while above cloud top it is prone to large artificial fluctuations. In contrast to that, NTIPA reduces those fluctuations but as the convolution can only be regarded as an estimate of horizontal transport its results inside the cloud are inferior compared to TIPA. These examples demonstrate the advantages and shortcomings of the different parameterizations. Their complementary aspects underline that none of them is an ideal solution for all features at a time.

Experiment 3: $\mu_o = 0.5$, $\varphi_o = 0°$, $A = 0.04$

As a last step, the surface of the model domain is assigned with a constant albedo of $A = 0.04$ which is realistic for this wavelength of $330nm$ according to Wendisch et al. (2004).
Comparison with the previous case shows almost no difference with regard to the overall results. Although this conclusion could have been inferred from the small albedo, the good news is that the qualitative results of the approximations hold in the case of weakly reflecting surfaces. In order to complement the result of Experiment 2 the 2D plots of ΔR for IPA and NTIPA, carried out with a 25×25 pixels kernel, are shown, see Figure 5.13.

(a) 2D field of ΔR for IPA.   (b) 2D field of ΔR for NTIPA(25).
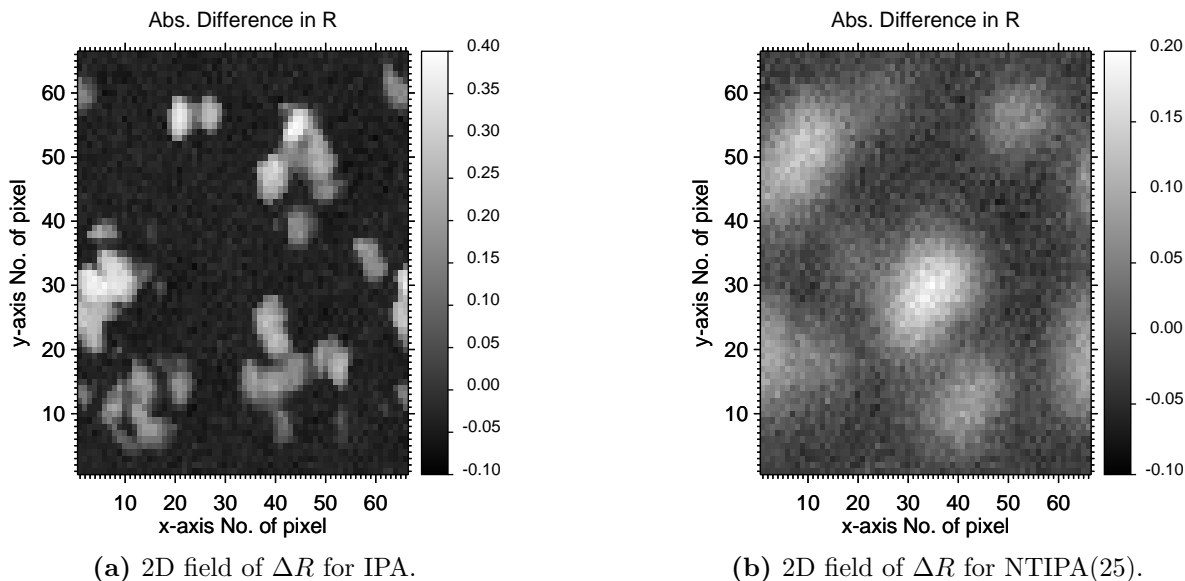
Figure 5.13: 2D field of ΔR for IPA and NTIPA of Experiment 3 of the ARM cumulus. See also Figure 5.11.

Compared to Figures 5.11 the visual impression is that that for IPA there is less structure and especially the variations of the errors are less significant than for the transmitted light while in the respective plot for NTIPA there is more structure. Because of the slant

Table 5.10: Domain averaged results for T and R for Experiment 2 and 3 of the ARM cumulus for all models.

	Experiment 2		Experiment 3	
Model	$\bar{T}$	$\bar{R}$	$\bar{T}$	$\bar{R}$
3DMC	0.467	0.419	0.475	0.409
IPA and NIPA	0.459	0.426	0.466	0.418
TIPA and NTIPA	0.455	0.429	0.462	0.421

coordinate the patterns are shifted to the right. As a result, the upwelling light is usually more accurately described by IPA than the downwelling light.

Domain averaged results also do not change qualitatively, see Table 5.10. Interestingly, the average reflection is slightly decreased compared to Experiment 2 although the ground is now reflecting. This might be explained by the trapping of the additional upwelling radiation inside the cloud which could be enhanced by the multiple reflections between cloud base and surface. However, a final conclusion of the reason behind this effect needs more detailed studies.

Example 2: I3RC Phase 1 Case 2

As mentioned in the beginning of this section, the adopted cloud scene from the Intercomparison of 3D Radiation Codes (I3RC, see Várnai (2006b), has been modified as a simple atmosphere is superimposed. The atmosphere uses O_3 absorption with $\sigma_a = 3.4 \cdot 10^{-7} m^{-1}$ and Rayleigh scattering with $\sigma_s = 8.5 \cdot 10^{-5} m^{-1}$, both homogeneously distributed throughout the medium. The domain is originally two-dimensional, but in order to avoid numerical problems with the convolution it was homogeneously extended along the y-axis to yield a lattice with $640 \times 50 \times 54$ grid cells. The horizontal resolution is $50m$, and the top of the domain is located at $2430m$. The single scattering properties of the cloud are $\omega_o = 1.0$ and $g = 0.85$ where higher orders of the phase function expansion coefficients are determined by the Henyey-Greenstein phase function. The distribution of the total optical depth along the x-axis is shown in Figure 5.14. It has the following values: $\tau_{max} = 51.73$, $\tau_{min} = 6.69$ and $\langle \tau \rangle = 19.71$.
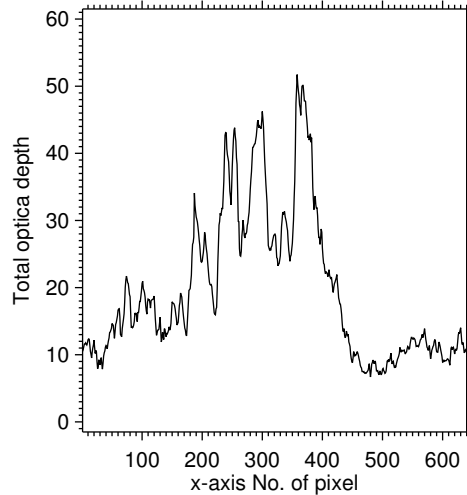
Figure 5.14: Total optical depth along the x-axis of the modified I3RC Phase 1 Case 2 cloud with 640×50 pixels and $\Delta x = \Delta y = 50m$.

Experiment 1: $\mu_o = 1.0$, $\varphi_o = 0°$, $A = 0.0$

Although the cloud cover is 100%, notable 3D effects exist even for vertical illumination. The maximum and minimum errors of IPA and NIPA with respect to 3DMC results for transmission and reflection are presented in Table 5.11. One recognizes that NIPA roughly cuts the maximum and minimum errors in half by applying a kernel composed of 25×25 pixels $\equiv 1250m \times 1250m$. According to the horizontal resolution of the cloud scene and the computational burden associated no larger convolution kernel was applied.

In this example the fraction of pixels below a certain error threshold and the scaling behavior investigated by comparing residual errors are less meaningful as no distinct separation of IPA and NIPA can be drawn from these results. However, the influence of the convolution can be demonstrated not only by quantifying maximum and minimum errors but also

Table 5.11: Maximum and minimum errors of T and R of IPA and NIPA for the modified I3RC Phase 1 Case 2 Experiment 1.

Model	ΔT_{max}	ΔT_{min}	ΔR_{max}	ΔR_{min}
IPA	0.11	-0.09	0.09	-0.08
NIPA	0.06	-0.05	0.05	-0.03

by means of the power spectrum of the absolute values of the errors. In order to reduce the strongest fluctuations values are averaged along the y-direction which is meaningful in this case anyway. In Figure 5.15 the power spectra of $|\Delta R|$ for IPA and NIPA are shown.

(a) Power spectrum of $|\Delta R|$ of IPA.   (b) Power spectrum of $|\Delta R|$ of NIPA.
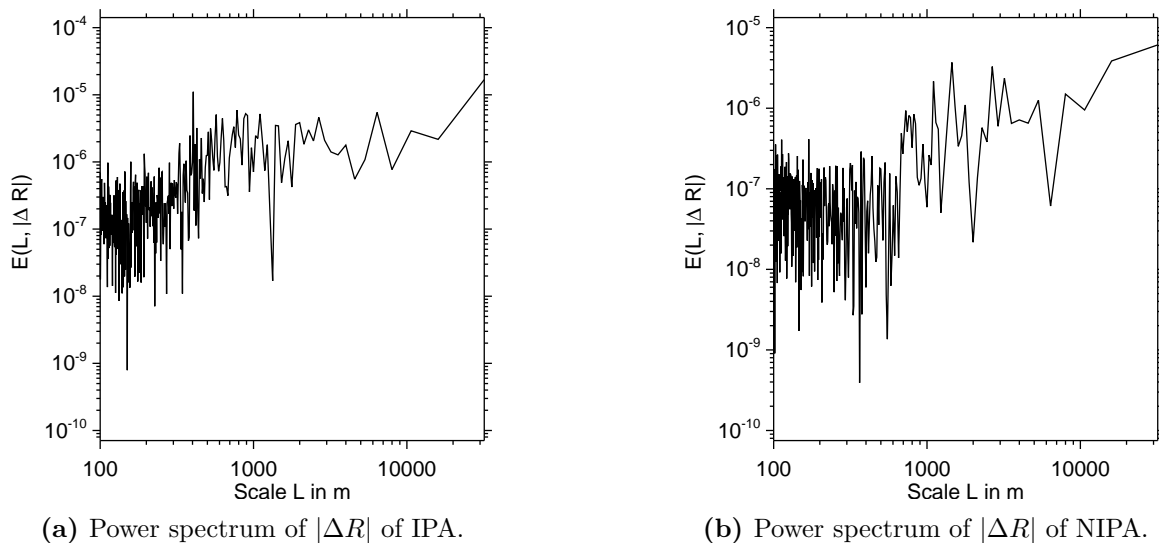
Figure 5.15: Power spectra of $|\Delta R|$ of IPA and NIPA for the modified I3RC Phase 1 Case 2 Experiment 1. $E(L, |\Delta R|)$ is plotted as a function of scale.

Although both curves are heavily fluctuating, it can be stated for IPA that the power increases for increasing scales. As for NIPA, there is an indifferent area reaching up to about $1000m$ clearly visible. This indifferent behavior, which is attributed to white noise, is a result of the averaging nature of the convolution. Even though the convolution kernel reaches to up to $1250m$ in both directions, the missing impact of the outermost $250m$ can be explained with the weights associated with those pixels. These contribute only with tenths of a percent to the kernel for a typical value of $\sigma = 500m$, see Figure 4.17.

In Figure 5.16 reflection values for IPA and NIPA are shown over the respective results of 3DMC. One clearly notes the narrowed distribution in case of NIPA. Results for the transmission behave analogously. This is reflected by the standard deviations of the errors, see Table 5.12, which also states the respective values for transmission. Domain averages agree with less than one percent error.

(a) Comparison of reflection values of IPA with 3DMC.

(b) Comparison of reflection values of NIPA with 3DMC.
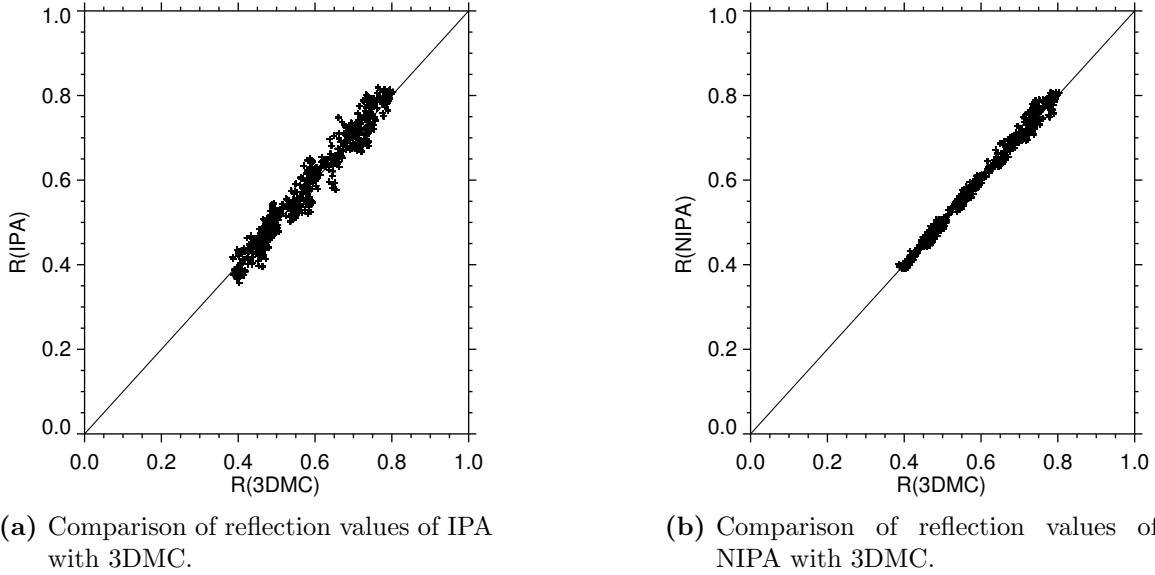
Figure 5.16: Comparison of reflection values of IPA and NIPA with 3DMC for the modified I3RC Phase 1 Case 2 Experiment 1.

Table 5.12: Standard deviation of ΔT and ΔR of IPA and NIPA for the modified I3RC Phase 1 Case 2 Experiment 1 as shown in Figure 5.16.

Model	$\sigma_{dev}(\Delta T)$	$\sigma_{dev}(\Delta R)$
IPA	0.034	0.026
NIPA	0.022	0.012

Experiment 2: $\mu_o = 0.5$, $\varphi_o = 0°$, $A = 0.0$

For this example with inclined illumination the overall impression of the results changes. So far TIPA, NIPA and NTIPA have been superior to IPA with regard to local improvements. Domain averages have been equally good or slightly inferior if compared to IPA. However, in this experiment TIPA, NIPA and NTIPA do not significantly improve results. Table 5.13 gives an overview of the maximum and minimum errors of all calculations with respect to 3DMC. For TIPA and NTIPA ΔR_{min} and ΔT_{min} results deteriorate by several percent, only NIPA can insignificantly reduce the already low errors if compared to IPA. These inabilities become more obvious when observing the 5% error threshold, see Table 5.14. TIPA as well as NTIPA fall significantly back behind IPA for the transmitted light. The reason for this result remains unclear.

Table 5.13: Maximum and minimum errors of T and R for all four approximations for the modified I3RC Phase 1 Case 2 Experiment 2.

Model	ΔT_{max}	ΔT_{min}	ΔR_{max}	ΔR_{min}
IPA	0.1	-0.07	0.13	-0.14
TIPA	0.12	-0.13	0.12	-0.18
NIPA	0.09	-0.05	0.12	-0.14
NTIPA	0.09	-0.12	0.11	-0.18

Table 5.14: Comparison of the pixel fractions for the 5% error threshold of T and R for the four simulations for the modified I3RC Phase 1 Case 2 Experiment 2 for $\varphi_o = 0°$ and $\varphi_o = 180°$.

	$\varphi_o = 0°$		$\varphi_o = 180°$	
Model	$\Delta T \leq 5\%$	$\Delta R \leq 5\%$	$\Delta T \leq 5\%$	$\Delta R \leq 5\%$
IPA	83%	73%	84%	74%
TIPA	68%	68%	66%	45%
NIPA	91%	74%	90%	73%
NTIPA	68%	71%	67%	46%
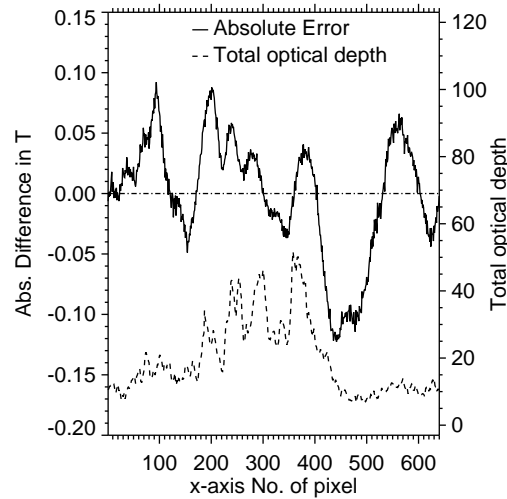
Figure 5.17: Total optical depth and ΔT of NTIPA along the x-axis of the modified I3RC Phase 1 Case 2 Experiment 2.

Figure 5.17 depicts ΔT together with the total optical depth along the x-axis. Gradients of the optical depth seem to be accompanied by peaks of ΔT most obvious in the region

beyond pixel 380 where the error changes its sign and reaches its largest negative value during the drop of the optical depth. This region seems to be crucial for the overall performance of the approximations as large errors last for about a sixth of the total domain. As a further test, the solar azimuth was changed from $0°$ to $180°$ thus illuminating the scene from the opposite direction. However, no significant qualitative change in the results can be observed, see Table 5.14. Again, NIPA can only increase the fraction of pixels which is below 5% error by several percent in case of transmission when compared to IPA. One even observes a significant deterioration of the results of TIPA and NTIPA with respect to the fraction of the reflected light. The other approximations roughly maintain their performance.

Example 3: I3RC Phase 1 Case 3

Another example for a high resolution cloud field is Case 3 of Phase 1 of the I3RC project, see again Várnai (2006a). This cloud field is determined by a horizontally variable but vertically homogeneous extinction coefficient of the cloud, a constant Henyey–Greenstein phase function with $g = 0.85$, a uniform cloud base height at $200m$ above ground, and a two-dimensionally variable cloud top height. The cloud's single scattering albedo was equally set to the constant value of $\omega_o = 1.0$. Superimposed are again the homogeneous values for Rayleigh scattering with $\sigma_s = 8.5 \cdot 10^{-5} m^{-1}$ and O_3 absorption with $\sigma_a = 3.4 \cdot 10^{-7} m^{-1}$. The whole scene is composed of $128 \times 128 \times 417$ grid cells. The large number of vertical layers is a result of the fine structure of the cloud top height distribution. The domain is limited to an overall vertical extension of $2580m$, and the horizontal resolution is $30m$ in each direction. The resulting two-dimensional total optical depth field with $\tau_{max} = 43.33$, $\tau_{min} = 0.22$, and $\langle \tau \rangle = 10.28$ is shown in Figure 5.18.
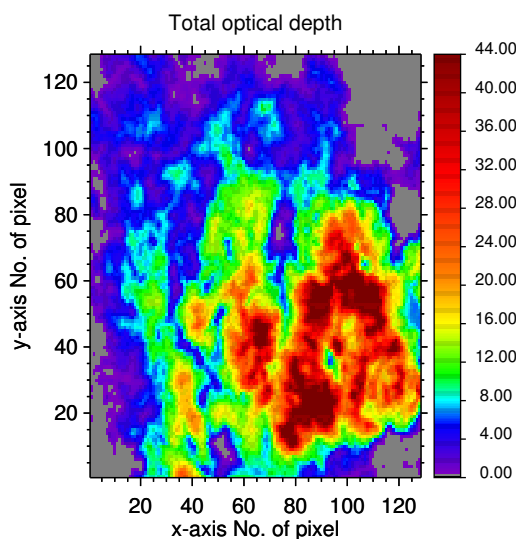
Figure 5.18: Total optical depth of the modified I3RC Phase 1 Case 3 cloud. The scene is composed of 128×128 pixels with $\Delta x = \Delta y = 30m$ horizontal resolution.

Experiment 1: $\mu_o = 1.0$, $\varphi_o = 0°$, $A = 0.0$

As this cloud has a very high resolution small scale structure even for vertical illumination strong 3D effects are expected. Hence, cumulative distributions for both IPA and NIPA show slow increase, see Figure 5.19. NIPA, which has been applied with a 35×35 pixels kernel which is equivalent to $1050m$ edge length, can improve the results with limited success.

(a) Cumulative distributions of ΔT and ΔR for IPA.

(b) Cumulative distributions of ΔT and ΔR for NIPA.
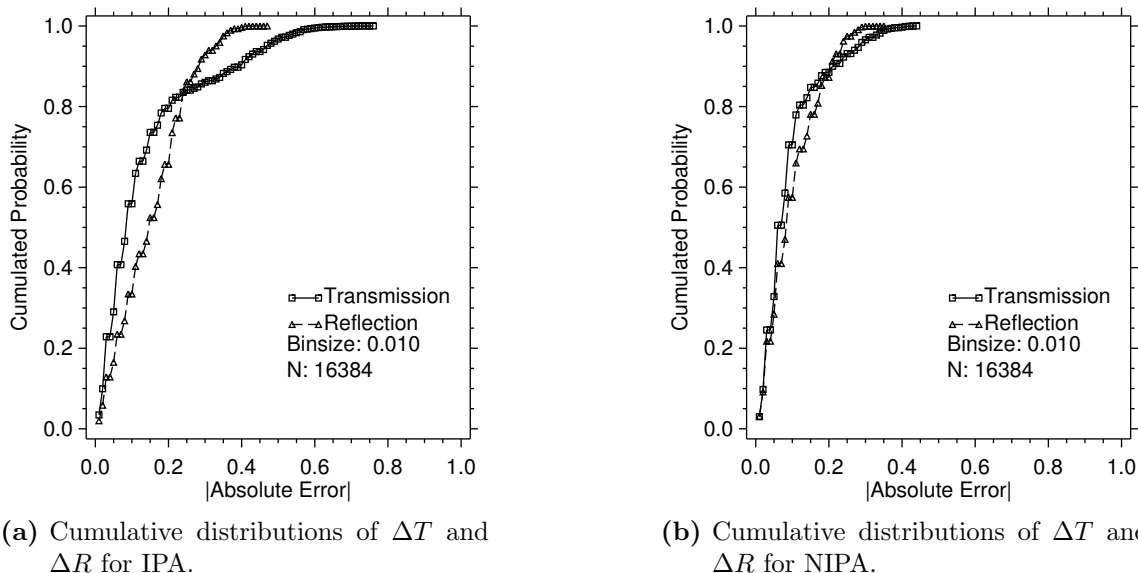
Figure 5.19: Cumulative distributions of ΔT and ΔR for IPA and NIPA for Experiment 1 of the modified I3RC Phase 1 Case 3.

Table 5.15: Comparison of the pixel fractions for a 5% and 10% error threshold of T and R for both IPA and NIPA for Experiment 1 of the modified I3RC Phase 1 Case 3.

Model	$\Delta T \leq 5\%$	$\Delta R \leq 5\%$	$\Delta T \leq 10\%$	$\Delta R \leq 10\%$
IPA	29%	17%	56%	33%
NIPA	33%	28%	70%	57%

Table 5.16: Comparison of the coarse grained moving averages of $|\Delta T|_{max}$ and $|\Delta R|_{max}$ of IPA and NIPA for edge lengths of one, five, 15, and 35 pixels for Experiment 1 of the modified I3RC Phase 1 Case 3 cloud.

Model	$|\Delta T|(1)$	$|\Delta T|(5)$	$|\Delta T|(15)$	$|\Delta T|(35)$
IPA	76%	56%	45%	34%
NIPA	44%	35%	32%	25%
	$|\Delta R|(1)$	$|\Delta R|(5)$	$|\Delta R|(15)$	$|\Delta R|(35)$
IPA	46%	40%	35%	27%
NIPA	35%	29%	26%	23%

However, the technique in this case arrives at a point where a further increase of the convolution kernel is no longer meaningful as no significant improvement is expected, and at the same time the computational burden heavily increases. This is of course also a result of the tremendous number of vertical layers of this example. To quantify the improvement NIPA achieves, the contributions for errors thresholds of 5% and 10% are given in Table 5.15. Differences between IPA and NIPA for the 5% threshold are rather insignificant for transmission and about 10% for reflection while NIPA can gain at least an advantage over IPA of 14% and 24%, respectively in case of the 10% error threshold. However, results become more positive if the maximum residual errors are investigated. This task has been carried out for averaging kernels of one, five, 15, and 35 pixels edge length, see Table 5.16. As smoothing is already inherent in NIPA by means of the convolution kernel, the maximum residual errors decline more slowly than with IPA. Yet, with an averaging kernel of 5pixels $\equiv 150m$ edge length the maximum residual errors of NIPA already nearly match the ones of IPA for the 15pixels $\equiv 1050m$ edge length kernel. However, although tremendous local errors exist, see Table 5.16 for one pixel edge length, the domain averages are underestimated by IPA and NIPA only by two percent.

Experiment 2: $\mu_o = 0.5$, $\varphi_o = 0°$, $A = 0.0$

The slant illumination in this experiment again causes a superposition of pure horizontal diffusion effects and geometric effects. Later in the discussion a brief investigation of the respective impact will be given. In Figure 5.20 the histograms of ΔT and ΔR of IPA, TIPA, NIPA, and NTIPA are shown. TIPA again produces a rather pronounced but quite ragged distribution of errors. Contrary to this, the distribution for NIPA is smoother and has a narrow Gaussian shaped central part but suffers for transmission from larger outliers than IPA. NTIPA clearly shows a mixed characteristic which means that due to the additional convolution the distributions are less ragged, and at least for the transmitted light they do not include large outliers.

This result is confirmed by the error thresholds given in Table 5.17. As in other examples, TIPA generally produces better results for the transmitted light than IPA especially for the 10% error threshold which is a result of the significant number of large outliers of IPA. For reflection TIPA stays at the level of IPA. For NIPA the result is qualitatively vice versa but quantitatively NIPA can still improve the transmitted light by several percent. NTIPA combines these features to some extent meaning that it can even slightly excel TIPA's values for transmission yet fails to match NIPA for the reflected light and only slightly outperforms TIPA in this respect. This is a deterioration of NTIPA's applicability and might be explained with the highly structured cloud top height. As the primary parameterization is TIPA, these structures cause rather large errors, see below, which the succeeding convolution is unable to smooth and diminish any further.
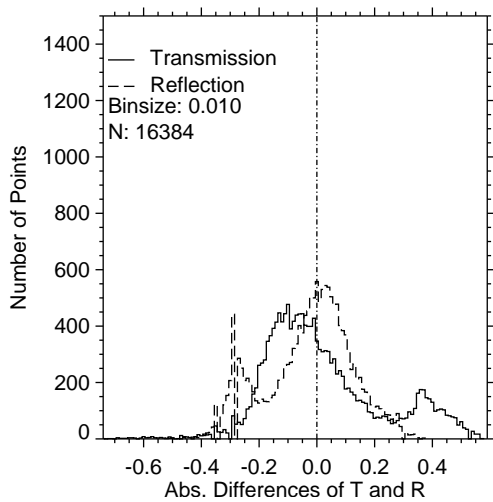
(a) Histogram of ΔT and ΔR of IPA.
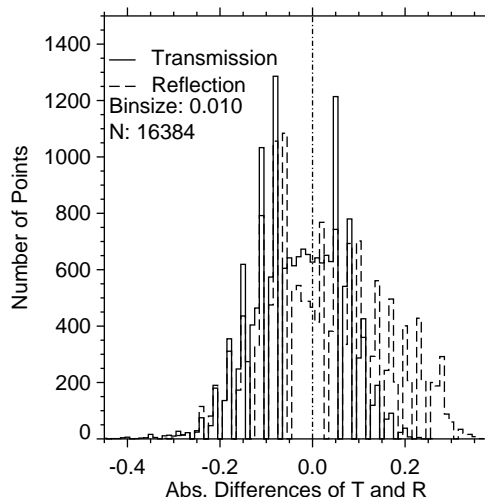
(b) Histogram of ΔT and ΔR of TIPA.
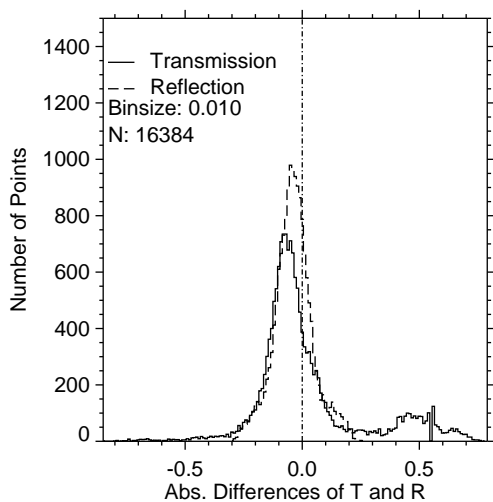
(c) Histogram of ΔT and ΔR of NIPA.
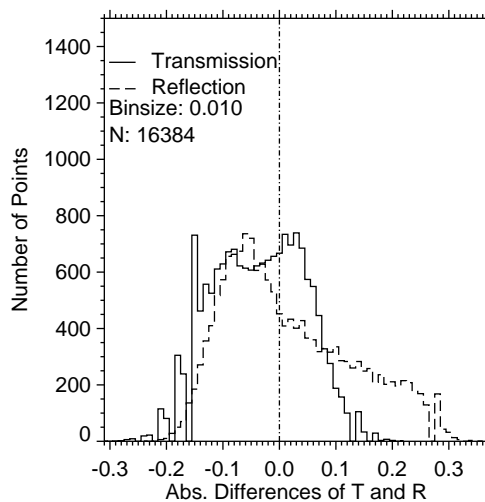
(d) Histogram of ΔT and ΔR of NTIPA.

Figure 5.20: Histograms of ΔT and ΔR of IPA, TIPA, NIPA and NTIPA for the modified I3RC Phase 1 Case 3 Experiment 2.

Concerning the scaling behavior, values of the maximum residual errors for averaging kernels of four different edge lengths are given in Table 5.18. As for the transmitted light, NTIPA produces significantly smaller errors than TIPA without averaging while both result in the same error for 35 pixels edge length of the averaging kernel. The first result might not have been expected judging from the rather small differences indicated in Table 5.17 for the 5% error threshold. The same is true for IPA and TIPA with the reflected light, see Table 5.18. Here, TIPA produces significantly smaller maximum errors for one and five pixels averaging edge length while judging from Table 5.17 both seem to be equal. Similarly, Table 5.17 suggests that NIPA is by far superior to NTIPA with respect to reflection, but Table 5.18 puts this finding into perspective.

Table 5.17: Comparison of the pixel fractions for a 5% and 10% error threshold of T and R for both IPA and NIPA for Experiment 2 of the modified I3RC Phase 1 Case 3.

Model	$\Delta T \leq 5\%$	$\Delta R \leq 5\%$	$\Delta T \leq 10\%$	$\Delta R \leq 10\%$
IPA	21%	28%	42%	52%
TIPA	35%	25%	70%	52%
NIPA	26%	44%	55%	75%
NTIPA	37%	29%	72%	60%

Obviously, for slant illumination a mixture of geometric and diffuse effects exists. When comparing the 2D fields of ΔR for TIPA and NIPA, see Figure 5.21, one notes that the geometric blurring of the former is strong enough to dissolve any distinct structure of the cloud which would have been present in the IPA field. It is also evident that the blurring is directional according to the slant path. Contrary to that, the smoothing exerted by NIPA is omnidirectional as the convolution kernel is symmetric with regard to both horizontal directions. This might be an advantage of TIPA over IPA as the TIPA results seem to be less biased towards the local total optical depth than the ones of IPA in this example. The last conclusion is also supported by Figure 5.22 which shows ΔR and τ as a function of the x-coordinate where the position in y-direction is held constant with y=35.

Table 5.18: Comparison of the coarse grained moving averages of $|\Delta T|_{max}$ and $|\Delta R|_{max}$ of IPA and NIPA for edge lengths of one, five, 14, and 35 pixels for Experiment 2 of the modified I3RC Phase 1 Case 3.

Model	$|\Delta T|(1)$	$|\Delta T|(5)$	$|\Delta T|(15)$	$|\Delta T|(35)$
IPA	74%	62%	44%	34%
TIPA	45%	32%	20%	15%
NIPA	84%	29%	26%	23%
NTIPA	31%	20%	17%	15%
	$|\Delta R|(1)$	$|\Delta R|(5)$	$|\Delta R|(15)$	$|\Delta R|(35)$
IPA	53%	42%	29%	24%
TIPA	38%	31%	29%	26%
NIPA	30%	24%	23%	18%
NTIPA	37%	29%	27%	25%

(a) 2D field of ΔR for TIPA.

(b) 2D field of ΔR for NIPA.
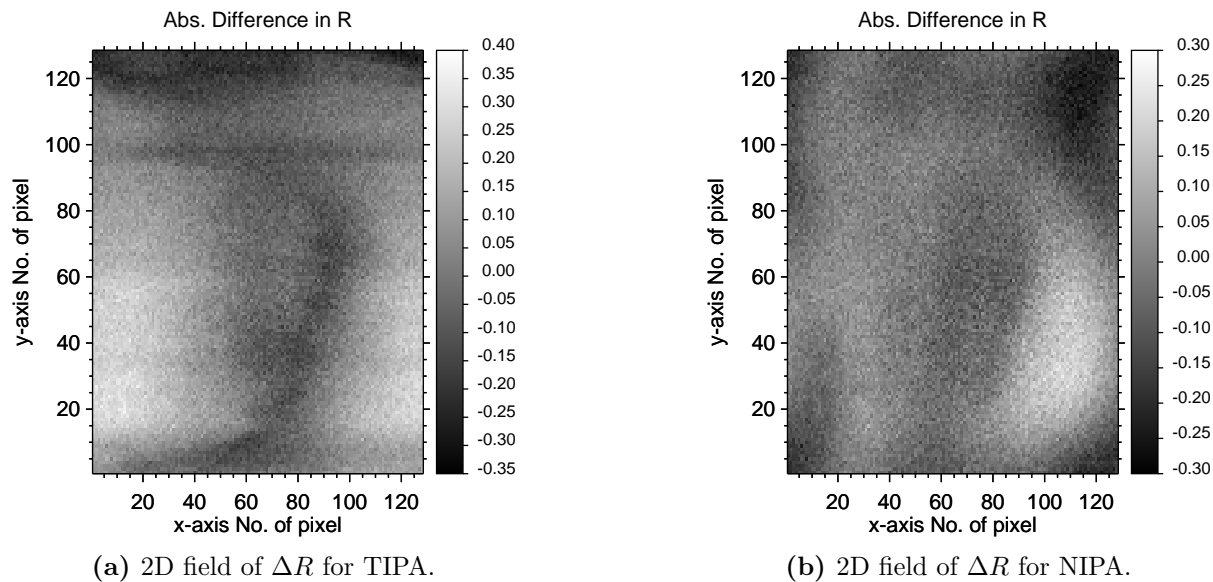
Figure 5.21: 2D fields of ΔR for TIPA and NIPA of Experiment 2 of the modified I3RC Phase 1 Case 3.
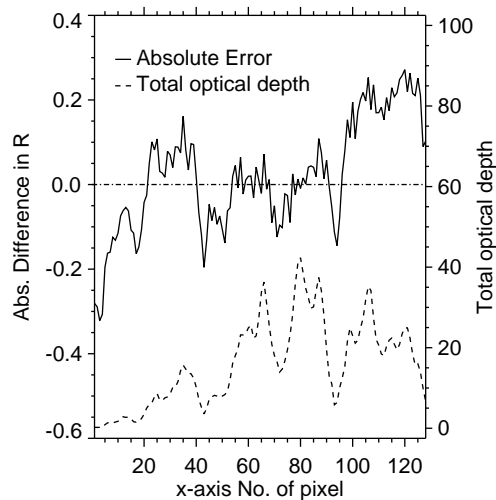
Figure 5.22: Total optical depth and ΔR of IPA as function of the x-coordinate in y=35 for Experiment 2 of the modified I3RC Phase 1 Case 3.

When observing the same feature for TIPA and NIPA, see Figure 5.23, it is easily recognized that the pattern TIPA produces fundamentally differs from the one of NIPA. Although that has been demonstrated numerous times, it is worth mentioning as almost the same structure as for TIPA is yielded by NTIPA, not shown here, meaning that the geometric blurring dominates the diffuse one in case of NTIPA. One has to keep in mind that this conclusion only applies to the chosen approximations in this specific example. The real effects in the cloud might be different and should be investigated in conjunction with a

(a) τ and ΔR for TIPA.

(b) τ and ΔR for NIPA.
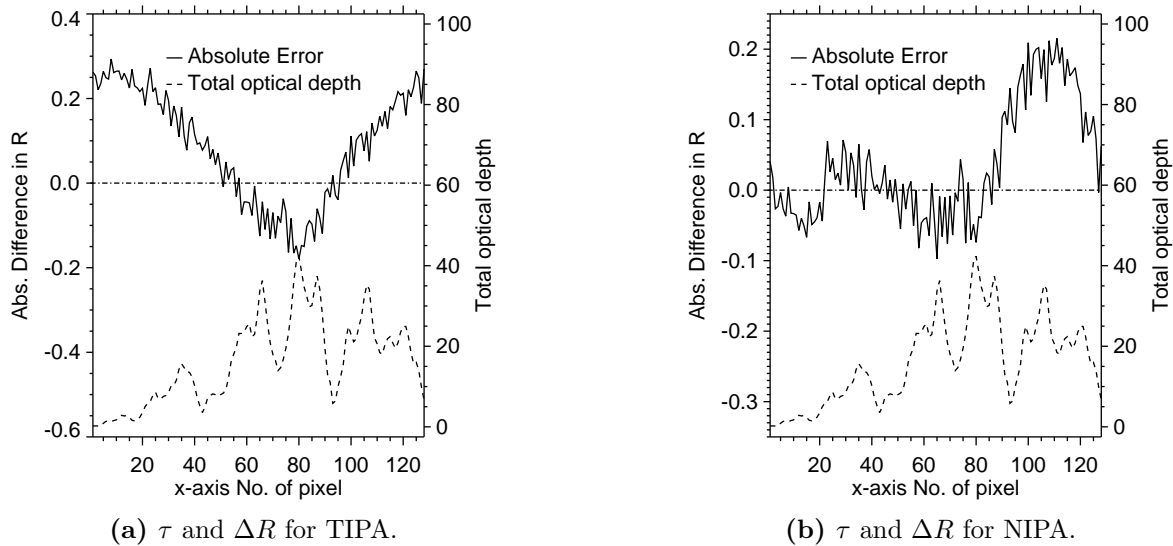
Figure 5.23: Total optical depth and ΔR for TIPA and NIPA as a function of the x-coordinate in y=35 for Experiment 2 of the modified I3RC Phase 1 Case 3.

model realistically treating diffuse horizontal transport. As for the domain averages, no parameterizations stands out, errors are about 3% for all of them.

5.2.2   Medium Resolution Cloud

Example 4: INSPECTRO stratocumulus

The optical properties of this medium resolution cloud have been kindly provided by A. Kniffka and are based on data derived during the INSPECTRO campaign, for details see the INSPECTRO Webpage (2002). This cloud scene is the upper right part of the scene used for the RTPT experiment presented on page 96. The optical properties of the cloud ,which comprise Rayleigh scattering, aerosol scattering and absorption, cloud scattering and absorption, and gaseous absorption of NO_2 and O_3, all characteristic for a wavelength of $550nm$, are defined on $100 \times 50 \times 75$ grid cells. The domain reaches up to $60000m$ and has a horizontal resolution of $200m$. For further details concerning the derivation of the optical properties see page 96. The resulting optical depth is shown in Figure 5.24.
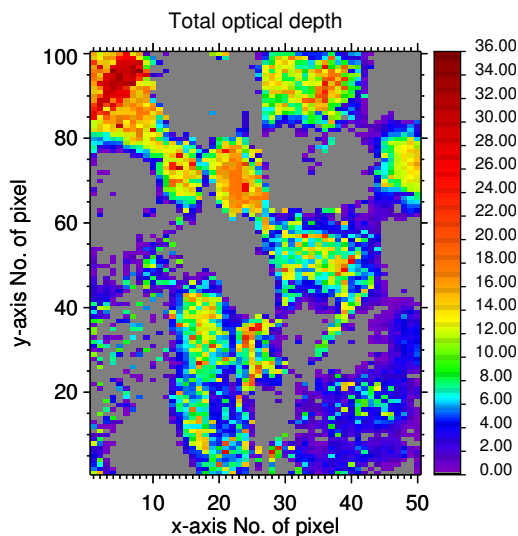
Figure 5.24: Total optical depth of the INSPECTRO Sc cloud. The scene consists of 100×50 pixels with a horizontal resolution of $\Delta x = \Delta y = 200m$.

The cloud field is highly structured and has a mean optical depth of $\langle \tau \rangle = 4.3$ with $\tau_{max} = 34.0$ and $\tau_{min} = 0.141$. In the vertical, the cloud forms a geometrically thin deck located between $1425m$ and $1725m$.

Experiment 1: $\mu_o = 1.0$, $\varphi_o = 0°$, $A = 0.0$

As usual, the investigation is started with the pure diffusion. The histograms for both IPA and NIPA are shown in Figure 5.25. The size of the kernel was set to 25×25 pixels $\equiv 5000m \times 5000m$ due to the increased horizontal resolution. One recognizes a sharp peak at about an error of -0.15 for the reflection of IPA. Although this peak is missing for NIPA, the distributions there show a more bimodal character, and NIPA reduces the maximum and minimum errors of the transmitted light which are nearly cut in half. However, NIPA does not significantly diminish the maximum errors for the reflected light. Yet, although

the peak contributes to the errors of R below 5%, differences between IPA and NIPA are rather larger compared to their counterparts of the transmitted light, see Table 5.19.

(a) Histograms of ΔT and ΔR of IPA.

(b) Histograms of ΔT and ΔR of NIPA.
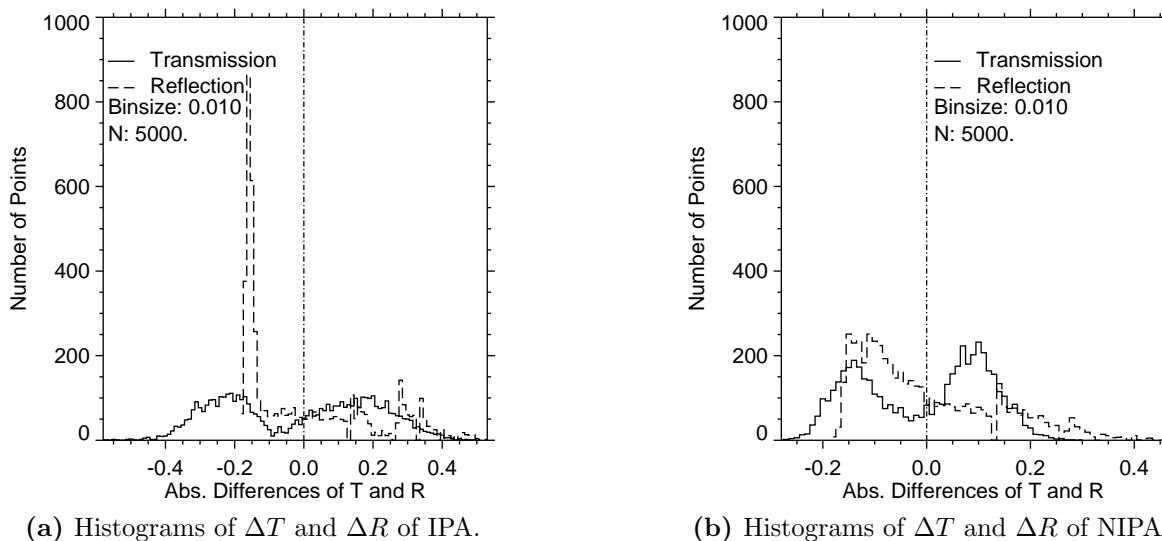
Figure 5.25: Histograms of ΔT and ΔR of IPA and NIPA for Experiment 1 of the IN-SPECTRO cloud.

Table 5.19: Comparison of the pixel fractions for error thresholds of 5%, 10%, 15% and 25% of T and R for both IPA and NIPA for Experiment 1 of the INSPECTRO cloud.

Model	$\Delta T \leq 5\%$	$\Delta T \leq 10\%$	$\Delta T \leq 15\%$	$\Delta T \leq 25\%$
IPA	7%	17%	34%	72%
NIPA	10%	40%	78%	100%
	$\Delta R \leq 5\%$	$\Delta R \leq 10\%$	$\Delta R \leq 15\%$	$\Delta R \leq 25\%$
IPA	11%	22%	67%	84%
NIPA	21%	48%	82%	95%

Regarding the scaling behavior, see Table 5.20, differences are notable, yet not extraordinarily large. However, one has to remark that considerable areas have to be used as averaging kernels to finally yield convergence between IPA and NIPA. The large residual errors of NIPA at this resolution show that it is not able to completely dissolve the primary IPA error structures.

This feature becomes more obvious when comparing ΔT for both IPA and NIPA along the transection in x-direction at y=95, see Figure 5.26. One recognizes in Figure 5.26(a) and Figure 5.26(b) the distinct gradients of the errors which appear in direct vicinity of

gradients of the optical depth. Although in case of NIPA the jumps and drops have reduced magnitudes compared to IPA, a ragged behavior still persists even in the cloud gaps due to the horizontal transport which is unaccounted for by NIPA.

Table 5.20: Comparison of the coarse grained moving averages of $|\Delta T|_{max}$ and $|\Delta R|_{max}$ for edge lengths of 5, 15, and 29 pixels for IPA and NIPA for Experiment 1 of the INSPECTRO cloud.

Model	$|\Delta T|(5)$	$|\Delta T|(15)$	$|\Delta T|(29)$	$|\Delta R|(5)$	$|\Delta R|(15)$	$|\Delta R|(29)$
IPA	30%	17%	5%	49%	25%	10%
NIPA	22%	13%	4%	41%	21%	10%

(a) τ and ΔR for IPA.   (b) τ and ΔR for NIPA.
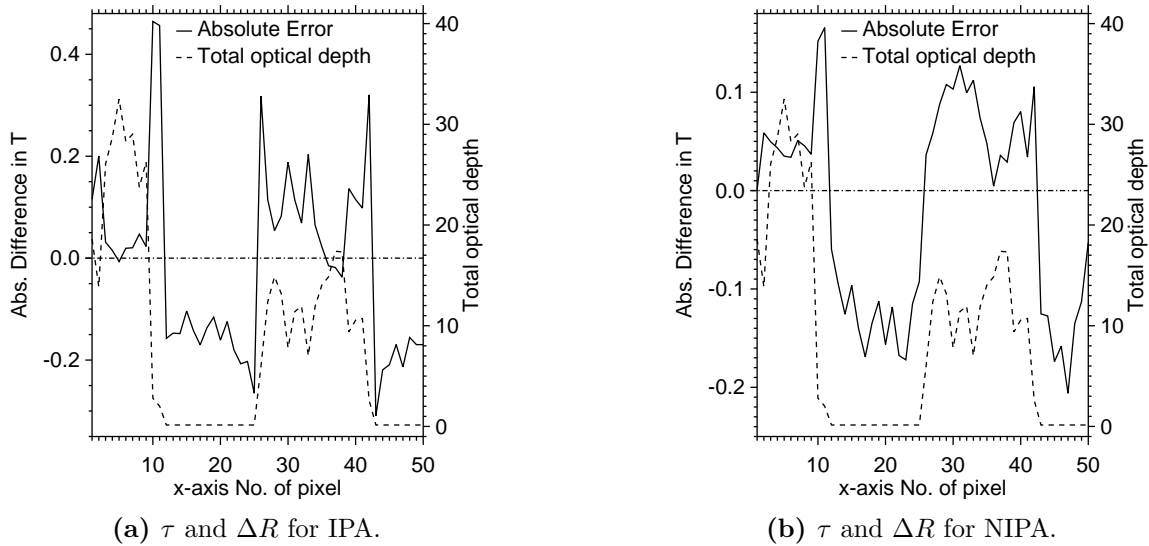
Figure 5.26: Total optical depth and ΔT of IPA and NIPA as a function of x in y=95 for Experiment 1 of the INSPECTRO cloud.

The result can be interpreted as a hint that NIPA loses its ability to smooth out errors if the horizontal resolution is in the range of the smoothing scale and the optical depth has significant horizontal gradients.

Experiment 2: $\mu_o = 0.5$, $\varphi_o = 0°$, $A = 0.0$

Although the vertical structure of this cloud is limited, in this example IPA suffers from the largest errors concerning the transmitted light due to its strong horizontal inhomogeneity. In order to illuminate this feature, the cumulative distributions of ΔT and ΔR for IPA and NTIPA are depicted in Figure 5.27. Similar results are obtained for NIPA and TIPA. NTIPA reduces not so much the maximum errors of the reflected light, these are just

diminished by several percent, but influences more the lower parts of the distribution. Yet, for the transmitted light the improvement is remarkable cutting the maximum error in half. This fact is especially noteworthy as the maximum error of IPA for the transmitted light slightly exceeds unity. This is only possible if at the respective position the local photon balance violates the law of energy conservation as discussed in section 4.1. None of the developed parameterization approaches can adequately simulate such a surplus of photons as all of them are based on 1D approaches and explicitly demand and assure energy conservation even at the local level. However, as stated above, NTIPA at least diminishes the errors to more favorable magnitudes. To quantitatively assess the performance of all four approximations the error thresholds for 5%, 10%, 20%, and 30% percent error are evaluated in Table 5.21.

(a) Cumulative distributions of ΔT and ΔR for IPA.

(b) Cumulative distributions of ΔT and ΔR for NTIPA.
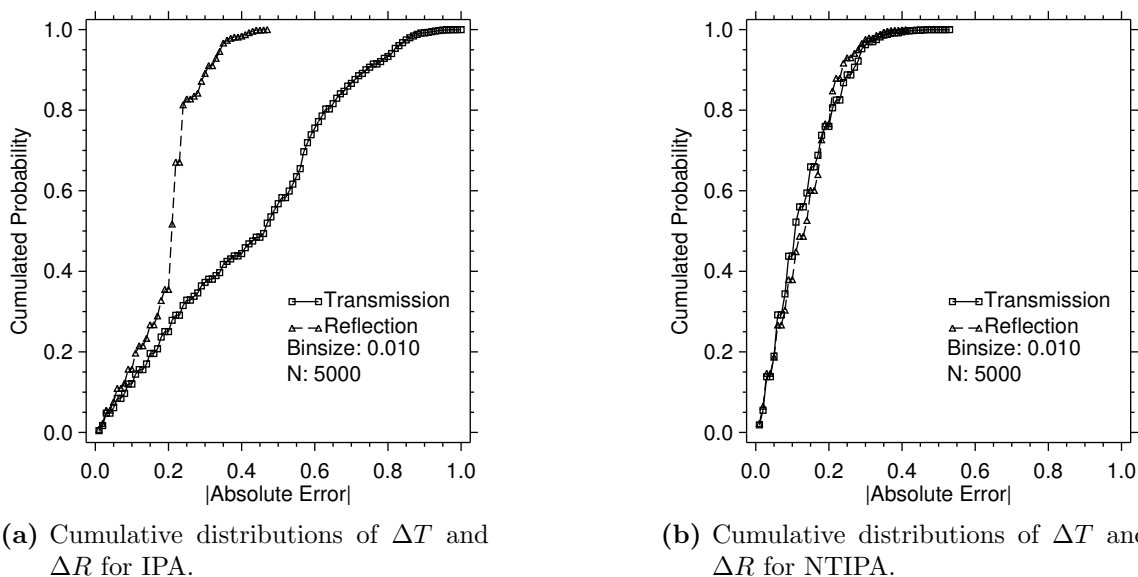
Figure 5.27: Cumulative distributions of ΔT and ΔR of IPA and NTIPA for Experiment 2 of the INSPECTRO cloud.

Obviously, even NTIPA struggles in accounting for the 3D effects. However, it manages to yield results of almost identical quality for both ΔT and ΔR. This is not the case for any of the other three parameterizations. For transmission the pair IPA and NIPA has about the same limitations while NTIPA is enhanced by the horizontal diffusion and therefore yields slightly better results than TIPA. For the reflected light IPA and TIPA can be grouped together while NIPA and NTIPA are almost identically outperforming the former. In general, the reflected light seems to be less crucial and prone to 3D effects than the transmitted light which is as a matter of course heavily affected by geometric effects at this resolution.

These findings are certainly not unexpected, nevertheless it is a) remarkable that very serious errors occur at this scale and with that type of cloud and b) nevertheless the overall performance and relations of the parameterizations are confirmed. The same conclusion is

Table 5.21: Comparison of the pixel fractions for a 5%, 10%, 20% and 30% error threshold of T and R for Experiment 2 of the INSPECTRO cloud for all four approximations.

Model	$\Delta T \leq 5\%$	$\Delta T \leq 10\%$	$\Delta T \leq 20\%$	$\Delta T \leq 30\%$
IPA	6%	12%	25%	37%
TIPA	16%	48%	59%	90%
NIPA	10%	19%	32%	39%
NTIPA	19%	44%	76%	96%
	$\Delta R \leq 5\%$	$\Delta R \leq 10\%$	$\Delta R \leq 20\%$	$\Delta R \leq 30\%$
IPA	8%	16%	36%	90%
TIPA	9%	19%	43%	91%
NIPA	17%	36%	77%	98%
NTIPA	19%	38%	77%	98%

valid for the scaling behavior which is omitted for this reason.

To shed some light on the local features of NTIPA ΔT is plotted as a function of x in y=95, see Figure 5.28. Again, the spatial correlation of cloud gaps coincides with significant variations of the errors in case of IPA. As for NTIPA, several distinct peaks are obvious in the "radiative luff" of the clouds. NTIPA strongly overestimates the exact 3DMC result in these areas. This might be caused by insufficiently modeled horizontal transport which is not able to successfully diminish the downwelling light. Changing the edge length of the convolution kernel has no significant influence on this feature as it is inherent in TIPA, not shown here. One way to alleviate this problem might be a more accurate NIPA, namely a convolution with vertically variable kernel.

To further investigate this feature, the vertical profiles in position (13,95) from the bottom of the atmosphere to $5000m$ of the net flux-density of NTIPA and 3DMC are shown in Figure 5.29(a). NTIPA overestimates only the flux directly at the ground. However, NTIPA quite accurately models the bow of the net flux-density below the cloud, but starts the previously addressed unsteady ragged behavior above cloud top. It has to be noted that this feature, which stems from the discretization errors of the upwelling flux, persists till TOA is reached. The downwelling flux, not shown, does not seem to be affected. Although both effects heavily deteriorate the results of NTIPA, the IPA result is by far more unrealistic leaving an almost vertically constant net flux-density of about $0.43Wm^{-2}$ in this pixel. In Figure 5.29(b) the same profiles are shown for pixel (12,95) demonstrating that the overestimation of the downwelling flux is a spatially limited error which Figure 5.28(b) already suggests.

To conclude the discussion of this example, the domain averages of T and R are given in Table 5.23. IPA and NIPA again yield superior results, even so local values are strongly

erroneous. The reason why TIPA and NTIPA are not able to at least match the accuracy of IPA remains unclear.

**(a)** τ and ΔR for IPA.

(b) τ and ΔR for NTIPA.
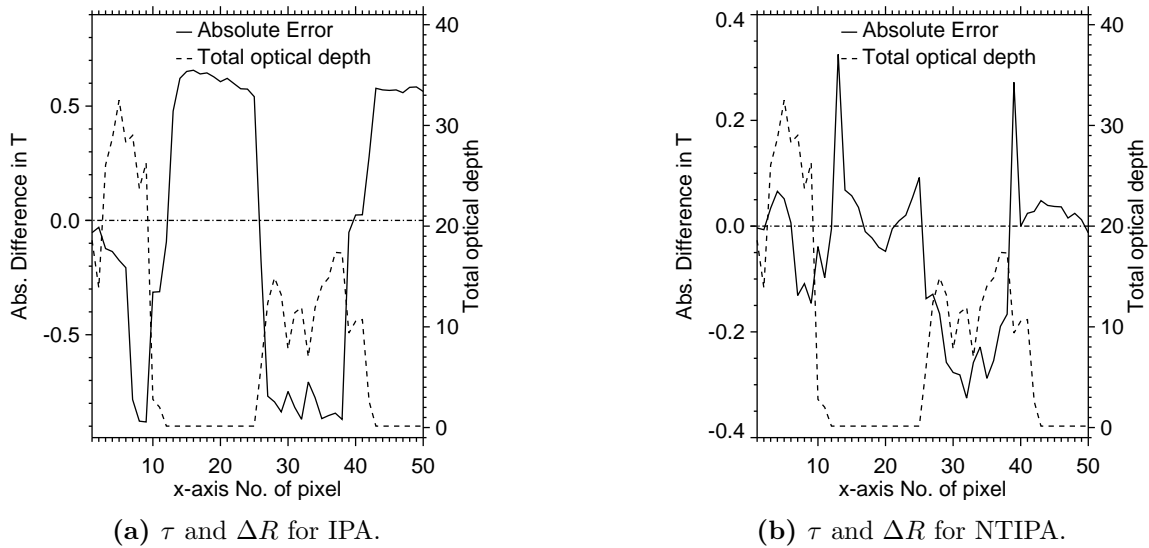
Figure 5.28: Total optical depth and ΔT of IPA and NTIPA as a function of x in y=95 for Experiment 2 of the INSPECTRO cloud.

(a) Profile of the net flux-density in pixel (13,95).

(b) Profile of the net flux-density in pixel (12,95).
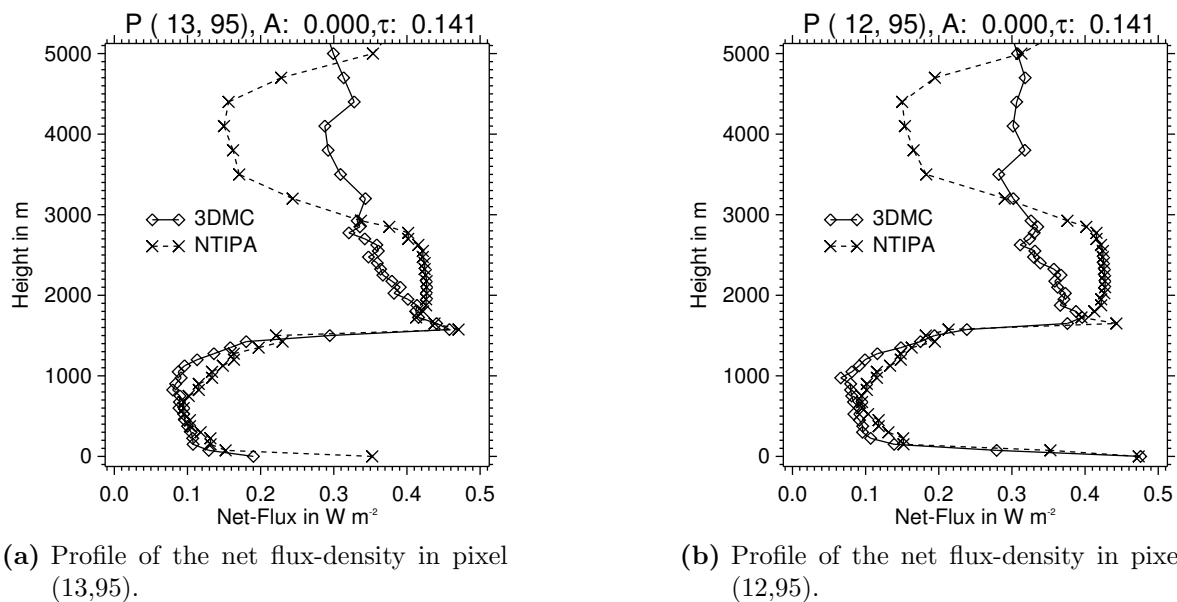
Figure 5.29: Vertical profiles of the net flux-density of 3DMC and NTIPA in pixels (13,95) and (12,95), both with $\tau = 0.141$, of Experiment 2 of the INSPECTRO cloud.

Experiment 3: $\mu_o = 0.5$, $\varphi_o = 0°$, $A = 0.1$

In this example a surface albedo of 10% is applied. All other parameters remain unchanged. The error thresholds for five, ten, 20, and 30 percent error are given in Table 5.22. Generally speaking, results and conclusions concerning this feature are maintained if compared to Experiment 2. However, TIPA shows some mixed characteristic which can be observed in the values for $T(10\%)$ and $R(20\%)$ where the former is worse and the latter better than in Experiment 2.

Table 5.22: Comparison of the pixel fractions for a 5%, 10%, 20% and 30% error threshold of T and R for Experiment 3 of the INSPECTRO cloud for all four approximations.

Model	$\Delta T \leq 5\%$	$\Delta T \leq 10\%$	$\Delta T \leq 20\%$	$\Delta T \leq 30\%$
IPA	6%	12%	25%	37%
TIPA	16%	32%	58%	88%
NIPA	10%	19%	32%	40%
NTIPA	19%	43%	74%	95%
	$\Delta R \leq 5\%$	$\Delta R \leq 10\%$	$\Delta R \leq 20\%$	$\Delta R \leq 30\%$
IPA	7%	15%	40%	87%
TIPA	10%	21%	64%	94%
NIPA	15%	31%	67%	95%
NTIPA	16%	42%	84%	98%

As for domain averages, see Table 5.23, the relationships of Experiment 2 are qualitatively maintained. Conclusively it can be said this experiment supports the results of Example 3 on page 114, and TIPA and NTIPA yield meaningful results.

Table 5.23: Domain averaged results for Experiment 2 and 3 of the INSPECTRO cloud for all models.

	Experiment 2		Experiment 3	
Model	$\bar{T}$	$\bar{R}$	$\bar{T}$	$\bar{R}$
3DMC	0.625	0.309	0.645	0.286
IPA and NIPA	0.628	0.306	0.642	0.289
TIPA and NTIPA	0.614	0.319	0.629	0.301

5.2.3 Coarse Resolution Clouds

Example 5: DAQUA cloud

The data of this cloud field was kindly provided by F. Ament, University of Bonn, and has been generated during the DAQUA project. This project aims at the improvement of short range quantitative precipitation forecasting with high resolution weather prediction models, see DAQUA Webpage (2004). As a result, output from a number of model runs of the LM featuring several distinct convective cloud structures were made available to the author. One of those was chosen for the presented example. The generation of the optical properties from the provided thermodynamic quantities during an offline calculation of the 2-stream module is described in section 2.4 on page 26.

To limit the computational time of the simulation, only a section of the original cloud field was used. It comprises $171 \times 101 \times 35$ cells with a horizontal resolution of $2.8km$. The 2D field of the total optical depth for this case is depicted in Figure 5.30. A wide spectrum of optical depths is covered reaching from $\tau_{min} = 0.086$ to $\tau_{max} = 179.8$ with $\langle \tau \rangle = 14.85$. Particularly remarkable are the isolated spots of extreme optical depths and the relatively large areas of low to intermediate optical depths. As a matter of course, both are closely related to the method the LM uses for the derivation of clouds from thermodynamic properties. The model explicitely forecasts cloud liquid water. In the cells where this is the case, it is assumed that the cloud completely occupies the cell meaning that the partial cloud cover is 100% which in turn leads to the maximum values of the optical depth.
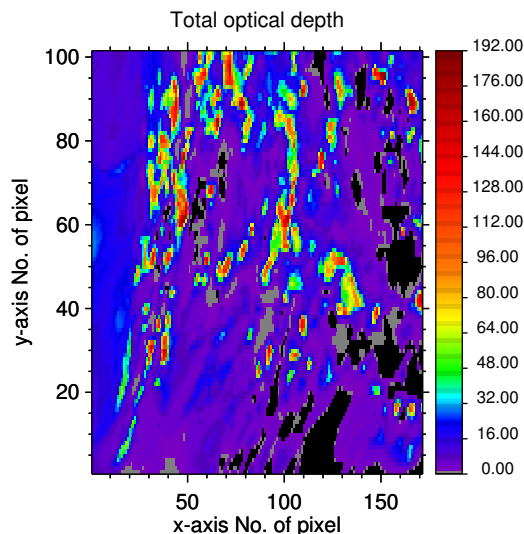
Figure 5.30: Total optical depth of the DAQUA cloud with 171×101 pixels and $\Delta x = \Delta y = 2800m$ horizontal resolution.

In all other cells where no cloud liquid water is explicitly predicted the cloud optical properties are derived by a parameterization scheme which uses the current relative humidity,

the vertical velocity, and other thermodynamic properties to arrive at a partial cloud cover, a subgrid cloud liquid water content, and subsequently a cloud optical depth.

Experiment 1: $\mu_o = 1.0$, $\varphi_o = 0°$, $A = 0.0$

Although the horizontal resolution is $2800m$ for overhead sun, 3D effects exist as can be gathered from Figure 5.31. The reflected light computed by IPA is more affected by 3D errors than the transmitted light. However, NIPA calculations cannot be employed as only the IPA results are regained. This can be understood by the fact that even the smallest kernel, 3×3 pixels $\equiv 8.4km \times 8.4km$, is already that large that the Gaussian distributions, see equation 4.6 and Figure 4.17, have declined to a value at the edges of the center pixel which is numerically zero. As a result, the center pixel is assigned with the weight of approximately one which makes NIPA reproduce the IPA results.
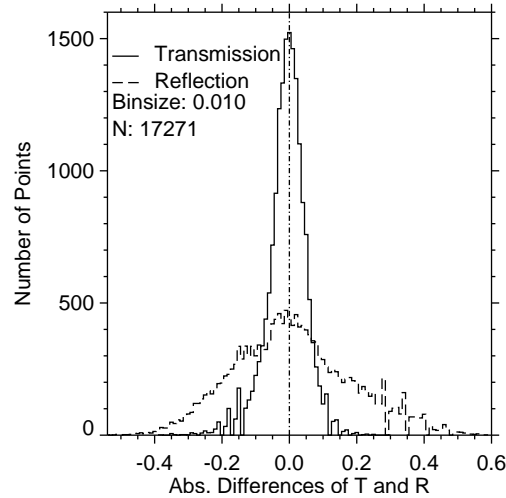
Figure 5.31: Histograms of ΔT and ΔR of IPA for Experiment 1 of the DAQUA cloud.

In order to parameterize horizontal diffuse transport effects different techniques seem to be necessary in order to associate the pixels with sub scale information which might be used to approximate horizontal transport across cell boundaries.

Figure 5.32 depicts the scaling behavior of the maximum and minimum residual errors of R and T of IPA for different sizes of averaging kernels. One can observe a rapid decline with increasing edge length of the averaging kernel for both $|\Delta R|_{max}$ and $|\Delta T|_{max}$. However, the steep slope is followed by a very slow decline for large edge lengths. While this seems to be reasonable, interestingly the residual errors associated with this slow decline still mount up to several percent. For example, $|\Delta R|_{max}(s = 53.2km) = 0.148$ and $|\Delta T|_{max}(s = 53.2km) = 0.027$.

These maximum errors especially for the reflected light are certainly remarkable. It has to be noted that a total of $1.0 \cdot 10^7$ photons was used for the 3DMC calculation. Judging from the domain averages, see Table 5.27, the results fit very well with errors of less than one percent. However, it can be argued whether the number of photons employed is sufficient.

To this end, the data was compared with another 3DMC simulation with $1.3 \cdot 10^8$ photons. The results of the individual pixels of course change, yet $|\Delta R|_{max}(s = 53.2km) = 0.145$ and $|\Delta T|_{max}(s = 53.2km) = 0.024$ remain almost the same. The relatively large error of ΔR_{max} for large averaging kernels seems to hint at a physical explanation of the phenomenon rather than at a numerical one.

(a) Scaling behavior of $|\Delta T|_{max,min}$ as a function of edge length.

(b) Scaling behavior of $|\Delta R|_{max,min}$ as a function of edge length.
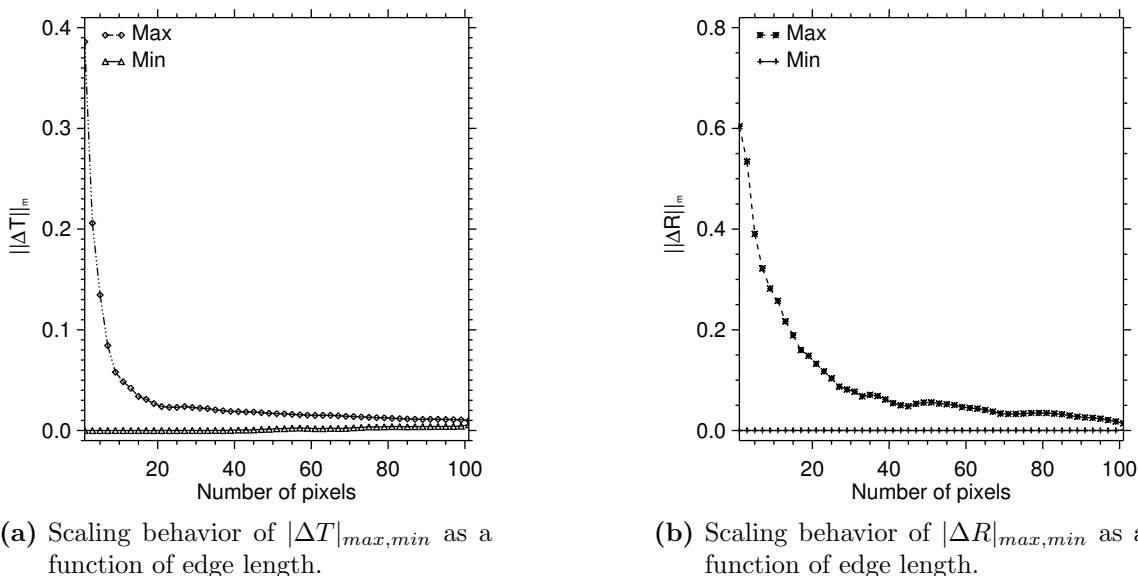
Figure 5.32: Coarse grained moving averages of $|\Delta T|_{max,min}$ and $|\Delta R|_{max,min}$ as functions of edge length of the averaging area for Experiment 1 of the DAQUA cloud. For the 3DMC a total number of $1.0 \cdot 10^7$ photons was used.

As a result, it must be assumed that the transmitted light is affected by 3D effects to a minor extent while the reflected light is strongly affected. To further investigate this phenomenon as a second experiment the solar zenith angle is set to $\mu_o = 0.5$ which makes is possible to employ TIPA and IPA.

Experiment 2: $\mu_o = 0.5$, $\varphi_o = 0°$, $A = 0.0$

The slant illumination of the cloud scene in this experiment leads to large errors in several pixels for the transmitted light computed by IPA, see Figure 5.33(a). Maximum and minimum errors for the transmitted light are -1.26 and 0.74. Errors larger than unity again stem from a local photon gain due to 3D effects. This results in a surplus of downwelling radiation compared to the incoming radiation at the top of the domain which is the IPA unable to account for. However, both distributions for ΔT and ΔR have Gaussian shape and are centered around zero. TIPA significantly reduces the errors of the transmitted light, see Figure 5.33(b). Maximum errors of the reflected light deteriorate while the peaked Gaussian shape of the distribution is only maintained for the transmitted light. TIPA returns for the reflected light a wider and far less pronounced and centered distribution.

(a) Histograms of ΔT and ΔR of IPA.

(b) Histograms of ΔT and ΔR of TIPA.
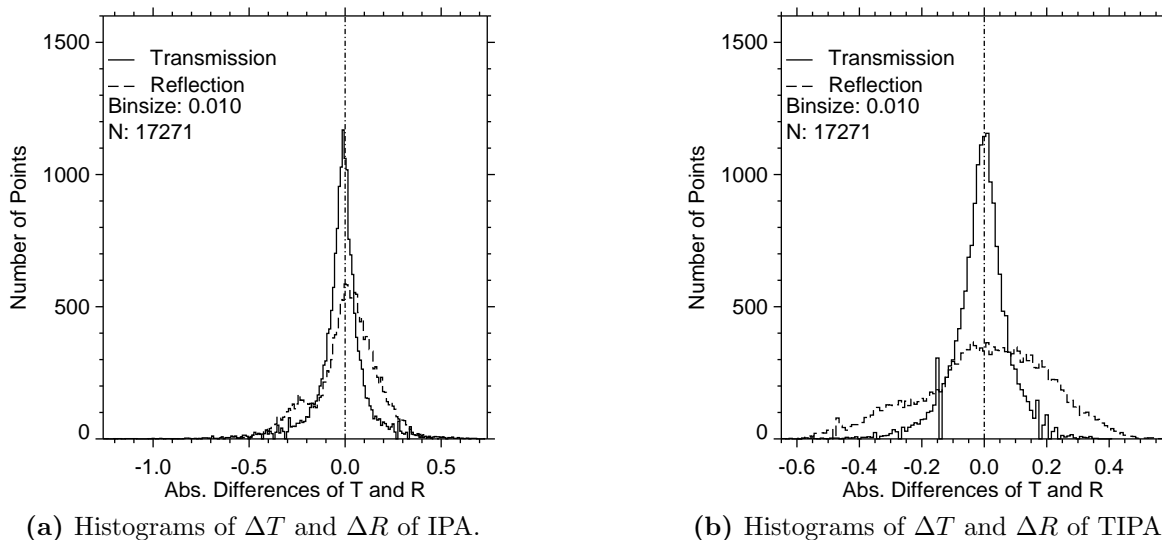
Figure 5.33: Histograms of ΔT and ΔR of IPA and TIPA for Experiment 2 of the DAQUA cloud.

Both aforementioned features result in the values for the error thresholds of five, ten, and 20 percent presented by Table 5.24. TIPA can only improve the transmitted light by several percent, the large outliers of IPA mainly contribute to errors beyond 20%, but TIPA also falls significantly back behind IPA for the reflected light. Moreover, although the errors of the transmitted light are by far larger than the ones for the reflected light, the area associated with significant errors of the latter outnumbers the one of the former. This result might not have been obvious from the pure investigation of the histograms.

Table 5.24: Comparison of the pixel fractions for a 5%, 10% and 20% error threshold of T and R for Experiment 2 of the DAQUA cloud for IPA and TIPA.

Model	$\Delta T \leq 5\%$	$\Delta T \leq 10\%$	$\Delta T \leq 20\%$
IPA	47%	72%	89%
TIPA	50%	77%	95%
	$\Delta R \leq 5\%$	$\Delta R \leq 10\%$	$\Delta R \leq 20\%$
IPA	27%	50%	77%
TIPA	18%	36%	65%

Similar to Experiment 1 even for large averaging kernels significant differences prevail between 3DMC and IPA, respectively TIPA. The relevant information has been compiled in Table 5.25 for an edge length of one, five, and 19 pixels. The large errors for transmission have already been briefly addressed. TIPA can cut them roughly in half, and this ratio

persists for the shown averaging kernels. For the reflected light the un-averaged maximum residual errors are about the same for IPA and TIPA while for all other averaging kernels IPA can achieve an advantage of 10%. Both values of $|\Delta T|_{max}$ and $|\Delta R|_{max}$ for IPA and TIPA suggest as in Experiment 1 a remaining non-statistical error associated with the residual 3D effect. In order to further explore its relation with the cloud field, the dependence of the locations of the errors on the geometrical height of cloud base and top are briefly investigated.

Table 5.25: Comparison of the coarse grained moving averages of $|\Delta T|_{max}$ and $|\Delta R|_{max}$ for edge lengths of one, five, and 19 pixels of IPA and TIPA for Experiment 2 of the DAQUA cloud.

Model	$|\Delta T|(1)$	$|\Delta T|(5)$	$|\Delta T|(19)$	$|\Delta R|(1)$	$|\Delta R|(5)$	$|\Delta R|(19)$
IPA	126%	41%	12%	57%	39%	16%
TIPA	65%	22%	7%	60%	49%	27%

(a) Cloud top height of the DAQUA cloud.

(b) 2D field of ΔR of IPA for Experiment 2 of the DAQUA cloud.
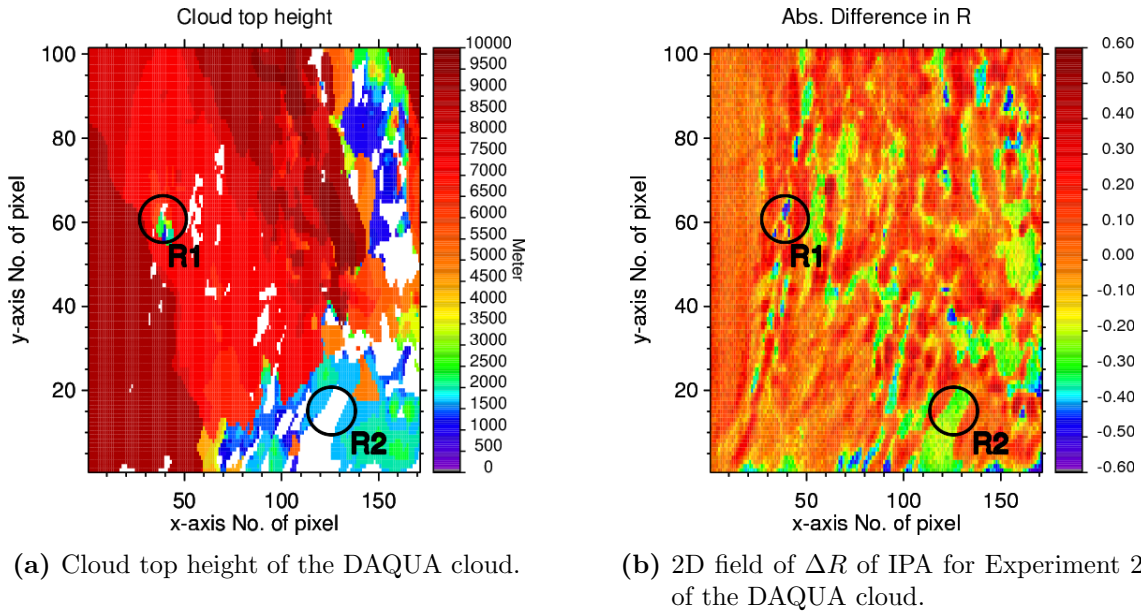
Figure 5.34: Cloud top height and ΔR of IPA for Experiment 2 of the DAQUA cloud. The criteria for an encounter of cloud matter was $g > 0.8$, $\omega_o > 0.95$ and $\tau > 0.9$. For the optical depth see also Figure 5.30.

In Figure 5.34(a) and 5.35(a) the 2D fields of the lowest cloud bases and the highest cloud tops are depicted. To deduce this information, it was assumed that a cloud is encountered in a cell if the asymmetry factor is larger than 0.8, the single scattering albedo is larger than 0.95, and the pixel under consideration has an optical depth in excess of 0.9. One

recognizes, for both the cloud base and cloud top, a rather inhomogeneous structure where clear sky areas, low and high clouds alternate in close vicinity. It has to be noted that the difference between both figures does not necessarily yield the cloud geometric thickness as only the first and the last encounter of clouds in the vertical has been counted according to the aforementioned criteria, and the vertical space between lowest cloud base and highest cloud top is not necessarily completely filled with cloud matter.

(a) Cloud base height of the DAQUA cloud.

(b) 2D field of ΔT of IPA for Experiment 2 of the DAQUA cloud.
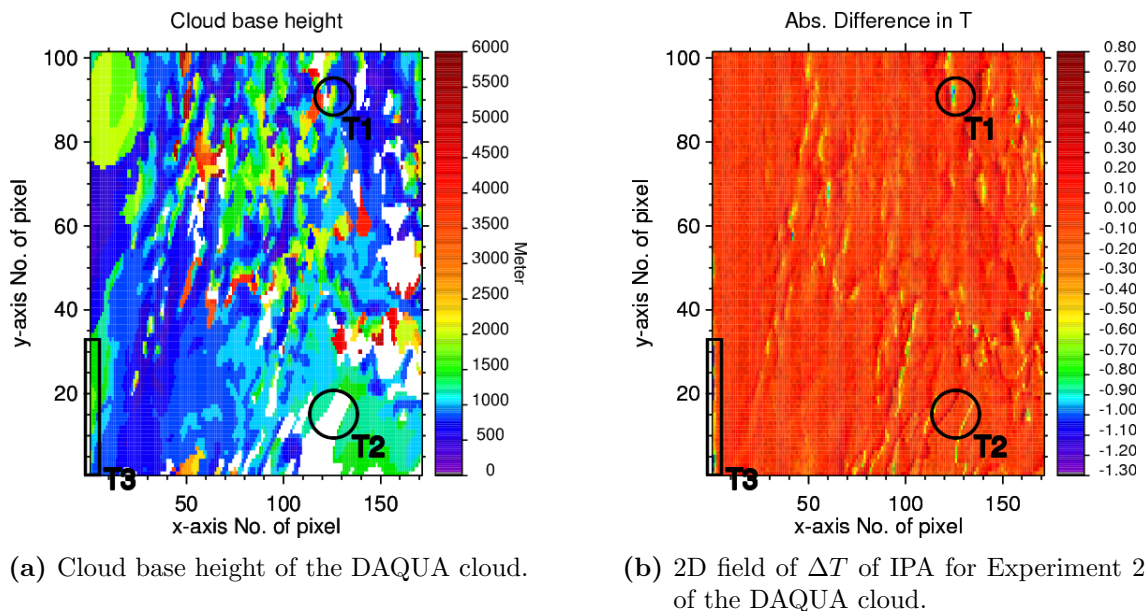
Figure 5.35: Cloud base height and ΔT of IPA for Experiment 2 of the DAQUA cloud. Criteria as for Figure 5.34. See also Figure 5.30.

Nevertheless, some interesting features are worth mentioning. Maximum errors of the reflected light occur in regions of transitions between clear sky areas and cloudy pixels, as well as in regions of disrupted cloud top heights. One example for this feature has been marked with "**R1**" in both Figure 5.34(a) and 5.34(b). Furthermore, large errors are assigned with variations of the cloud top height ranging from several hundreds of meters to several thousand meters and within small clear sky areas. The larger clear sky areas, see area "**R2**", are less erroneous as these seem to act as plan-parallel areas themselves and large errors occur predominantly at the fringes.

As for the transmitted light, the error patterns are less pronounced and large errors occupy only a small number of pixels, see Figure 5.35(b). The explanation of this characteristic is analogous to the one given for the reflected light. The area marked with "**T1**" features some pixels of very large errors. These can be connected with variations of the cloud base height of several thousand meters, see Figure 5.35(a). Large clear sky areas are less affected by errors compared to the reflected light but also have a small fringe of larger errors, see area "**T2**". Maximum errors occur in region "**T3**". Although located directly at the boundary and thus being artificial, this area gives a good example as cloud base

heights vary significantly due to the periodic boundary conditions. Similar features and characteristics can be found for TIPA. By comparing Figure 5.35(a) and 5.34(a), it is also evident that in the regions discussed the variations of cloud top and cloud base height are correlated to a certain degree. As a result, at least for the transmitted light a superposition of the influences of both is likely.

Table 5.26: Vertical coordinate for the DAQUA cloud.

Level	Height in m	Level	Height in m	Level	Height in m	Level	Height in m
1	0.0	11	1461.85	21	5566.94	31	13630.05
2	67.71	12	1719.99	22	6147.36	32	14977.85
3	153.02	13	2016.33	23	6768.02	33	16567.65
4	256.36	14	2354.33	24	7435.49	34	18464.05
5	378.33	15	2727.09	25	8158.13	35	20782.75
6	519.59	16	3126.76	26	8924.55	36	23590.75
7	680.99	17	3556.36	27	9717.9		
8	854.29	18	4019.46	28	10567.25		
9	1040.1	19	4506.87	29	11484.25		
10	1239.11	20	5021.53	30	12484.25		

The reason for the strong and abrupt variations of both cloud base and more significantly cloud top might be not so much a true physical variation but could also stem from the structure of the LM's coordinate system. One can gather from Table 5.26, which shows the vertical coordinate for the presented example, that at low levels the z-increments are rather small but later, above $3000m$, quickly increase to several hundreds of meters. Thus, in vertical regions where predominantly the cloud tops of vertically extended clouds are located a variation of the cloud top of one vertical index is assigned to a local depression or curvature of the cloud. Hence, an increased number of coordinate levels or even an adaptive scheme might be desirable but difficult to implement.

During the explanation of the derivation of the cloud optical properties in section 2.4, it has been mentioned that explicit cloud ice has been neglected due to technical difficulties and that the exact synoptic situation has only little relevance for these case studies. However, although explicit cloud ice is not included, implicit cloud ice is generated by the RT module due to a parameterization scheme involving the partial cloud cover, see above. This implicit cloud ice is responsible for the very high cloud tops. One can argue that the inconsistent treatment of the cloud ice makes it difficult to interpret the above mentioned structures. Yet, the 2D fields of the total cloud cover which are directly deduced from the original model output and thus unaffected by the inconsistent treatment, show the same patterns of variations as for example in area "**R1**". This finding implies that neglecting the explicit cloud ice does not significantly alter the results and conclusions in this respect.

To finish this experiment in Table 5.27 the domain averaged results are given. For both approximations errors slightly exceed one percent with TIPA being insignificantly more precise.

Table 5.27: Domain averaged results for Experiment 1 and 2 of the DAQUA cloud for all models. For Experiment 1 TIPA was not applicable.

	Experiment 1		Experiment 2	
Model	$\bar{T}$	$\bar{R}$	$\bar{T}$	$\bar{R}$
3DMC	0.570	0.393	0.427	0.535
IPA	0.562	0.401	0.415	0.547
TIPA	–	–	0.416	0.546

Example 6: QUEST cloud

In order to confirm the results of the DAQUA cloud another coarse resolution cloud has been investigated. This cloud was deduced in the same manner as the DAQUA cloud, yet the original data was generated within the project QUEST. This project focuses on the quantitative assessment of precipitation forecasts using remote sensing observations, see QUEST Webpage (2005). The generated LM data has been kindly provided by Nicole van Lipzig from the University of Leuven, then at the University of Munich, and features like the previous example a mixture of stratified and convective cloud structures.
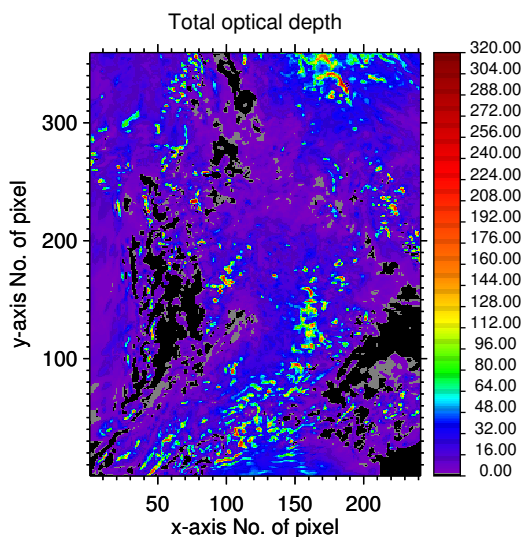
Figure 5.36: Total optical depth of the QUEST cloud. The domain is 241×259 pixels large with $\Delta x = \Delta y = 2800m$.

Just as Example 5, the data actually used is only a subset of the full model domain but still consists of $241 \times 259 \times 35$ grid cells with a horizontal resolution of $2.8km$. In Figure 5.36 the 2D field of the total optical depth is depicted. It contains some speckled areas of even larger optical depth than in the previous example. It has $\tau_{max} = 317.6$, $\tau_{min} = 0.062$ and $\langle \tau \rangle = 18.3$.

Experiment 1: $\mu_o = 1.0$, $\varphi_o = 0°$, $A = 0.0$

As in previous examples, even for overhead sun significant 3D effects exist which is shown by the histograms in Figure 5.37. Although ΔT is again more nicely Gauss-shaped than ΔR, maximum errors of the transmitted light have indeed risen compared to Experiment 1 of the DAQUA cloud. With absolute values of $|\Delta T|_{max} = 0.6$ and $|\Delta R|_{max} = 0.65$, both are now of about the same magnitude.

Table 5.28 again shows the pixel fraction for error thresholds of five, ten, and 20 percent. The pixels associated with transmission errors exceeding 20% are singular and far less numerous than the errors of the reflected light. This was already implicitly contained in
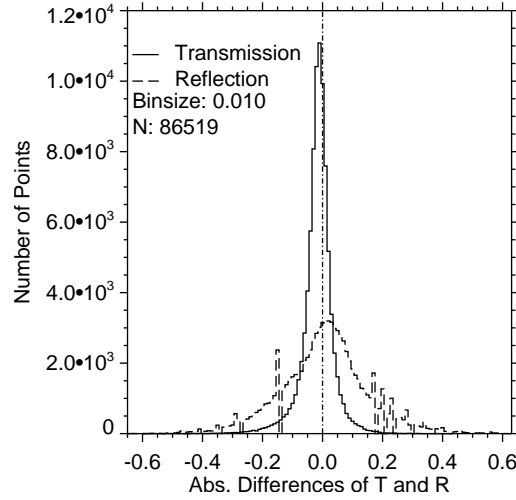
Figure 5.37: Histograms of ΔT and ΔR of IPA for Experiment 1 of the QUEST cloud.

the histograms. Concerning the scaling behavior, previous results are again confirmed. Table 5.28 also lists the maximum residual errors of both transmission and reflection for averaging edge lengths of one, five, and 19 pixels. As before, the maximum residual errors decay for the transmitted light by far faster than for the reflected light. A discussion of the heights of cloud top and cloud base leading to these effects is postponed to Experiment 2, yet individual pixels are investigated by means of Figure 5.38. There the individual results of 3DMC and IPA are plotted together. From Figure 5.38(a) it is obvious that the large errors of T do not result from an extremely large spread of the values but rather from some very large outliers where even for overhead sun a transmission in excess of 1.0 is reached while IPA gets only close to 1.0. Opposed to that the reflected light seems to be that strongly affected by 3D effects that almost for any increment of exact 3D values the whole range of (wrong) IPA results is returned. The 3DMC calculation employed $1.3 \cdot 10^8$ photons which leads again to marginal domain averaged errors of less than one percent, see Table 5.30.

Table 5.28: Comparison of the pixel fractions for a 5%, 10% and 20% error threshold of T and R (upper part) and coarse grained moving averages of $|\Delta T|_{max}$ and $|\Delta R|_{max}$ for edge lengths of one, five, and 19 pixels (lower part) for Experiment 1 of the QUEST cloud for IPA.

$\Delta T \leq 5\%$	$\Delta T \leq 10\%$	$\Delta T \leq 20\%$	$\Delta R \leq 5\%$	$\Delta R \leq 10\%$	$\Delta R \leq 20\%$
76%	93%	99%	31%	56%	84%
$|\Delta T|(1)$	$|\Delta T|(5)$	$|\Delta T|(19)$	$|\Delta R|(1)$	$|\Delta R|(5)$	$|\Delta R|(19)$
60%	13%	3%	65%	43%	16%

(a) Comparison of transmission values of IPA with 3DMC.

(b) Comparison of reflection values of IPA with 3DMC.
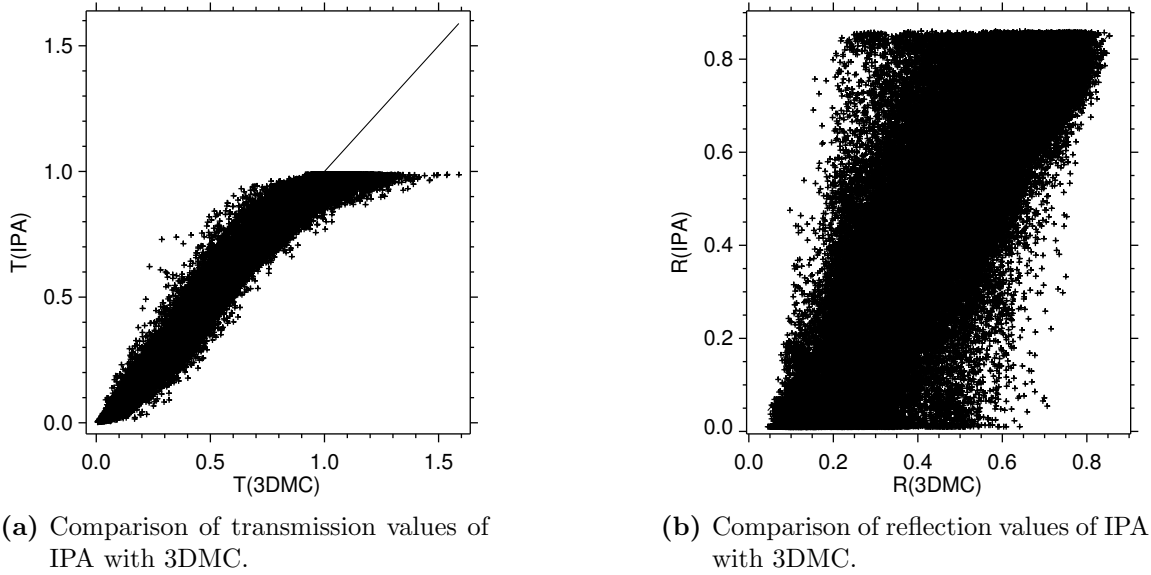
Figure 5.38: Comparison of transmission and reflection values of IPA with 3DMC for Experiment 1 of the QUEST cloud.

Experiment 2: $\mu_o = 0.5$, $\varphi_o = 0°$, $A = 0.0$

The transmitted light calculated by IPA is again affected by very large errors exceeding 1.0 by far while TIPA still suffers from significant errors yet successfully eliminates the very large outliers of IPA, see Figure 5.39. As before, the distributions of TIPA are less peaked than the ones of IPA and in case of the reflected light also contain larger errors.

(a) Histograms of ΔT and ΔR of IPA.

(b) Histograms of ΔT and ΔR of TIPA.
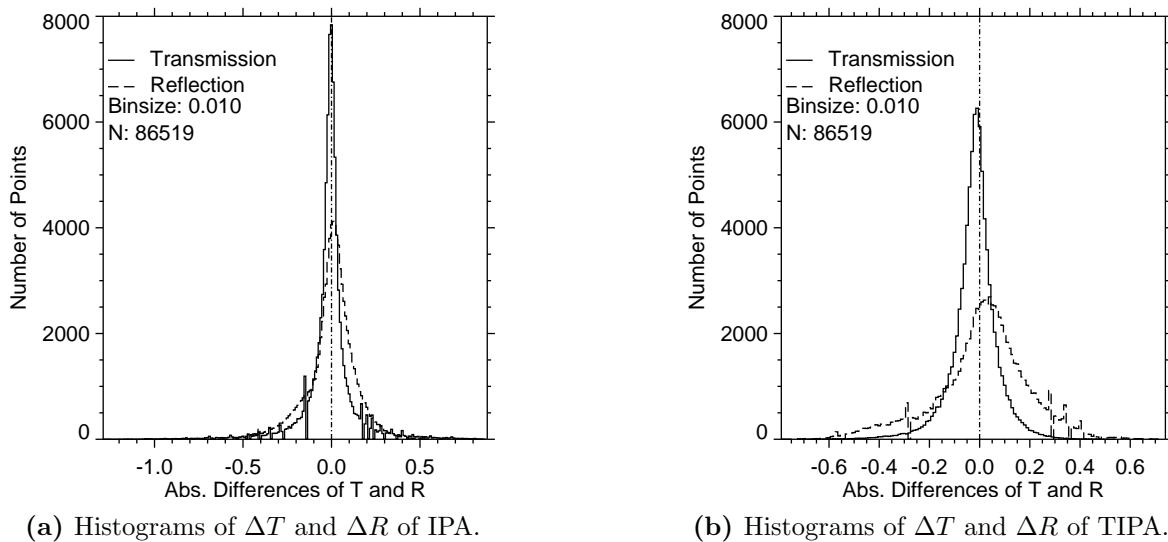
Figure 5.39: Histograms of ΔT and ΔR of IPA and TIPA for Experiment 2 of the QUEST cloud.

Table 5.29 demonstrates that TIPA can gain only an advantage of several percent with regard to the transmitted light for the error thresholds of 10% and 20%. For the reflected light previous impressions are confirmed. TIPA fails to match IPA which in turn is not able to deliver satisfactory results as large portions of the domain are affected by errors over 10%.

Table 5.29: Comparison of the pixel fractions for a 5%, 10% and 20% error threshold of T and R (upper part) and coarse grained moving averages of $|\Delta T|_{max}$ and $|\Delta R|_{max}$ for edge lengths of one, five, and 19 pixels (lower part) for Experiment 2 of the QUEST cloud for IPA and TIPA.

Model	$\Delta T \leq 5\%$	$\Delta T \leq 10\%$	$\Delta T \leq 20\%$	$\Delta R \leq 5\%$	$\Delta R \leq 10\%$	$\Delta R \leq 20\%$
IPA	56%	76%	90%	36%	61%	86%
TIPA	52%	79%	95%	25%	48%	75%
	$|\Delta T|(1)$	$|\Delta T|(5)$	$|\Delta T|(19)$	$|\Delta R|(1)$	$|\Delta R|(5)$	$|\Delta R|(19)$
IPA	129%	58%	19%	73%	44%	21%
TIPA	69%	33%	10%	79%	60%	39%

As for the scaling behavior, TIPA shows due to its internal smoothing a more preferable characteristic which is represented by its ability to cut transmission errors in half compared to IPA, see also Table 5.29. For the reflected light the conclusion is reversed, here IPA maintains its advantage as expected, yet the difference between IPA and TIPA is smaller than for the transmitted light.

In Figure 5.40 the 2D fields of the cloud base height and the distribution of the errors of the transmitted light for IPA are shown. In region "**T1**" one notes very large errors which coincide with a region of relatively narrow clear sky areas and which are surrounded by cloud base heights of several hundred to several thousand meters. As before, the patterns are more pronounced for the reflected light, see Figure 5.41 for the 2D plot of the cloud top height and ΔR for IPA. The regions marked with "**R1**" and "**R2**" show that large negative errors occur in clear sky areas and at the fringes of those whereas large positive errors are located at cloudy areas where significant changes of the cloud top height occur. The same conclusions as in Experiment 2 of the DAQUA cloud for the variations of the cloud top height apply here as well as the vertical coordinate has almost the same structure.

Figure 5.42 depicts the dependence of ΔT and ΔR calculated by IPA on the optical depth. As for ΔT, largest errors occur at small to intermediate optical depths which confirms the notion that at cloud fringes maximum errors occur where predominantly changes of the cloud base height are located. Interestingly, only for negative errors, that is where the 3DMC result is larger than the IPA result, some spread of the values occurs. For large optical depths errors decline and quickly approach zero. However this is contrasted by the reflected light.

(a) Cloud base height of the QUEST cloud.

(b) 2D field of ΔT of IPA for Experiment 2 of the QUEST cloud.
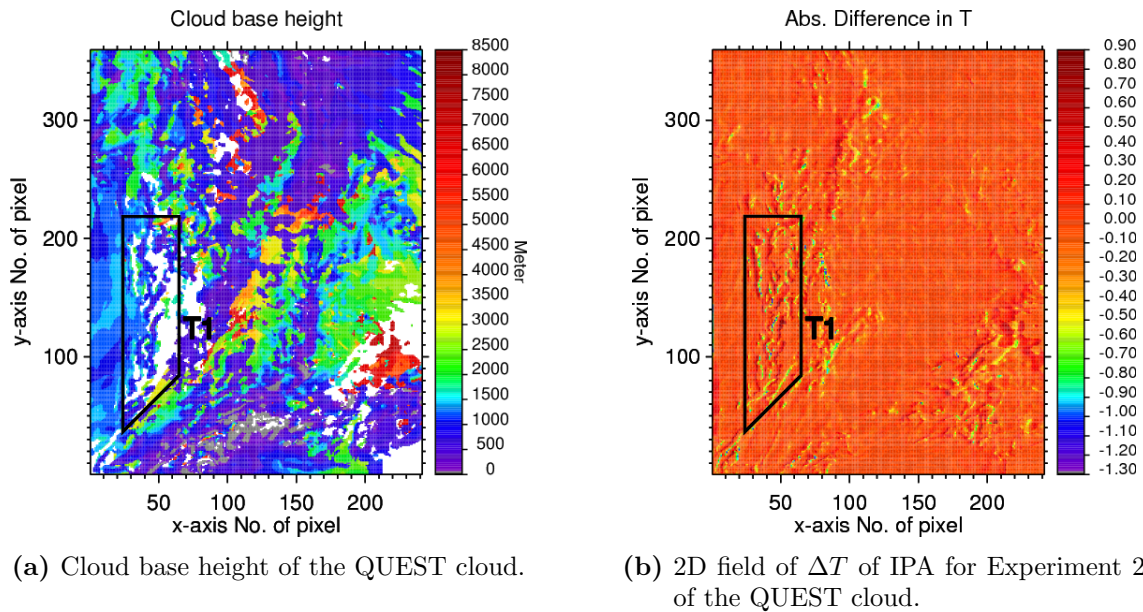
Figure 5.40: Cloud base height and ΔT of IPA for Experiment 2 of the QUEST cloud. Criteria as for Figure 5.34. See also Figure 5.36.

(a) Cloud top height of the QUEST cloud.

(b) 2D field of ΔR of IPA for Experiment 2 of the QUEST cloud.
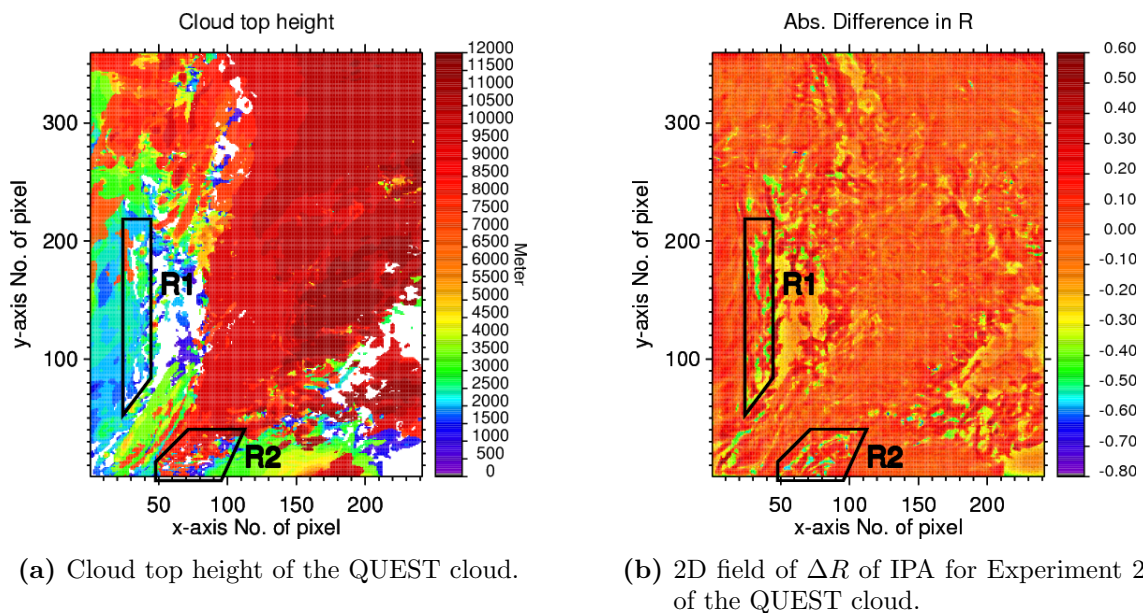
Figure 5.41: Cloud top height and ΔR of IPA for Experiment 2 of the QUEST cloud. Criteria as for Figure 5.34. See also Figure 5.36.

Although the values show a distinct behavior for small optical depths, large errors occur over almost the whole range of optical depths covering values from small negative to large

positive errors. It underlines the above findings that, although the maximum errors of R are smaller than the ones of T, the overall impact of the 3D effects on the reflected light is larger. The remarks of the previous example concerning the cloud ice contributions apply here as well.

(a) ΔT as a function of the total optical depth.

(b) ΔR as a function of the total optical depth.
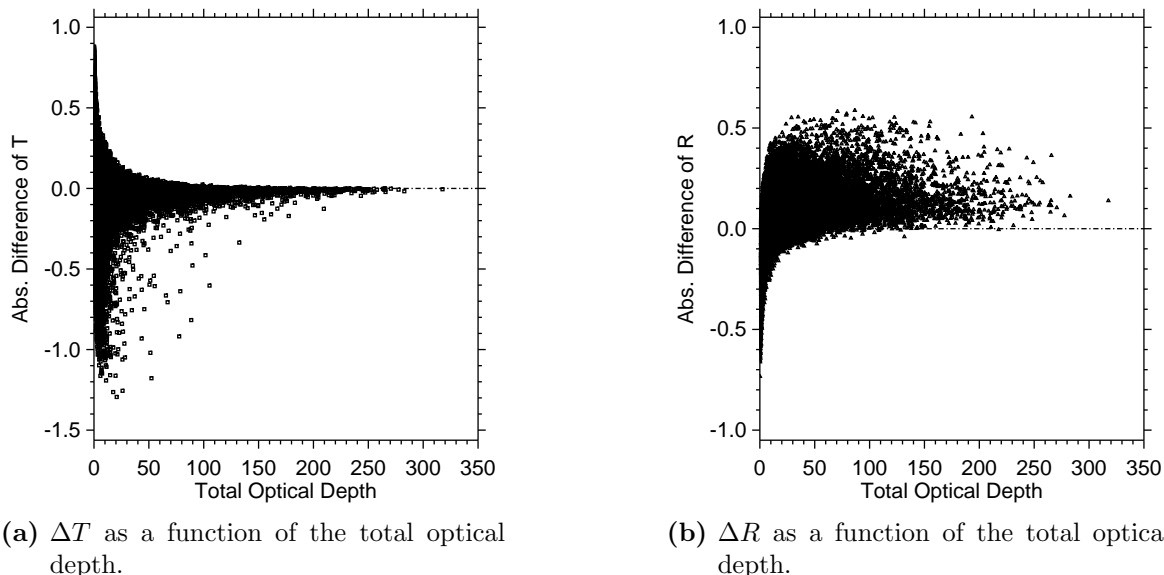
Figure 5.42: Absolute errors ΔT and ΔR of IPA as functions of the total optical depth for the QUEST cloud.

To conclude the discussion of this experiment, in Table 5.30 domain averaged results are shown. IPA and TIPA accurately describe the mean results with errors less than one percent while the differences between both approximations are marginal.

Table 5.30: Domain averaged results for Experiment 1 and 2 of the QUEST cloud for 3DMC, IPA and TIPA. For Experiment 1 TIPA was not applicable.

Model	Experiment 1		Experiment 2	
	$\bar{T}$	$\bar{R}$	$\bar{T}$	$\bar{R}$
3DMC	0.502	0.461	0.378	0.586
IPA	0.496	0.468	0.369	0.596
TIPA	–	–	0.368	0.597

Chapter 6

Discussion and Conclusions

> The whole is more than the sum of
> the parts.
>
> ――――――――――――――――――――
>
> Metaphysica
> Aristotle

6.1   Review of the Results

Radiative Transfer Perturbation Theory

In the course of the presented study, an adjoint calculation mode for azimuthally averaged radiative transfer properties has been implemented in the radiative transfer model DIS-ORT. Building up on this implementation, the Radiative Transfer Perturbation Theory (RTPT) has been constructed around the model core. It allows by linearizing the radiative transfer problem to consider the optical properties as being composed of a base case and perturbations of this base case. The realized concept permits the base case, as well as the perturbations, to arbitrarily vary with height. Perturbations include variations of the scattering and absorption coefficient as well as the phase function expansion coefficients. In turn, results for the upwelling- and downwelling flux, the net flux-density, and the actinic flux can be rapidly derived at any computational level separately and independently while the number of computational streams with a minimum of four is freely selectable.

As this basic concept can only account for perturbations in the linear range around the base case with reasonable error, an extension in order to employ multiple base cases was constructed. With the help of the Hermite-interpolation a third order interpolation with respect to perturbations of the total optical depth between pairs of base cases was realized. The number and the arrangement of the base cases is freely selectable, the only restriction is that the maximum and minimum optical depth considered by the perturbation is represented by one base case each. Within this framework perturbations of the phase function expansion coefficients are still accounted for linearly. In order to keep all results as flexible as possible Lambertian surface reflection is included via a superposition approach which

allows all equations to be solved with respect to vacuum boundary conditions. All of the above developments have been first realized in a stand-alone version of the model and were then, after slight alteration according to technical needs, translated into an independent pixel realization which allows the operation on three-dimensionally variable cloud fields. For this technical part of the work it can be stated that the developed model is the first and so far the only one of its kind within the presented complexity. Thus, a flexible and at the same time comprehensive tool for a comparatively new and innovative way to derive radiative transfer results has been gained. Tests with the stand-alone model applied to idealized atmospheric columns and perturbations yield promising results especially with the Hermite-interpolation being able to significantly reduce errors with respect to the results derived by DISORT in forward mode.

The aim of the application of the completed work to realistic cloud scenes was firstly to investigate whether reasonable results can be obtained at all and secondly whether the method has the potential to accelerate the calculation of radiative properties. It turned out that the applicability with respect to both criteria depends in a complex manner on the cloud field and the required resolution of the results. Concerning the overall precision of the method, in general the achieved accuracy depends on the magnitude of the variation of the optical properties in 3D space. The more uniform for example cloud top and cloud base are, the more precise the method is as then the interpolation is applied to only internally variable columns of otherwise the same extent within the cloud. If the cloud field is very inhomogeneous, broken and if the clouds have a ragged structure results degrade. This was demonstrated with several high resolution cloud fields where maximum errors of transmission and albedo assigned to individual pixels range from just a few percent in case of the former structure to over ten percent for clouds with the latter characteristics. However, the concept has proven that an application is possible and yields, with the above remarks in mind, meaningful results. As for the second intention, the possible acceleration of the radiative transfer computation, it was found that a number of prerequisites have to be met in order to achieve this aim. First, it is required that the cloud scene is composed of a sufficiently large number of pixels. This is especially meaningful if the scene is highly inhomogeneous. In this case, the RTPT has to be applied with several base cases whose radiative transfer calculations are time consuming and only the rapid execution of the Hermite-interpolation on a sufficiently large number of pixels can make up for this delay. Furthermore it is necessary to constrain the number of positions in the columns where radiative transfer perturbation results are derived to just a few. This is necessary as for each position in each base case pixel where a result is demanded the adjoint radiative transfer equation has to be solved. Moreover, the interpolation and the perturbation integrals with respect to the phase function and the surface albedo have to be evaluated in each pixel of the domain in this position. If these limitations are observed the method has proven to be able to gain a significant acceleration of up to a factor of four for one of the investigated cases, although no importance could be attached to computational optimization of the developed routines. The actual implementation of the technique and its implications on the forecast of atmospheric models is yet to be achieved and explored. Suggestions and hints concerning this point are given in the next section.

In summary it can be said that the development of the presented technique was successful and new and important insights in its features related to real world applications have been gained.

3D Parameterizations

The developed parameterizations for cloud-radiation interactions are composed of two separate approaches, each tackling a different component of 3D effects, and a combination of both. The primary parameterization is the Tilted Independent Pixel Approximation (TIPA) which is based on the tracking of the oblique path the direct light travels within the atmosphere. Technically, the optical properties are encountered, registered, and subsequently stored in a new slant vertical coordinate. This procedure leads to a more realistic succession of the optical parameters, as encountered by the direct light, compared to the always vertically aligned order the usual Independent Pixel Approximation (IPA) is based on and which effectively ignores the geometry of the solar illumination.

This part of the work has been carried out in a computationally simple fashion which permits the straightforward implementation of the new tilted domain in 1D radiative transfer models. As a new variant of the TIPA, the developed approach is also able to carry out the inverse transformation meaning that the computed radiative properties in the slant coordinate system are mapped to the original rectangular Cartesian grid by means of the information stored during the first processing of the optical properties. By virtue of this novel feature of this development the method is capable of yielding true 3D resolution of the results. This way geometric 3D effects like the shifted location of cloud shadows can be accounted for at the ground and below cloud base.

However, just as the original IPA, this concept as well does not include the estimation of horizontal exchange of photons between the single columns of the model. As a result, as a second approximation the concept of the Nonlocal Independent Pixel Approximation (NIPA) was investigated. With this method it is possible to mimic horizontal radiative transfer by means of a convolution product of 1D results. However, existing realizations were not fully autonomous from exact 3D radiative transfer as the parameters of the convolution kernel have to be acquired one way or another. In order to overcome this limitation a direct yet idealized estimation of the parameters in physical space was introduced in this study as a novelty. This estimation utilized an analytic solution of a technique termed diffusion approximation in order to gain the convolution parameters from the radial moments of this analytic solution. Thus, the whole method becomes independent of any other information provided by exact 3D models or other approximations and estimates.

Both methods, TIPA and NIPA, are then combined by applying NIPA to the results gained by TIPA which finally results in the successive approximate consideration of both geometric and diffuse 3D effects. While similar concepts have been conceived in the past, the new features mentioned above stand out to some extent as two crucial characteristics which are indispensable for real world applications are realized and combined for the first time.

Yet, there are certainly some concerns and shortcomings the parameterizations suffer from. Beginning with the TIPA, it was found that technically the inverse transformation of the

radiative transfer results works fine, yet leads at times to very ragged vertical profiles. For most realistic applications investigated here, this shortcoming seems to be restricted to the upwelling flux above cloud top. The origin of this effect has to be sought in the independence of the slant columns and in the confinement of one path-tracking per pixel. While in the slant columns the profiles are smooth and steady, the inverse transformation arranges results originating from different neighboring slant columns in vertical succession in the same column in the Cartesian lattice. Thus, radiative transfer results from slant columns, which in general penetrate different parts of the atmosphere, are mixed. In other terms, the rough horizontal 2D distribution of radiative quantities, which is also known to occur with IPA calculations, is partly translated by the inverse transformation into a vertical roughness. The problem is believed to be most prominent if clouds are first encountered by the slant path through their sides while encounters of the top are less crucial. An alleviation of this defect can be partly achieved by the NIPA as it accounts for the missing horizontal transport. With the investigated idealized clouds it was proven that indeed NIPA not only improves the 2D results of TIPA but also partly eliminates or at least weakens the ragged behavior in the vertical. 2D transmission and reflection fields are already smoothed by TIPA alone as the slant coordinate blurs the rough optical depth field. With regard to NIPA itself there are also some concerns and assumptions. For the analytic diffusion solution to exist it is necessary that all optical properties are homogeneously distributed throughout the convolution kernel. That is achieved by averaging the columns of the optical properties which are supposed to be covered by the kernel. Although this seems to be a crude manner, it is justified not only by the demonstrated improvement of the pure 1D calculations which NIPA can gain but also from fundamental prerequisites for the diffusion approximation to work.

As mentioned above, the conceptual development was succeeded by some more or less idealized examples which already shed some light on the main features of the parameterizations. For the realistic validation of the techniques cloud fields from different sources were selected and classified according to their horizontal resolution. The first group consisted of high resolution cloud fields where the horizontal resolution is in the range of several dozens of meters and reaches up to $100m$. This range was deliberately chosen to encounter small scale effects like radiative smoothing. The second class is represented by one cloud with a horizontal resolution of $200m$ which is supposed to be the upper limit for dominant photon diffusion to occur. Lastly, coarse resolution cloud fields from a weather prediction model with $2800m$ horizontal resolution have been investigated. While for the preceding cases a complete application of all parameterization approaches is possible, for the coarse resolution NIPA and as a result NTIPA as well cannot be used. This results from the large resolution and the rapid decay of the convolution kernel with radial distance from the center. All pixels but the center pixel are then occupied by values which are numerically zero. Thus, in this case NIPA reproduces the IPA values.

A generally valid numerical quantification of the respective impact of each of the parameterizations is hard to find. Results are diverse and vary not only from group to group but also within groups of clouds and even with the same cloud as usually numerical experiments for different solar zenith angles have been carried out. It has to be stressed that

comparisons of domain averaged results have shown to be no adequate measure to assess the quality of parameterizations for a given cloud. This follows from the negligibly small differences these comparisons show. Although that is not entirely a bad result as it at least shows that mean values are derived almost equally good for any of the approximations, it requires to focus on more sophisticated parameters. Qualitatively, this has been achieved by comparing the shape of the error distributions, their cumulative distributions, and the shape of the decay of the maximum residual errors prevailing in the reflection and transmission fields after averaging over areas differing in size. On the quantitative side, those measures are represented by the fraction of pixels which are assigned to errors below certain thresholds and by the value of the maximum residual errors for a limited set of averaging areas. Those criteria were believed to be meaningful for the following reasons. First, the error threshold gives a feasible estimate that permits an atmospheric modeler to get an impression how strong the impact of the 3D errors might be on the surrounding atmospheric model and on the forecasted meteorological variables closely related to the radiative transfer field. The decay of the maximum residual errors gives in turn an estimate of the worst error which might be encountered at different scales. This measure is believed to be meaningful for effects which are sought on a larger scale or area than the single pixel resolution. Applications might not only be atmospheric models but also remote sensing instruments whose horizontal resolution is generally larger than the high and medium resolutions introduced here.

As mentioned above, a statistically reliable result has not been gained yet as the number of investigated clouds is too small. Despite that, averaged results for the different resolutions are roughly presented in the following tables. Table 6.1 presents the gain of pixels due to the different approximations relative to the IPA which have a maximum error of 5% or less for ΔT and ΔR for all clouds and both solar zenith angles $\mu_o = 1.0$ and $\mu_o = 0.5$. The deduced variable is defined as:

$$A_{gain}(\Delta P \leq 5\%) = |A_{para}(\Delta P \leq 5\%) - A_{IPA}(\Delta P \leq 5\%)| \tag{6.1}$$

Table 6.2 shows the reduction of the absolute values of the maximum errors of transmission and reflection gained by the approximations relative to the maximum absolute error of IPA. In detail:

$$\Delta P_{\substack{gain \\ max}} = \frac{|\Delta P_{\substack{para \\ max}} - \Delta P_{\substack{IPA \\ max}}|}{|\Delta P_{\substack{IPA \\ max}}|} \tag{6.2}$$

where P stands either for R or T and the subscript $para$ refers to $TIPA$, $NIPA$ or $NTIPA$. From Table 6.1 one can learn that for both investigated solar zenith angles the approximations work best for the high resolution part. For the medium resolution results with regard to $A_{gain}(\Delta T \leq 5\%)$ deteriorate while $A_{gain}(\Delta R \leq 5\%)$ maintains its performance. For the coarse resolution cloud fields the application was either not feasible or gained only little or no improvements. From Table 6.2 a similar yet in detail different conclusion can be drawn. While again the reduction of the maximum errors is largest for the high resolution

Table 6.1: Increase in percent of the area affected by errors with 5% or less due to the developed parameterizations with respect to values gained by IPA related to the entire domain as defined by rule 6.1. Values for $\mu_o = 1.0$ and $\mu_o = 0.5$ are shown. "n.a." stands for "not applicable" and "n.i." stands for "no improvement" which was assigned if the difference was close to zero or even negative.

Resolution	Model	$A_{gain}(\Delta T \leq 5\%)$	$A_{gain}(\Delta R \leq 5\%)$
		$\mu_o = 1.0$	
High	NIPA	$10\% - 40\%$	10%
Medium	NIPA	3%	10%
Coarse		n.a.	
		$\mu_o = 0.5$	
High	TIPA	20%	n.i.
High	NIPA	$1\% - 5\%$	$10\% - 15\%$
High	NTIPA	$15\% - 40\%$	$5\% - 10\%$
Medium	TIPA	10%	1%
Medium	NIPA	5%	10%
Medium	NTIPA	$10\% - 15\%$	10%
Coarse	TIPA	$3\% - 4\%$	n.i.

clouds in the medium range, the approximations can keep up their improvement, if there is any, with respect to ΔT_{gain} whereas ΔR_{gain} degrades. For the coarse resolution clouds this behavior prevails as ΔT_{gain}^{max} is on the level of the medium resolution and ΔR_{gain}^{max} shows no improvement. It has to be noted that for this highly condensed analysis the overall subjective judgment of all approximations in combination and both solar zenith angles was taken into account. These results are certainly somewhat unexpected as one would have rather expected the coarse resolution to be the least crucial range as the dimensions and the cloud structure were expected to be closest to the plane-parallel and independent pixel assumption. However, the details of those clouds seem to contradict these characteristics. Especially the discussed structure of the cloud top height where large areas form abrupt staircase-like surfaces seems to add to the unexpected challenges these clouds pose. Nevertheless, the large spread of values, the singularity of those, and the holes in Tables 6.1 and 6.2 make well clear how necessary a larger series of results is in order to pin down the range of values and uncertainties in the individual resolutions.

Based not only on Tables 6.1 and 6.2 but also on material presented in Chapter 5 as well as on material not shown at all, in order not to overload the presentation, a subjective recommendation of the different approximations for different radiative effects is given in Table 6.3. To deduce this information two separate categories have been included. First, "Precision" stands for the preferred choice if in the relation between accuracy and compu-

Table 6.2: Reduction of the maximum errors by the different approximations with respect to the maximum errors of IPA as defined by rule 6.2. Values for $\mu_o = 1.0$ and $\mu_o = 0.5$ are shown. "n.a." stands for "not applicable" and "n.i." stands for "no improvement" which was assigned if the difference was close to zero or even negative. "n.d." stands for "not definite" and was assigned once as the results of different clouds were ambiguous.

Resolution	Model	$\Delta T_{gain \atop max}$	$\Delta R_{gain \atop max}$
		$\mu_o = 1.0$	
High	NIPA	$40\% - 50\%$	$20\% - 50\%$
Medium	NIPA	50%	13%
Coarse		n.a.	
		$\mu_o = 0.5$	
High	TIPA	40%	$2\% - 30\%$
High	NIPA	n.d.	$30\% - 45\%$
High	NTIPA	$60\% - 70\%$	$30\% - 50\%$
Medium	TIPA	54%	n.i.
Medium	NIPA	n.i.	13%
Medium	NTIPA	45%	10%
Coarse	TIPA	45%	n.i.

tational speed the emphasis is on accuracy. The section "Computational time" should be considered if for the reader an efficient computation is more valuable. As stated numerous times, this "final verdict" can only be regarded as preliminary due to the statistical unreliability of the results and is by no means a definite conclusion.

A general comprehensive discussion of 3D effects and the respective dependence of those on the geometry of the solar illumination, the horizontal and vertical resolution and shape of the clouds was not the intention of this thesis. To arrive at definite results concerning this topic the number of clouds and 3DMC results available was certainly not sufficient. However, from the gained results it is clear that in general for slant solar illumination 3D effects are more prominent than for vertical illumination, which is also documented by the fact that in those cases the transmission even can exceed unity. Although this statement is slightly commonplace, the existing 3D effects for overhead illumination are still surprisingly strong. Concerning the resolution and shape of the clouds the influence exerted by the coarse resolution clouds on the radiative field was also startlingly strong. As discussed, this feature mainly results from the areas with irregular shaped cloud top and bottom. A comprehensive analysis and discussion of 3D effects and their causal dependence on the mentioned parameters can be found in Gimeno García (2006).

Table 6.3: Recommended application of the approximations. Compiled from all resolutions and solar zenith angles with respect to the criteria precision and computational time for reflection and transmission. The three lines in each of the two criteria are referred to in Table 6.4.

Criteria	T	R
	IPA	IPA
Precision	NTIPA	NIPA
	NTIPA	NIPA
	IPA	IPA
Computational time	TIPA	NIPA
	TIPA	NIPA

Table 6.4: Explanation of the three lines in each criteria in Table 6.3.

Feature
Domain averages
Vertical structure
2D fields

Finally, in order to come full circle it can be stated that several already existing approaches have been improved, physically enhanced and extended, and combined. Furthermore, the study has not been limited to one characteristic of the clouds or the radiative properties but has rather addressed a diverse set of clouds while the investigated results are numerous and have been illuminated from several views to gain insights in the respective features of the parameterization approaches.

From the findings of the presented study, it is obvious that from the radiative transfer point of view an implementation of 3D parameterizations in atmospheric models seems to be necessary in that the developed, more sophisticated, techniques are better suited to describe 3D effects than the usual IPA. The illumination of this question was one of the main purposes of this work. However, the consequences of the 3D effects and their treatment by the various parameterizations on meteorological quantities were beyond the scope of this study and are therefore still unclear. Interesting issues do not only touch on directly cloud related questions like cloud formation and precipitation but might also have consequences for atmospheric dynamics. To tackle these questions, it is finally inevitable to implement both the preferred set of parameterizations as well as an exact 3D radiative transfer model in an atmospheric model. In conjunction with that challenging task not only the technical implementation has to be carried out carefully, but also several other pressing issues have to be clarified beforehand. One of them is the validation of the fluxes

computed by the already embedded 1D RT module with satellite measurements. This work seems to be necessary to arrive at a first estimate of the 3D effects and to gain confidence in the correct implementation of the 1D RT module as most applicable 3D parameterizations would be building up on this part of the model.

An interesting point concerning this issue, especially with regard to large scale models, is the treatment of partial cloudiness. There does not seem to exist any study detailing the finest resolution where this concept can still be applied with reasonable justification. As the resolution of weather prediction models can be expected to reach $1km$ in the near future, it is however necessary to be investigated. The validation of the cloud shape and properties computed by atmospheric models is connected to this problem. At least for large scale models the realistic prediction of these parameters can be questioned. To do so, radar and satellite data could provide interesting information for comparisons not only with existing cloud modules but also with possible new techniques like cloud generators which might replace the classical microphysical parameterizations.

Finally, if all of these tasks have been at least partly accomplish, a detailed investigation of the results has to be carried out. In the light of the number of approaches and parameters available and given the diversity of meteorological situations and the necessary computational time to operate such a model system, a study of this kind is supposed to be rather painstaking and tedious. However, until it has been completed most notions about the feedback of 3D cloud-radiation interactions on atmospheric dynamics and climate remains speculative.

Another question is the future development of the 3D approximations themselves. As for the ones developed here, thoughts concerning future studies and the implementation in atmospheric models are conveyed in the next section. However, it seems to be necessary and meaningful to carry on with the development of true 3D parameterizations as well. That means that approximate techniques for the solution of the 3D radiative transfer equation should replace and/or complement the parameterizations based on 1D models in the long term. The direct solution of the 3D diffusion equation might emerge as one of the most promising techniques in this respect. A number of studies and developments have already been carried out during the past years, see Chen et al. (2005) and Davis (2000).

6.2   Future Research and Improvements

In this section, suggestions for future research and improvements closely related to the implementation of the methods building up on the achieved results are given.

Radiative Transfer Perturbation Theory

In order to focus on a utilization of the presented techniques it is inevitable to implement the adjoint mode in an analytical 2- and/or 4-stream radiative transfer model which is part of an atmospheric model. Pioneer work in this respect has been carried out by Gabriel et al. (1998). In this context the fully automatic selection of the base cases is also a necessity.

The realization of this task could be achieved in combination with a criterion which checks the quality of the selected base cases by analyzing the structure of the optical properties of the atmosphere. As similar techniques are used in remote sensing an adaption might be possible. However, this package of tasks is challenging as it would make considerable restructuring of the model environment necessary to get complete and simultaneous access to the three-dimensional optical properties. This is usually not the case as the forward independent pixel approximation does not require the accessibility of 3D optical properties but rather optical properties in successive 1D columns.

Another involved problem is the perturbation of the phase function. It was shown that this element of the perturbation is largely responsible for the growing errors in case of inhomogeneous cloud fields. One aspect of the solution is the incorporation of the base case phase function in the automatic selection of the base cases, see above. Another is the treatment of the phase function perturbation itself. In the presented study its contribution was only added linearly to the interpolated result. However, to significantly reduce the errors a multivariate interpolation of the base cases in the phase space of the optical properties seems to be necessary. As the potential application of the RTPT would be mainly 2-stream models one could limit this problem to two dimensions namely the perturbation of the total optical depth and the asymmetry factor. Since most of these measures would consume even more computational time it remains necessary to limit the number of output levels at which results of the RTPT are derived.

Moreover, to determine whether all these efforts make sense any of the proposed improvements should be preceeded by careful studies. These should comprise the exploration of the meaningful update interval of the radiative properties which are fed into the atmospheric model under consideration and the investigation of the reasonable number and positions of output levels.

3D Parameterizations

The above remarks concerning the 3D availability of the optical properties apply for the 3D parameterizations as well as both TIPA and NIPA make use of the 3D distribution of optical parameters while preparing the slant optical coordinate and the averaged convolution kernel, respectively.

Furthermore, both require an adaption to curvilinear coordinate systems as these are state-of-the-art in most atmospheric models. As for TIPA, that would mean the development of a more sophisticated tracking of the direct beam. Furthermore, the tracking would be required to be repeated for each pixel as the structure of the coordinate system generally would be inhomogeneous itself. Concerning NIPA the implementation might be more simple as the averaging to gain a homogeneous local domain for the space of each kernel can be carried out regardless of the coordinate system.

Another problem concerning TIPA, if applied to large scale models, is the treatment of the solar zenith angle. As these models cover vast areas of the earth, the local solar zenith angle of the respective geographic area is used. This does not pose a significant problem to IPA and NIPA, yet for TIPA a multi solar zenith angle variant would have to be developed.

In this connection close attention has to be paid to the steady derivation of the optical properties in the slant columns as well as to the contiguous computation of the radiative results of the inverse transformation.

After all it might be preferable to preceed this work by several case studies of 3D effects in atmospheric models with the help of Monte-Carlo models as these models have proven to be able to handle irregularly gridded meshes and variable solar zenith angles.

All of the problems mentioned above rather concern the implementation of the 3D approximations in atmospheric models. However, a number of investigations can be carried out for the approximations themselves. One approach of modifying TIPA could be the investigation of other inverse transformations. First steps in this direction have been carried out during this study. Another approach might be the exploration of different concepts concerning the tracking of the slant path.

As already mentioned, a more systematic and statistically reliable investigation of the 3D parameterizations is highly desirable. Special focus should be on the sound study of the dependence of the results on the solar zenith and azimuth angle for clouds of different horizontal resolutions as well as on the realistic wavelength dependence of the surface albedo. Regarding the last point, it would also be preferable to carry out calculations with realistic 2D values of a larger domain. For this study data was available for the LM clouds, yet the application was omitted as the 3DMC model was not ready to handle a 2D variable surface albedo. As for the different resolutions, it would be interesting to fill the gap between $200m$ and $2800m$ which could not be investigated during this work. This range would include both the resolution of existing high resolution mesoscale models as well as the future resolution of weather prediction models.

With regard to NIPA improvements could be achieved by the implementation of different convolution kernels. Apart from other technical details worth investigating especially the Gamma-distribution originally proposed by Marshak et al. (1995) might be more advantageous to use.

Finally, in principle both RTPT and the 3D approximations are combinable. In order to energetically drive an atmospheric model, it might be sufficient to gain only results at a few output levels which could be rapidly computed by combining RTPT and NTIPA. As stated numerous times before, this approach should be preceeded by thorough investigations whether this reduction of vertical levels for radiative transfer results still leads to reliable predictions of the meteorological quantities. Moreover, special attention should be paid to the comparison of the predicted cloud structure and resulting radiative transfer with measured cloud fields which could be achieved by consulting satellite data. This way both major problems, the lack of a realistic treatment of 3D RT effects and slow update rate, which atmospheric models usually suffer from, could be tackled at the same time.

Appendix A

First Order Perturbation Expansion

The derivation of the linear perturbation formula after Ustinov (1991) is briefly addressed. The basic equations are restated as:

$$LI = Q \qquad \text{(A.1)} \qquad L_b I_b = Q_b \qquad \text{(A.2)} \qquad L_b^+ I_b^+ = R \qquad \text{(A.3)}$$

Multiplying A.3 by I_b and multiplying A.2 by I_b^+ leads to:

$$I_b L_b^+ I_b^+ = R I_b \qquad \text{(A.4)} \qquad I_b^+ L_b I_b = Q_b I_b^+ \qquad \text{(A.5)}$$

Subtracting A.5 from A.4 and applying the phase space integral $\langle \cdot, \cdot \rangle$ leads to:

$$E_b = \langle Q_b, I_b^+ \rangle - \langle I_b^+, L_b I_b \rangle + \langle I_b, L_b^+ I_b^+ \rangle \qquad \text{(A.6)}$$

Multiplying now A.3 by I and multiplying A.1 by I_b^+ leads to:

$$I L_b^+ I_b^+ = R I \qquad \text{(A.7)} \qquad I_b^+ L I = Q I_b^+ \qquad \text{(A.8)}$$

Subtraction of A.8 from A.7 and integration leads to:

$$E = \langle Q, I_b^+ \rangle - \langle I_b^+, L I \rangle + \langle I, L_b^+ I_b^+ \rangle \qquad \text{(A.9)}$$

Finally:

$$E - E_b = \Delta E = \langle I_b^+, \Delta Q - \Delta L I_b \rangle \qquad \text{(A.10)}$$

with:

$$\begin{aligned} \Delta Q &= Q - Q_b \\ \Delta L &= L - L_b \end{aligned} \qquad \text{(A.11)}$$

Appendix B

Expressions for the Albedo Related Perturbation Integral

The remaining identities from page 49 are defined as follows:

$$\mathcal{F}_1(z) = F_{v,b}(0)\ \Xi_1(z) \qquad\qquad ;\ \mathcal{F}_{\xi_1}(z) = \Xi_{\xi_1}(z)F_{v,b}(0)$$

$$\mathcal{F}_2(z) = F_{v,b}^+(0)\ \Xi_2(z) \qquad\qquad ;\ \mathcal{F}_{\xi_2}(z) = \Xi_{\xi_2}(z)F_{v,b}^+(0)$$

$$\mathcal{F}_3(z) = F_{v,b}(0)F_{v,b}^+(0)\Xi_s(z) \qquad ;\ \mathcal{F}_{\xi_3}(z) = F_{v,b}(0)F_{v,b}^+(0)\Xi_{\xi_3}(z)$$

$$\Xi_1(z) = \int\limits_{-1}^{1} d\mu\, I_{v,b}^+(z,\mu)I_{s,b}(z,\mu) \quad ;\ \Xi_{\xi_1}(z) = \xi_{l,v}^+(z)\xi_{l,s}(z)$$

$$\Xi_2(z) = \int\limits_{-1}^{1} d\mu\, I_{s,b}(z,-\mu)\bar{I}_{b,v}(z,\mu) \ ;\ \Xi_{\xi_2}(z) = \xi_{l,s}^+(z)\xi_{l,v}(z)$$

$$\Xi_s(z) = \int\limits_{-1}^{1} d\mu\, I_{s,b}(z,-\mu)I_{s,b}(z,\mu) \ ;\ \Xi_{\xi_3}(z) = \xi_{l,s}^+(z)\xi_{l,s}(z)$$

$$\xi_{l,s}(z) = \int\limits_{-1}^{1} d\mu\, I_{s,b}(z,\mu)P_l(\mu) \qquad ;\ \xi_{l,s}^+(z) = \int\limits_{-1}^{1} d\mu\, I_{s,b}(z,-\mu)P_l(\mu)$$

Symbols

In the following, the most important symbols, their meaning, and their common units are listed. "-" stands for "dimensionless" and "variable" was assigned if no definite unit was applicable. Units in parentheses denote wavelength dependence.

Symbol	Meaning	Unit
	Latin letters	
a	particle radius	μm
a_e	effective radius	μm
c	speed of light	ms^{-1}
c_p	specific heat capacity at constant pressure	$JK^{-1}kg^{-1}$
f_ν	photon density	$m^{-3}sr^{-1}(\mu m^{-1})$
g	asymmetry factor	1
g_{part}	single particle asymmetry factor	1
h	Planck's constant	$6.625 \cdot 10^{-34}Js$
j	emission coefficient	$m^{-3}s^{-1}sr^{-1}(\mu m^{-1})$
k	wavenumber	m^{-1}
$\dfrac{dn(a)}{da}$	differential particle number concentration	$cm^{-3}\mu m^{-1}$
p	phase function	sr^{-1}
s	geometric pathlength	m
A	surface albedo	-
$\boldsymbol{E}$	vector of the net flux-density	$Wm^{-2}(\mu m^{-1})$
E	effect	variable
F_{act}	actinic flux	$Wm^{-2}(\mu m^{-1})$
F_o	solar constant	$Wm^{-2}(\mu m^{-1})$
I	intensity	$Wm^{-2}sr^{-1}(\mu m^{-1})$
I^+	adjoint intensity	variable
J	source function	$Wm^{-3}sr^{-1}(\mu m^{-1})$
J_o	source strength	$Wsr^{-1}(\mu m^{-1})$
N_c	molecular absorbing gas concentration	cm^{-3}
N_{air}	molecular air concentration	cm^{-3}

Symbol	Meaning	Unit
N_{part}	particle number concentration	cm^{-3}
Q	source term	$Wm^{-2}sr^{-1}(\mu m^{-1})$
Q^+	adjoint source	variable
Q_s	scattering efficiency	-
Q_t	extinction efficiency	-
R	reflection	-
R	response function	variable
S	solar flux	$Wm^{-2}(\mu m^{-1})$
T	transmission	-
T	temperature	K
U_d	radiative density	$Wm^{-2}sr^{-1}(\mu m^{-1})$
	Greek letters	
θ	zenith angle	$°$ or rad
θ_o	solar zenith angle	$°$ or rad
λ	wavelength	μm
ρ	density	kgm^{-3}
ρ_a	absorber density	kgm^{-3}
ρ_l	liquid water content	kgm^{-3}
ρ_w	water density	kgm^{-3}
σ_a	absorption coefficient	m^{-1}
$\hat{\sigma}_a$	absorption cross section	cm^2
$\hat{\sigma}_{ray}$	Rayleigh scattering cross section	cm^2
$\hat{\sigma}_s$	scattering cross section	cm^2
$\hat{\sigma}_t$	extinction cross section	cm^2
σ_s	scattering coefficient	m^{-1}
σ_t	extinction coefficient	m^{-1}
τ	optical depth	-
φ	azimuthal angle	$°$ or rad
φ_o	solar azimuthal angle	$°$ or rad
χ	extrapolation length	m
χ_a	mass absorption coefficient	m^2kg^{-1}
ω_o	single scattering albedo	1
Θ	scattering angle	$°$ or rad
Σ_l	liquid water path	gcm^{-2}
Ψ	pseudo intensity	variable
Ω	solid angle	sr

Symbol	Meaning	Unit
$\boldsymbol{\Omega}$	direction of propagation	-

Acronyms

Acronym	Meaning
3DMC	3D Monte-Carlo
ARM	Atmospheric Radiation Measurement
BBC	Baltex Bridge Campaign
DAQUA	Combined Data Assimilation with
	Radar and Satellite Retrievals
	and Ensemble Modeling for the
	Improvement of
	Short Range Quantitative Precipitation Forecasts
DISORT	DIscrete Ordinate Radiative Transfer
DiA	Diffusion Approximation
DWD	Deutscher Wetterdienst/German Weather Service
FIRE	First ISCCP Regional Experiment
FW	Forward
GCM	Global Circulation Model
I3RC	Intercomparison of 3D Radiation Codes
IAAFT	Iterative Amplitude Adapted Fourier Transform
INSPECTRO	Influence of Clouds on the Spectral Actinic Flux in the lower Troposphere
IPA	Independent Pixel Approximation
ISCCP	International Satellite Cloud Climatology Project
LES	Large Eddy Simulation
LIDAR	LIght Detection And Ranging
LM	Lokal-Modell/Local Model
LMCM	Leipzig Monte-Carlo Model
NIPA	Nonlocal Independent Pixel Approximation
NTIPA	Nonlocal Tilted Independent Pixel Approximation
NWP	Numerical Weather Prediction
PPA	Plane Parallel Assumption
QUEST	Quantitative Evaluation of Precipitation Forecasts

Acronym	Meaning
RADAR	RAdio Detection And Ranging
RP	Radiative Properties
RT	Radiative Transfer
RTE	Radiative Transfer Equation
RTPT	Radiative Transfer Perturbation Theory
SHDOM	Spherical Harmonics Discrete Ordinate Method
ST	Strahlungstransport
SZA	Solar Zenith Angle
TIPA	Tilted Independent Pixel Approximation
TOA	Top Of Atmosphere

Bibliography

4D-clouds, 2005. URL http://www.meteo.uni-bonn.de/projekte/4d-clouds/.

ARM Webpage, 2004. URL http://www.arm.gov.

BBC2 Webpage, 2003. URL http://www.knmi.nl/samenw/bbc2/.

G. I. Bell and S. Glasstone. *Nuclear reactor theory*. Van Nostrand Reinhold, New York, 1970.

M. A. Box. Radiative perturbation theory: A review. *Environmental Modeling and Software*, 17:95–106, 2002.

M. A. Box, S. A. W. Gerstl, and C. Simmer. Application of the adjoint formulation to the calculation of atmospheric radiative effects. *Contributions to Atmospheric Physics*, 61: 303–311, 1988.

R. F. Cahalan, W. Ridgway, S. Gollmer, and Harshvardan. Independent pixel and monte carlo estimates of stratocumulus albedo. *Journal of the Atmospheric Sciences*, 51:3776–3790, 1994a.

R. F. Cahalan, W. Ridgway, W. J. Wiscombe, and T. L. Bell. The albedo of fractal stratocumulus clouds. *Journal of the Atmospheric Sciences*, 51:2434–2455, 1994b.

B. Cairns, A. A. Lacis, and B. E. Carlson. Absorption within inhomogeneous clouds and its parameterization in general circulation models. *Journal of the Atmospheric Sciences*, 57:700–714, 2000.

K. M. Case and P. F. Zweifel. *Linear transport theory*. Addison-Wesley, Reading, Mass., 1967.

S. Chandrasekhar. *Radiative transfer*. Dover Publications Inc., New York, 1960.

Y. Chen, K. N. Liou, and Y. Gu. An efficient diffusion approximation for 3D radiative transfer parameterization: Application to cloudy atmospheres. *Journal of Quantitative Spectroscopy and Radiative Transfer*, 92:189–200, 2005.

S. Corrsin. On the spectrum of isotropic temperature fluctuations in isotropic turbulence. *Journal of Applied Physics*, 22:469–473, 1951.

DAQUA Webpage, 2004. URL http://www.meteo.uni-bonn.de/projekte/daqua/.

A. Davis, 2000. URL http://i3rc.gsfc.nasa.gov/approximations.html.

A. Davis and A. Marshak. Multiple scattering in clouds: Insights from three-dimensional diffusion/P_1 theory. *Nuclear Science and Engineering*, 137:251–280, 2001.

A. Davis, A. Marshak, R. Cahalan, and W. Wiscombe. The landsat scale break in stratocumulus as a three-dimensional radiative transfer effect: Implications for cloud remote sensing. *Journal of the Atmospheric Sciences*, 54:241–260, 1997.

A. Davis, R. Cahalan, J. Spinhirne, M. McGill, and S. Love. Off-beam lidar: An emerging technique in cloud remote sensing based on radiative Green-function theory in the diffusion domain. *Physics and Chemistry of the Earth (B)*, 24:757–765, 1999.

A. Davis, A. Marshak, H. Gerber, and W.J. Wiscombe. Horizontal structure of marine boundary layer clouds from centimeter to kilometer scales. *Geophysical Research Letters*, 30(10), 1507,doi:10.1029/2003GL017192, 2003.

G. Doms and U. Schättler. *The nonhydrostatic limited-area model LM (Lokal-Modell) of DWD. Part I: Scientific documentation.* Deutscher Wetterdienst (DWD), Geschäftsbereich Forschung und Entwicklung, PO box 100465, D-63004 Offenbach, January 1999.

G. Doms, U. Schättler, and J.-P. Schulz. *Kurze Beschreibung des Lokal-Modells LM und seiner Datenbanken auf dem Datenserver (DAS) des DWD.* Deutscher Wetterdienst (DWD), Geschäftsbereich Forschung und Entwicklung, PO box 100465, D-63004 Offenbach, September 2003.

P. G. Duynkerke, S. R. d. Roode, M. C. v. Zanten, J. Calvo, J. Cuxart, S. Cheinet, A. Chlond, H. Grenier, P. J. Jonker, M. Köhler, G. Lenderink, D. Lewellen, C.-L. Lappen, A. P. Lock, C.-H. Moeng, F. Müller, D. Olmeda, J.-M. Piriou, E. Sánchez, and I. Sednev. Observations and numerical simulations of the diurnal cycle of the EUROCS stratocumulus case. *Quarterly Journal of the Royal Meteorological Society*, 130:3245–3268, 2004.

K. F. Evans. The spherical harmonic discrete ordinate method for three-dimensional atmospheric radiative transfer. *Journal of the Atmospheric Sciences*, 55:429–446, 1998.

FIRE I Webpage, 2002. URL http://asd-www.larc.nasa.gov/fire/fire1.html.

B. Früh. *Entwicklung und Evaluierung einer Modellhierarchie zur Simulation der aktinischen Strahlung in aerosolbelasteter und bewölkter Atmosphäre.* PhD thesis, Institute for Physics of the Atmosphere, University of Mainz, 2000.

Q. Fu, M.C. Cribb, H.W. Barker, S.K. Krueger, and A. Grossman. Cloud geometry effects on atmospheric solar absorption. *Journal of the Atmospheric Sciences*, 57:1156–1168, 2000.

P. Gabriel, J. Harrington, G. L. Stephens, and T. Schneider. Adjoint perturbation method applied to two-stream radiative transfer. *Journal of Quantitative Spectroscopy and Radiative Transfer*, 59:1–24, 1998.

P. Gabriel, G. L. Stephens, and I. L. Wittmeyer. Adjoint perturbation and selection rule method for solar broadband two-stream fluxes in multi-layer media. *Journal of Quantitative Spectroscopy and Radiative Transfer*, 65:693–728, 2000.

S. Gimeno García. *Preliminary title: Radiative transfer modeling in inhomogeneous clouds by means of the Monte Carlo method.* PhD thesis, Institute for Meteorology, University of Leipzig, 2006.

S. Gimeno García and T. Trautmann. Radiative transfer modeling in inhomogeneous clouds by means of the monte carlo method. Wiss. Mitt. 30, Institut für Meteorologie Universität Leipzig, 2003.

J.T. Houghton, Y. Ding, D.J. Griggs, M. Noguer, P.J. van der Linden, X. Dai, K. Maskell, and C.A. Johnson. *Climate Change 2001: The scientific basis. Contribution of working group I to the third assessment report of the Intergovernmental Panel on Climate Change.* Cambridge University Press, Cambridge, United Kingdom and New York, 2001.

Y. Hu. *A study of the link between cloud microphysics and climate change.* PhD thesis, University of Alaska, Fairbanks, 1994.

INSPECTRO Webpage, 2002. URL `http://imk-ifu.fzk.de/inspectro/`.

A. Ishimaru. *Wave propagation and scattering in random media.* IEEE Press, 1997.

J. L. W. V. Jensen. Sur les fonctions convexes et les inegalités entre les valeur moyennes. *Acta Mathematica*, 30:789–806, 1906.

D. Kahaner, C. Moler, and S. Nash. *Numerical methods and software.* Prentice-Hall, Englewood Cliffs, NJ, 1989.

J.T. Kiehl and K.E. Trenberth. Earth's anual global mean energy budget. *Bulletin of the American Meteorological Society*, 78:197–1208, 1997.

A. K. Kniffka. *Einfluß von Aerosol-, Wolken- und Bodenalbedoinhomogenitäten auf das dreidimensionale aktinische Strahlungsfeld in der Atmosphäre.* PhD thesis, Institute for Meteorology, University of Leipzig, 2006.

A. Kolmogorov. Local structure of turbulence in incompressible viscous fluid at a very high reynolds number. *Doklady Akademii Nauk SSSR*, 30:299–302, 1941.

J. Landgraf, O. P. Hasekamp, and T. Trautmann. Linearization of radiative transfer with respect to surface properties. *Journal of Quantitative Spectroscopy and Radiative Transfer*, 72:327–339, 2002.

D. E. Lane-Veron and R. C. J. Sommerville. Stochastic theory of radiative transfer through generalized cloud fields. *Journal of Geophysical Research*, 109, D18113, doi:10.1029/2004JD004524, 2004.

J. Lenoble. *Atmospheric radiative transfer*. Deepak Publishing, Hampton, Va., 1993.

K. N. Liou. *An introduction to atmospheric radiation*. Academic Press, New York, 1980.

K. N. Liou. *An introduction to atmospheric radiation*. Academic Press, New York, 2nd edition, 2002.

U. Löhnert, S. Crewell, and C. Simmer. An integrated approach toward retrieving physically consistent profiles of temperature, humidity, and cloud liquid water. *Journal of Applied Meteorology*, 43:1295–1307, 2004.

P. E. Loughlin. *Efficient calculations of UV changes due to atmospheric variability*. PhD thesis, School of Physics, University of New South Wales, 1995.

G. Maess. *Vorlesungen über numerische Mathematik*. Birkhäuser Verlag, Basel, 1988.

G. Marchuk, G. Mickhailov, M. Nazaraliev, R. Darbinjan, B. Kargin, and B. Elepov. *The Monte Carlo method in atmospheric optics*. Springer-Verlag, Berlin, 1980.

G. I. Marchuk. Equation for the value of information from weather satellites and formulation of inverse problems. *Cosmic Research*, 2:394–409, 1964.

A. Marshak and A.B. Davis. *3D Radiative transfer in cloudy atmospheres.* Springer, 2005.

A. Marshak, A. Davis, W. Wiscombe, and R. Cahalan. Radiative smoothing in fractal clouds. *Journal of Geophysical Research*, 100:26247–26261, 1995.

A. Marshak, A. Davis, R. F. Cahalan, and W. Wiscombe. Nonlocal independent pixel approximation: Direct and inverse problems. *IEEE Transactions on Geoscience and Remote Sensing*, 36:192–205, 1998.

A. Marshak, L. Oreopoulos, A. B. Davis, W. J. Wiscombe, and R. F. Cahalan. Horizontal radiative fluxes in clouds and accuracy of the independent pixel approximation at absorbing wavelength. *Geophysical Research Letters*, 26:1585–1588, 1999.

W.E. Meador and W.R. Weaver. Two-stream approximations to radiative transfer in planetary atmospheres: a unified description of existing methods and a new improvement. *Journal of the Atmospheric Sciences*, 37:630–643, 1980.

G. Mie. Beiträge zur Optik trüber Medien, speziell kolloidaler Metallösungen. *Annalen der Physik*, 25:377–445, 1908.

M. I. Mishchenko. Maxwell's equations, radiative transfer, and coherent backscattering: A general perspective. *Journal of Quantitative Spectroscopy and Radiative Transfer*, 101: 540–555, 2006.

M. I. Mishchenko, A. A. Lacis, B. E. Carlson, and L. D. Travis. Nonsphericity of dust-like tropospheric aerosols: Implications for aerosol remote sensing and climate modeling. *Geophysical Research Letters*, 22:1077–1080, 1995.

M. I. Mishchenko, L. D. Travis, and D. W. Mackowski. T-matrix computations of light scattering by nonspherical particles: a review. *Journal of Quantitative Spectroscopy and Radiative Transfer*, 55:535–575, 1996.

T. Z. Muldashev, A. I. Lyapustin, and U. M. Sultangazin. Spherical harmonics method in the problem of radiative transfer in the atmosphere-surface system. *Journal of Quantitative Spectroscopy and Radiative Transfer*, 61:393–404, 1999.

NCEP, 2005. URL `http://www.nco.ncep.noaa.gov/pmb/docs/on388/`.

W. O'Hirok and C. Gautier. A three-dimensional radiative transfer model to investigate the solar radiation within a cloudy atmosphere. Part I: Spatial effects. *Journal of the Atmospheric Sciences*, 55:2162–2179, 1998.

Y. Peng and U. Lohmann. Sensitivity study of the spectral dispersion of the cloud droplet size distribution on the indirect aerosol effect. *Geophysical Research Letters*, 30(10), 1507,doi:10.1029/2003GL017192, 2003.

G. W. Petty. Area-average solar radiative transfer in three-dimensionally inhomogeneous clouds: The independently scattering cloudlet model. *Journal of the Atmospheric Sciences*, 59:2910–2929, 2002.

I. Polonsky, S. Love, and A. Davis. Wide-angle lidar deployment at the ARM Southern Great Plains Site: Intercomparison of cloud property retrievals. *Journal of Atmospheric and Oceanic Technology*, 22:628–648, 2005.

I. N. Polonsky and A. B. Davis. Exponential tails in lidar returns from dense clouds: A theoretical proof and the dependence on physical parameters. *Proceedings of SPIE*, 5059: 15–20, 2003.

G. C. Pomraning. A variational principle for linear systems. *Journal of the Society for Industrial and Applied Mathematics*, 13:511–519, 1965.

QUEST Webpage, 2005. URL `http://loeffler.meteo.physik.uni-muenchen.de/quest/`.

Lord Rayleigh. On the light from the sky, its polarization and colour. *Philosophical Magazine*, 41:107–120, 1871.

B. Ritter and J.-F. Geleyn. A comprehensive radiation scheme for numerical weather prediction models with potential applications in climate simulations. *Monthly Weather Review*, 120:303–325, 1992.

M. L. Salby. *Fundamentals of atmospheric physics*. Academic Press, 1995.

R. Scheirer and S. Schmidt. CLABAUTAIR: A new algorithm for retrieving three-dimensional cloud structure from airborne microphysical measurements. *Atmospheric Chemistry and Physics*, 5:2333 – 2340, 2005.

U. Schumann, A. Dörnbrack, and B. Mayer. Cloud-shadow effects on the structure of the convective boundary layer. *Meteorologische Zeitschrift*, 11(4):285–294, 2002.

A. Slingo. A GCM parameterization for the SW radiative properties of water clouds. *Journal of the Atmospheric Sciences*, 46:1419–1427, 1989.

K. Stamnes, S. C. Tsay, W. Wiscombe, and K. Jayaweera. Numerically stable algorithm for discrete-ordinate-method radiative transfer in multiple scattering and emitting layered media. *Applied Optics*, 27:2502–2509, 1988.

G. E. Thomas and K. Stamnes. *Radiative transfer in the atmosphere and ocean*. Cambridge University Press, 1999.

E. A. Ustinov. Inverse problem of thermal sounding: Retrieval of vertical profile of the coefficient of absorption of an optically active constituent of the planetary atmosphere. *Cosmic Research*, 28:347–355, 1990.

E. A. Ustinov. Inverse problem of the photometry of the solar radiation reflected by an optically thick planetary atmosphere: Mathematical framework and weighting functions of the linearized inverse problem. *Cosmic Research*, 29:519–532, 1991.

H. C. v. d. Hulst. *Multiple light scattering (tables, formulas, and applications)*, volume 2. Academic Press, New York, 1980.

T. Várnai, 2006a. URL http://i3rc.gsfc.nasa.gov/cases_new.html.

T. Várnai, 2006b. URL http://i3rc.gsfc.nasa.gov/I3RC-intro.html.

T. Várnai and R. Davies. Effects of cloud heterogeneities on shortwave radiation: Comparison of cloud-top variability and internal heterogeneity. *Journal of the Atmospheric Sciences*, 56:4206–4224, 1999.

V. Venema, S. Meyer, S. G. García, A. Kniffka, C. Simmer, S. Crewell, U. Löhnert, T. Trautmann, and A. Macke. Surrogate cloud fields generated with the iterative amplitude adapted fourier transform algorithm. *Tellus A*, 58:104–120, 2006.

M. Wendisch, P. Pilewski, S. Jäkel, S. Schmidt, J. Pommier, S. Howard, H.H. Jonsson, H. Guan, M. Schröder, and B. Mayer. Airborne measurements of areal spectral surface albedo over different sea and land surfaces. *Journal of Geophysical Research*, 109, D08203, doi:10.1029/2003JD004392, 2004.

W. Zdunkowski and A. Bott. *Thermodynamics of the atmosphere.* Cambridge University Press, 2004.

T. Zinner. *Fernerkundung inhomogener Bewölkung und deren Einfluß auf die solare Strahlungsbilanz.* PhD thesis, Faculty of Physics, Ludwig-Maximilians-University Munich, 2004.

P. Zuidema and K. F. Evans. On the validity of the independent pixel approximation for boundary layer clouds observed during ASTEX. *Journal of Geophysical Research*, 103: 6059–6074, 1998.

Acknowledgment

Lebenslauf

Persönliche Daten:

Name	<u>Matthias</u> Peter Jerg
	geboren am 25. Januar 1975 in Ludwigshafen am Rhein
Adresse	Meginhardstr. 33
	82205 Gilching

Schulbildung:

1981–1985	Grundschule Flomborn
1985–1994	Elisabeth-Langgässer-Gymnasium Alzey
	Schulabschluß: Allgemeine Hochschulreife

Wehrdienst:

1994–1995	Grundwehrdienstleistender

Studium:

10/1995 – 01/2002	Meteorologiestudium, Johannes Gutenberg-Universität Mainz
01/2002	Diplom in Meteorologie
	Titel der Diplomarbeit: "Implementation einer hochreichenden Filterung in ein nichthydrostatisches mesoskaliges Klimamodell"
03/2002 – 02/2003	Forschungs- und Praktikumsaufenthalt an der School of Physics, University of New South Wales, Sydney, Australien
04/2003 – 09/2006	Anfertigung der Dissertation Doktorand am Institut für Meteorologie, Ludwig-Maximilians-Universität München und parallel Gast am Institut für Methodik der Fernerkundung des Deutschen Zentrums für Luft- und Raumfahrt angestellt am Institut für Meteorologie der Universität Leipzig.